

Experimental Investigation of Stirling Engine Modelling Techniques at Reduced Source  
Temperatures

by

David Andrew Miller

A thesis submitted in partial fulfillment of the requirements for the degree of

Master of Science

Department of Mechanical Engineering  
University of Alberta

© David Andrew Miller, 2019

---

# ABSTRACT

---

A Stirling engine was studied experimentally with two objectives. The first was to determine the effects of flywheel polar moment of inertia on the transient and steady-state performance of a Stirling engine. The second was to investigate the accuracy of a 2<sup>nd</sup> order thermodynamic model with a range of thermal source temperatures and determine how to best improve the model for low-temperature difference Stirling engines.

Experiments were performed on a low-temperature configuration of the ST05G-CNC Stirling engine. It was heated with electric cartridge heaters, cooled with 21°C water, and charged with air at 517 kPa or 621 kPa. Sensors measured the angular position of the crankshaft, torque load on the engine, gas temperatures, coolant temperatures, and gas pressures. Experiments examined the transition from engine startup to free-running, steady-state and loaded, steady-state operation.

A 2<sup>nd</sup> order model that was primarily constructed from procedures in literature was studied. The model calculated the reference cycle with an adiabatic model of the engine with imperfect heat transfer in the heater, regenerator, and cooler. Decoupled loss calculations determined the heat exchanger flow friction, appendix gap losses, conduction loss, gas spring hysteresis, and mechanical losses. An iterative correction was added so the model would reflect the experimentally measured gas temperatures in the expansion space and compression space.

The transient and steady-state behavior of the low-temperature ST05G was studied experimentally with four flywheel polar moments of inertia. Flywheel polar moment of inertia did not change the free-running, steady-state engine frequency, except for one case. This case had a higher steady-state frequency and was from experiments with the smallest flywheel at the lower of two charge pressures. Increased flywheel polar moment of inertia increased the settling time of

the transient engine frequency and decreased the overshoot of the engine frequency. At loaded, steady-state operation, increased flywheel polar moment of inertia decreased the angular velocity fluctuations. This did not significantly influence the shaft power or thermodynamics. The angular velocity fluctuated twice per cycle, as one would expect from the Fundamental Efficiency Theorem. A method to calculate flywheel size was developed from the Fundamental Efficiency Theorem. The method estimated the order of magnitude of flywheel polar moment of inertia.

The 2<sup>nd</sup> order model was compared to experiments at seven thermal source temperatures from 242 °C to 418 °C. The model inaccurately estimated engine performance at all conditions and less accurately estimated engine performance at lower thermal source temperatures. Methods to improve the model were deduced from the inaccuracies. The reference cycle of the model could improve if a semi-adiabatic model that includes leakage replaces the adiabatic model. This change may also improve the accuracy of the mechanical losses. To improve the accuracy of the decoupled power losses, the model could employ a more sophisticated mechanical loss calculation and replace the current gas spring hysteresis correlation. The model would have to be evaluated again to confirm that these changes improved its accuracy.

---

# PREFACE

---

This thesis is an original work by David Miller. Aspects of this research have been published in the following conference publications:

Speer, C.P., Michaud, J.P., Miller, D.A., Stumpf, C.J.A. and Nobes, D.S. (2017) Empirical Heat Transfer Correlations of Finned-Tube Heat Exchangers in Pulsatile Flow. World Academy of Science, Engineering and Technology, International Journal of Mechanical, Aerospace, Industrial, Mechatronic and Manufacturing Engineering, 11(6), 1150-1155.

Speer, C.P., Michaud, J.P., Miller, D.A., Stumpf, C.J.A. and Nobes, D.S. (2017) 'Empirical heat transfer correlations of finned-tube heat exchangers in oscillating flow for low temperature Stirling engines', ICFMHTT 2017: 19th International Conference on Fluid Mechanics, Heat Transfer and Thermodynamics, Venice, Italy June, 21-22, 2017

Speer, C.P., Michaud, J.P., Miller, D.A., Stumpf, C.J.A. and Nobes, D.S. (2017) 'Modification of an ST05G-CNC Stirling Engine to Use a Low Temperature Heat Source', AIAA-2017-4793, 14th International Energy Conversion Engineering Conference, AIAA Propulsion and Energy Forum 2017, Atlanta, Georgia, USA, July, 10-12, 2017

Speer, C.P., Miller, D.A. and Nobes, D.S. (2017) "Preliminary Model Validation for a Gamma Type Stirling Engine", Okanagan Fluid Dynamics Meeting, Kelowna, British Columbia, Canada, Aug 22-23, 2017

Michaud, J.P., Miller, D.A., Speer, C.P., Nicol-Seto, M. and Nobes, D.S. (2017) "Dimensionless Heat Transfer Correlations of Finned-Tube Radiators in Fully Reversed Oscillating Flow", Okanagan Fluid Dynamics Meeting, Kelowna, British Columbia, Canada, Aug 22-23, 2017

Miller, D.A., Speer, C.P. and Nobes, D.S. (2018) Performance of ST05G-CNC Stirling Engine Modified for Operation with Reduced Source Temperature, 18th ISEC International Stirling Engine Conference, Tainan, Taiwan, Sept 19-21, 2018

---

# ACKNOWLEDGEMENTS

---

The author appreciates the assistance of his supervisor,

Dr. David S. Nobes

lab mates (Team Stirling),

Connor Speer

Calynn Stumpf

Jason Michaud

Steven Middleton

Michael Nicol-Seto

Linda Hasanovich

Alex Hunt

Gabriel Salata

Jackson Kutzner

co-op students, volunteers, and others that helped make this project a success.

The author would also like to recognize the financial support for this project from:

Natural Sciences and Engineering Research Council (NSERC) of Canada,

Alberta Innovates Energy and Environment Solutions,

Innovative Solar Power,

Terrapin Geothermics, and

Future Energy Systems (FES).

---

# TABLE OF CONTENTS

---

Abstract .....	ii
Preface.....	iv
Acknowledgements.....	v
Table of Contents.....	vi
List of Tables .....	xiv
List of Figures .....	xvi
List of Symbols.....	xxi
1 Introduction .....	1
1.1 Motivation.....	2
1.1.1 Competing Technology .....	3
1.2 Introduction to Stirling Engines .....	5
1.2.1 The Ideal Stirling Cycle.....	5
1.2.2 Components of Stirling Engines.....	9
1.2.3 The Thermodynamic Cycle of Real Stirling Engines.....	13
1.2.4 Stirling Engine Configurations.....	14
1.3 Kinematic Stirling Engines .....	19
1.3.1 Kinematic Stirling Engine Work Transfer.....	19
1.3.2 Slider-Crank, Gamma-Type Stirling Engine Volume Functions .....	22

1.4	Stirling Engine Thermodynamic Models .....	27
1.4.1	1 <sup>st</sup> Order Models .....	27
1.4.2	2 <sup>nd</sup> Order Model Reference Cycles.....	29
1.4.3	Decoupled Losses .....	37
1.4.4	3 <sup>rd</sup> Order Models.....	46
1.4.5	Dynamic Models for Kinematic Stirling Engines .....	46
1.5	Low-Temperature-Difference Stirling Engines .....	48
1.5.1	LTDSE Characteristics .....	48
1.5.2	LTDSE Models and Validation .....	50
1.6	The ST05G Stirling Engine.....	53
1.6.1	ST05G-CNC Construction .....	53
1.6.2	ST05G and Derivative Engines in Literature .....	56
1.7	Stirling Engine Flywheel Size.....	63
1.7.1	Flywheel Size .....	64
1.7.2	Stirling Engine Flywheels in Literature.....	65
1.8	Thesis Objectives and Structure.....	69
2	Experiment Setup and Procedures.....	70
2.1	Low-Temperature ST05G Stirling Engine.....	72
2.1.1	Heater.....	73
2.1.2	Regenerator.....	73

2.1.3	Cooler .....	74
2.1.4	Displacer .....	74
2.1.5	Connecting Pipe.....	74
2.1.6	Piston and Power Cylinder .....	76
2.1.7	Mechanism.....	77
2.1.8	Crankcase.....	78
2.1.9	Variable Inertia Flywheel .....	79
2.2	Operating Condition Management .....	81
2.2.1	Thermal Source.....	81
2.2.2	Thermal Sink .....	82
2.2.3	Charge Pressure .....	83
2.2.4	Engine Frequency and Load Torque .....	85
2.3	Instrumentation.....	86
2.3.1	Crankshaft Angular Position .....	86
2.3.2	Crankshaft Torque .....	89
2.3.3	Working Gas Temperature .....	89
2.3.4	Coolant Temperature .....	92
2.3.5	Working Gas Pressure .....	95
2.4	Data Acquisition.....	101
2.4.1	Transient Experiment Data Acquisition .....	102



2.4.2	Steady-State Data Acquisition.....	103
2.5	Experiment Procedures .....	104
2.5.1	Experiment Start-Up.....	104
2.5.2	Transient Experiments.....	105
2.5.3	Steady-State Experiments.....	106
2.5.4	Experiment Cool-Down.....	107
2.6	Data Processing.....	110
2.6.1	Angular position from rotary encoder .....	112
2.6.2	Voltage Data Averaging .....	113
2.6.3	Instantaneous Angular Velocity Calculation.....	114
2.6.4	Data Cropping.....	115
2.6.5	Thermocouple Data Averaging .....	116
2.6.6	RTD Data Averaging.....	116
2.6.7	Data Sorting.....	117
2.6.8	Engine Volumes and Volume Changes .....	118
2.6.9	Indicated Work .....	118
2.6.10	Shaft Power.....	118
2.6.11	Modelling of Experiment Results.....	118
2.7	Experimental Uncertainty .....	119
2.7.1	Random Uncertainty.....	119

2.7.2	Systematic Uncertainty.....	119
2.7.3	Angular Velocity Uncertainty .....	120
2.7.4	Pressure Wave Transport Uncertainty.....	120
2.7.5	Volume and Volume Change Uncertainty.....	122
2.7.6	Propagation of Uncertainty.....	123
2.7.7	Indicated Work Uncertainty .....	123
2.8	Experiment Setup and Procedures Summary .....	124
3	2 <sup>nd</sup> Order Thermodynamic Model .....	125
3.1	Volumes and Volume Changes.....	127
3.1.1	Constant Volume Spaces.....	127
3.1.2	Variable Volume Spaces .....	127
3.2	Reference Cycle .....	128
3.2.1	Adiabatic Model .....	129
3.2.2	Regenerator Simple Analysis .....	131
3.2.3	Heater and Cooler Simple Analysis.....	133
3.2.4	Combined Adiabatic Model and Simple Analysis Solution.....	134
3.3	Mass and Temperature Correction .....	136
3.3.1	Mass of Working Gas Correction.....	136
3.3.2	Heat Exchanger Wall Temperature Correction .....	137
3.4	Decoupled Losses.....	140

3.4.1	Heat Exchanger Flow Friction.....	140
3.4.2	Appendix Gap Losses.....	141
3.4.3	Conduction Loss.....	141
3.4.4	Gas Spring Hysteresis.....	143
3.4.5	Mechanical Losses.....	143
3.4.6	Decoupled Loss Inclusion.....	143
3.5	Summary.....	145
4	The Influence of Flywheel Size on Stirling Engine Performance.....	146
4.1	Flywheel Size Influence on Transient Engine Frequency.....	147
4.1.1	Transient Engine Frequency.....	148
4.1.2	Steady-State Engine Frequency.....	150
4.1.3	Settling Time.....	152
4.1.4	Frequency Overshoot.....	153
4.1.5	Transient Engine Frequency Summary.....	154
4.2	Flywheel Size Influence on Steady-State Performance.....	155
4.2.1	Angular Velocity Fluctuations.....	155
4.2.2	Coefficient of Speed Fluctuation.....	158
4.2.3	Shaft Power.....	161
4.2.4	Indicator Diagrams.....	163
4.2.5	Steady-State Performance Summary.....	166

4.3	Flywheel Size from the Fundamental Efficiency Theorem .....	168
4.3.1	FET Method Description .....	168
4.3.2	FET Method Validation.....	170
4.3.3	FET Method Summary .....	176
4.4	Conclusions .....	177
5	The Accuracy of a 2 <sup>nd</sup> Order Thermodynamic Model at Reduced Thermal Source Temperature .....	179
5.1	Overall Model Accuracy .....	182
5.1.1	Shaft Power Accuracy .....	182
5.1.2	West Number Accuracy.....	185
5.1.3	Overall Model Accuracy Summary .....	187
5.2	Reference Cycle Accuracy .....	188
5.2.1	Indicated Work Accuracy .....	188
5.2.2	Cumulative Indicator Diagram Difference .....	191
5.2.3	Dimensionless Indicator Diagrams.....	194
5.2.4	Reference Cycle Accuracy Summary .....	197
5.3	Decoupled Power Losses Accuracy .....	199
5.3.1	Mechanical Efficiency .....	199
5.3.2	Gas Spring Hysteresis.....	202
5.3.3	Forced Work .....	204

5.3.4	Decoupled Loss Summary.....	206
5.4	Model Accuracy Summary.....	208
6	Conclusions.....	210
	References.....	212
	Appendixes.....	222

---

# LIST OF TABLES

---

Table 1-1: List of operating conditions and performance of three ST05G configurations.....	61
Table 1-2: Minimum thermal source temperatures of modified ST05G configurations [79].....	62
Table 1-3: List of coefficients of speed fluctuation for historic Stirling engine applications [81]. .....	64
Table 1-4: Operating condition, flywheel polar moment of inertia, and coefficient of speed fluctuation of engines simulated with dynamic models. ....	68
Table 2-1: List of flywheel properties. ....	79
Table 2-2: Range of operating conditions studied in experiment and the possible ranges with the current equipment. ....	81
Table 2-3: List of data acquisition start times.....	115
Table 2-4: Example of pressure wave transport uncertainty calculation. ....	122
Table 3-1: List of temperatures and performance metrics from an experiment, the MCM, and the M&TCM (used in this work).....	138
Table 3-2: List of conduction loss parameters [79]. ....	142
Table 4-1: List of the constant and manipulated parameters of the transient experiments.....	147
Table 4-2: The steady-state engine frequency of the transient experiments for all flywheels at both charge pressures.....	150
Table 4-3: The steady-state engine frequency, gas temperature difference, and mean pressure of the transient experiments for all flywheels at the 517 kPa charge pressure. ....	151
Table 4-4: List of settling times from engine start for all flywheel configurations and both charge pressures. ....	152

Table 4-5: List of overshoot frequencies for all flywheel configurations and both charge pressures.  
..... 153

Table 4-6: List of the constant and manipulated parameters of the steady-state experiments. .. 155

Table 4-7: List of parameters for the dimensionless indicator diagrams presented in Figure 4-5.  
..... 164

Table 4-8: List of variables to calculate flywheel polar moment of inertia with the FET method.  
..... 171

Table 4-9: List of variables to calculate flywheel polar moment of inertia with the method from  
Scollo et al [82]..... 172

Table 4-10: Comparison of the flywheel size calculation methods..... 173

Table 5-1: List of the constant and controlled parameters of the steady-state experiments. .... 180

Table 5-2: List of operating conditions for the dimensionless indicator diagrams in Figure 5-8.  
..... 195

---

# LIST OF FIGURES

---

Figure 1-1: Schematic of a generic thermodynamic cell undergoing (a) isochoric heat addition, (b) isothermal expansion, (c) isochoric heat rejection and (d) isothermal compression. ....	6
Figure 1-2: Indicator diagram of the ideal Stirling cycle.....	9
Figure 1-3: Schematic of generic gamma-type Stirling engine. ....	10
Figure 1-4: Indicator diagram of a real Stirling engine. ....	13
Figure 1-5: Schematic of a Generic Beta-Type Stirling Engine .....	15
Figure 1-6: Schematics of the ideal Stirling cycle in a gamma-type Stirling engine. ....	16
Figure 1-7: Schematics of the ideal Stirling cycle in an alpha-type Stirling engine.....	18
Figure 1-8: (a) A schematic of a piston undergoing efficacious work and (b) an indicator diagram showing efficacious work in a Stirling engine. ....	20
Figure 1-9: (a) A schematic of a piston undergoing forced work and (b) an indicator diagram showing forced work in a Stirling engine.....	21
Figure 1-10: Energy transfer diagram of a kinematic heat engine, <i>after Senft</i> [32]. ....	22
Figure 1-11: Schematic of a generic slider-crank mechanism, <i>after Cleghorn and Dechev</i> [33].	23
Figure 1-12: Schematic of a 90 ° gamma-type Stirling engine slider-crank mechanism. ....	24
Figure 1-13: Schematic of generic thermodynamic unit cell for zero-dimensional Stirling engine models <i>after Urieli and Berchowitz</i> [29].....	30
Figure 1-14: Temperature distribution and engine schematic for the ideal isothermal model <i>after Urieli and Berchowitz</i> [29].....	31
Figure 1-15: Temperature distribution and engine schematic for the ideal adiabatic model <i>after Urieli and Berchowitz</i> [29].....	33



Figure 1-16: Diagrams of (a) shuttle transfer and (b) gas enthalpy transfer appendix gap losses.	39
Figure 1-17: Pressure-volume diagram of an arbitrary, finite volume buffer space with non-zero, finite heat transfer.	42
Figure 1-18: Energy transfer diagram for FET, <i>after Senft</i> [32].	45
Figure 1-19: Flow chart of a dynamic model solution process, <i>after Cheng and Yu</i> [35].	47
Figure 1-20: CAD model of the original ST05G-CNC Stirling engine.	54
Figure 1-21: Free body diagram of a flywheel, <i>after Cleghorn and Dechev</i> [33].	63
Figure 2-1: Image of the low-temperature ST05G test cart and data acquisition equipment.	71
Figure 2-2: CAD model of the low-temperature ST05G Stirling engine.	72
Figure 2-3: Cross-section of the low-temperature ST05G heater.	73
Figure 2-4: Top view of the low-temperature ST05G cooler.	74
Figure 2-5: Section views of the original [79] (a) and modified (b) connecting pipe.	75
Figure 2-6: Image of the as-built piston assembly and the 44 mm piston-cylinder set.	76
Figure 2-7: Section view of the precision glass cylinder and mounting components.	77
Figure 2-8: Front and top views of the four flywheel configurations: (a) configuration A, (b) configuration B, (c) configuration C, and (d) configuration D.	80
Figure 2-9: P&ID of the thermal source and heating system.	82
Figure 2-10: P&ID of the coolant circuit and coolant temperature measurement system.	83
Figure 2-11: P&ID of the charge pressure system.	84
Figure 2-12: Image of the friction brake and shaft power measurement instruments on the output shaft of the engine.	85
Figure 2-13: Image of the rotary encoder, timing belt, and pulleys.	87
Figure 2-14: P&ID of the crankshaft torque and position measurement systems.	88

Figure 2-15: Image of a thermocouple used for working gas temperature measurements. ....	90
Figure 2-16: P&ID of the working gas temperature measurement system.....	91
Figure 2-17: Plots of (a) un-calibrated and (b) calibrated thermocouple measurement error at corresponding absolute temperatures. ....	92
Figure 2-18: Image of a RTD used for coolant temperature measurements.....	93
Figure 2-19: Section view of the RTD elbow assembly.....	93
Figure 2-20: Plots of (a) un-calibrated and (b) calibrated RTD measurement error at corresponding thermometer temperatures. ....	95
Figure 2-21: P&ID of the working gas pressure measurement system. ....	96
Figure 2-22: Images of the (a) power cylinder and (b) crankcase static pressure transducers. ....	97
Figure 2-23: Plots of (a) un-calibrated and (b) calibrated Validyne pressure transducer measurement error at corresponding calibration device pressures (absolute pressure).....	99
Figure 2-24: (a) Images of both dynamic pressure transducers with dimensions and (b) an image of a dynamic pressure transducer mounted flush in the power cylinder head.....	100
Figure 2-25: Screenshot of the data acquisition program user interface. ....	101
Figure 2-26: Plot of the transient engine frequency and transient cooler heat transfer rate. ....	102
Figure 2-27: Data processing program flow chart. ....	111
Figure 2-28: Plot of raw voltage data from the rotary encoder.....	112
Figure 2-29: Plot of raw voltage data averaged from the torque transducer and pressure sensors. .....	113
Figure 2-30: Plot of the angular position with time and the fit quadratic polynomial curve used to calculate angular velocity. ....	114

Figure 2-31: Plot of raw thermocouple data averaged in intervals of 10 discrete angular positions. .....	116
Figure 2-32: Plot of some raw RTD data averaged over a complete rotation. ....	117
Figure 3-1: Flow chart of the 2 <sup>nd</sup> order thermodynamic model. ....	126
Figure 3-2: Engine schematic and working gas temperature distribution in the adiabatic model with the Simple Analysis <i>after Urieli and Berchowitz</i> [29]. ....	129
Figure 3-3: Ideal and imperfect regenerator temperature distribution <i>after Urieli and Berchowitz</i> [29]. ....	132
Figure 3-4: Experimental, MCM, and M&TCM dimensionless indicator diagrams. ....	139
Figure 4-1: Plots of the free, transient engine frequency from start for all flywheels with (a) 517 kPa and (b) 621 kPa charge pressure. ....	149
Figure 4-2: Plots of the phase-averaged relative angular velocity with crank angle for four flywheel configurations at (a) 517 kPa and (b) 621 kPa charge pressure. ....	157
Figure 4-3: Plots of the coefficient of speed fluctuation for four flywheel configurations at (a) 517 kPa and (b) 621 kPa charge pressure with fit curves. ....	159
Figure 4-4: Experimental shaft power for four flywheel configurations at (a) 517 kPa and (b) 621 kPa charge pressure with fit curves. ....	162
Figure 4-5: Dimensionless indicator diagrams for flywheel configurations and charge pressures defined in Table 4-7. ....	165
Figure 4-6: Arbitrary indicator diagram with efficacious and forced work areas. ....	169
Figure 4-7: Energy transfer diagram of the flywheel in the Fundamental Efficiency Theorem. ....	170
Figure 4-8: Plots of the coefficient of speed fluctuation difference for four flywheels at (a) 517 kPa and (b) 621 kPa charge pressures. ....	175

Figure 5-1: Shaft power curves of the engine charged to (a) 517 kPa and (b) a 621 kPa. ....	181
Figure 5-2: Plot of the relative shaft power difference at (a) a 517 kPa charge pressure and (b) a 621 kPa charge pressure. ....	184
Figure 5-3: Plots of the relative West number difference at (a) the 517 kPa charge pressure and (b) the 621 kPa charge pressure. ....	186
Figure 5-4: Modelled (a) and experimental (b) indicator diagrams with indicated work filled. ....	189
Figure 5-5: Plot of the relative indicated work difference at (a) the 517 kPa charge pressure and (b) the 621 kPa charge pressure with fit curves.....	190
Figure 5-6: Arbitrary indicator diagram with the indicator diagram difference area filled.....	192
Figure 5-7: Plot of the cumulative indicator diagram difference at (a) the 517 kPa charge pressure and (b) the 621 kPa charge pressure with fit curves.....	193
Figure 5-8: Dimensionless indicator diagrams for the maximum power experiments at the operating conditions: (a) $T_H = 271$ °C and $p_T = 517$ kPa, (b) $T_H = 271$ °C and $p_T = 620$ kPa, (c) $T_H = 359$ °C and $p_T = 517$ kPa, and (d) $T_H = 359$ °C and $p_T = 620$ kPa. ....	196
Figure 5-9: Plot of the mechanical efficiency difference at (a) the 517 kPa charge pressure and (b) the 621 kPa charge pressure with fit curves. ....	201
Figure 5-10: Plot of the relative GSH difference at (a) the 517 kPa charge pressure and (b) the 621 kPa charge pressure with fit curves. ....	203
Figure 5-11: Plot of the normalized forced work difference at (a) the 517 kPa charge pressure and (b) the 621 kPa charge pressure.....	205

---

# LIST OF SYMBOLS

---

## Roman Alphabet Variables

Variable	Definition	Units
$A$ :	Area	$m^2$
$b$ :	Appendix Gap Width	m
$c_p$ :	Isobaric Specific Heat Capacity	J / kg
$CS$ :	Coefficient of Speed Fluctuation	-
$c_v$ :	Isochoric Specific Heat Capacity	J / kg
$d$ :	Diameter	m
$E$ :	Mechanism Effectiveness	-
$f$ :	Engine Frequency	Hz
$f_{overshoot}$ :	Overshoot Engine Frequency	Hz
$f_{Reynolds}$ :	Reynolds Friction Factor	-
$h$ :	Coefficient of Convective Heat Transfer	W / $m^2$ K
$I$ :	Polar Moment of Inertia	kg m <sup>2</sup>
$k$ :	Thermal Conductivity	W / m K
$KE$ :	Kinetic Energy	J
$l$ :	Length	m
$m$ :	Mass	kg
$\dot{m}$ :	Mass Flow Rate or Angular Mass Flow Rate	kg / s, or kg / rad
$MEP$ :	Mean Effective Pressure	Pa
$n$ :	Number of Samples	-
$N_B$ :	Beale Number	-
$N_{polytropic}$ :	Polytropic Exponent	-
$NTU$ :	Number of Transfer Units	-
$N_W$ :	West Number	-
$p$ :	Pressure	kPa
$Pr$ :	Prandtl Number	-
$Q$ :	Heat Transfer	J

---

Variable	Definition	Units
$Q$ :	Heat Transfer Rate	W
$R$ :	Gas Constant	J / kg K
$Re$ :	Reynolds Number	-
$S$ :	Piston or Displacer Stroke	m
$St$ :	Stanton Number	-
$T$ :	Temperature	K
$t$ :	Time	s
$t_{settle}$ :	Settling Time	s
$U$ :	Uncertainty	-
$V$ :	Volume	m <sup>3</sup>
$v$ :	Velocity	m / s
$V_{cld}$ :	Displacer Clearance Volume	m <sup>3</sup>
$V_{clp}$ :	Piston Clearance Volume	m <sup>3</sup>
$V_{dead}$ :	Dead Volume	m <sup>3</sup>
$V_{sw}$ :	Engine Swept Volume	m <sup>3</sup>
$V_{swd}$ :	Displacer Swept Volume	m <sup>3</sup>
$V_{swp}$ :	Piston Swept Volume	m <sup>3</sup>
$W$ :	Work	J
$\dot{W}$ :	Power	W

## Greek Alphabet Variables

Variable	Definition	Units
$\alpha$ :	Thermal Diffusivity	$\text{m}^2 / \text{s}$
$\gamma$ :	Specific Heat Ratio	-
$\Delta pV^*$ :	Cumulative Indicator Diagram Difference	-
$\varepsilon$ :	Heat Transfer Effectiveness	-
$\eta$ :	Efficiency	-
$\theta$ :	Angular Position (Crankshaft Position)	rad
$\dot{\theta}$ :	Angular Velocity	rad / s
$\mu$ :	Dynamic Viscosity	kg / m s
$\sigma$ :	Standard Deviation	-
$\tau$ :	Torque	N m
$\phi$ :	Displacer Phase Angle	rad
$\psi$ :	Engine Pressure Phase Angle	rad

## Subscripts

Subscript	Definition
<i>A</i> :	Rotary Encoder A-Pulse
<i>adiab</i> :	From the Adiabatic Model
<i>b</i> :	Buffer Space
<i>C</i> :	Thermal Sink
<i>c</i> :	Compression Space
<i>Carnot</i> :	Carnot Efficiency
<i>charge</i> :	Charge Pressure
<i>comp</i> :	Compression Stroke
<i>conduction</i> :	Due to Conduction
<i>cool</i> :	Of the Coolant
<i>cross-section</i> :	Cross-Sectional Area
<i>d</i> :	Displacer
<i>E</i> :	Engine
<i>e</i> :	Expansion Space
<i>Eff</i> :	Efficacious Work
<i>exp</i> :	Expansion Stroke
<i>F</i> :	Forced Work
<i>FET</i> :	Fundament Efficiency Theorem
<i>fly</i> :	Flywheel
<i>FPS</i> :	Finite Piston Speed Loss
<i>friction</i> :	Due to Mechanical Friction
<i>g</i> :	For the Working Gas
<i>GSH</i> :	Gas Spring Hysteresis
<i>H</i> :	Thermal Source
<i>h</i> :	Heater
<i>I</i> :	Indicated or Indicator Diagram
<i>i</i> :	For an Arbitrary Engine Cell
<i>in</i> :	Into a Control Volume
<i>k</i> :	Cooler
<i>leak</i> :	Due to Leakage



Subscript	Definition
<i>load</i> :	Resistive Torque Acting on Engine
<i>max</i> :	Maximum
<i>mean</i> :	Mean
<i>mec</i> :	Mechanism
<i>min</i> :	Minimum
<i>new</i> :	From Current Iteration
<i>old</i> :	From Previous Iteration
<i>other</i> :	From Other Components
<i>out</i> :	Out of a Control Volume
<i>p</i> :	Piston
<i>pump</i> :	Due to Gas Enthalpy Transport
<i>r</i> :	Regenerator
<i>S</i> :	Shaft
<i>shuttle</i> :	Due to Shuttle Transfer
<i>simple</i> :	From the Simple Analysis
<i>steady-state</i> :	At Steady-State
<i>w</i> :	On the Surface or Wall
<i>wetted</i> :	Area of a Solid in Contact With a Fluid
<i>Z</i> :	Rotary Encoder Z-Pulse

---

# 1 INTRODUCTION

---

This chapter provides the relevant knowledge to comprehend this research. It begins with a brief section outlining the motivation for this work. That is followed by an introduction to kinematic Stirling engines and an overview of Stirling engine modelling techniques. Next, a summary of the literature related to low-temperature-difference Stirling engines, the ST05G Stirling engine, and Stirling engine flywheels is presented. The chapter concludes with the objectives and outline for the remainder of this thesis.

## 1.1 Motivation

---

The recent special report by the Intergovernmental Panel on Climate Change (IPCC) [1] identifies the risk of global warming greater than 1.5 °C. Probable consequences include reduced biodiversity, sea level rise, increased poverty, and more natural disasters [1]. The severity of these consequences increases with additional global warming above 1.5 °C [1]. The recommended solution is to eliminate greenhouse gas (GHG) emissions before 2040 [1].

The electricity industry in Alberta produced 59 % of Canada's GHG emissions from electricity generation in 2015 [2]. This is the result of coal and natural gas combustion power facilities accounting for 89 % of Alberta's total electricity generation (82.4 TWh in 2017) [2]. The Alberta government plans to phase out electricity generation from coal combustion by 2030 to mitigate GHG emissions [3]. To significantly reduce GHG emissions, renewable energy technologies should replace the current coal combustion electricity generation facilities.

Coal power provides base load electricity in Alberta [4]. Coal facilities in Alberta had a capacity factor (CF)—the fraction of the actual electricity delivered to the grid to the potential electricity generation—of 67 % in 2017 [4]. Hydro power and wind power—the prominent renewable electricity sources in Alberta—had CFs near 25 % and 35 %, respectively [4]. These renewable electricity sources are not reliable enough to replace the base load electricity generated by the existing coal facilities. As a result, high-CF renewable electricity technologies are necessary to generate base load electricity in Alberta.

Geothermal heat and industrial waste heat are potential renewable energy sources for base load electricity in Alberta [5,6]. Alberta has 139 GW of geothermal heat suitable for power generation at 5 % recovery [7]. Seventeen industrial facilities in the Edmonton area produce enough waste

heat to generate 5 MW of electricity at 33 % recovery[6]. Both of these energy sources require technology capable of converting heat at temperatures as low as 80 °C to electricity [5,6].

Stirling engines convert heat from external sources to mechanical work [8]. The source of heat, because it is external, can be combustion exhaust, solar radiation, nuclear fission, and hot fluids [9,10]. Stirling engines are capable of operating with a temperature difference as low as 0.5 °C [11]. They are a technology capable of converting low-grade heat (<150 °C) to mechanical energy or electricity [10]. Commercial systems are available that convert heat above 150 °C to up to 25 kW electricity [12]. Attempts to commercialize Stirling engines for low-grade heat applications have been less successful [13].

Historic applications for Stirling engines include automobile propulsion, remote electricity generation, and domestic combined heat and power [14,15]. These applications typically relied on combustion and higher-grade heat (>450 °C) [14,15]. Consequently, more resources have been devoted to high-temperature-difference Stirling engines (HTDSEs) [14]. More specifically, many thermodynamic models, used to predict engine performance and evaluate designs, have been validated with HTDSEs [16]. The influence of specific loss mechanisms in low-temperature-difference Stirling engines (LTDSEs) is different than in HTDSEs [17,18]. As a result, the validity of these modelling methods comes into question.

### 1.1.1 Competing Technology

Stirling engines are not the only technology capable of generating electricity for low-grade heat sources. Rankine cycle systems and thermo-electric generators (TEGs) are other technologies with potential for low-grade heat conversion [19–21]. The potential applications and commercial status of these technologies are described below.

### 1.1.1.1 Rankine Cycle Systems

Organic Rankine cycle systems (ORCs) and Kalina cycle systems operate on the Rankine cycle with low-grade heat [22–24]. ORCs use an organic working fluid that usually has a boiling temperature below that of water at atmospheric pressure [22]. Current ORCs can convert 116 °C heat sources to 35 kW electricity with 5.4 % efficiency [19]. Most commercial ORCs are larger than 200 kW power output and require heat sources above 150 °C [22]. The Kalina cycle uses an ammonia-water mixture where more ammonia evaporates than water. This allows the Kalina cycle to be more efficient than ORCs [24]. Commercial systems can utilize heat sources at as low as 80 °C and are built at scales down to 50 kW electricity [20]. These systems are more complex and expensive than Stirling engine systems at smaller scales because they require turbines, compressors, pumps, and condensers [10].

### 1.1.1.2 Thermoelectric Generators

TEGs are solid state heat engines that directly convert heat into electricity using the Seebeck effect [21]. TEG efficiency depends on the material properties and the heat source and sink temperatures [21]. They are simple devices but current TEGs are inefficient compared to Stirling engines and ORCs [21]. Moreover, TEGs are not expected to become as efficient as well developed Stirling engines, ORCs, and Kalina cycle systems [21].

## 1.2 Introduction to Stirling Engines

---

Stirling engines convert heat to work with a closed, regenerative thermodynamic cycle [25]. The ideal Stirling cycle is a simplified thermodynamic cycle useful for describing the principles of Stirling engines [25]. However, Stirling engines are more complex machines than the ideal Stirling cycle presents [25]. The following sub-sections describe the ideal Stirling cycle, Stirling engine components, Stirling engine types, and the thermodynamic cycle in practical Stirling engines.

### 1.2.1 The Ideal Stirling Cycle

The ideal Stirling cycle consists of four sequential thermodynamic processes—isochoric heat addition, isothermal expansion, isochoric heat rejection, and isothermal compression [9]. A regenerator absorbs all the heat from the isochoric heat rejection process and returns it during the isochoric heat addition process [9]. It is one of the Reitlinger cycles which ideally perform at the Carnot efficiency, the maximum thermal efficiency of a heat engine with a given thermal source and thermal sink temperature ( $T_H$  and  $T_C$ ), as shown in Equation 1-1 [26]. To accomplish this, the ideal cycle assumes that: the working fluid is an ideal gas, regeneration is perfect, heat exchange is perfect, the machine is frictionless, the engine does not leak, the processes are discontinuous, and the processes are reversible [9].

$$\eta_{Carnot} = 1 - \frac{T_C}{T_H} \quad 1-1$$

The following sub-sections describe the thermodynamic processes of the ideal Stirling cycle. Figure 1-1 (a-d) depict the schematics of a generic thermodynamic cell undergoing the ideal Stirling cycle processes. The working volume of a Stirling engine ( $V_E$ ) is the internal, closed

volume of the engine contained by the piston. The working gas of a Stirling engine is a fixed mass of gaseous working fluid that occupies the entire working volume. It has properties of temperature ( $T_E$ ) and pressure ( $p_E$ ).

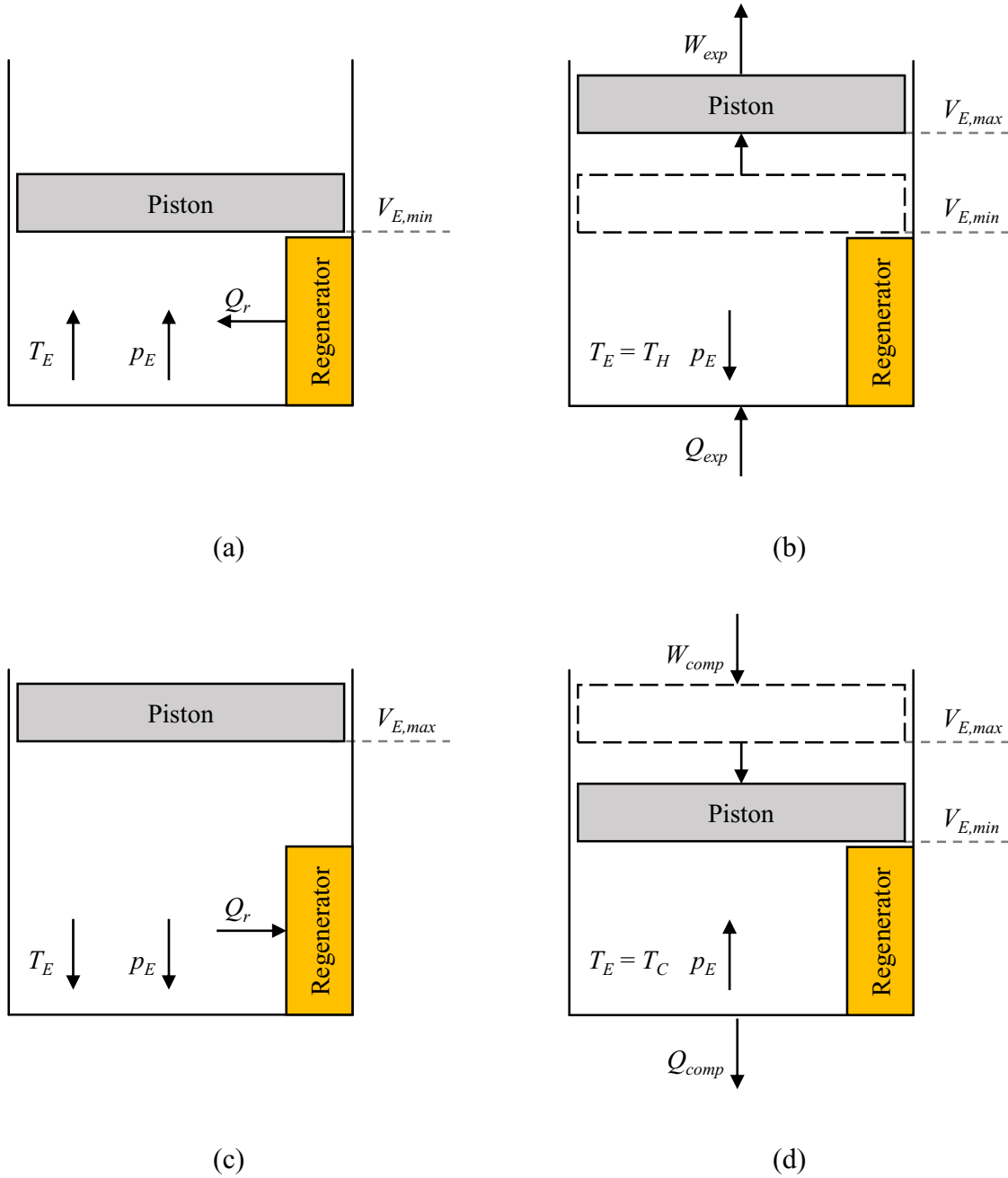


Figure 1-1: Schematic of a generic thermodynamic cell undergoing (a) isochoric heat addition, (b) isothermal expansion, (c) isochoric heat rejection and (d) isothermal compression.

### 1.2.1.1 Isochoric Heat Addition

Heat is added to the working gas at a constant working volume during the isochoric heat addition process. Figure 1-1 (a) shows the schematic of this process. The working volume is at its minimum ( $V_{E,min}$ ) and the working gas absorbs heat  $Q_r$  from the regenerator [9]. Consequently, the working gas temperature increases from  $T_C$  to  $T_H$  and the working gas pressure increases from  $p_{E,1}$  to  $p_{E,2}$ , as described by Equation 1-2.

$$p_{E,2} = p_{E,1} \cdot \frac{T_H}{T_C} \quad 1-2$$

### 1.2.1.2 Isothermal Expansion

The working volume expands at a constant temperature through the isothermal expansion process, as shown in Figure 1-1 (b). The working volume expands from minimum to maximum ( $V_{E,max}$ ) while the working gas absorbs heat  $Q_{exp}$  from the thermal source to maintain a constant temperature throughout the process [9]. Throughout the isothermal expansion, the working gas pressure decreases according to Equation 1-3. Due to the volume change, the working gas performs expansion stroke work ( $W_{exp}$ ) on its surroundings quantified by Equation 1-4.

$$p_{E,3} = p_{E,2} \cdot \frac{V_{E,min}}{V_{E,max}} \quad 1-3$$

$$Q_{exp} = W_{exp} = \int_{V_{min}}^{V_{max}} p_E \cdot dV_E = m \cdot R \cdot T_H \cdot \ln \left( \frac{V_{E,max}}{V_{E,min}} \right) \quad 1-4$$

### 1.2.1.3 Isochoric Heat Rejection

The working gas rejects heat at constant volume during the isochoric heat rejection process as shown in Figure 1-1 (c). While at constant volume, the working gas rejects heat  $Q_r$  to the



regenerator [9]. As a result, working gas temperature decreases and working gas pressure decreases (Equation 1-5).

$$p_{E,4} = p_{E,3} \cdot \frac{T_C}{T_H} \quad 1-5$$

#### 1.2.1.4 Isothermal Compression

The working volume decreases at constant temperature for the isothermal compression process. Figure 1-1 (d) is a schematic of the process. Working volume decreases from maximum to minimum and the working gas rejects heat  $Q_{comp}$  to the thermal sink to maintain a constant working gas temperature [9]. Consequently, working gas pressure increases by Equation 1-6 and the working gas receives compression stroke work ( $W_{comp}$ ) from the surroundings that amounts to Equation 1-7.

$$p_{E,1} = p_{E,4} \cdot \frac{V_{E,max}}{V_{E,min}} \quad 1-6$$

$$Q_{comp} = W_{comp} = \int_{V_{max}}^{V_{min}} p_E \cdot dV_E = m \cdot R \cdot T_C \cdot \ln \left( \frac{V_{E,min}}{V_{E,max}} \right) \quad 1-7$$

#### 1.2.1.5 Indicated Work

Indicated work is the net work performed by the working volume in one cycle. Figure 1-2 illustrates expansion stroke work, compression stroke work, and indicated work ( $W_I$ ) as areas on the ideal cycle pressure-volume diagram (indicator diagram). Indicated work is the integral of engine pressure and volume, or the sum of expansion stroke work and compression stroke work, as shown in Equation 1-8. The ideal indicated work can be calculated with the following constant parameters: the mass of working gas ( $m$ ), the gas constant ( $R$ ), the thermal source temperature, the

thermal sink temperature, and the compression ratio ( $V_{E,max} / V_{E,min}$ ). The ideal Stirling cycle indicated work increases indefinitely with the mass of working gas, temperature difference ( $T_H - T_C$ ), and compression ratio.

$$W_I = \oint p_E \cdot dV_E = W_{exp} + W_{comp} = m \cdot R \cdot (T_H - T_C) \cdot \ln \left( \frac{V_{E,max}}{V_{E,min}} \right) \quad 1-8$$

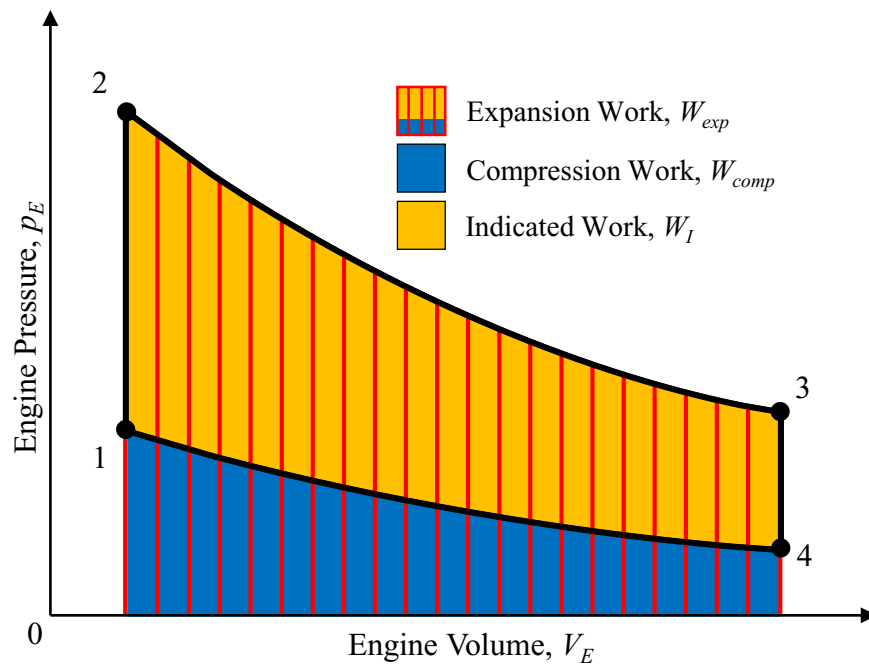


Figure 1-2: Indicator diagram of the ideal Stirling cycle.

### 1.2.2 Components of Stirling Engines

Real Stirling engines require more components than the generic thermodynamic cell presented in Figure 1-1. Figure 1-3 presents an example of the construction of a generic Stirling engine, specifically a gamma-type Stirling engine. All Stirling engines have two variable volume spaces—the expansion space and the compression space [9]. The volumes of these spaces are manipulated

by a moving boundary (piston) and/or an internal gas transfer driver (displacer) [25]. The regenerator stores heat during the heat rejection process and returns heat during the heat addition process [25]. Dedicated heat exchangers—the heater and cooler—enhance heat exchange within the engine [25]. The heat exchangers, regenerator, expansion space, and compression space have an associated volume ( $V_i$ ), working gas temperature ( $T_i$ ), and working gas pressure ( $p_i$ ). This subsection describes the function and typical characteristics for each of these components.

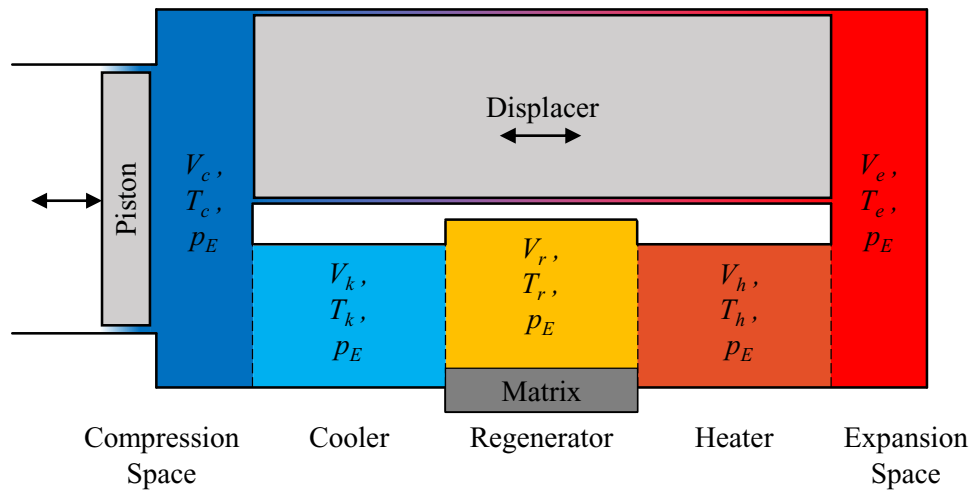


Figure 1-3: Schematic of generic gamma-type Stirling engine.

### 1.2.2.1 Expansion Space

The expansion space is the variable volume space on the hot side of the engine. It is represented by the subscript  $e$  in Figure 1-5 and throughout this thesis. In the ideal cycle, the expansion space increases in volume and receives heat from the thermal source through the isothermal expansion process [9]. The expansion space often has poor heat transfer characteristics and consequently is more closely resembled by an adiabatic volume than an isothermal volume [25]. The expansion space of all Stirling engines, ideal or non-ideal, produce net positive work [9].

### 1.2.2.2 Compression Space

The compression space is the variable volume space on the cold side of the engine. It is represented by the subscript  $c$ . In the isothermal compression process of the ideal cycle, the compression space decreases in volume and rejects heat to the thermal sink [9]. The compression space also has poor heat transfer characteristics and therefore is better represented as adiabatic rather than isothermal [25]. The compression space of all Stirling engines require a work input to perpetuate the thermodynamic cycle [9].

### 1.2.2.3 Piston

The piston is a generic description for a moving boundary of the working volume. Pistons are referred to with subscript  $p$  in this thesis. The piston(s) of a Stirling engine change the working volume of the engine and, as a result, receive and impart work on the working gas [9]. They can take the form of a piston, reciprocating enclosure, diaphragm or liquid boundary [25]. Piston motion is generally restricted by kinematic mechanisms, mechanical springs or gas springs [27].

### 1.2.2.4 Displacer

The displacer transports working gas through the heat exchangers and regenerator [8]. It is described with subscript  $d$  in this thesis. Unlike the piston, the displacer does not change the working volume [9]. The displacer influences pressure by changing the bulk working gas temperature [8]. Heat is added to the working gas during the cold blow when the displacer transports gas from the compression space to the expansion space [8]. Heat is removed from the working gas during the hot blow when the displacer transports gas from the expansion space to the compression space [8]. Displacer position is often manipulated by kinematic mechanisms, mechanical springs, gas springs, or linear actuators [25,28].

#### 1.2.2.5 Regenerator

The regenerator (subscript  $r$ ) stores heat from the working gas during the hot blow and returns heat to the working gas during the cold blow [9]. In the ideal Stirling cycle, the regenerator provides all the heat for the isochoric heat addition process and absorbs all the heat during the isochoric heat rejection process [9]. The regenerator also insulates the heated components of the engine from the cooled components of the engine [29]. Regenerators are highly influential on efficiency by reducing the necessary heat input and rejection in the heat exchangers for a unit of output work [8,14]. To fulfil the heat transfer, heat storage, and insulation requirements of the regenerator, it is often a porous media with a large wetted area, high heat capacity, and low thermal conductivity [8,9].

#### 1.2.2.6 Heater

The heater enhances heat transfer from the thermal source to the working fluid [25]. Subscript  $h$  refers to the heater in this thesis. A heater is an unnecessary heat exchanger in an ideal Stirling engine because the expansion space receives all the heat from the thermal source [29]. In real Stirling engines, the heater compensates for an imperfect regenerator and the poor heat transfer characteristics of the expansion space, among other inefficiencies [29]. The heater resides between the regenerator and expansion space [25]. It is specifically designed to maximize heat transfer from the thermal source to the working fluid during the cold blow with minimal flow resistance [25]. Its design therefore depends significantly on the thermal source, and by extension the application of the Stirling engine [30].

#### 1.2.2.7 Cooler

The cooler enhances heat transfer from the working gas to the thermal sink [25]. Like the heater, the cooler is unnecessary in an ideal engine because the compression space performs all

the heat transfer to the thermal sink [29]. The cooler rejects all the extra heat introduced to the engine to overcome imperfections, inefficiencies, and the poor heat transfer characteristics of the compression space [29]. Its goal is to remove heat from the working gas during the hot blow with minimal flow resistance and reject heat from inefficiencies [9,25].

### 1.2.3 The Thermodynamic Cycle of Real Stirling Engines

The thermodynamic cycle of a real Stirling engine varies significantly from the ideal Stirling cycle due to continuous motion of the piston and displacer [9]. Figure 1-4 displays an example of the indicator diagram of a real Stirling cycle. The continuous cycle is rounded because the thermodynamic processes occur simultaneously rather than sequentially [9].

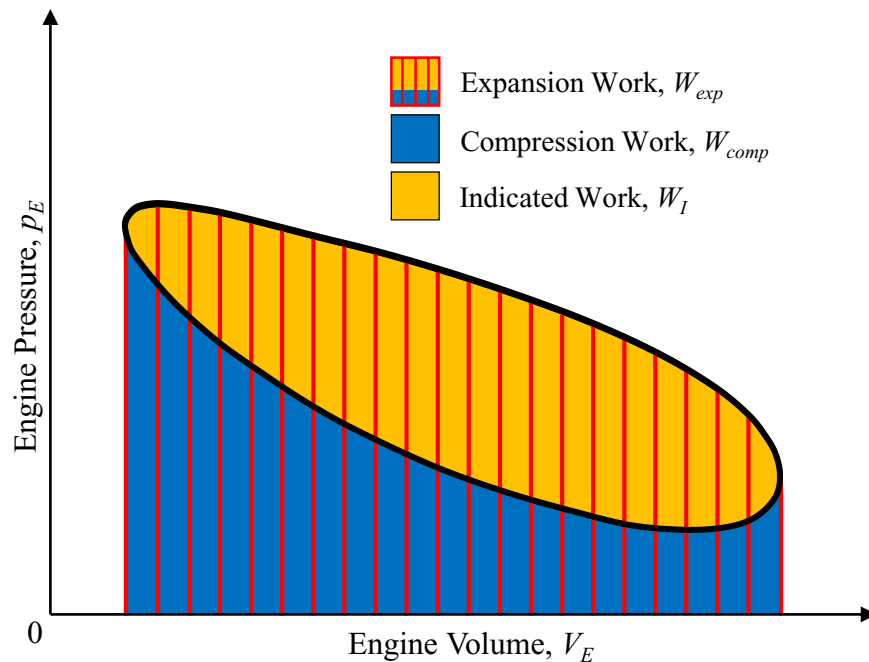


Figure 1-4: Indicator diagram of a real Stirling engine.

Heat transfer in real Stirling engines occurs in a finite time and is imperfect [9]. As a result, gas temperatures cannot equate to the thermal source and thermal sink temperatures [31]. The

expansion space and compression space are often incapable of transferring sufficient heat to remain isothermal during expansion and compression [8]. Therefore, the expansion and compression processes are non-isothermal [8].

The ideal Stirling cycle assumes that all of the working gas changes temperature in the isochoric heat addition and rejection processes [9]. The volumes of working gas in the heater, regenerator, cooler, and cylinder clearances are the dead volume of the engine ( $V_{dead}$ ) because they are not swept by the piston or displacer [9]. The dead volume reduces the influence of volume changes and gas temperature changes on the engine pressure [25]. Consequently, dead volume reduces engine performance[9,27].

#### 1.2.4 Stirling Engine Configurations

There are three configurations of Stirling engines—alpha, beta and gamma-type [30]. These are divided into two functionally similar groups. Beta and gamma-type Stirling engines are piston-displacer engines [9]. They use a displacer to transport working gas through the heat exchangers and a piston to change the engine volume [9]. Alpha-type engines are two-piston engines [9]. They use in-phase motion of two pistons to transport working gas through the heat exchangers and out-of-phase motion to change the engine volume [9]. This subsection presents how these groups of Stirling engines perform the thermodynamic processes of the ideal Stirling cycle.

##### 1.2.4.1 Beta and Gamma-Type Stirling Engines

The piston-displacer engines use a displacer to change the bulk gas temperature and a piston to change the working volume [8,9]. The key difference between the beta and gamma-type Stirling engines is the number of cylinders they have [30]. In gamma-type Stirling engines, the piston and displacer are in different cylinders (Figure 1-3 above) [30]. The piston and displacer share a common cylinder in beta-type engines (Figure 1-5) [30]. Beta-type Stirling engines often have a

higher compression ratio ( $V_{E,max} / V_{E,min}$ ) because the piston swept volume and displacer swept volume overlap [8]. Otherwise, beta and gamma-type engines are thermodynamically similar [8].

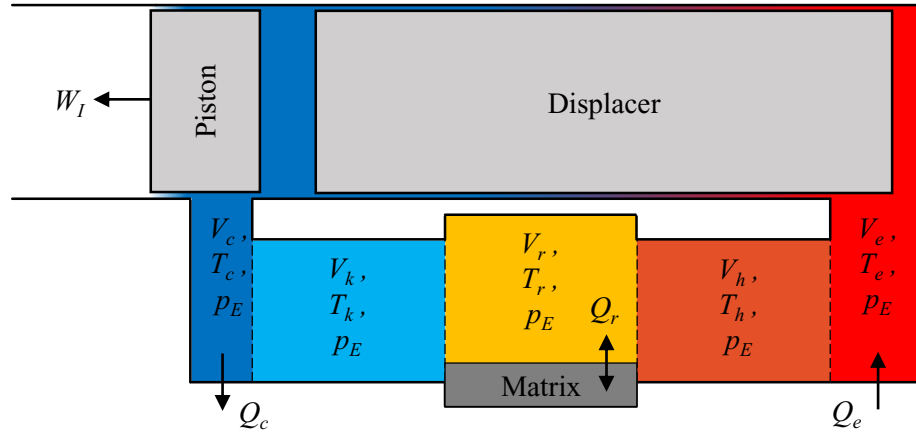


Figure 1-5: Schematic of a Generic Beta-Type Stirling Engine

Figure 1-6 (a-d) presents schematics of the ideal Stirling cycle processes for a gamma-type Stirling engine. This description also applies to beta-type Stirling engines. The isochoric heat addition process occurs when the displacer transports gas from the compression space to the expansion space through the heat exchangers and increases the bulk gas temperature (Figure 1-6 a). Next, the piston expands the working volume for isothermal expansion (Figure 1-6 b). The displacer then transports the working gas through the heat exchangers from the expansion space to the compression space for isochoric heat rejection (Figure 1-6 c). Finally, the cycle completes with the isothermal compression process when the piston reduces the working volume (Figure 1-6 d).



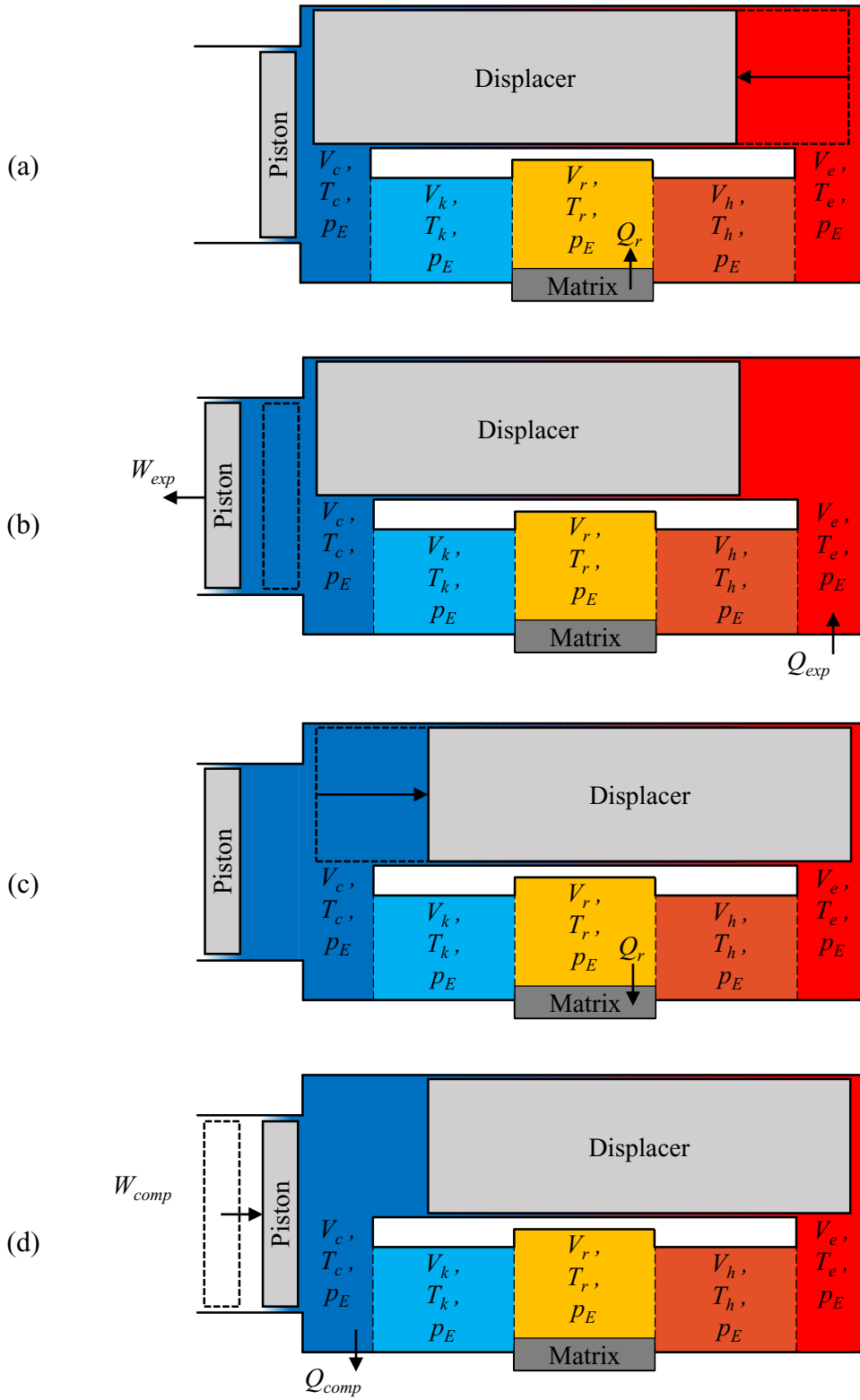
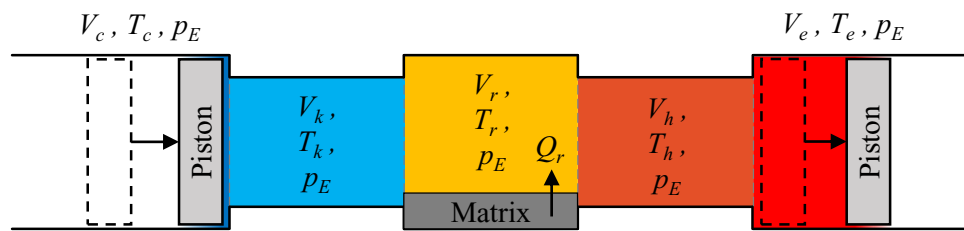


Figure 1-6: Schematics of the ideal Stirling cycle in a gamma-type Stirling engine.

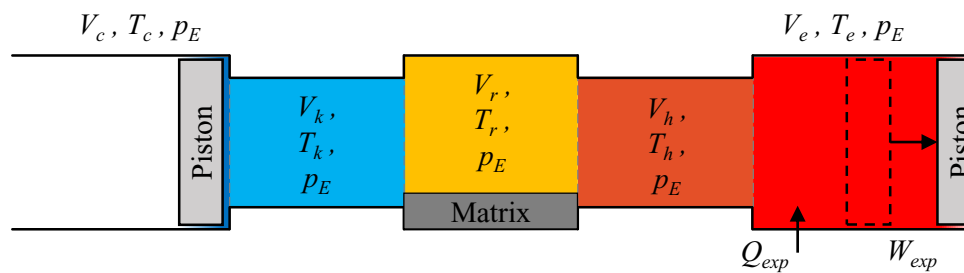
#### 1.2.4.2 Alpha-Type Stirling engines

In alpha-type Stirling engines (two-piston engines) the pistons have two roles. The in-phase motion of the pistons transfers working gas through the heat exchangers to change the bulk gas temperature [9]. The out-of-phase motion of the pistons change the working volume of the engine with positive work through expansion and negative work during compression [9,29].

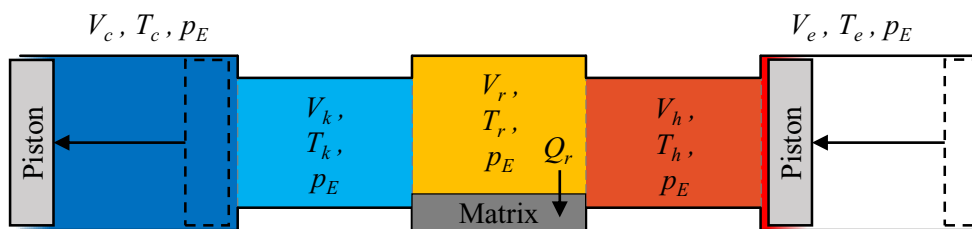
Figure 1-7 (a-d) is a schematic of a generic alpha-type Stirling engine executing the four processes of the ideal Stirling cycle. In Figure 1-7 (a), the pistons move in-phase to transfer the working gas through the heat exchangers to add heat and increase pressure for the isochoric heat addition process. The expansion piston expands the working volume and receives work while heat enters the engine to perform isothermal expansion (Figure 1-7 b). The pistons move in-phase to transfer gas from the expansion space to the compression space, through the heat exchangers, for the isochoric heat rejection process (Figure 1-7 c). The cycle is complete when the compression piston reduces the working volume for the isothermal compression process (Figure 1-7 d).



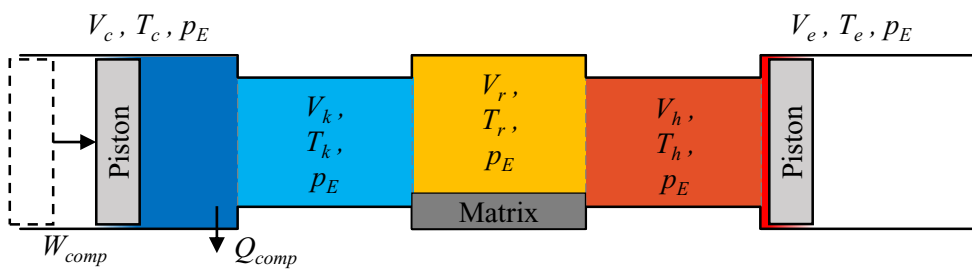
(a)



(b)



(c)



(d)

Figure 1-7: Schematics of the ideal Stirling cycle in an alpha-type Stirling engine.

## 1.3 Kinematic Stirling Engines

---

In kinematic Stirling engines, piston and displacer motion are constrained by kinematic mechanisms [32]. This section describes the work transfer in kinematic Stirling engines and derives the volume functions in a slider-crank, gamma-type Stirling engine.

### 1.3.1 Kinematic Stirling Engine Work Transfer

Senft [27,32] provides a valuable description of the work transfer in kinematic heat engines. The description views heat engine work from the perspective of the piston rather than the working volume. This is described in detail below.

#### 1.3.1.1 The Buffer Space

The buffer space is the volume ( $V_b$ ) in contact with the external face of the piston and the buffer pressure ( $p_b$ ) acts on the external face of the piston [32]. Buffer pressure can be constant or volume dependent (finite volume buffer space), among other possibilities [27]. As the piston moves for thermodynamic processes in the engine, the buffer space volume changes with opposite sign of the working space [32]. As a result, the buffer space receives compression work ( $W_{b,comp}$ ) and imparts expansion work ( $W_{b,exp}$ ) on the piston [32].

#### 1.3.1.2 The Piston

The piston is the mobile boundary between the engine and buffer space [32]. Consequently, a net pressure ( $p_p$ ), defined by Equation 1-9, acts on the piston. The piston receives expansion work and imparts compression work on both the working volume and buffer space [32]. The piston transfers significant amounts of work directly between the working volume and the buffer space.

$$p_p = p_E - p_b \quad 1-9$$

### 1.3.1.3 Efficacious and Forced Work

Efficacious work ( $W_{Eff}$ ) is work that the piston transfers to the mechanism because the piston is moving in the direction of the net pressure acting on it, as described in Figure 1-8 (a) [27]. Figure 1-8 (b) is an indicator diagram of a Stirling engine with the efficacious work regions highlighted. Efficacious expansion work occurs when the engine volume increases while the engine pressure is greater than the buffer pressure (1 to 2 in Figure 1-8 b). Then, efficacious compression work occurs when the engine volume decreases while the buffer pressure is greater than the engine pressure (3 to 4 in Figure 1-8 b). The efficacious work is the output work of the piston and, in most cases, a fraction of it must return to the engine as forced work [32].

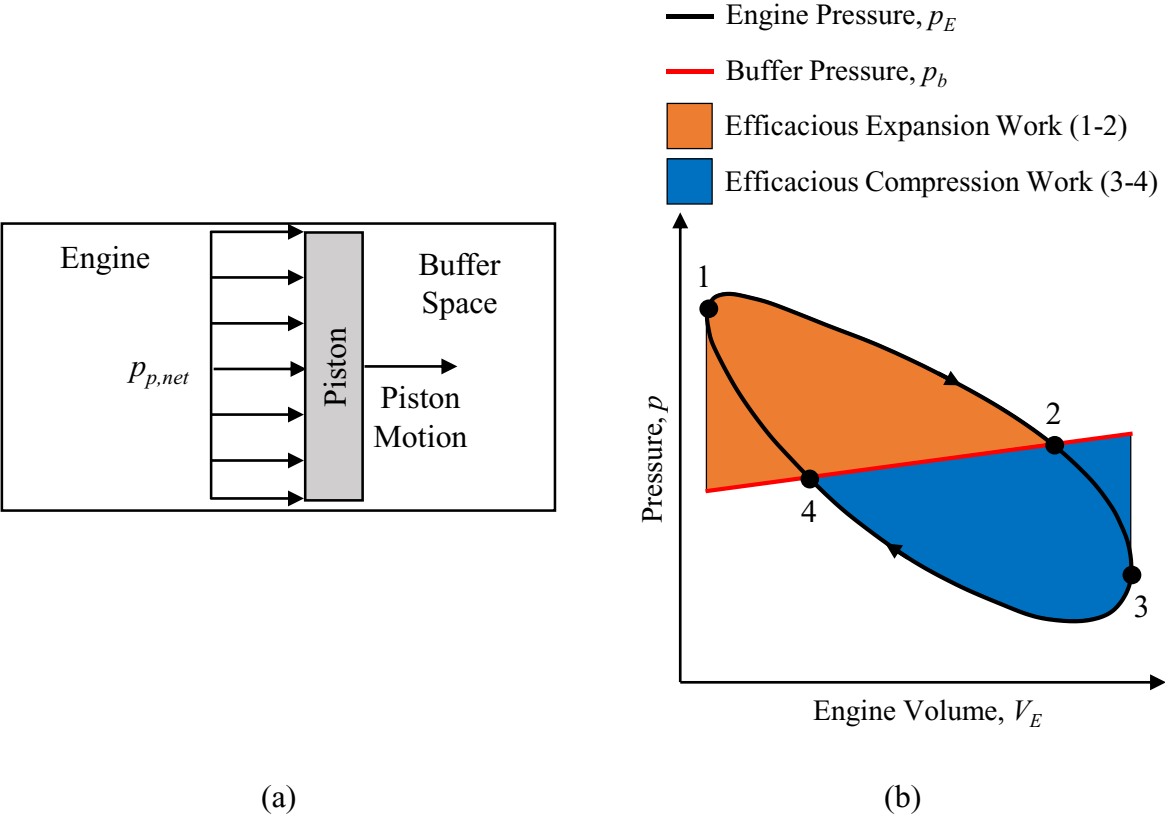


Figure 1-8: (a) A schematic of a piston undergoing efficacious work and (b) an indicator diagram showing efficacious work in a Stirling engine.

Asynchronous to efficacious work is forced work [27]. Forced work ( $W_F$ ) is the work that the mechanism transfers to the piston because the piston is moving against the net pressure acting on it, as shown in Figure 1-9 (a) [27]. Figure 1-9 (b) presents an indicator diagram of a Stirling engine with the forced work regions highlighted. Forced expansion work occurs when the engine volume expands while the buffer pressure is greater than the engine pressure (2 to 3 in Figure 1-8 b). Forced compression work occurs when the engine volume compresses while the engine pressure is greater than the buffer pressure (4 to 1 in Figure 1-8 b). The heat engine requires forced work to perpetuate the thermodynamic cycle [27].

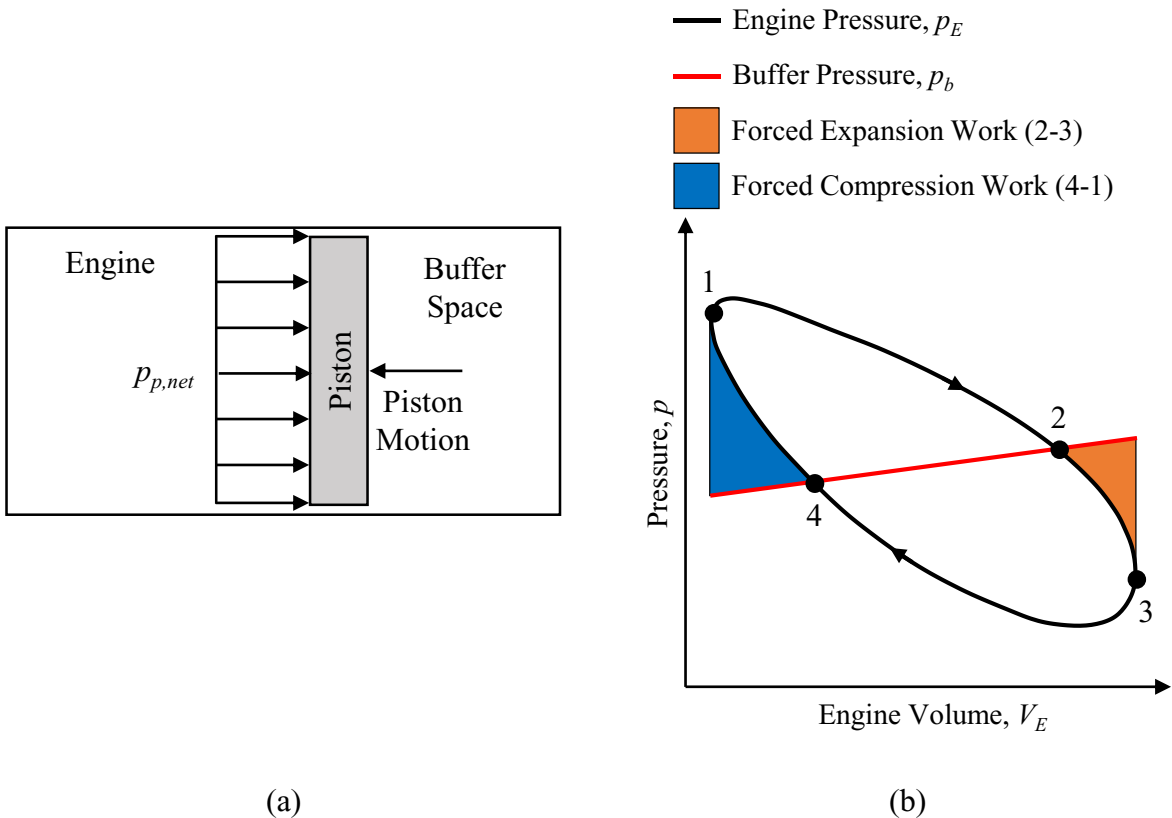


Figure 1-9: (a) A schematic of a piston undergoing forced work and (b) an indicator diagram showing forced work in a Stirling engine.

### 1.3.1.4 Complete Kinematic Heat Engine Work Transfer

Figure 1-10 describes the work transfer of a kinematic heat engine. Some of the expansion work from the engine enters the buffer space as buffer space compression work [32]. Likewise, some of the compression work transfers to the engine from the buffer space expansion work [32]. Work from the piston to the mechanism is efficacious work and work from the mechanism to the piston is forced work [27]. The difference between efficacious work and forced work is the indicated work, as shown in Equation 1-10 [27]. Although significant energy is stored in the buffer space, the net work transferred to the mechanism over a complete cycle is the indicated work.

$$W_I = W_{Eff} - W_f \tag{1-10}$$

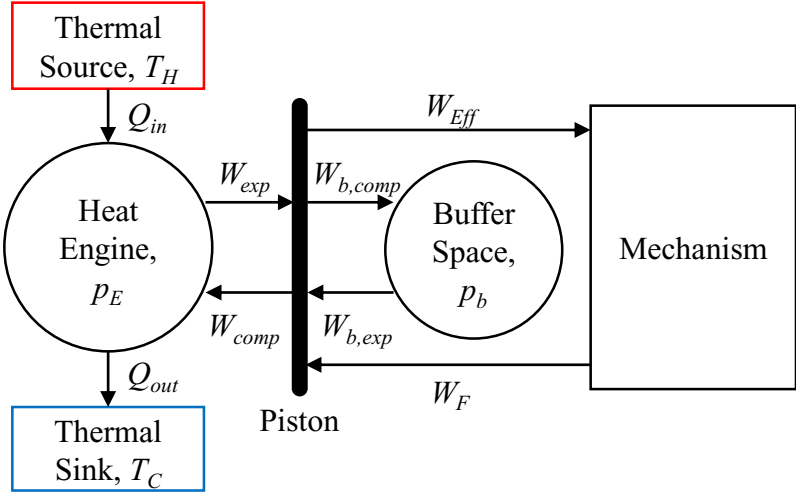


Figure 1-10: Energy transfer diagram of a kinematic heat engine, after Senft [32].

### 1.3.2 Slider-Crank, Gamma-Type Stirling Engine Volume Functions

The engine studied in this thesis is a slider-crank, gamma type Stirling engine. Slider-crank mechanisms, similar to the mechanism in Figure 1-11, constrain motion of the piston and the displacer. The slider position ( $l_4$ ), in Equation 1-11, depends on the Desaxe offset ( $l_1$ ), crankshaft

eccentricity ( $l_2$ ), connecting rod length ( $l_3$ ), crank angle ( $\theta_2$ ) and connecting rod angle ( $\theta_3$ ) determined with Equation 1-12) [33]. Slider position change is related to the derivative of slider position with respect to the crank angle shown in Equation 1-13.

$$l_4 = l_2 \cdot \cos(\theta_2) - l_3 \cdot \cos(\theta_3) \quad 1-11$$

$$\theta_3 = \pi - \sin^{-1}\left(\frac{-l_1 + l_2 \cdot \sin(\theta_2)}{r_3}\right) \quad 1-12$$

$$\frac{dl_4}{d\theta_2} = -l_2 \cdot \sin(\theta_2) + l_3 \cdot \sin(\theta_3) \cdot \frac{d\theta_3}{d\theta} \quad 1-13$$

$$\frac{d\theta_3}{d\theta} = \frac{l_2 \cdot \cos(\theta_2)}{l_3 \cdot \sqrt{1 - \theta_3^2}} \quad 1-14$$

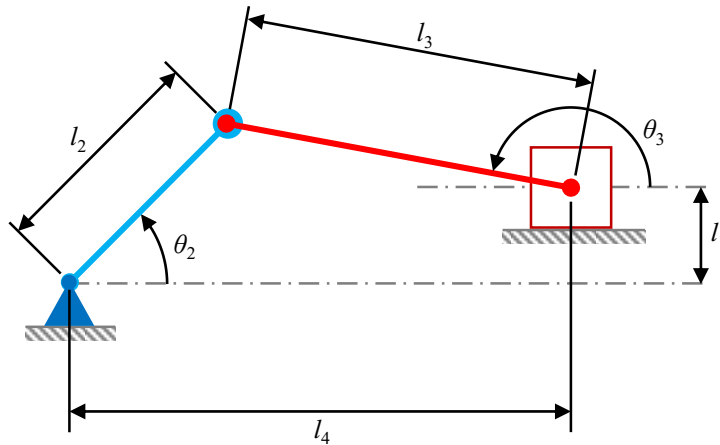


Figure 1-11: Schematic of a generic slider-crank mechanism, after Cleghorn and Dechev [33].

The slider-crank mechanisms for the piston and the displacer are laid out in Figure 1-12. The crankshaft angular position ( $\theta$ ) increases in the clockwise direction to match the rotational direction of the running engine and the displacer's slider-crank mechanism leads the piston's mechanism by the phase angle  $\phi$ . The instantaneous displacer position ( $l_{4,d}$ , Equation 1-15) and



instantaneous piston position ( $l_{4,p}$ , Equation 1-16) are the solution to Equation 1-11 with dimensions from the displacer mechanism and piston mechanism, respectively.

$$l_{4,d} = l_2 \cdot \cos(-\theta - \phi) + l_{3,d} \cdot \cos(\theta_{3,d}) \quad 1-15$$

$$l_{4,p} = l_2 \cdot \cos(-\theta) + l_{3,p} \cdot \cos(\theta_{3,p}) \quad 1-16$$

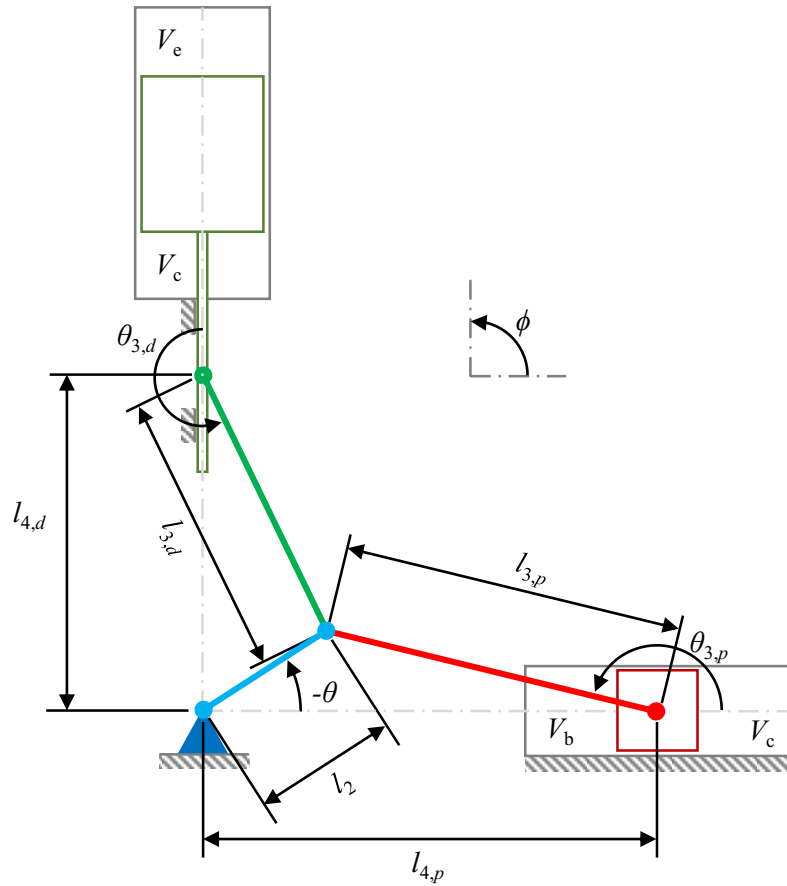


Figure 1-12: Schematic of a 90 ° gamma-type Stirling engine slider-crank mechanism.

### 1.3.2.1 Expansion Space Volume

The expansion space volume depends on the displacer position only. Equation 1-17 calculates the instantaneous expansion space volume ( $V_e$ ), which includes half of the displacer clearance

volume ( $V_{cld}$ ) and the volume between the instantaneous displacer position and its top-dead-center (TDC) position. Equation 1-18 calculates the derivative of expansion space volume with crankshaft angular position ( $dV_e / d\theta$ ).

$$V_e = \frac{V_{cld}}{2} + \left( \frac{\pi}{4} \cdot d_d^2 \right) \cdot \left( (l_2 + l_{3,d}) - l_{4,d} \right) \quad 1-17$$

$$\frac{dV_e}{d\theta} = \left( \frac{\pi}{4} \cdot d_d^2 \right) \cdot \frac{-dl_{4,d}}{d\theta} \quad 1-18$$

### 1.3.2.2 Compression Space Volume

The compression space volume depends on both the displacer position and the piston position. Equation 1-19 calculates the instantaneous compression space volume ( $V_c$ ). It includes the other half of the displacer clearance volume, the piston clearance volume ( $V_{clp}$ ) and the volume between the piston and its TDC position. The displacer does not change the volume of the engine, if the displacer rod is neglected, so part of the compression space volume is the displacer swept volume ( $V_{swd}$ ) minus the instantaneous expansion space volume. Equation 1-20 calculates the derivative of compression space volume with respect to crankshaft angular position ( $dV_c / d\theta$ ). The compression space volume increases as expansion space volume and piston position decrease.

$$V_c = (V_{cld} + V_{swd} - V_e) + V_{clp} + \left( \frac{\pi}{4} \cdot d_p^2 \right) \cdot \left( (l_2 + l_{3,p}) - l_{4,p} \right) \quad 1-19$$

$$\frac{dV_c}{d\theta} = -\frac{dV_e}{d\theta} + \left( \frac{\pi}{4} \cdot d_p^2 \right) \cdot \frac{-dl_{4,p}}{d\theta} \quad 1-20$$

### 1.3.2.3 Total Engine Volume

The total engine volume ( $V_E$ ) includes the expansion space volume, compression space volume and the volume of the heat exchangers ( $V_{dead}$ ). It is calculated with Equation 1-21. The derivative

of total engine volume with respect to crankshaft angular position ( $dV_E / d\theta$ ) is calculated with Equation 1-22. It is only a function of the derivative of piston position ( $dl_{4,p} / d\theta$ ) because the displacer does not change the total engine volume.

$$V_E = V_c + V_e + V_{dead} \quad 1-21$$

$$\frac{dV_E}{d\theta} = \frac{dV_c}{d\theta} + \frac{dV_e}{d\theta} = \left( \frac{\pi}{4} d_p^2 \right) \cdot \frac{-dl_{4,p}}{d\theta} \quad 1-22$$

#### 1.3.2.4 Buffer Space Volume

Only the piston position influences buffer space volume if the displacer rod is neglected. Equation 1-23 calculates the buffer space volume ( $V_b$ ) as the maximum buffer space volume ( $V_{b,max}$ ) minus the volume between the instantaneous piston position and its TDC position. The buffer space volume increases as the piston position increases. The derivative of buffer space volume with respect to crankshaft angular position ( $dV_b / d\theta$ ) is calculated with Equation 1-24.

$$V_b = V_{b,max} - \left( \frac{\pi}{4} \cdot d_p^2 \right) \cdot \left( (l_2 + l_{3,p}) - l_{4,p} \right) \quad 1-23$$

$$\frac{dV_b}{d\theta} = \left( \frac{\pi}{4} \cdot d_p^2 \right) \cdot \frac{dl_{4,p}}{d\theta} \quad 1-24$$

## 1.4 Stirling Engine Thermodynamic Models

---

Many thermodynamic models exist to model the performance of Stirling engines [16,34]. Martini [34] defined three orders of thermodynamic models based on their level of complexity. 1<sup>st</sup> order models are closed-form calculations. 2<sup>nd</sup> order models are zero-dimensional solutions to the transport equations, often with additional loss terms. 3<sup>rd</sup> order models are, at minimum, one-dimensional solutions to the transport equations. Dynamic models simultaneously solve the mechanism kinematics with a 2<sup>nd</sup> or 3<sup>rd</sup> order thermodynamic model [35]. This section describes modelling assumptions and techniques with emphasis on 2<sup>nd</sup> order models and loss terms.

### 1.4.1 1<sup>st</sup> Order Models

First order models are closed-form estimates of Stirling engine power and efficiency [34]. Empirical correlations used to predict engine power include the Beale Number and the West number [8,34]. The Schmidt analysis is an analytical method to predict power [8,29]. 1<sup>st</sup> order models are useful for relating the size and the power of an engine, but provide minimal design insight [16,34].

#### 1.4.1.1 Beale Number

The Beale number ( $N_{B,I}$ ) is a dimensionless characterization of Stirling engine performance [8]. It is based on the observation that the shaft power ( $\dot{W}_S$  in W) produced from well-developed Stirling engines is proportional to mean pressure ( $p_{E,mean}$  in Pa), engine frequency ( $f$  in Hz), and swept volume ( $V_{sw}$  in m<sup>3</sup>), as shown in Equation 1-25 [8]. The Beale number is useful for determining the realistic potential of a Stirling engine design by correlating the performance of similar engines [8,34]. The mean Beale number is 0.15 for a group of engines presented by West [8] with a source temperature near 650 °C. The Beale number can be used to compare the shaft power of engines with different geometry, frequency and mean pressure [8].

$$N_B = \frac{\dot{W}_s}{p_{E,mean} \cdot f \cdot V_{sw}} \approx 0.15 \quad 1-25$$

The Beale number fails to include the effects of thermal source and thermal sink temperatures on the performance of a Stirling engine [8]. LTDSEs are less effective at converting heat to work compared to HTDSEs. As a result, the Beale number decreases as the thermal source temperature decreases [8].

#### 1.4.1.2 West Number

The West number ( $N_W$ ), similar to the Beale number, is a dimensionless measure of Stirling engine performance [8]. It is a function of shaft power ( $\dot{W}_s$  in W), mean pressure ( $p_{E,mean}$  in Pa), engine frequency ( $f$  in Hz), swept volume ( $V_{sw}$  in  $m^3$ ), thermal source temperature ( $T_H$  in K), and thermal sink temperature ( $T_C$  in K) (Equation 1-26) [8]. The influence of thermal source and sink temperature on shaft power is defined by a dimensionless temperature factor. The dimensionless temperature factor, described in Equation 1-27, relates mean pressure to the mean effective pressure ( $MEP$ ) of the ideal Stirling cycle [36]. West number is Beale number divided by the temperature factor [8]. West [8] calculated the mean West number to be 0.25 for a group of engines with thermal source temperatures ranging from 340-900 °C. Stumpf [37] calculated the mean West number to be 0.21 for 12 LTDSEs. West number is useful for comparing the performance of Stirling engines with different thermal source and thermal sink temperatures [8].

$$N_W = \frac{\dot{W}_s}{p_{E,mean} \cdot f \cdot V_{sw}} \cdot \left( \frac{T_H - T_C}{T_H + T_C} \right)^{-1} = N_B \cdot \left( \frac{T_H - T_C}{T_H + T_C} \right)^{-1} \approx 0.25 \quad 1-26$$

$$MEP = p_{E,mean} \cdot 2 \cdot \left( \frac{T_H - T_C}{T_H + T_C} \right) \quad 1-27$$

### 1.4.1.3 Schmidt Analysis

The Schmidt analysis is a closed form thermodynamic model of a Stirling engine [27]. The analysis is a simplification of the ideal isothermal model described in section 1.4.2.1 made possible by assuming sinusoidal volume changes [27]. The equations for the Schmidt analysis are different for piston-displacer Stirling engines and piston-piston Stirling engines. Senft [27] presents the beta and gamma-type equation set and Urieli and Berchowitz [29] present the alpha-type equation set. Outputs from the Schmidt analysis include: engine pressure, expansion space heat transfer, compression space heat transfer, and indicated work [29].

### 1.4.2 2<sup>nd</sup> Order Model Reference Cycles

2<sup>nd</sup> order models are zero-dimensional simulations of a Stirling engine that require numerical methods for solutions [38]. These typically comprise of an idealized reference cycle calculation with decoupled heat and power loss terms [34]. They use a reference cycle from either the ideal isothermal model, the ideal adiabatic model, or semi-adiabatic models [16]. Decoupled losses can be calculated from empirical correlations and simplified theoretical analyses after the idealized analysis [16].

The reference cycles of 2<sup>nd</sup> order models are derived from the zero-dimensional transport equations within engine cells [29]. The generic thermodynamic cell in Figure 1-13 represents a simplified, arbitrary Stirling engine component, such as the regenerator or the compression space. The volume of the cell ( $V_i$ ) can increase or decrease with work ( $W_i$ ) to or from a piston. The total mass of working gas in the engine ( $m_E$ ) remains constant while masses of working gas can transfer into ( $m_{in}$ ), transfer out of ( $m_{out}$ ), or accumulate in individual cells ( $m_i$ ). The total internal energy of the working gas within the cell ( $c_v m_i T_i$ ) depends on the enthalpy transfer ( $c_p m_{in/out} T_{in/out}$ ), heat transfer ( $Q_i$ ), and work. The energy equation often neglects the kinetic energy and potential energy

of the working gas [29]. The zero-dimensional conservation of mass (Equation 1-28) and conservation of energy (Equation 1-29), and the ideal gas law equation of state (Equation 1-30) are necessary to derive the reference cycle calculations [29].

$$\text{constant} = m_E = \sum m_i \text{ and } dm_i = m_{in} - m_{out} \quad 1-28$$

$$c_v \cdot d(m_i \cdot T_i) = (m_{in} \cdot c_p \cdot T_{in} - m_{out} \cdot c_p \cdot T_{out}) + Q_i - W_i \quad 1-29$$

$$p_i \cdot V_i = m_i \cdot R \cdot T_i \quad 1-30$$

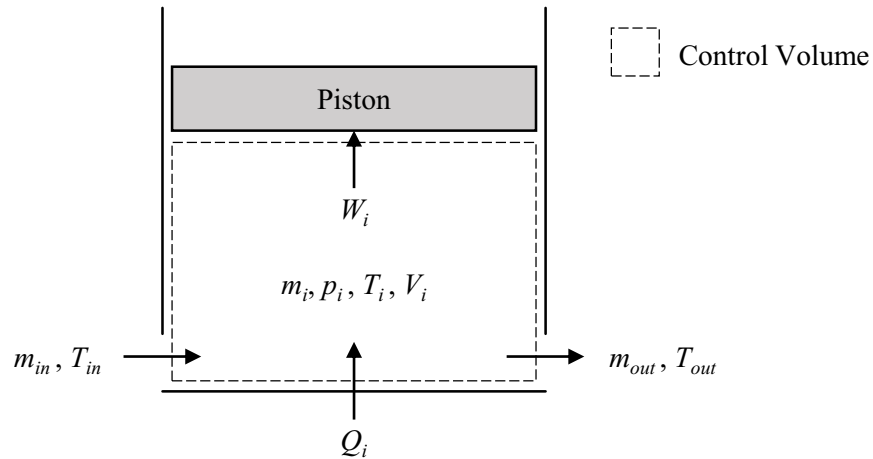


Figure 1-13: Schematic of generic thermodynamic unit cell for zero-dimensional Stirling engine models *after Urieli and Berchowitz* [29].

#### 1.4.2.1 Ideal Isothermal Model

The ideal isothermal model is most similar to the ideal Stirling cycle. Figure 1-14 is a Stirling engine schematic and its temperature distribution for the ideal isothermal model. All cells of the engine (compression space, cooler, regenerator, heater and expansion space) are isothermal throughout the cycle and engine pressure is uniform across the engine [29]. The assumptions of the ideal isothermal model are:

- perfect heat exchange and perfect regeneration,
- uniform engine pressure,
- a closed working volume (no mass transfer in/out of engine),
- an ideal working gas,
- negligible working gas kinetic and potential energy change,
- no spatial variations with cells,
- operation at cyclic steady-state, and
- a constant angular velocity (for kinematic engines) [9,29].

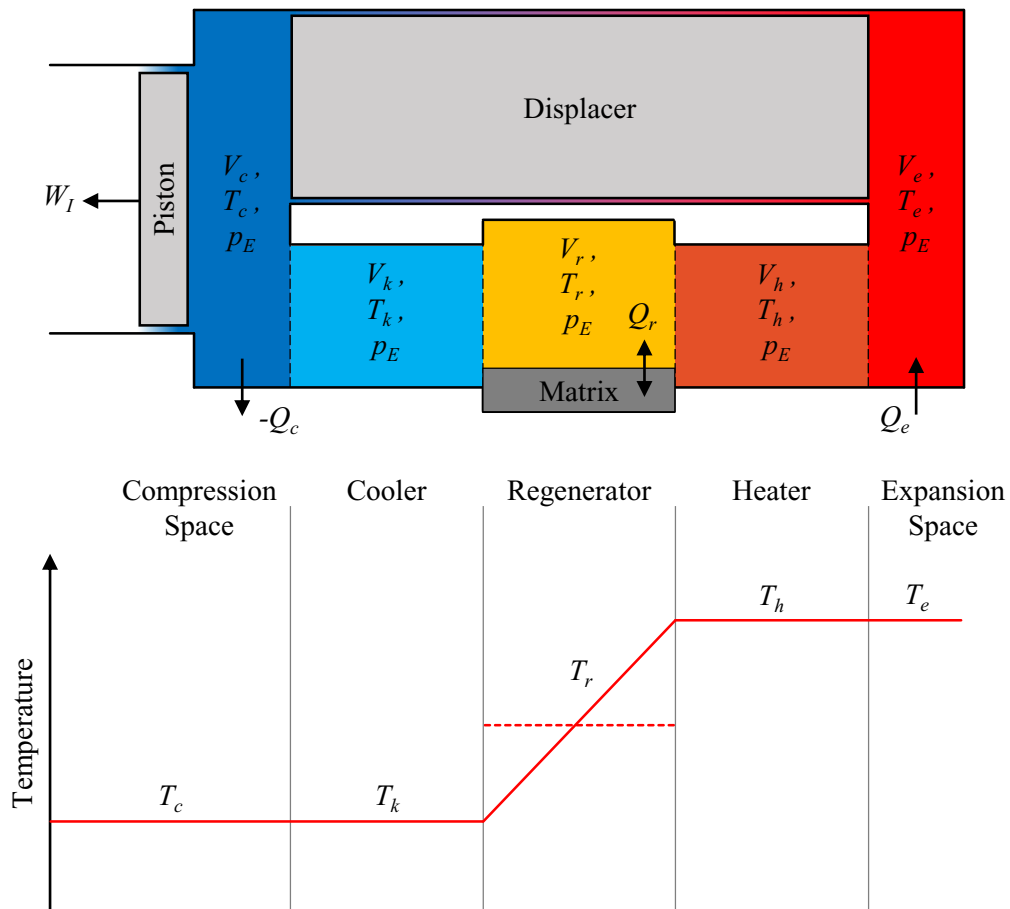


Figure 1-14: Temperature distribution and engine schematic for the ideal isothermal model after Urieli and Berchowitiz [29].



The solutions to the transport equations with the ideal isothermal model assumptions are available in Urieli and Berchowitz [29]. Due to perfect regeneration, all the heat that enters the expansion space ( $Q_e$ ) becomes expansion space work ( $W_e$ ). Similarly, all the heat that leaves the compression space ( $Q_c$ ) is work that must be input in the compression space ( $W_c$ ). The ideal isothermal model converts heat to work with the Carnot efficiency. The heater and cooler do not transfer heat to the working fluid because the expansion space, regenerator, and compression space are perfect heat exchangers. As a result, the heater and cooler are unnecessary components in the ideal isothermal model.

#### 1.4.2.2 Ideal Adiabatic Model

In the ideal adiabatic model, no heat transfer occurs in the expansion and compression spaces [29]. Figure 1-15 is the temperature distribution and schematic of an engine for the ideal adiabatic model. Temperature is uniform and constant in the heater, regenerator and cooler, like in the isothermal model. The expansion space and compression space temperatures ( $T_e$  and  $T_c$ ) are uniform and variable with engine pressure. The interfaces between cells have instantaneous mass transfer rates and temperatures (for example,  $\dot{m}_{ck}$  and  $T_{ck}$  for the compression space-cooler interface) [29]. The ideal adiabatic model assumes:

- isothermal heater, regenerator and cooler cells (perfect heat transfer),
- adiabatic expansion and compression spaces (no heat transfer),
- uniform engine pressure,
- a closed working volume (no mass transfer in/out of engine),
- an ideal working gas,
- negligible working gas kinetic and potential energy change,
- no spatial variations with cells,

- operation at cyclic steady-state, and
- a constant angular velocity (for kinematic engines) [9,29].

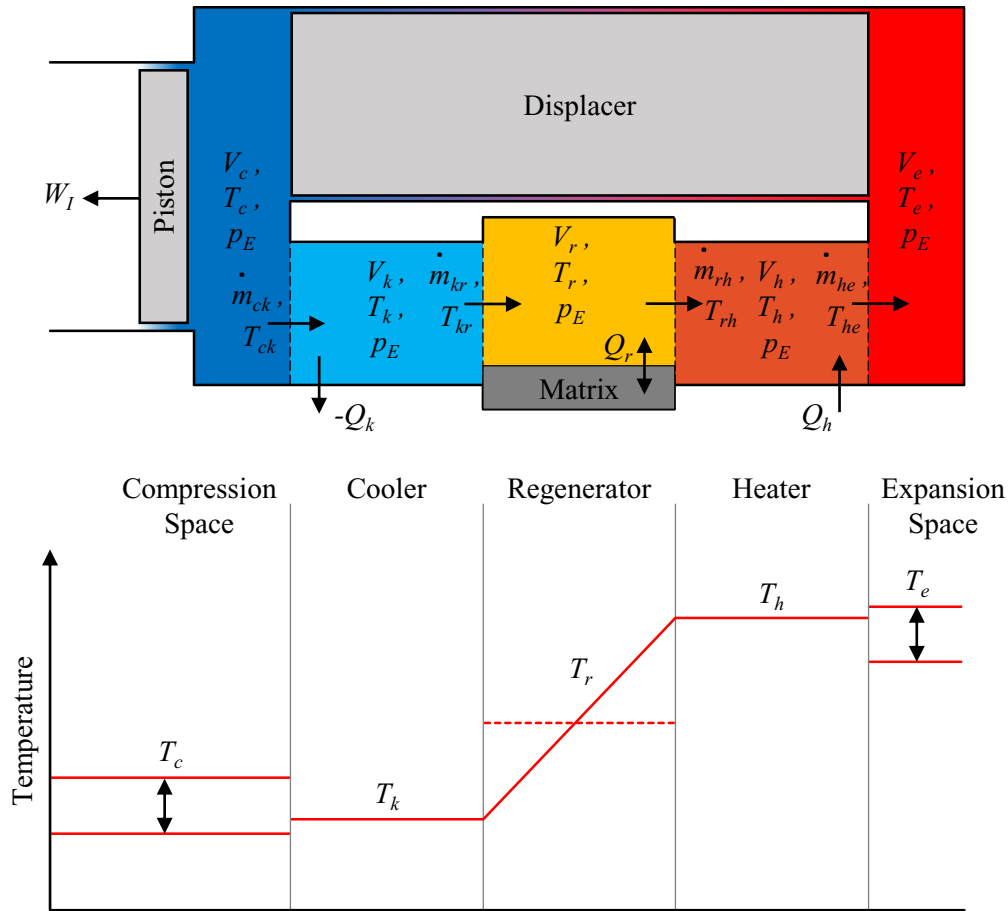


Figure 1-15: Temperature distribution and engine schematic for the ideal adiabatic model *after Urieli and Berchowitz* [29].

An equation set and solution method for the ideal adiabatic model are available in Urieli and Berchowitz [29]. Heat exchange occurs in the heater and cooler rather than in the expansion space and compression space [29]. The regenerator is perfect and the heat exchange throughout the engine is reversible [29]. Consequently, the indicated work is similar to that calculated by the ideal isothermal model [39]. The ideal adiabatic model better represents most real Stirling engines

compared to the ideal isothermal model because the expansion space and compression space are usually not designed for heat transfer [29]. However, the ideal adiabatic model ignores many loss mechanisms and is not accurate alone [29].

The ideal adiabatic model of Stirling engines represents the maximum cyclic pressure change of a Stirling engine [34]. Equation 1-31 is the pressure-volume relationship of a polytropic process [23]. An isothermal process has a polytropic exponent ( $N_{polytropic}$ ) of 1 and, at the other extreme of Stirling engine modelling, an adiabatic process has a polytropic exponent equal to the specific heat ratio ( $\gamma$ , equal to 1.4 for air) [23]. The pressure change is largest with a polytropic exponent of 1.4 compared to the other possibilities. This carries over into Stirling engine modelling where the ideal adiabatic model calculates the maximum possible cyclic pressure change [34].

$$p \cdot V^{N_{polytropic}} = \text{Constant} \quad 1-31$$

#### 1.4.2.3 Semi-Adiabatic Models

Semi-adiabatic models treat the expansion space and compression space as neither isothermal nor adiabatic [16]. They calculate the reference cycle with a non-zero, finite heat transfer coefficients in the expansion space and compression space [16]. Indicated work is lost to the irreversible heat transfer in the expansion space and compression space [34]. As a result, Semi-adiabatic models determine that engines are less efficient and produce less power than both the ideal isothermal and ideal adiabatic reference cycles [16,34].

#### 1.4.2.4 Imperfect Heat Exchange

A flaw with the ideal reference cycles is the assumption of perfect heat exchange and regeneration [29]. The heat exchanger walls and regenerator matrix have a finite heat transfer rate ( $Q_i$ ) with the working gas [29]. It is governed with Newton's law of cooling (Equation 1-32) at

any instant with the heat transfer coefficient ( $h_i$ ), the area wetted by working gas ( $A_{wetted,i}$ ) and the temperature difference between the heat exchanger wall and the working gas ( $T_{w,i} - T_i$ ) [29]. Some 2<sup>nd</sup> order models include imperfect heat exchange and regeneration in the reference cycle solution [16,29,40].

$$\dot{Q}_i = h_i \cdot A_{wetted,i} \cdot (T_{w,i} - T_i) \quad 1-32$$

Selection of a heat transfer coefficient is difficult due to the complex nature of flow in Stirling engine heat exchangers [39]. Flow through Stirling engine heat exchangers is transient, developing, non-isothermal, and occasionally compressible [39]. This eliminates many simplifications common in thermo-fluids modelling [39].

Urieli and Berchowitz [29] present a method of incorporating imperfect heat exchange into the adiabatic model—the Simple Analysis. The Simple Analysis calculates the additional heat exchange in the heater and cooler from imperfect regeneration [29]. Then it recalculates the heater and cooler gas temperatures with a finite convective heat transfer rate [29]. These calculations use steady flow correlations to predict the mean heat transfer rates in the heat exchangers [29]. They use a correlation from empirical data of steady flow through wire mesh for the regenerator mean heat transfer coefficient [29]. Urieli and Berchowitz [29] use Reynolds' simple analogy and the Blasius correlation for heater and cooler mean heat transfer coefficients.

Alfarawi et al. [40] introduce imperfect heat exchange with similar methods to Urieli and Berchowitz' [29] Simple Analysis. They use different steady flow correlations. The heater and cooler heat transfer coefficients are calculated with the Colburn J-factor for turbulent flow over a flat plate [40,41]. The regenerator heat transfer coefficient is calculated with the empirical, oscillating flow correlations by Gedeon and Wood [42] for random-fiber regenerators [40].

Thomas and Pittman [43] evaluated seven regenerator Nusselt number and friction factor correlations. Of these, five were steady flow correlations and two, by Gedeon and Wood [42], were oscillating flow correlations [43]. The correlations by Gedeon and Wood [42] have higher Nusselt numbers and friction factors than the steady flow correlations at similar Reynolds numbers [43].

Attempts have been made to create Nusselt number and friction factor correlations for oscillating flow heat exchangers [44–46]. These typically use the dimensionless flow characteristics of dimensionless oscillation amplitude of the fluid and kinetic Reynolds number (Valensi number) [44–46]. Zhao and Chen [46] developed an analytical solution in fully-developed, laminar, oscillating flow in a circular pipe. Zhao and Chen [44] developed empirical correlations for fully-developed, turbulent, oscillating flow in a circular pipe. Barreno et al. [45] numerically determined correlations for developing, transitional, oscillating flow in a circular pipe. These all have limited ranges of validity and apply only to circular pipes. Therefore, ranges of the flow characteristics and many duct geometries are not described by the existing correlations. Consequently, the correlations are difficult to use for engine design.

#### 1.4.2.5 Seal Leakage

Seal leakage is another loss mechanism that can be included in the reference cycle calculation. Seal leakage can occur: (1) across the displacer between the expansion space and compression space, (2) across the piston(s) between the working space and buffer space, and (3) between the engine and ambient [29,47]. Seal leakage past piston rings and other contact seals is typically considered negligible [29]. Leakage influences the mass of working gas participating in the thermodynamic cycle and generates a net enthalpy leak that can be calculated as a decoupled heat loss [29,47].

Several methods have been developed to calculate the mass transfer across leaks. Urieli and Berchowitz [29] derived an incompressible, quasi-steady flow method to calculate mass transfer across clearance seals. Huang [48] derived a quasi-steady, compressible flow equation for mass transport across a clearance. Mabrouk et al. [47] stated that quasi-steady methods are only valid at low engine frequencies. They derived a mass transfer equation for incompressible, transient flow across piston and displacer clearance seals [47]. These methods increase in complexity and should be selected to match the conditions in the engine.

The mass transfer component of the loss is directly incorporated into the conservation of mass in the reference cycle [29]. Li et al. [49] examined different leak magnitudes in a thermodynamic model by changing the clearance size. They illustrated how the indicator diagram changed from leakage [49]. As leak magnitude increased, expansion pressure decreased and compression pressure increased [49]. This reduced the amount of indicated work [49]. Further, the maximum engine pressure and minimum engine pressure occurred earlier in the cycle as leak magnitude increased [49].

### 1.4.3 Decoupled Losses

Decoupled losses are added to the solution of reference cycles to correct for simplifications in the idealized thermodynamic analysis of 2<sup>nd</sup> order models [34]. The losses can be classified as heat losses and power losses. Heat losses influence the heat transfer in Stirling engine components and include heat exchanger flow friction, enthalpy leakage, appendix gap losses, and conduction losses [34]. Power losses reduce the power output of the engine and include heat exchanger flow friction, gas spring hysteresis, heat transfer hysteresis, finite piston speed loss, mechanical losses, and auxiliary component losses. These loss mechanisms and the methods to predict them are overviewed below.

### 1.4.3.1 Heat Exchanger Flow Friction

Flow friction is a consequence of improved heat transfer in heat exchangers [9]. Transport equations for developing, oscillating flow accompanied with density changes are difficult to solve even in simple geometries [8]. Therefore, Stirling engine analysis often neglects these complexities by using correlations for friction factor [8]. Correlations for friction factor are determined in parallel with correlations for the heat transfer coefficient or Nusselt number [43–45,50].

### 1.4.3.2 Enthalpy Leakage

Net enthalpy leakage is the decoupled heat loss portion of the losses generated from leakage. The mean enthalpy leak rate ( $\dot{Q}_{leak}$ ) changes the heat transfer rates in the heat exchangers [29]. It is calculated by integrating the instantaneous enthalpy transfer over the whole cycle, as shown in Equation 1-33 with the engine frequency, the instantaneous mass transfer rate ( $\dot{m}_{leak}$ ), the isobaric specific heat capacity ( $c_p$ ), and the conditional leaking gas temperature ( $T_i$ , different for inflow and outflow) [47]. If the temperature of the leaving the cell is different than the temperature of the gas entering the cell without a net mass flow, there will be a net enthalpy leak [29].

$$\dot{Q}_{leak} = f \cdot \int_0^f \dot{m}_{leak} \cdot c_p \cdot T_i \cdot dt \quad 1-33$$

### 1.4.3.3 Appendix Gap Losses

Appendix gap losses are a group of thermal shortcuts that occur in the annular gap between the displacer and displacer cylinder wall [29]. A review by Pfeiffer and Kuehl [51] describe four loss mechanisms—shuttle transfer, gas enthalpy transfer, hysteresis heat transfer and loss of thermal

compression. Shuttle transfer and gas enthalpy transfer are the most significant of these losses [29,51].

Shuttle transfer is heat transfer between the displacer cylinder and displacer that changes direction with displacer position [29]. Figure 1-16 (a) illustrates shuttle transfer. Both the displacer cylinder and displacer have a temperature gradient from the compression space temperature to the expansion space temperature. When the displacer is closer to the expansion space its surface is colder than the neighboring cylinder surface [29]; as a result, heat  $Q_{shuttle}$  transfers from the displacer cylinder to the displacer [29]. The heat returns to the displacer cylinder when the displacer is closer to the compression space and its surface is hotter than the neighboring cylinder surface. [29].

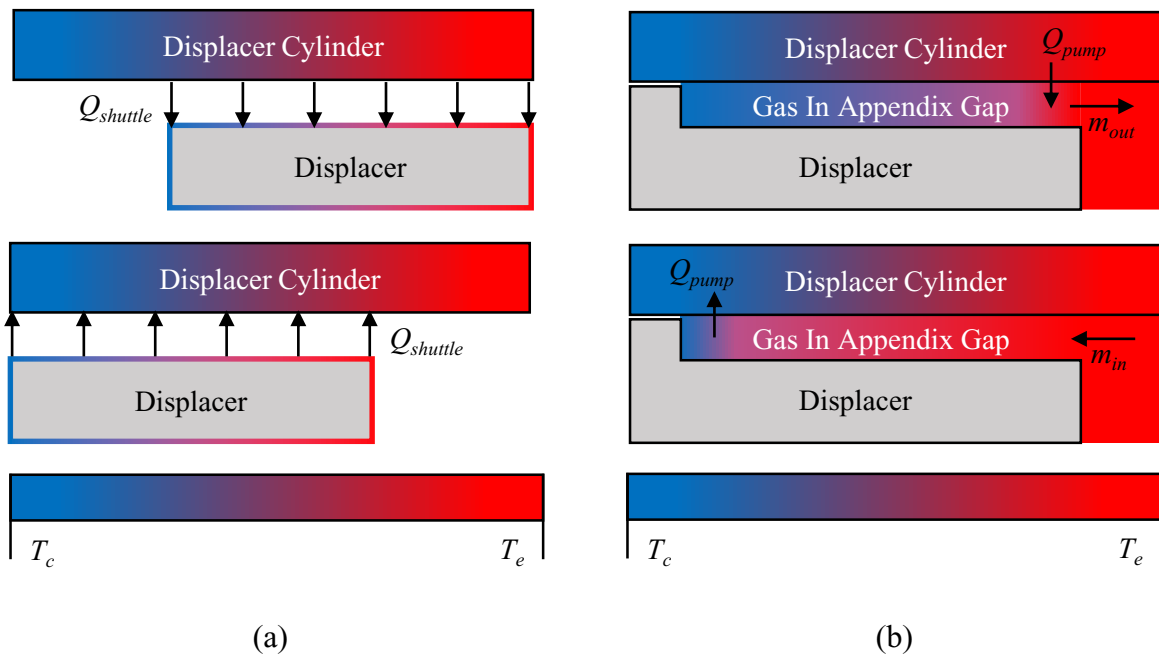


Figure 1-16: Diagrams of (a) shuttle transfer and (b) gas enthalpy transfer appendix gap losses.

Urieli and Berchowitz [29] and West [8] present a common solution for shuttle transport ( $Q_{shuttle}$ ). It is calculated with Equation 1-34 by assuming sinusoidal displacer motion and constant,



linear temperature gradients in the axial and radial dimensions. Shuttle transport depends on the displacer cylinder diameter ( $d_d$ ), the thermal conductivity of the working gas ( $k_g$ ), the displacer stroke ( $S_d$ ), the temperature difference between the expansion and compression space ( $T_e - T_c$ ), the length of the displacer cylinder ( $l_{cylinder}$ ), and the appendix gap width ( $b$ ). Other researchers derived similar equations with different coefficients (replacing  $\pi / 2$ ) due to different assumptions, such as non-sinusoidal displacer motion [51].

$$\dot{Q}_{shuttle} = \frac{\pi}{2} \cdot \frac{d_d \cdot k_g \cdot S_d^2 \cdot (T_e - T_c)}{l_{cylinder} \cdot b} \quad 1-34$$

Gas enthalpy transport (or pumping loss) results from gas flow into and out of the appendix gap [51]. It is driven by engine pressure changes, temperature changes, and displacer motion [51]. Figure 1-16 (b) describes gas enthalpy transfer. Gas exiting the appendix gap is colder than its surroundings and absorbs heat  $Q_{pump}$  [8]. Later the gas returns to the appendix gap and is compressed towards the displacer seal [8]. This gas is now hotter than its surroundings and rejects heat  $Q_{pump}$  to the displacer cylinder [8].

Urieli and Berchowitz [29] provide Equation 1-35 to predict the rate of gas enthalpy transport ( $Q_{pump}$ ). This method assumes that the axial and radial temperature profiles are linear, the displacer is adiabatic, the displacer seal does not leak, pressure change is sinusoidal, gas properties are constant, and the engine is at steady-state [29]. It depends on variables similar to shuttle loss: displacer cylinder diameter, appendix gap width, displacer stroke, expansion space temperature, compression space temperature, and working gas thermal conductivity. The displacer cylinder material influences gas enthalpy transport with the cylinder wall thermal diffusivity ( $\alpha_w$ ) and cylinder wall thermal conductivity ( $k_w$ ). The remaining variables are the engine frequency, the

working gas specific heat ratio ( $\gamma$ ), the engine pressure change ( $\Delta p_E$ ), and the phase angle that the engine pressure leads displacer position ( $\psi$ ).

$$\dot{Q}_{pump} = -\frac{d_d \cdot b \cdot S_d \cdot f}{2} \cdot \left[ \frac{\gamma}{\gamma-1} \cdot \ln\left(\frac{T_e}{T_c}\right) \cdot \left( \frac{1}{2} - \sqrt{\frac{4 \cdot \pi \cdot \alpha_w}{f}} \cdot \frac{k_g}{k_w} \right) - \frac{1}{2} \right] \cdot \Delta p_E \cdot \sin(\psi) \quad 1-35$$

Shuttle transfer decreases with increasing appendix gap width and gas enthalpy transport increases with gap width [8,29]. As a result, there is an optimum appendix gap width that minimizes appendix gap losses [8,29]. Pfeiffer and Kuehl [51] explained that the optimum appendix gap width from Urieli and Berchowitz' [29] method is larger than the true optimum appendix gap width.

#### 1.4.3.4 Conduction Loss

In Stirling engines, there are large thermal gradients across the regenerator, regenerator housing, and displacer that can allow for significant conduction loss [14,29]. Conduction pathways include the working gas, structural components, and the regenerator matrix [8,14]. Fourier's law of conduction (Equation 1-36) with a linear temperature gradient is sufficiently accurate for conduction loss calculations [29]. It requires a thermal conductivity ( $k$ ), cross-sectional area ( $A_{cross-section}$ ), a temperature difference ( $\Delta T$ ), and a length ( $l$ ) to calculate the loss.

$$\dot{Q}_{conduction} = \frac{k \cdot A_{cross-section} \cdot \Delta T}{l} \quad 1-36$$

### 1.4.3.5 Gas Spring Hysteresis

Gas spring hysteresis loss is the total irreversibility generated from thermal effects in the buffer space [29]. An ideal, finite-volume buffer space is either adiabatic or isothermal, but non-zero, finite heat transfer occurs in a real buffer space [29]. Figure 1-17 presents the pressure-volume diagram of a buffer space with gas spring hysteresis. As the buffer space is compressed, the bulk temperature of the working gas increases and gas near the wetted surfaces of the buffer space reject heat to those surfaces [29]. Then, as the buffer space expands, the bulk temperature of the working gas decreases and gas near the wetted surfaces of the buffer space receive the same heat back from those surfaces [29]. As a result, the compression process occurs at a higher pressure than the expansion process and work is lost without net heat transfer [25,29]. Work lost to gas spring hysteresis is the area of the pressure volume diagram in the buffer space [25]. Urieli and Berchowitz [29] present an analytical solution for the work lost to gas spring hysteresis, but their analysis does not account for mixing generated by mechanical components in the buffer space of kinematic Stirling engines.

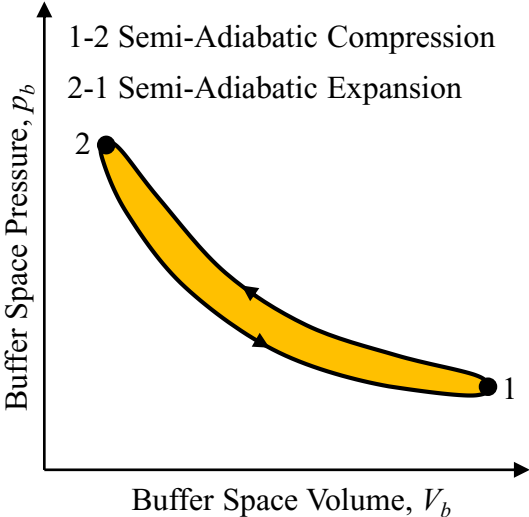


Figure 1-17: Pressure-volume diagram of an arbitrary, finite volume buffer space with non-zero, finite heat transfer.

### 1.4.3.6 Heat Transfer Hysteresis

Heat transfer hysteresis is similar to gas spring hysteresis but for working gas in the engine [29]. Irreversible heat transfer throughout the engine during expansion and compression reduces the indicated work produced by the engine [34]. The impact of this loss on the engine performance requires accurate estimates of the heat transfer coefficient throughout the engine [34]. At typical Stirling engine frequencies, the loss decreases as engine frequency increases [18].

### 1.4.3.7 Finite Piston Speed Loss

Petrescu et al. [52] stated that the pressure acting on translating piston face does not equal the pressure of the working space. The pressure acting on the piston face is higher during compression and lower during expansion. As a result, the expansion and compression processes occur at with a smaller pressure difference between them and work is lost. Equation 1-37 calculates the work lost to the finite piston speed loss ( $W_{FPS}$ ) in an adiabatic space with the engine pressure, specific heat ratio ( $\gamma$ ), piston velocity ( $v_p$ , positive during expansion), specific gas constant, and the local working gas temperature ( $T_i$ ). This loss increases with piston speed and therefore engine frequency.

$$W_{FPS} = \oint p_E \cdot \left( -\frac{v_p \cdot \sqrt{3 \cdot \gamma}}{\sqrt{3 \cdot R \cdot T_i}} \right) \cdot dV_E \quad 1-37$$

### 1.4.3.8 Mechanical Losses

Mechanical losses are the total power loss to mechanical friction in the engine [34]. This includes friction from piston rings, mechanical springs, shaft seals, bearings, and diaphragms [27]. The most accurate method to determine mechanical losses is to measure the loss on the engine itself [34]. However, this method is not useful for the design of a new engine.

Senft's [32] Fundamental Efficiency Theorem (FET) is a general method to estimate mechanical losses in kinematic heat engines. FET evaluates the work transfer through the mechanism between the piston to the flywheel, as shown in Figure 1-18 [32]. The mechanism is imperfect and only a fraction of the work entering the mechanism ( $W_{in}$ ) exits the mechanism ( $W_{out}$ ), described by Equation 1-38 [32]. The fraction of work transferred through the mechanism is the constant mechanism effectiveness ( $E$ ) [32]. In a Stirling engine, the output work from the piston is the efficacious work ( $W_{Eff}$ ) and it loses energy in the mechanism. The piston requires forced work ( $W_F$ ) to perpetuate the cycle, so additional work must enter the mechanism to overcome mechanical losses. FET (Equation 1-39) calculates shaft work ( $W_S$ ) with conservation of energy on the flywheel at steady-state [32]. The mechanical efficiency ( $\eta_{mec}$  in Equation 1-40) is at best equal to the mechanism effectiveness. It decreases as forced work increases and as mechanism effectiveness increases. Mechanical losses from FET are independent of engine frequency [32].

$$W_{out} = E \cdot W_{in} \quad 1-38$$

$$W_S = E \cdot W_{eff} - \frac{1}{E} \cdot W_F = E \cdot W_I - \left( \frac{1}{E} - E \right) \cdot W_F \quad 1-39$$

$$\eta_{mec} = \frac{W_S}{W_I} = E - \left( \frac{1}{E} - E \right) \cdot \frac{W_F}{W_I} \quad 1-40$$

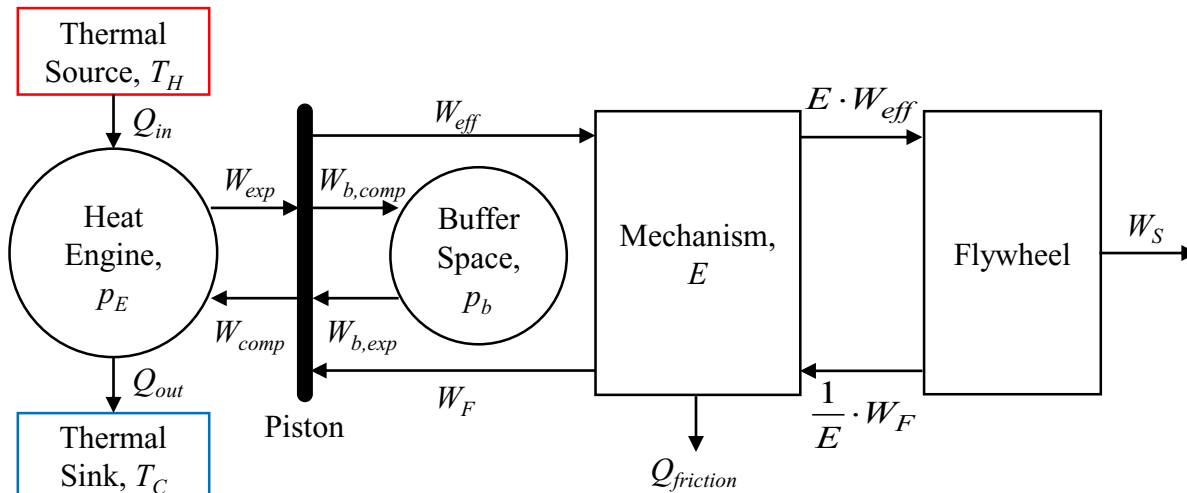


Figure 1-18: Energy transfer diagram for FET, *after Senft* [32].

Some models use mechanical loss calculations from internal combustion engines [16,53]. For example, Cheng and Yu [53] calculate mechanical losses from Millington and Hartles [54] diesel engine friction correlation. It depends on compression ratio and engine frequency [54]. These may include the frequency dependent mechanical losses but would need to be validated for Stirling engines.

Dynamic models completely model the kinematic mechanism [35]. This allows for mechanical losses to be calculated individually at each source, such as piston seal friction and connecting rod bearing friction [55]. Mechanical losses calculated in a dynamic model are specific to that mechanism design and are difficult to apply generally.

#### 1.4.3.9 Auxiliary Component Losses

A complete estimate of the useful power produced by a Stirling engine system includes the power consumed by auxiliary components necessary for operation [34]. Auxiliary components include fans, compressors, control systems and pumps necessary for operation [34]. Martini [34] suggested that auxiliary components consume more than 5 % of the shaft power.

#### 1.4.4 3<sup>rd</sup> Order Models

Third order models do not assume that the loss mechanisms are independent of the thermodynamics [34]. These models solve the transport equations—continuity, momentum and energy—with the equation of state simultaneously in nodes [29,34]. Conventional 3<sup>rd</sup> order models simplify the engine into one dimension [16,34]. They solve the complex flow with flow friction and heat transfer correlations [16,34]. Complete 2D and 3D engine simulations performed with modern, commercial computational fluid dynamics (CFD) software are classified as 3<sup>rd</sup> order models [38]. 3<sup>rd</sup> order models are computationally more expensive than 2<sup>nd</sup> order models and they are more difficult to use for design optimization [34,38]. However, a properly validated 3<sup>rd</sup> order model can provide insight to immeasurable flows and temperatures [34]. 3<sup>rd</sup> order models are not universally more accurate than 2<sup>nd</sup> order models and may require the addition of some decoupled loss terms [16,34].

#### 1.4.5 Dynamic Models for Kinematic Stirling Engines

Dynamic models of kinematic Stirling engines couple the thermodynamic and mechanical simulations [35]. There are two motivations for the use of dynamic models of Stirling engines. One is to remove the assumption of constant crankshaft angular velocity used in many thermodynamic models [55]. The other is to simulate the transient operation of an engine [35]. Dynamic models also allow for sophisticated mechanical loss calculations. Itemized mechanical losses, such as contact seal friction or bearing friction, can be calculated and added at the joint in the mechanical simulation [55]. Further, frequency dependent loads, such as shaking forces and inertial loads, are part of the load calculations in the engine [38]. Dynamic models require specific information about the kinematic mechanism and hence lack generality. This sub-section describes the typical solution process of dynamic models for kinematic Stirling engines.

Dynamic models follow a solution method similar to the methods of Cheng and Yu [35], shown in the flow chart (Figure 1-19). The process starts with the initial mechanism positions, mechanism velocities, and thermodynamic conditions. Then the time advances by a step ( $dt$ ) and the new positions and are calculated. The volumes are input into a thermodynamic model that returns pressure. Pressure is a force acting on the piston and is used to calculate the new mechanism forces, torques, accelerations, and velocities. The time advances again and flywheel angular velocity is used to calculate the new angular positions. The model is complete after a certain time or when it reaches steady-state.

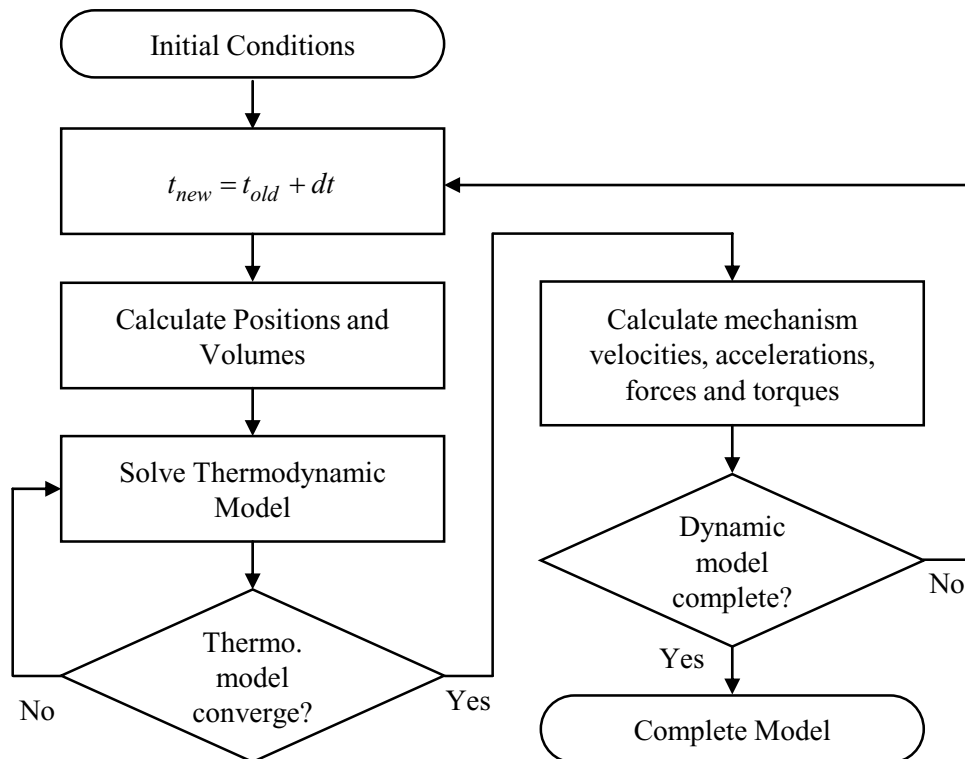


Figure 1-19: Flow chart of a dynamic model solution process, *after Cheng and Yu* [35].



## 1.5 Low-Temperature-Difference Stirling Engines

---

LTDSEs operate with a temperature difference ( $T_H - T_C$ ) less than 150 °C. Most commercially developed Stirling engines are HTDSEs (Stirling engines operating with a temperature difference greater than 450 °C) [14,15]. The Stirling engine studied in this thesis was converted from an HTDSE to an LTDSE but was studied at an intermediate temperature difference. This section overviews the characteristics of LTDSEs and works that validated thermodynamic models with LTDSEs.

Ivo Kolin [17] and James Senft [11] pioneered the development of LTDSEs. They both built palm-scale, gamma-type Stirling engines with flat plate heat exchangers [11,17]. The final iteration of Kolin's engine operated with a temperature difference of 15 °C [27]. Senft [11] built an engine that operated with a temperature difference of 0.5 °C. These engines proved that low-grade heat can be converted to mechanical power by Stirling engines.

### 1.5.1 LTDSE Characteristics

The engines of Kolin [17] and Senft [11] were designed with geometry and heat exchangers unorthodox for HTDSEs. Literature was reviewed to find the common characteristics of LTDSEs. This sub-section briefly presents these findings.

Kolin [17] reduced his experiences with LTDSE design to three rules. First, the engine must not leak to the buffer space or surroundings. The consequences of a leak are more severe in a LTDSE compared to a HTDSE. Second, the dead volume in the engine should be minimized. Third, the compression ratio ( $V_{E,max} / V_{E,min}$ ) of an LTDSE must be small. Some of these were explored further in other studies.

The optimal compression ratio for maximum power of LTDSEs has been studied by several researchers [17,27,37,56]. Kolin [17] generated an empirical relation for compression ratio to

temperature difference. Senft [27] describes the optimal compression ratio for maximum shaft work with the ideal Stirling cycle and mechanical losses. It depends on temperature ratio ( $N_T = T_H / T_C$ ). Egas and Clucas [56] equated the optimal compression ratio with temperature ratio from the efficacious, ideal Stirling cycle (no forced work) with maximum indicated work. Stumpf [37] compared the above methods for calculating the optimal compression ratio with experimentally optimized LTDSEs. Then, Stumpf [37] proposed that the optimal compression ratio was the mean of Kolin's [17], and Egas and Clucas' [56] methods. The commonality with all of these methods is that as thermal source temperature ( $T_H$ ) decreases, the optimal compression ratio decreases. Therefore, LTDSEs have a lower compression ratio compared to HTDSEs.

Other aspects of LTDSEs are different compared to HTDSEs. A review of LTDSEs by Kongtragool and Wongwises [57] focused on the design of solar-powered LTDSEs. They stated that gamma-type LTDSEs should have: (1) a large displacer swept volume compared to the piston swept volume, (2) a large diameter but short displacer, (3) a short displacer stroke with dwell periods at the extremes, (4) flat plate heat exchangers in the displacer cylinder, and (5) low engine frequencies.

Hoegel et al. [58] used a 3<sup>rd</sup> order model to compare LTDSE and HTDSE geometry. An alpha-type LTDSE with  $T_H = 150\text{ }^\circ\text{C}$  and an identical HTDSE with  $T_H = 750\text{ }^\circ\text{C}$  ( $T_C = 40\text{ }^\circ\text{C}$ ) were modelled with Sage, a commercial 3<sup>rd</sup> order modelling software. The impacts of engine frequency, phase angle, regenerator design and heat exchanger design on indicated power and thermal efficiency were studied. Hoegel et al. determined the following differences between LTDSEs and HTDSEs.

- LTDSEs achieve maximum indicated power at a lower engine frequency compared to HTDSEs.

- Alpha-type LTDSEs have a phase angle closer to  $180^\circ$ , whereas alpha-type HTDSEs have a phase angle close to  $90^\circ$ . In gamma-type LTDSEs this corresponds to a larger displacer swept volume compared to the piston swept volume.
- The optimum regenerator of a LTDSE is more porous than the optimum regenerator in a HTDSE.
- The optimum heat exchanger in a LTDSE has a higher number of shorter tubes than the optimum heat exchanger of a HTDSE.
- LTDSEs can use identical heaters and coolers without significantly reducing the performance of the engine.

From these studies, several conclusions can be made about the properties of gamma-type LTDSEs. First, LTDSEs have a small compression ratio. The displacer swept volume of a gamma-type LTDSE should be larger than the piston swept volume. The heat exchangers and regenerator of an LTDSE should have high surface area but small volume. LTDSEs will operate at lower engine frequencies than HTDSEs, which may increase the influence of losses in LTDSEs.

### 1.5.2 LTDSE Models and Validation

Stirling engine thermodynamic models are often validated with HTDSEs [16]. However, the influence of loss mechanisms may change for LTDSEs compared to HTDSEs, as pointed out by Kolin [17] for leakage loss and Yang and Gschwendtner [18] for heat transfer hysteresis. This subsection describes the studies that validate Stirling engine thermodynamic models with LTDSEs.

Berchowitz [59] validated a 3<sup>rd</sup> order model by Urieli [60] with a Stirling engine near LTDSE conditions. Unlike some 3<sup>rd</sup> order models, this model includes working gas inertia, working gas flow friction, and working gas kinetic energy in the transport equations [16]. The model was validated with an alpha-type engine near low-temperature-difference conditions [59]. Condensing

steam ( $T_H \approx 93$  °C) heated the engine and sublimating carbon dioxide ( $T_C \approx -73$  °C) cooled it [59]. The engine was incapable of producing power, so it was driven at frequencies of 2.5, 3.35, and 4.35 Hz [59]. Chen and Griffin [16] presented that Urieli's 3<sup>rd</sup> order model under-estimated heat absorption by 7 % and heat rejection by 13 %, and over-estimated power by 40 %.

Robson et al. [61] wrote and validated a dynamic model for a palm-scale, gamma-type, free-displacer LTDSE (Ringbom engine). The displacer motion was constrained by mechanical springs in its extreme positions and the piston motion was constrained by a slider-crank mechanism with a massless connecting rod. The thermodynamic analysis assumed that flow in the regenerator was laminar, the coefficients of heat transfer were constant, and the fluid was well mixed in the expansion space and compression space. This model over-estimated engine pressure change by 49 % and under-estimated engine speed by 25 %. The accuracy of shaft power and indicated work were not presented.

Li et al. [49] used a 2<sup>nd</sup> order model to evaluate the influence of decoupled losses in a palm-scale LTDSE. The model generated a reference cycle from the isothermal model with imperfect heat transfer in the heat exchangers and seal leakage. The model included decoupled losses for fluid friction, heat transfer hysteresis, shuttle transfer, finite piston speed loss, and conduction. The model was validated with the engine using a 14 °C temperature difference and  $f = 0.4$  Hz. The model estimated indicated work with 9.49 % error but the indicator diagram shape was different. Shaft power was not measured and the engine was not validated at other conditions.

Chen [62] used 3D CFD to model a palm-scale, gamma-type LTDSE. The CFD model was compared to data collected by Kato [63] at a single operating condition ( $T_H = 90$  °C,  $T_C = 20$  °C, and  $f = 0.63$  Hz). The model over-estimated indicated work by 16.6 %. The model was not compared to measured data at other operating conditions.

The models for LTDSEs described above were validated with palm-scale engines or engines that did not run. Additionally, some validations were incomplete and showed errors. More work can be done to improve the modelling and validation of models for LTDSEs.

## 1.6 The ST05G Stirling Engine

---

The ST05G is a  $90^\circ$  gamma-type Stirling engine designed by Dieter Veibach [64]. The original configuration of the engine was comprised of cast aluminum components. The ST05G is accessible to the public under a non-commercial Creative Commons license [64]. This section describes the construction of the ST05G-CNC, summarizes research publications, and introduces the previous work on this engine at the University of Alberta.

### 1.6.1 ST05G-CNC Construction

The ST05G-CNC is a CNC machined configuration of the ST05G Stirling engine. Figure 1-20 shows a CAD model of the ST05G-CNC Stirling engine. Mechanical drawings of this engine were sold by Ve-Ingenieure [64]. The components of this engine discussed in detail are the heater, regenerator, cooler, displacer, piston, connecting pipe, and mechanism.

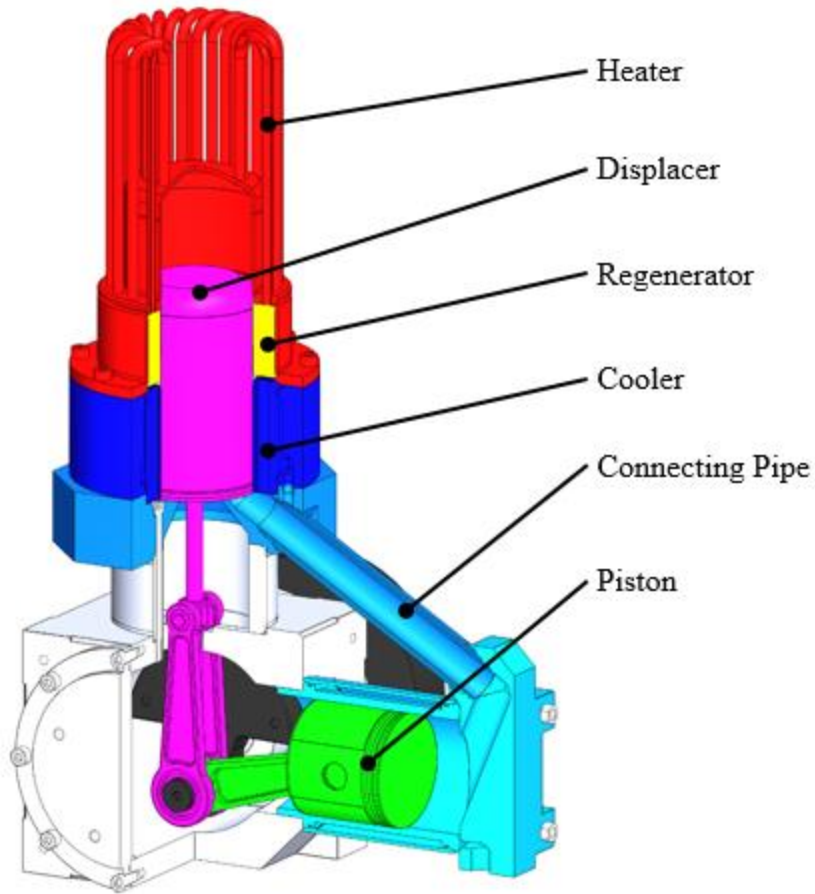


Figure 1-20: CAD model of the original ST05G-CNC Stirling engine.

#### 1.6.1.1 Heater

The ST05G was designed to receive heat from combustion exhaust gas, specifically biomass combustion [64]. The heater of the ST05G is located at the top of the displacer cylinder. It is constructed with 20 bent, stainless steel tubes with an 8 mm OD and 1 mm thick walls [65]. The tubes are welded to the regenerator housing and the top of the displacer cylinder [65]. Combustion gases flow across the tube bank to transfer heat to the heater.

### 1.6.1.2 Regenerator

The ST05G-CNC contains a random-fiber regenerator in an annulus outside the displacer cylinder. The regenerator cavity has dimensions 97.6 x 134 x 57.5 mm (ID x OD x Length) [65]. The matrix is 250 g of 0.05-0.06 mm stainless steel wire mesh for a porosity of 90 % [64,65].

### 1.6.1.3 Cooler

The cooler of the ST05G-CNC is located in the annulus around the displacer cylinder and below the regenerator. The working gas passes through 144 rectangular channels that are 1 mm wide, have a 10.5 mm radial depth, and are 84 mm long [65]. An annular water jacket over the cooler receives heat from the working gas [65]

### 1.6.1.4 Displacer

The ST05G displacer oscillates in the displacer cylinder which is comprised of the internal walls of the regenerator and cooler. It has a 96 mm bore and 75 mm stroke [65,66]. The displacer body is 156 mm long and hollow [65]. Three isolation plates in the displacer body provide structure and reduce radiative and convective heat transfer through the displacer [30,65]. The displacer seal is a Rulon piston ring that with a stepped joint and backing spring to apply outward load on the seal [65]. It slides against the internal wall of the cooler [65].

### 1.6.1.5 Power Cylinder and Piston

The power cylinder contains the piston and is located at a 90 ° angle to the displacer cylinder [65]. The piston has an 85 mm bore a 75 mm stroke [65,66]. Due to larger pressure differences across the piston compared to the displacer, the piston uses two Rulon piston rings with a stepped joint and backing spring [65]. Teflon sheets, adhered to the piston, transfer radial piston loads to a cylinder liner machined from aluminum alloy [65]. The cylinder is cooled by cooling water in an annular water jacket beyond the cylinder liner [65].



#### 1.6.1.6 Connecting Pipe

The connecting pipe joins the working volumes of the displacer cylinder and power cylinder. It has a doubled walled construction with working gas flowing through the internal tube and cooling water flowing through the annulus between the tubes [65]. The internal tube inside diameter is 26 mm [65].

#### 1.6.1.7 Mechanism

Piston and displacer motion are constrained by slider-crank mechanisms [65]. The radial loads applied on the displacer are supported by two linear bearing supporting a linear rod [65]. The radial loads applied on the piston are supported by the power cylinder [65]. Both mechanisms are linked on common pivot on a cantilevered crankshaft [65]. A single counterweight reduces the shaking forces generated by the displacer and piston [65].

### 1.6.2 ST05G and Derivative Engines in Literature

A derivative of the ST05G Stirling engine is the focus of the experimental and numerical analyses in this thesis. This subsection summarizes the published works organized by research group.

#### 1.6.2.1 Université de Monastir, Tunisia

Gheith et al. [67] developed a test station for the ST05G Stirling engine. It included 0.025 mm junction diameter, type-K thermocouples to measure dynamic temperature at 8 locations in the regenerator. Brake power of the engine was measured with an alternator on the crankshaft [67]. The pressure was measured in the compression space and expansion space. Measurements were timed with a rotary encoder for 360 acquisitions per rotation. The engine was not capable of starting at atmospheric pressure. Experiments determined that brake power increased with charge

pressure and cooling water flow rates. Dynamic temperature measurements in the regenerator provided evidence of asymmetric working fluid flow through the regenerator.

In their next work, Gheith et al. [68] tested four regenerator materials—304L stainless steel, copper, aluminum, and Monel 400—each at 90 % porosity. They concluded that 304L stainless steel was the best regenerator material because it produced the highest brake power and it resisted oxidation.

The regenerator temperature asymmetry was studied in greater detail by Gheith et al. [69]. Coolant flow rate, charge pressure, thermal source temperature and operating time were varied to study their influence on the temperature asymmetry in the regenerator. Thermal source temperature had the greatest impact on the temperature asymmetry. This study also found that the temperature asymmetry dissipates thermal energy in the engine.

Gheith et al. [70] manipulated thermal source temperature, thermal sink temperature, coolant flow rate, charge pressure, and engine speed to study the heat transfer rate, thermal efficiency and exergy efficiency of the heater. They determined that the heat absorbed by the heater increases with heater temperature, the temperature difference between the expansion and compression space, coolant flow rate and charge pressure. The heater was most efficient and transferred the most heat at  $T_H = 500 \text{ }^\circ\text{C}$ ,  $p_{E,mean} = 700 \text{ kPa}$ , and  $f = 6.1 \text{ Hz}$ .

To expand on their previous regenerator study, Gheith et al. [71] re-examined the four regenerator materials and stainless steel regenerators at 75, 80, 85, 90 and 95 % porosity. This study found that aluminum deformed in the regenerator cavity at temperatures above 500 °C over 15 hours of continuous operation. The engine with a 85 % porous, 304L stainless steel regenerator produced the maximum power and maximum efficiency at all thermal source temperatures and charge pressures studied.

Hachem et al. [72] developed a 2<sup>nd</sup> order model based on Urieli and Berchowitz' [29] Simple Analysis with the addition of displacer shuttle loss, conduction loss, gas flow friction and mechanical friction of the mechanism bearings. The modelled results for the ST05G confirmed the trends that increasing source temperature and charge pressure results in increasing shaft power. Further, this work determined that the regenerator contributes the greatest portion of engine losses.

Hachem et al. [73] performed an exergetic analysis with models of a Stirling engine—the ST05G—and an open Joule cycle Ericsson engine. Both engines operated with identical conditions ( $T_H = 727\text{ °C}$ ,  $T_C = 27\text{ °C}$ ,  $p_{E,mean} = 700\text{ kPa}$  and  $f = 10\text{ Hz}$ ). The Stirling engine outperformed the Ericsson engine for exergy efficiency and thermal efficiency even when heat in the exhaust gas of the Ericsson engine was recovered.

#### 1.6.2.2 University of Burgundy, France

Bert et al. [74] utilized a modified version of the ST05G-CNC Stirling engine to validate a 2<sup>nd</sup> order thermodynamic model for kinematic optimization. This configuration of the ST05G-CNC has a drilled block heater that receives heat from electric heaters. The 2<sup>nd</sup> order model divided the engine into 3 cells—hot volume, regenerator and cold volume. This model used time-dependent, semi-adiabatic (near isothermal) cells. The gas and regenerator matrix temperature was calculated in each time step with quasi-steady heat transfer coefficients using Newton's law of cooling. The model also included gas flow friction. The model's ability to predict indicated power was validated for both air and helium working fluids, charge pressures up to 1100 kPa, and heater wall temperatures from 200 to 700 °C. The model estimated indicated work but the modelled indicator diagram shape did not match the experimental indicator diagram. The model was also used to optimize indicated power by changing piston and displacer motion. Indicated power increased by 22 % with the optimal piston and displacer motion that included dwells at their extremes.

### 1.6.2.3 University of Birmingham, United Kingdom

Alfarawi et al. [40] created a 2<sup>nd</sup> order model and validated it with the ST05G-CNC Stirling engine. Their 2<sup>nd</sup> order model was based off the non-ideal adiabatic analysis, similar to Urieli and Berchowitz Simple Analysis, but with convective heat exchange calculated from the Colburn J-factor [29,40]. The model also included conduction loss, shuttle loss and the fundamental efficiency theorem to predict shaft power [32,40]. The accuracy of the model degraded with decreasing thermal source temperature for maximum deviation of 15 % and 7.5 % for shaft power and efficiency, respectively, at the lowest thermal source temperature ( $T_H = 450$  °C). With the validated model, Alfarawi et al. optimized the connecting pipe inside diameter for maximum power with 16 mm and maximum efficiency with 20 mm.

Alfarawi et al. [75] also performed 2D CFD simulations of the ST05G-CNC Stirling engine. They determined that the optimum connecting pipe inside diameter was 14 mm for maximum power. This contradicts the 2<sup>nd</sup> order model used earlier [40,75].

Later, Alfarawi et al. [76] used 3D CFD simulations to test miniature-channel regenerators with the ST05G-CNC Stirling engine. Miniature-channel regenerators are solid blocks with many  $\leq 1.5$  mm diameter holes bored through them. First, the porous media properties of the regenerator were determined with a 3D CFD simulation isolating the regenerator. Then, the porous media properties were used in a CFD simulation of the engine. The miniature-channel regenerators increased cooling power requirements and decreased the power output of the engine compared to a random-fiber regenerator.

### 1.6.2.4 University of Tehran, Iran

Hooshang et al. [77,78] studied the ST500 Stirling engine which is modified from the ST05G-CNC Stirling engine. It has a heater and cooler designed for use with a natural gas combustion

thermal source [77,78]. It produced a maximum power of 400 W at an unknown operating condition [77,78]. The following two paragraphs describe the studies performed with the ST500.

Hooshang et al. [77] validated the Nlog 3<sup>rd</sup> order modelling software with the ST500 Stirling engine. They determined the maximum deviation between the model and experiments was 11.4 % for shaft power and 17.8 % for heat rejection rate. Additionally, they concluded that the modelled and experimental indicator diagrams were similar in shape. With the validated model, Hooshang et al. optimized displacer stroke (102 mm), phase angle (92.7 °) and engine frequency (18.4 Hz) for maximum power.

Hooshang et al. [78] performed dynamic simulations of the ST500. They used a dynamic model with a 3<sup>rd</sup> order thermodynamic model. This dynamic model included friction loss at the piston seals but ignored gravity. The modelled and measured angular velocity fluctuations were 0.375 Hz and 0.4 Hz (6.25 % deviation), respectively, with a mean frequency of 15.7 Hz. No further conclusions were made on angular speed fluctuations for other operating conditions or flywheel sizes.

#### 1.6.2.5 University of Alberta, Canada

Speer [79] constructed a modified version of the ST05G Stirling engine to facilitate heating via conduction and instrumentation. The external geometry of the heater became a smooth cylinder built to fit inside a solid thermal storage block simulated by a steel cap containing electric cartridge heaters. Internally, the heater changed from bent tubes to rectangular slots in an annulus around the displacer cylinder. Speer included both temperature and pressure sensors in the crankcase and throughout the engine. Shaft power was measured with a torque transducer and rotary encoder. Minor modifications were made to the cooler, connecting pipe and mechanism. The piston was modified to use different seals and wear surfaces. Table 1-1 list the performance and operating

condition of three ST05G configurations. The modified ST05G-CNC was less powerful than the original ST05G.

Table 1-1: List of operating conditions and performance of three ST05G configurations.

Parameter	Original ST05G [66]	Modified ST05G-CNC (Speer) [79,80]	Low-Temperature ST05G (Speer) [79]
Thermal Source Temperature ( $^{\circ}\text{C}$ ), $T_H$	650	400	300
Thermal Sink Temperature ( $^{\circ}\text{C}$ ), $T_C$	-	21	21
Mean Engine Pressure (kPa), $p_{E,mean}$	1000	414	450
Working Fluid	Nitrogen or Air	Air	Air
Swept Volume (L), $V_{sw}$	0.426	0.426	0.114
Maximum Frequency (Hz), $f_{max}$	13.3	-	3.2
Maximum Power (W), $\dot{W}_S$	505	15	3

Speer [79] wrote a 2<sup>nd</sup> order model compiled from equations and processes in other works. The reference cycle of the model was calculated with the adiabatic model and Urieli and Berchowitz' [29] Simple Analysis for imperfect heat exchange. The model included decoupled losses for flow friction from Urieli and Berchowitz [29], mechanical friction from Senft [32], empirical gas spring hysteresis from Speer [79], appendix gap losses from Urieli and Berchowitz [29], and one dimensional conduction with Fourier's law.

Speer [79] then further modified the engine to operate at a reduced thermal source temperature. Three modifications were identified with the 2<sup>nd</sup> order model. A smaller diameter piston would reduce the modelled stall temperature by reducing gas spring hysteresis loss and mechanical losses (by reducing forced work). Enlarging the crankcase volume also reduced the modelled gas spring

hysteresis and mechanical loss. Reducing dead volume increased the modelled indicated work but could increase losses not accounted for in the 2<sup>nd</sup> order model. Speer sequentially introduced a 44 mm piston, 7.83 L crankcase and components to occupy 0.132 L of dead volume in the connecting pipe. Table 1-2 lists the minimum thermal source temperature the engine configurations stalled at without load. The 44 mm piston and crankcase extension modifications reduced the stall temperature; whereas, the dead volume reduction components did not significantly impact the stall temperature. Table 1-1 lists the performance and operating condition of the low-temperature ST05G with all modifications. The maximum power was significantly reduced but similar operating conditions to the original ST05G could not be achieved.

Table 1-2: Minimum thermal source temperatures of modified ST05G configurations [79].

Modified ST05G Configuration	Minimum Thermal Source Temperature (°C)
85 mm Piston	242
44 mm Piston	185
44 mm Piston and Crankcase Extension	144
44 mm Piston, Crankcase Extension and Dead Volume Reduction	145

Speer [79] evaluated the ability of the 2<sup>nd</sup> order model to predict experiment results with the low-temperature ST05G. The model over-predicted the heat input rate, heat rejection rate, and shaft power. Specific components of the model were also evaluated. The regenerator flow friction estimate accuracy improved with increasing engine frequency and mean pressure. The modelled conduction loss nearly doubled the measured rate in stationary experiments at several conditions. The model over-estimated indicated work to a greater extent at  $T_H = 200$  °C compared to  $T_H = 300$  °C. Beyond indicated work and conduction loss, the accuracy of the model and its components were not evaluated at different source temperatures.

# 1.7 Stirling Engine Flywheel Size

Flywheels are machine elements that store rotational kinetic energy to smooth angular velocity changes in a variable torque machine [81]. The instantaneous kinetic energy of the flywheel ( $KE_{fly}$  in Equation 1-41) depends on the flywheel’s polar moment of inertia ( $I_{fly}$ ) and its instantaneous angular velocity ( $\dot{\theta}$ ) [33]. Figure 1-21 displays a free body diagram of a flywheel. The engine torque ( $\tau_E$ ) alternates between positive to negative and the load torque ( $\tau_{load}$ ) resists the direction of motion [33]. As a result, the flywheel experiences positive angular acceleration ( $\ddot{\theta}$ ) when the net positive torque is acting on it and negative angular acceleration when the net negative torque is acting on it [33]. This acceleration is inversely proportional to the polar moment of inertia of the flywheel [33]. Hence, a flywheel with a larger polar moment of inertia experiences smaller angular velocity changes for a prescribed engine torque function [33].

$$KE_{fly} = \frac{1}{2} \cdot I_{fly} \cdot \dot{\theta}^2 \tag{1-41}$$

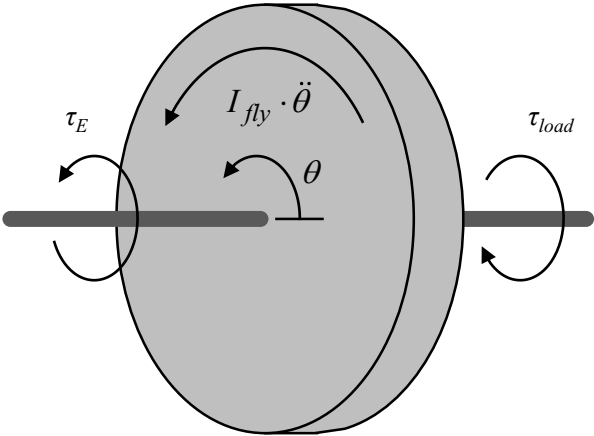


Figure 1-21: Free body diagram of a flywheel, after Cleghorn and Dechev [33].



### 1.7.1 Flywheel Size

The coefficient of speed fluctuation (*CS*) is a dimensionless measure of shaft speed fluctuations. It is calculated with Equation 1-42 from the maximum, minimum, and mean angular velocities in a cycle. [33]. Flywheel design begins by establishing a limit on the coefficient of speed fluctuation [81]. Table 1-3 lists coefficients of speed fluctuation acceptable for historic Stirling engine applications [81].

$$CS = \frac{\dot{\theta}_{max} - \dot{\theta}_{min}}{\dot{\theta}_{mean}} \tag{1-42}$$

Table 1-3: List of coefficients of speed fluctuation for historic Stirling engine applications [81].

Application	<i>CS</i>
Electric Generators	0.001-0.014
Pumps	0.03-0.05
Automobiles	0.1-0.2

The appropriate flywheel polar moment of inertia is calculated to remain below an allowable coefficient of speed fluctuation [33]. Equation 1-43 calculates the appropriate machine polar moment of inertia—sum of the polar moments of inertia of the flywheel and other machine elements (*I<sub>other</sub>*) [33]. It depends on the maximum kinetic energy change ( $\Delta KE_{max}$ ), mean angular velocity ( $\dot{\theta}_{mean}$ ), and coefficient of speed fluctuation. Flywheel polar moment of inertia is the remaining moment of inertia required after the polar moment of inertia of other mechanical components have been deducted [33].

$$I_{fly} + I_{other} = \frac{\Delta KE_{max}}{\dot{\theta}_{mean}^2 \cdot CS} \tag{1-43}$$

## 1.7.2 Stirling Engine Flywheels in Literature

This sub-section presents literature about Stirling engine flywheels. This includes flywheel size calculation methods and dynamic model studies with different size flywheels.

### 1.7.2.1 Flywheel Sizing Methods

Scollo et al. [82] derived an equation to calculate the necessary polar moment of inertia of a Stirling engine flywheel. Their method (Equation 1-44) assumes the maximum kinetic energy change is twice the ideal Stirling cycle compression work ( $W_{comp}$ ) plus the friction work in one cycle ( $W_{friction}$ ) [82]. Equation 1-45 is the work of isothermal compression of an ideal gas from constants: mass of working gas ( $m$ ), specific gas constant ( $R$ ), temperature ( $T$ ), minimum volume ( $V_{E,min}$ ), and maximum volume ( $V_{E,max}$ ). Cyclic friction work can be predicted with any means available or neglected [82]. This method may oversize the flywheel for some engines because it neglects the effects of buffer pressure on the piston.

$$I_{fly} + I_{other} = \frac{2 \cdot W_{comp} + W_{friction}}{\dot{\theta}_{mean}^2 \cdot CS} \quad 1-44$$

$$W_{comp} = \int_{V_{E,max}}^{V_{E,min}} P_E \cdot dV_E = m \cdot R \cdot T \cdot \ln \left( \frac{V_{E,min}}{V_{E,max}} \right) \quad 1-45$$

### 1.7.2.2 Flywheels in Dynamic Models

In addition to deriving an method to calculate flywheel size, Scollo et al. [82] used a dynamic model to simulate the transient behavior of an alpha-type Stirling engine with three different size flywheels (0.06, 0.6 and 6 kg m<sup>2</sup>). They coupled an isothermal 2<sup>nd</sup> order model to the mechanism dynamics. Mechanical friction torque was deducted from crankshaft torque with an empirical correlation. All flywheel sizes modelled converged on the same steady-state angular speed.

However, the larger flywheels required more time to reach steady-state and had smaller angular velocity fluctuations. Scollo et al. determined that a flywheel could be too small and cause the engine to stall.

Cheng and Yu [35] used a dynamic model for parametric optimization of a slider-crank drive, beta-type Stirling engine that included flywheel moment of inertia. The dynamic model used a 2<sup>nd</sup> order, semi-adiabatic model derived by Cheng et al. [83]. Cheng and Yu included a speed-dependent mechanical friction torque on the crankshaft from an empirical correlation. Five flywheels were studied ranging from 0.00008 to 0.008 kg m<sup>2</sup>. Cheng and Yu[35] showed that increasing the flywheel moment of inertia increased the time for the engine to reach steady-state and decreased the angular velocity fluctuations. None of the transient simulations overshoot steady-state. Flywheel moment of inertia influenced the shaft power and efficiency. The simulation with the nominal flywheel size (0.0008 kg m<sup>2</sup>) produced the highest power and efficiency; therefore, there was an optimal flywheel size with this model.

Cheng and Yu [53] investigated a rhombic-drive, beta-type Stirling engine with a dynamic model. This model also employs the 2<sup>nd</sup> order, semi-adiabatic model by Cheng et al. [83]. Mechanical losses were from Millington and Hartles [54] diesel engine friction correlation and depended on compression ratio and engine speed. Cheng and Yu studied six flywheels between 0.00004 and 0.0002 kg m<sup>2</sup>. All flywheels converged on the same steady-state frequency. Larger flywheels required more time to reach steady-state. Larger flywheels also had smaller angular velocity fluctuations. They did not investigate if flywheel size influenced engine performance.

Yang et al. [55] described and validated a dynamic model for a rhombic-drive, beta-type Stirling engine. It employed a 2<sup>nd</sup> order, semi-adiabatic model. The model included independent equations for piston and displacer ring friction. Yang et al. tuned the coefficients of ring friction

with experimental data. Three flywheel moments of inertia were studied. Simulations with all flywheels sizes approached the same steady-state engine frequency. The simulation with the smallest flywheel overshoot steady-state. Larger flywheels had smaller angular velocity fluctuations. In this work, flywheel size did not impact the engine performance.

Ipci and Karabulut [84] derived a dynamic model of a scotch-yoke-drive, alpha-type Stirling engine. The thermodynamic component of the model is the 3<sup>rd</sup> order nodal analysis [84,85]. The model includes both Coulomb and hydrodynamic friction on the pistons, and hydrodynamic friction in the bearings [85]. They assumed a flywheel moment of inertia equal to 0.1 kg m<sup>2</sup> was appropriate which corresponded to a 0.16 coefficient of speed fluctuation. The load torque and charge pressure were varied to find the maximum shaft power. The coefficient of speed fluctuation increased with increasing charge pressure and was equal to 1.22 at 1300 kPa charge pressure. Increasing load torque also increased coefficient of speed fluctuation.

Altin et al. [85] used the same model as Ipci and Karabulut [84] to optimize a different scotch-yoke-drive, alpha-type Stirling engine. The flywheel moment of inertia was varied and coefficient of speed fluctuation decreased as moment of inertia increased. The coefficient of speed fluctuation also decreased with increasing mean angular velocity.

The dynamic model studies both complimented and contradicted each other. All transient studies showed that larger flywheels required more time to transition to steady-state [35,53,55,82]. They also showed that all flywheel sizes converged on the same steady-state, mean angular velocity at identical conditions [35,53,55,82]. Yang et al. [55] showed that the engine frequency overshoot steady-state frequency with smaller flywheels. Cheng and Yu [35] found that flywheel polar moment of inertia influenced the shaft power of the engine.

The studies above selected the appropriate flywheel polar moment of inertia with a dynamic model. Table 1-4 summarizes the flywheel size determined by the dynamic models. The coefficients of speed fluctuation range from 0.02 to 0.16. These are all within the range specified for Stirling engine applications. The largest coefficient of speed fluctuation considered acceptable in the dynamic model studies is  $CS = 0.16$ . The flywheel size for the engines near the scale of the ST05G range from 0.06 to 0.13 kg m<sup>2</sup> [55,82]. These studies show that a dynamic model can be used to determine the appropriate flywheel polar moment of inertia for a Stirling Engine.

Table 1-4: Operating condition, flywheel polar moment of inertia, and coefficient of speed fluctuation of engines simulated with dynamic models.

Parameter	Scollo et al. [82]	Cheng and Yu [35]	Cheng and Yu [53]	Yang et al. [55]	Ipci et al. [84]	Altin et al. [85]
Swept Volume (L), $V_{sw}$	0.440	0.0029	0.0033	0.547	0.800 <sup>1</sup>	0.304 <sup>1</sup>
Source Temperature (°C), $T_H$	N/P	727	727	850	727	727
Sink Temperature (°C), $T_C$	N/P	27	27	27	127	127
Working Gas	N/P	Air	Air	Helium	Helium	Helium
Mean Pressure (kPa), $p_{E,mean}$	660	101.3	101.3	911.9	512	497
Engine Frequency (Hz), $f$	13.8	15.0	13.2	12.1	14.5	25
Flywheel Polar Moment of Inertia (kg m <sup>2</sup> ), $I_{fly}$	0.06	$8 \times 10^{-4}$	$8 \times 10^{-5}$	0.13	0.1	0.11
Coefficient of Speed Fluctuation, $CS$	0.10 <sup>2</sup>	0.11 <sup>2</sup>	0.03	0.02	0.16	0.10 <sup>2</sup>

<sup>1</sup> Expansion piston swept volume

<sup>2</sup> Estimate from plot

## 1.8 Thesis Objectives and Structure

---

This thesis has two objectives. The first is to study the influence of flywheel polar moment of inertia on the transient and steady-state performance of a Stirling engine. The second is to assess if a 2<sup>nd</sup> order model is suitable for modelling LTDSEs and determine how to most effectively improve the model. Both objectives are addressed through experiments with the low-temperature ST05G Stirling engine.

The remainder of this thesis is structured as follows. Chapter two details the experiment apparatus, instrumentation, test procedures, data acquisition, data processing, and uncertainty calculations. Chapter three describes the 2<sup>nd</sup> order model used to predict the performance of the low-temperature ST05G. The influence of flywheel size on transient and steady-state engine performance is studied in Chapter four. Chapter five evaluates the accuracy of the 2<sup>nd</sup> order model at a range thermal source temperatures. Finally, Chapter six concludes the work of this thesis and suggests future work.

---

## 2 EXPERIMENT SETUP AND PROCEDURES

---

The goals for this thesis require experimental data of a Stirling engine with different flywheels and a range of thermal source temperatures. This chapter describes the experiment methods used to collect and process this data. The chapter begins with a brief overview of the experiment setup. Then it details the construction of the Stirling engine tested in experiments. It follows with descriptions of the operating condition management systems and the instruments. The chapter completes with explanations of the data acquisition program, experiment procedures, data processing program, and uncertainty calculations.

Figure 2-1 overviews the experiment setup. Experiments were performed on the low-temperature ST05G that is fixed to an aluminum extrusion test cart. The heating system was managed by a temperature controller and the cooling system was regulated by both a water bath and a peristaltic pump. The engine was charged with air to pressures set by a pressure regulator. Power was extracted from the engine with a friction brake. That power was measured with a rotary encoder and torque transducer. Gas temperature, gas pressure, and coolant temperature were also measured. Conditioned signals were collected by multiple data acquisition devices and passed to a common computer. These methods were developed in collaboration with Speer [79] and Stumpf [37], then refined and improved to meet the specific goals of this thesis.

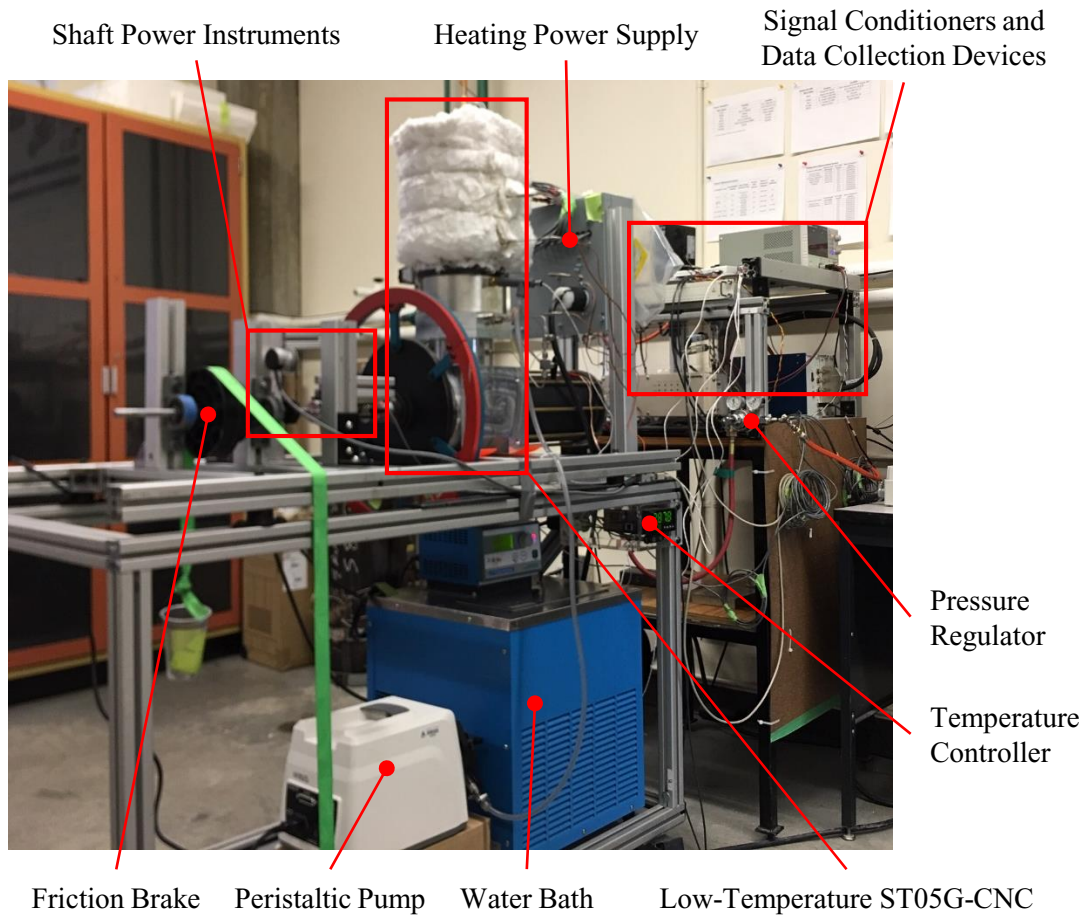


Figure 2-1: Image of the low-temperature ST05G test cart and data acquisition equipment.



## 2.1 Low-Temperature ST05G Stirling Engine

---

The low-temperature ST05G Stirling engine used in this work is shown in Figure 2-2. It was modified by Speer [79] from the engine design by Ve-Ingenieure [64] to receive heat from a solid thermal source, to operate at lower thermal source temperatures, and for instrumentation. Additional modifications were made to improve the reliability of the engine and for the use of multiple flywheel configurations. Appendix D. contains the mechanical drawings of components of the low-temperature ST05G not provided by Speer [79]. This section describes the low-temperature ST05G and its components.

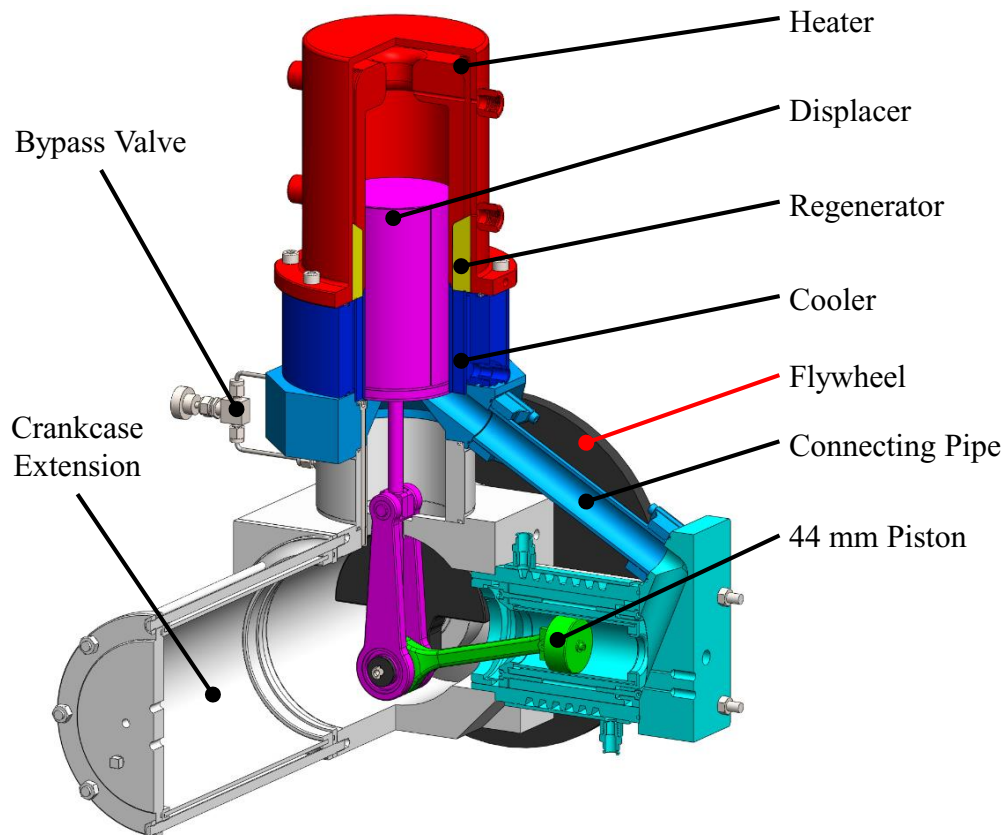


Figure 2-2: CAD model of the low-temperature ST05G Stirling engine.

### 2.1.1 Heater

The most significant design change from the original ST05G-CNC is the heater. It was redesigned to absorb heat by conduction from a solid thermal source [79]. The thermal source was simulated by a steel cap with electric cartridge heaters [79]. This required that a cylindrical heater replace the existing tube cage design [79]. Figure 2-3 shows the cross-section geometry of the heater. The internal geometry of the heater is 64 rectangular channels in an annulus (3.18 mm width, 5.17 mm radial depth and 123 mm length).

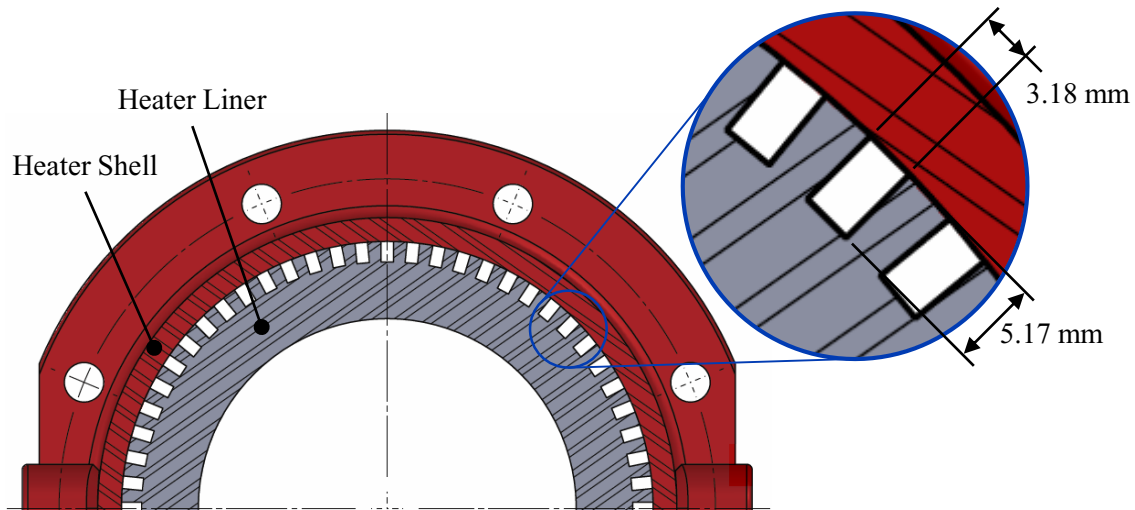


Figure 2-3: Cross-section of the low-temperature ST05G heater.

### 2.1.2 Regenerator

The regenerator cavity geometry was changed with the redesign of the heater [79]. The annulus dimensions changed to a 135.5 mm OD, a 103 mm ID and a 55 mm mean length. The annulus was packed with 302.7 g of 0.05 mm AISI 316 stainless steel felt for a porosity of 89.3 % to replicate the original porosity (90 %) [65,79].

### 2.1.3 Cooler

The cooler geometry largely remained unchanged from the original ST05G-CNC [65]. Figure 2-4 depicts the cross-section of the 144 rectangular channels that make up the cooler. The channels remained 1 mm wide and 84 mm long, but their depth was reduced to 10 mm compared to 10.5 mm in the original ST05G-CNC [65].

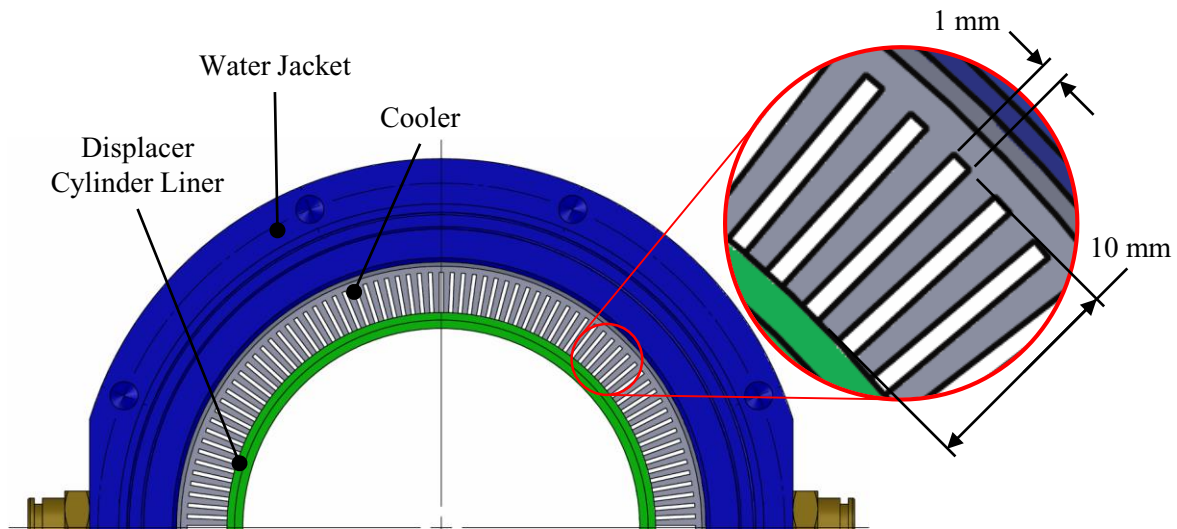


Figure 2-4: Top view of the low-temperature ST05G cooler.

### 2.1.4 Displacer

The displacer body and seal were redesigned by Speer [79]. The flat end cap on the displacer body (visible in Figure 2-2) replaced the torispherical end cap specified on the original configuration. The displacer seal gland was designed for a PTFE contact seal that was replaced by a clearance seal in experiments.

### 2.1.5 Connecting Pipe

The connecting pipe was updated from the double-tube configuration with a water jacket used by Speer [79], shown in Figure 2-5 (a). Leaks through a sealing adhesive between the engine and

water jacket were a concern. Figure 2-5 (b) is a section view of the design that replaced Speer's [79]. The 6061 aluminum alloy internal tube remained unchanged and the second tube was removed. 3D printed blocks were adhered to the ends of the tube and compressed O-rings in adjacent parts to seal the engine.

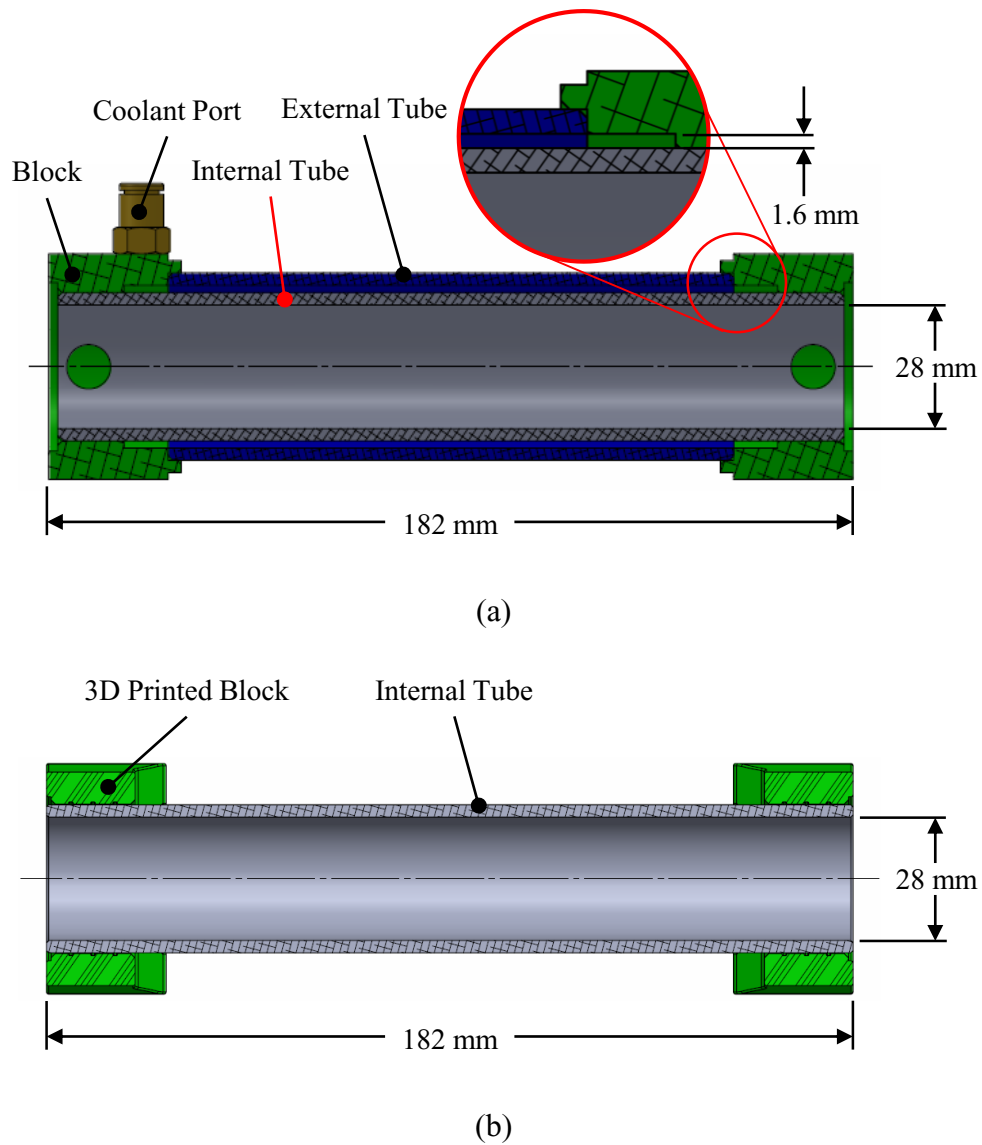


Figure 2-5: Section views of the original [79] (a) and modified (b) connecting pipe.

## 2.1.6 Piston and Power Cylinder

Speer [79] showed with a model and experiments that a smaller piston reduced the minimum thermal source temperature that a Stirling engine could operate at. The low-temperature ST05G uses a 44 mm precision graphite piston and glass cylinder set (2KS444-3.0CP, Airpot Corp.) recommended by Senft [11]. Figure 2-6 displays the original, 85 mm piston and the 44 mm piston-cylinder set used in the low-temperature ST05G.



Figure 2-6: Image of the as-built piston assembly and the 44 mm piston-cylinder set.

Previous iterations of the design used a 3D printed, plastic piston backer that would fail at operating conditions exceeding a 300 °C source temperature and 414 kPa charge pressure [79]. It was replaced with a machined aluminum piston backer. A carbon-fiber reinforced, 3D printed connecting rod links the piston to the crankshaft. The new combination of connecting rod and

piston backer increased the moment on the piston and could cause the piston to bind. Further, the piston could bind if the piston backer was fastened too tightly.

Speer [79] retrofit the glass cylinder within the original cylinder with a series of 3D-printed parts. Figure 2-7 illustrates the cylinder mounting components. O-rings sealed the mounting components against the original cylinder. The glass cylinder was compressed against a gasket to seal the glass cylinder against the mounting components. The graphite piston would bind in the glass cylinder if the cylinder was over-compressed.

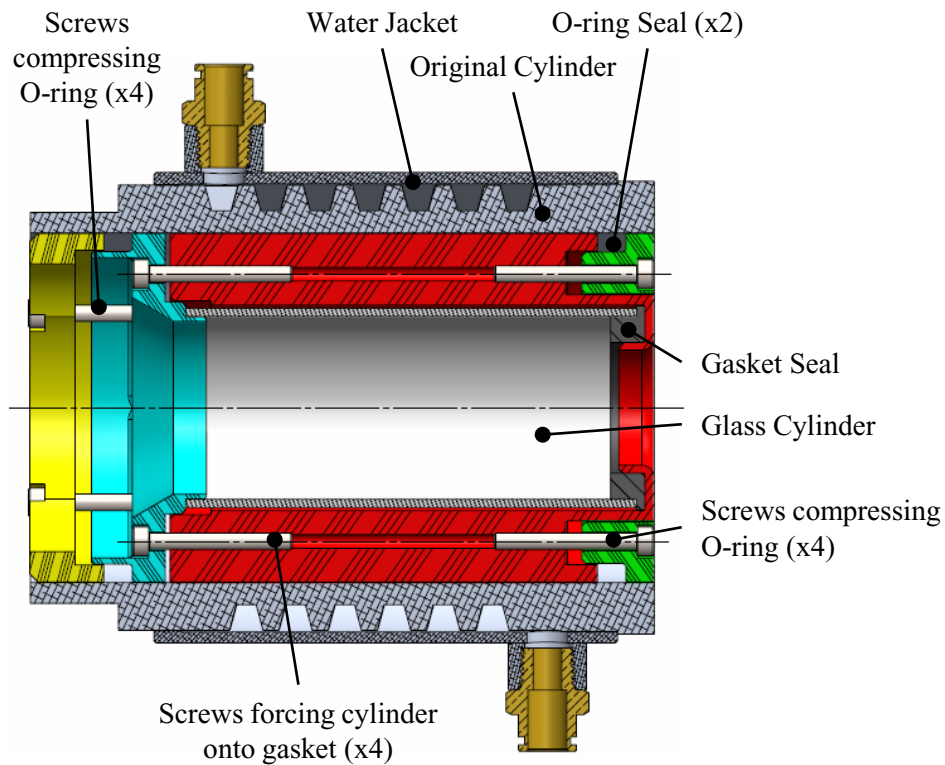


Figure 2-7: Section view of the precision glass cylinder and mounting components.

### 2.1.7 Mechanism

With the exception of the connecting rod of the piston, the mechanism geometry in the low-temperature ST05G remained unchanged. The mass of the piston was significantly reduced from

the original piston. As a result, shaking force and imbalance increased. This generated significant vibrations in the aluminum extrusion frame. Engine frequencies above 4.6 Hz were avoided to prevent excessive vibration.

### 2.1.8 Crankcase

A crankcase extension introduced by Speer [79] was used. It improved the low-temperature performance of the engine by reducing gas spring hysteresis and mechanical losses [79]. The extension increased the crankcase volume by 4.63 L for a maximum volume of 7.83 L [79].

The gas in the crankcase and engine were separated by a bypass line with a valve (visible in Figure 2-2 earlier in the section). The bypass valve allowed the operator to equilibrate the pressures in the engine and crankcase. Additionally, it increased leakage to slow the engine. The valve was opened when changing the charge pressure and when stopping the engine.

### 2.1.9 Variable Inertia Flywheel

Four flywheel configurations were constructed to influence the crankshaft angular velocity fluctuations experienced by the engine. Table 2-1 lists the mass, outside diameter and polar moment of inertia of the four flywheel configurations calculated in SOLIDWORKS®. The mass of the flywheel components was measured and they equaled the masses calculated in SOLIDWORKS®. Figure 2-8 displays the front and top views of the flywheel CAD models. Configuration A is the original configuration of the flywheel used by Speer [79]. Configuration B introduces a spoked extension with holes to fix masses on its extremity. Configuration C includes six masses on the front side of the extension. Configuration D has an additional six masses on the rear side of the extension for a total of 12.

Table 2-1: List of flywheel properties.

Property	Flywheel Configuration			
	A (Original)	B	C	D
Mass (kg), $m_{fly}$	6.88	11.06	14.58	17.97
Outer Diameter (mm), $d_{fly}$	285	480	480	480
Flywheel Polar Moment of Inertia (kg m <sup>2</sup> ), $I_{fly}$	0.0641	0.2539	0.4292	0.5995



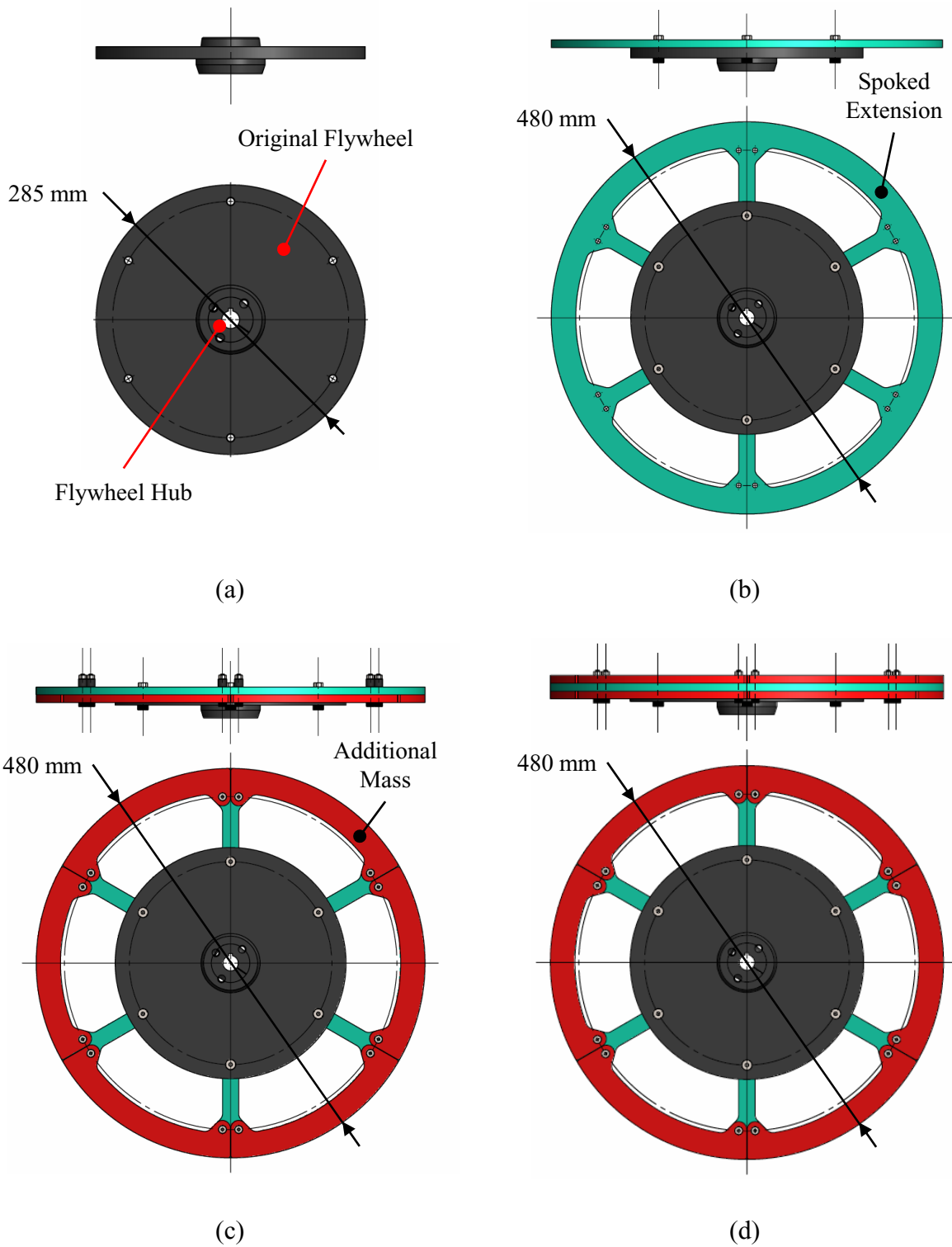


Figure 2-8: Front and top views of the four flywheel configurations: (a) configuration A, (b) configuration B, (c) configuration C, and (d) configuration D.

## 2.2 Operating Condition Management

---

Thermal source temperature, thermal sink temperature, coolant flow rate, charge pressure and engine frequency were controlled. Table 2-2 lists the range of the operating conditions studied and the range possible with the current equipment. This section describes the systems used for operating condition management.

Table 2-2: Range of operating conditions studied in experiment and the possible ranges with the current equipment.

Operating Condition	Studied Range	Possible Range
Thermal Source Temperature ( $^{\circ}\text{C}$ ), $T_H$	242 - 418	< 600
Thermal Sink Temperature ( $^{\circ}\text{C}$ ), $T_C$	21	5 - 95
Coolant Flow Rate (L/min)	0.8	0.034 - 3.4 [86]
Charge Pressure (kPa absolute), $p_{charge}$	93 - 621	93 - 689
Engine Frequency (Hz), $f$	< 4.6	< 4.6

### 2.2.1 Thermal Source

The thermal source provides heat to the Stirling engine. Figure 2-9 displays the process and instrumentation diagram (P&ID) of the thermal source control system. The heater receives heat from a 25.4 kg steel cap with ten  $\text{\O} 9.5 \text{ mm} \times 152 \text{ mm}$  and five  $\text{\O} 9.5 \text{ mm} \times 38 \text{ mm}$  cartridge heaters (35025K263 and 35025K173, McMaster-Carr Supply Company). Combined, the cartridge heaters could convert 3 921 W of 240 V AC power to heat (rated for 5 000 W) [79]. A thermocouple (KMTSS-062G-6, Omega Engineering Inc.) located in the top, center of the heating cap measured the thermal source temperature. A temperature controller with PID control (CN8DPT-440-C24, Omega Engineering Inc.) regulated the thermal source temperature by managing the power supplied to the heaters via a solid state relay. The PID tuning coefficients changed during operation with fuzzy logic adaptive tuning programmed into the temperature

controller [87]. During experiments the measured thermal source temperature remained within  $\pm 2\text{ }^{\circ}\text{C}$  of the set point.

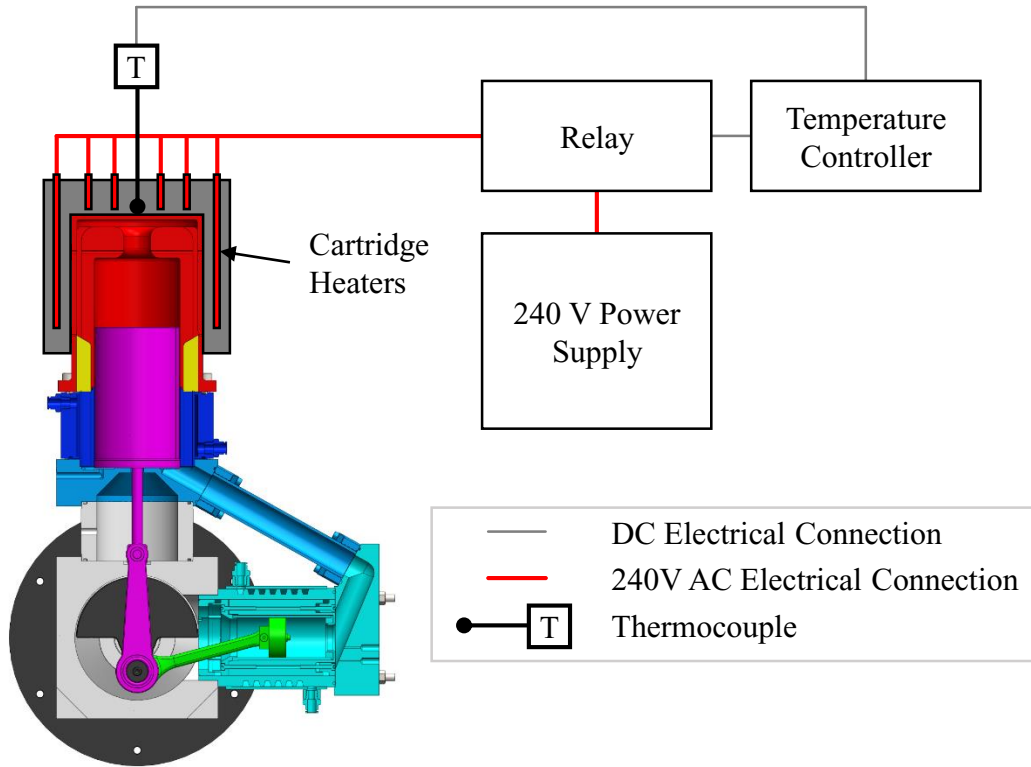


Figure 2-9: P&ID of the thermal source and heating system.

### 2.2.2 Thermal Sink

The engine rejected heat to cooling water flowing through the cooler and power cylinder water jackets. Figure 2-10 is the P&ID of the experiment coolant circuit. A refrigerated water bath, with a built-in controller, maintained the coolant temperature at  $21 \pm 2\text{ }^{\circ}\text{C}$  (12101-41, Cole-Parmer Instrument Company, LLC.). A peristaltic pump in the return line of the coolant circuit maintained a flow rate of  $0.80 \pm 0.01\text{ L/min}$  (7523-80 with pump head 77200-62, Cole-Parmer Instrument Company, LLC.). The engine was cooled in two zones connected in series: (1) the cooler and (2) the power cylinder. This differed from the experiments performed by Speer [79] where cooling

zone two included the connecting pipe. Coolant temperature was measured with RTDs at the inlet and outlet of each cooling zone (details in section 2.3.4).

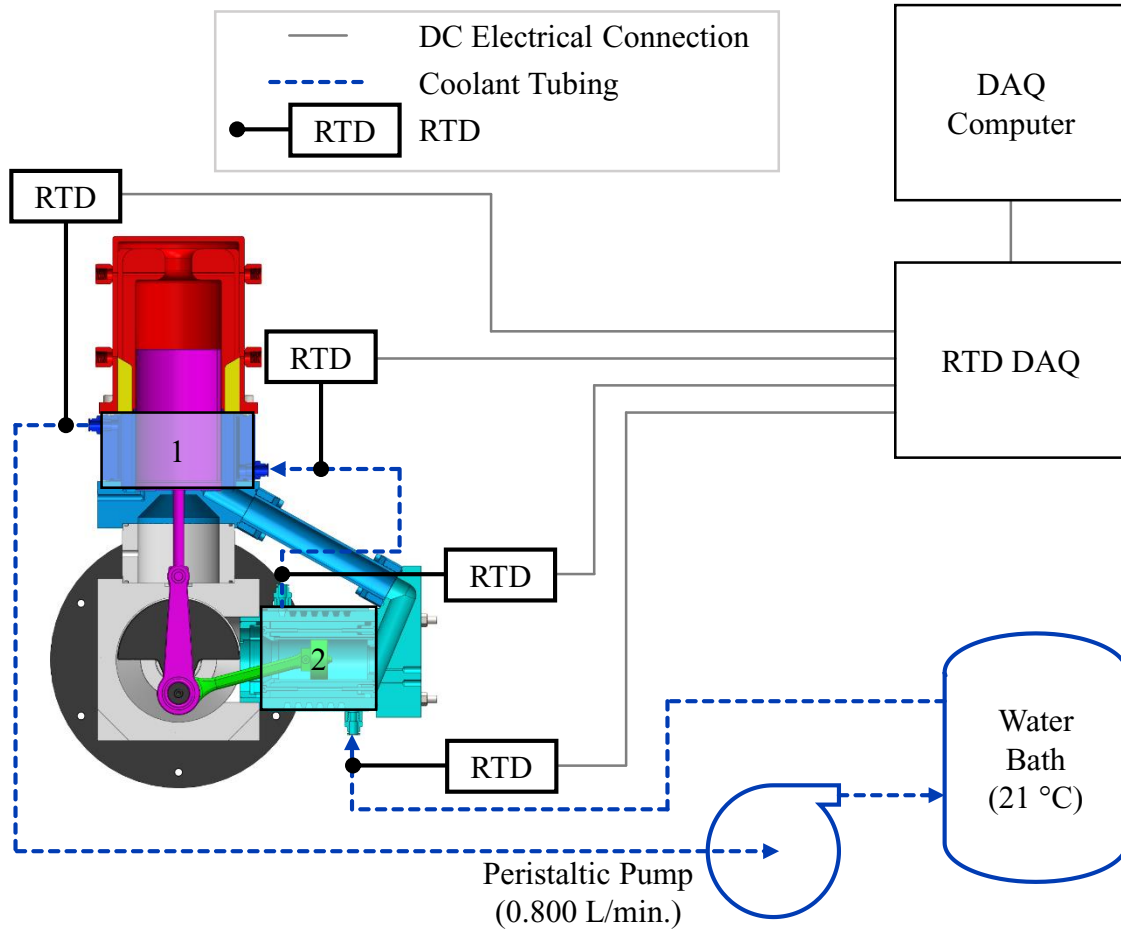


Figure 2-10: P&ID of the coolant circuit and coolant temperature measurement system.

### 2.2.3 Charge Pressure

The charge pressure was not repeatable in previous experiments with this engine [79]. The original system used a 15 L air compressor with a built in regulator (C2004, PORTER-CABLE) to supply air to the engine through a 34.5 kPa (5 psi) check valve [79]. Sources of unrepeatability in the Speer's [79] method were the pressure regulator's resolution and the inconsistent regulator supply pressure.

The charge pressure system was changed to increase repeatability. Figure 2-11 is a P&ID of the charge pressure system. An air compressor with a built-in regulator (C2004, PORTER-CABLE) supplied air near 960 kPa (absolute) to a 75 L pressure vessel. A ball valve between the compressor and pressure vessel was closed after the pressure vessel was charged. A second, more precise pressure regulator (3320, MATHESON) received air from the pressure vessel and regulated the engine charge pressure. The minimum possible charge pressure was the local atmospheric pressure (near 93 kPa [88]) and the maximum was 689 kPa (absolute).

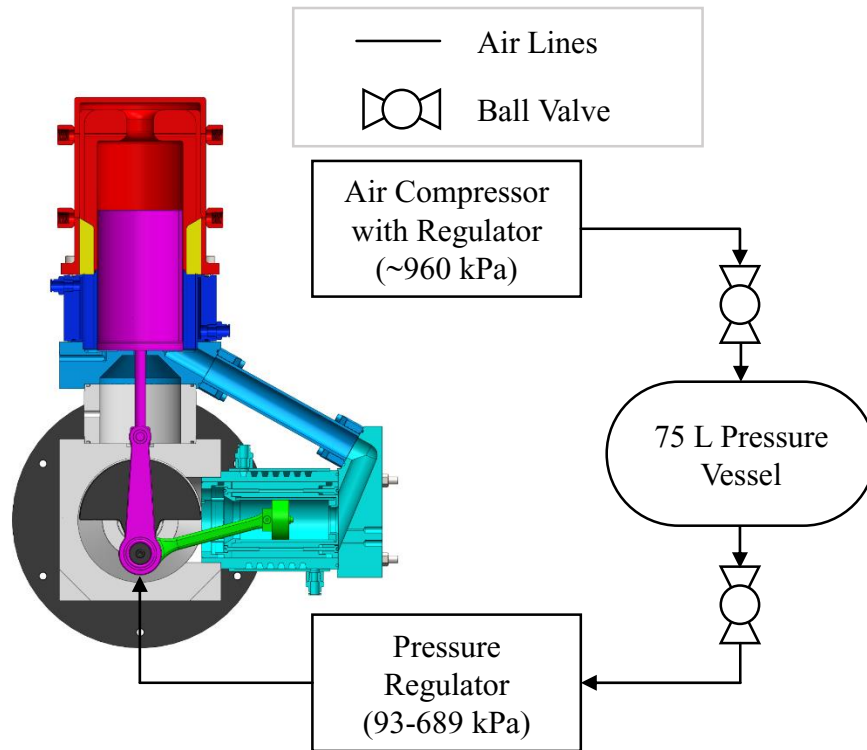


Figure 2-11: P&ID of the charge pressure system.

## 2.2.4 Engine Frequency and Load Torque

The engine frequency was manipulated by applying a load torque via a friction brake to the output shaft of the engine. Figure 2-12 depicts the friction brake and its position at the end of the output shaft. A belt, fixed to the cart on one end and tensioned with mass in a load basket on the other end, slipped on a three-tier pulley. The three pulley tiers were 46, 97, and 147 mm in diameter and masses from 12 to 450 g were placed in the load basket to access a wide range of load torques. The belt was removed from the pulley for free-running experiments. Minimum loads were used at several operating conditions to prevent the engine from significantly exceeding a frequency of 4.6 Hz.

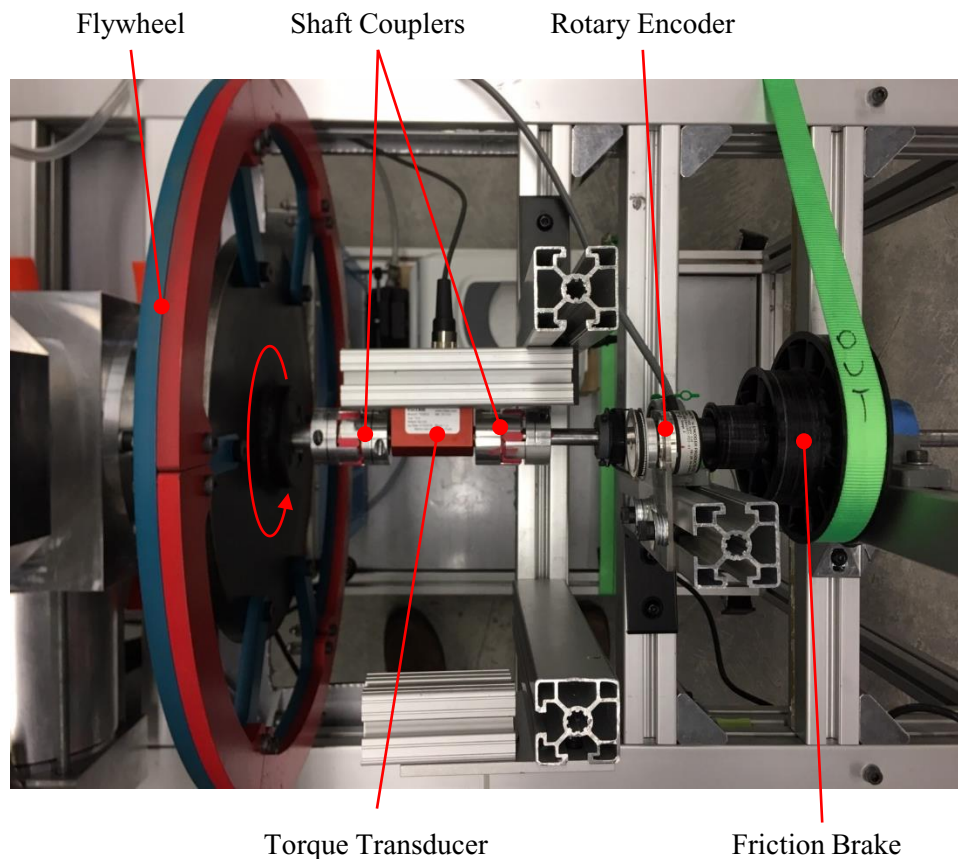


Figure 2-12: Image of the friction brake and shaft power measurement instruments on the output shaft of the engine.

## 2.3 Instrumentation

---

The crankshaft angular position, engine load torque, working gas temperature, coolant temperature, and working gas pressure were measured to quantify engine performance and define conditions to model. This section details the instruments, signal conditioners and data acquisition devices used for measurements. In addition, this section describes instrument calibration procedures and summarizes instrument specific uncertainties.

### 2.3.1 Crankshaft Angular Position

Angular position of the shaft is used to calculate the volumes of the working spaces in the engine, the angular speed of the crankshaft, and the power produced by the engine. A 500 pulse-per-revolution (PPR) rotary encoder measured the angular position of the crankshaft (15S-19M1-0500NV1ROC-F03-S1, Encoder Products Company). The encoder had three outputs. An A-pulse and a B-pulse, both with 500 PPR measure position and direction of rotation. A Z-pulse with 1 PPR measure complete rotations. With the current setup, the low-temperature ST05G will only operate with one direction of rotation, so the B-pulse was ignored.

A timing belt and two pulleys linked the rotary encoder to the shaft, as shown in Figure 2-13. One 60-tooth pulley was fixed to the shaft with set screws on a 3D-printed hub. Another 60-tooth pulley was fixed to the rotary encoder shaft with set screws on the pulley hub. The rotary encoder was fixed to the aluminum extrusion frame with tension on the timing belt.

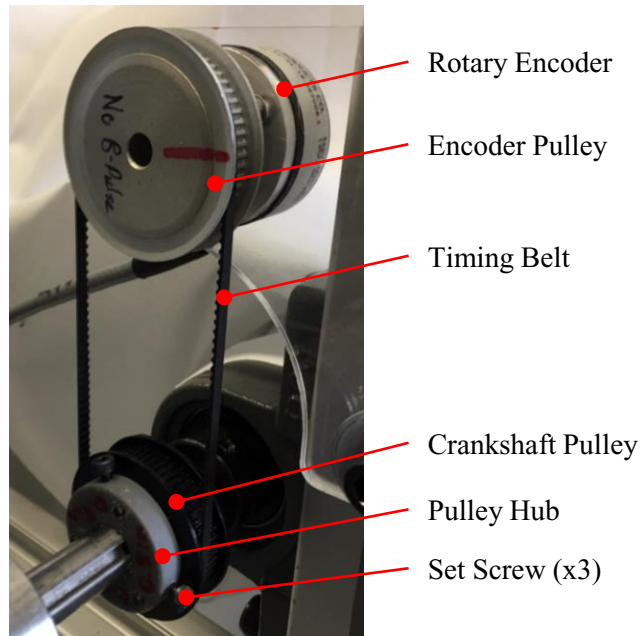


Figure 2-13: Image of the rotary encoder, timing belt, and pulleys.

Figure 2-14 is a P&ID of the angular position measurement system. The rotary encoder received 5 V DC electricity from channel one of the power supply (GDP3303S, Good Will Instrument Co., Ltd.). The A and Z-pulses of the rotary encoder produced square wave voltage signals. These were sampled at a rate of 30 kHz per channel by a multifunction I/O device (USB-6211, National Instruments Inc.). This rate minimized uncertainty when calculating instantaneous angular velocity. Digitized signals were forwarded to the data acquisition computer. Further data processing was required to quantify crankshaft position from the discrete voltage measurements.



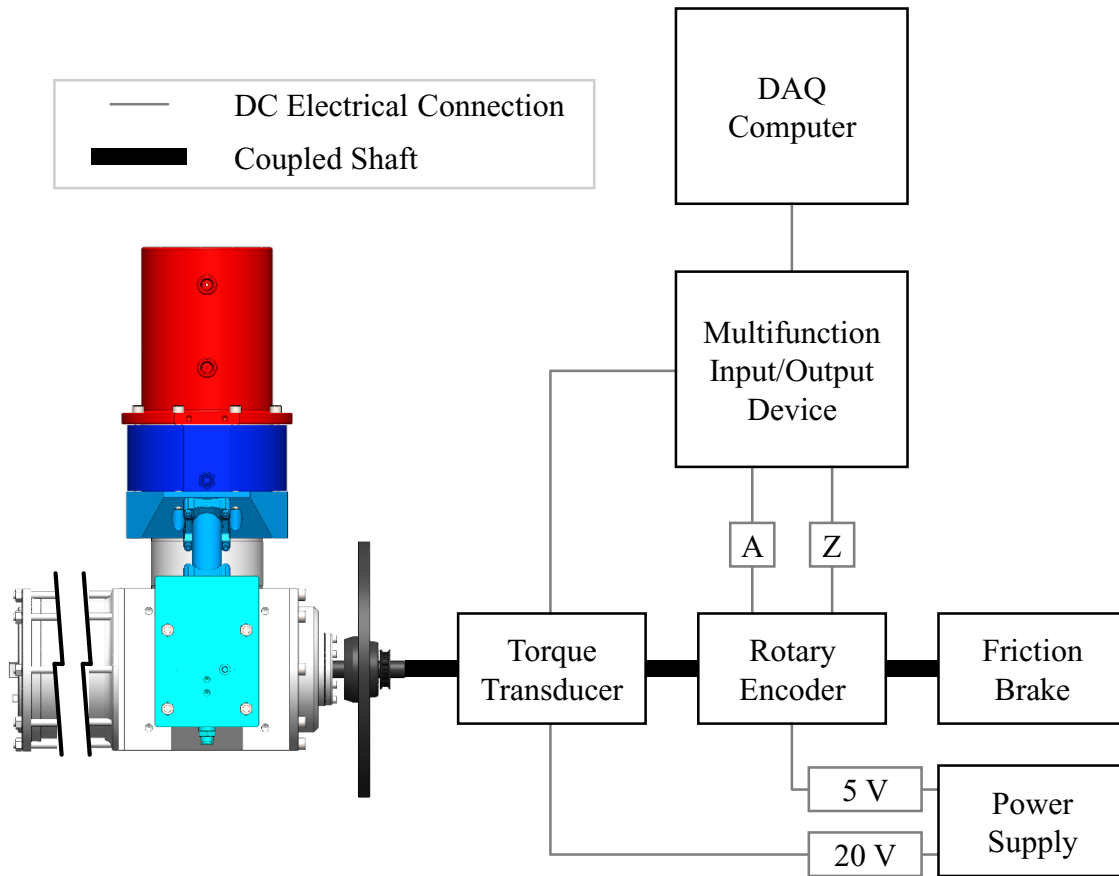


Figure 2-14: P&ID of the crankshaft torque and position measurement systems.

Absolute angular position accuracy is necessary for accurate calculations of engine volumes and indicated work. The rotary encoder alignment procedure aimed to minimize inaccuracies. With the power cylinder head removed, a dial indicator with 0.001" (0.0254 mm) resolution was placed on the piston face. It was used to determine the piston's top-dead-center position. This position was matched with the Z-pulse of the rotary encoder by adjusting the position of the pulley hub on the shaft. The rotary encoder was aligned when the engine was set-up for experiments, then checked every experiment day and after experiments were complete. The uncertainty of this method was the angular position change corresponding to linear piston motion equal to 0.0127 mm

(half the resolution of the dial indicator). Through the cosine law with the slider-crank mechanism, the uncertainty of the alignment procedure was 0.0232 rad.

### 2.3.2 Crankshaft Torque

Crankshaft torque is the measure of load applied to the engine and is necessary to calculate shaft power. A 1 Nm, contactless torque transducer (TRS600-1Nm, FUTEK Advanced Sensor Technology, Inc.) measured the crankshaft torque. Figure 2-12 shows the torque transducer coupled to the output shaft of the engine between the flywheel and friction brake. The shaft couplers (9845T5, McMaster-Carr Supply Company) allowed for misalignment with zero backlash [89]. The torque transducer measurements were corrected for zero and gain with a linear regression from the manufacturer calibration data.

Figure 2-14 illustrates the torque measurement system. The torque transducer was supplied 20 V DC electricity from the channel two of the power supply (GDP3303S, Good Will Instrument Co., Ltd.). The torque transducer output was measured by the multifunction I/O device at a rate of 30 kHz and passed a digitized signal to the data acquisition computer.

Previous experiments were conducted with a 10 Nm torque transducer (TRS600-10Nm, FUTEK Advanced Sensor Technology, Inc.) [79]. It was oversized for the application and resulted in a large torque measurement uncertainty [79]. The extreme conditions in this work were first tested with the 10 Nm torque transducer because the shaft power measurement system did not include an over-torque prevention device. Once it was confirmed that the torque did not exceed 1 Nm, experiments were performed with the 1 Nm torque transducer.

### 2.3.3 Working Gas Temperature

Working gas temperatures provide insight into the heat transfer performance of the engine and are used as thermodynamic model inputs. Figure 2-15 is an image of the exposed junction, type-K

thermocouples (HKMTSS-062E-6, Omega Engineering Inc.) used to measure the working gas temperature. The thermocouple junctions were inserted roughly 5 mm into the working space and sealed with Swagelok® fittings. The predicted, quasi-steady response times of the 0.76 mm spherical junctions ranged from 17.9 to 36.6 s compared to the 0.22 s minimum cycle period. Therefore, mean temperature, rather than time-resolved temperature, was valuable for analysis.

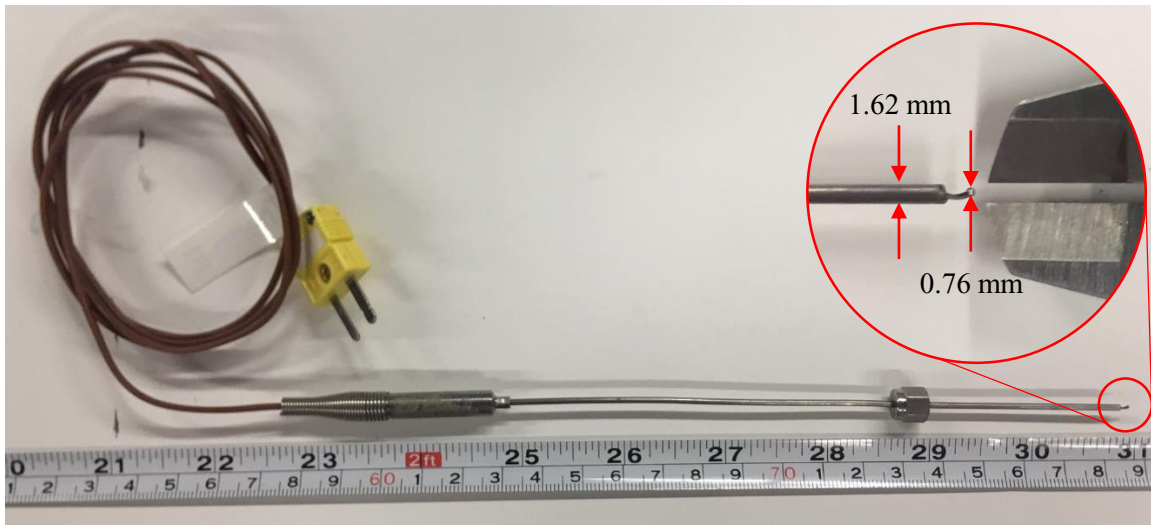


Figure 2-15: Image of a thermocouple used for working gas temperature measurements.

Figure 2-16 shows the P&ID of the gas temperature measurement system. Working gas temperature was measured at 6 locations in the engine (from top to bottom): the expansion space, heater-regenerator interface, regenerator-cooler interface, cooler-compression space interface, power cylinder, and crankcase. Signals from the thermocouples were gathered by a thermocouple terminal block (TC-2095, National Instruments Inc.) then passed to a thermocouple data acquisition module (SCXI-1102B, National Instruments Inc.) in the SCXI-1000 data acquisition chassis (National Instruments Inc.). Analog voltage measurements were digitized with the SCXI-1600 digitization module (National Instruments Inc.) and forwarded to the data acquisition computer. The digitization module was only compatible with 32 bit operating systems.

Consequently, computer memory was restricted to 4 GB and process memory was limited to 2 GB [90]. Thermocouple data was collected at a rate of 5 kHz.

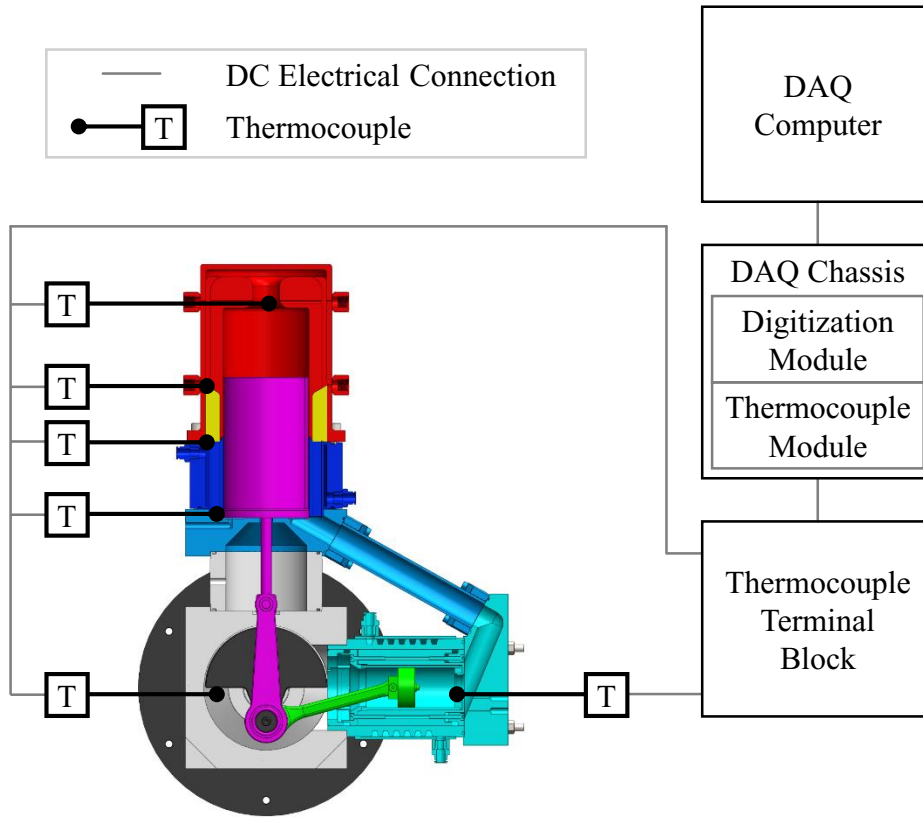


Figure 2-16: P&ID of the working gas temperature measurement system.

The absolute temperature and accuracy of the thermocouples was unknown without calibration. The thermocouples were calibrated to a thermometer (1005-3S, Ever Ready Thermometer Co. Inc.). All of the thermocouples and the thermometer were taped together and placed in the water bath at set points of 5, 20, 40, 60, 80, and 95 °C. After 20 minutes at a stable set point, a 10 s sample of data was collected and the thermometer temperature was manually recorded.

Figure 2-17 (a) is a plot of the measured temperature error of the un-calibrated thermocouples at the recorded thermometer temperatures. The measured temperature error of all thermocouples

increases with thermometer temperature. To correct for this, unique linear correction functions were calculated with the calibration data for each thermocouple. This correction function was applied during data processing to calibrate the thermocouple measurements. Figure 2-17 (b) is a plot of the measured temperature error of the calibrated thermocouples. After calibration, thermocouple measurement error was less than  $\pm 1$  °C for all thermocouples at temperatures less than 100 °C.

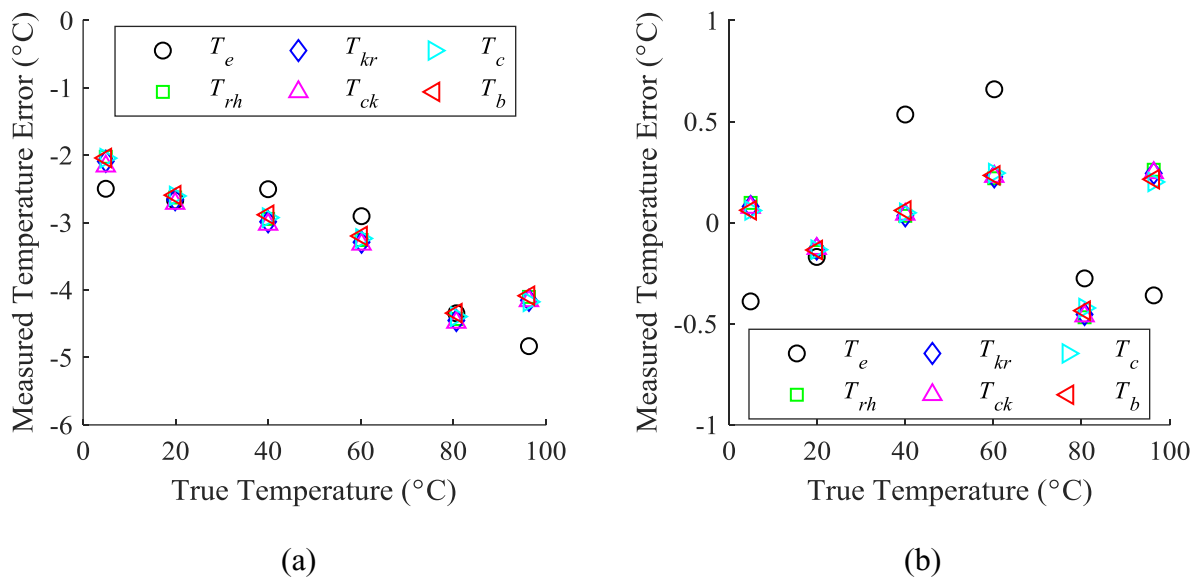


Figure 2-17: Plots of (a) un-calibrated and (b) calibrated thermocouple measurement error at corresponding absolute temperatures.

### 2.3.4 Coolant Temperature

Coolant temperature was measured to calculate the heat rejection rate from the engine to the thermal sink. RTDs (RTD-810, Omega Engineering Inc.) measured the coolant temperature. Figure 2-18 depicts one of the 114 mm long,  $\varnothing$  3.18 mm (0.125”) RTDs. The RTD elbows, shown in Figure 2-19, were built to minimize the influence of heat transfer with the surroundings on the

measurements. These maximize wetted area of the RTD sheath and position the probe tip in the cooling jacket inlet or outlet.

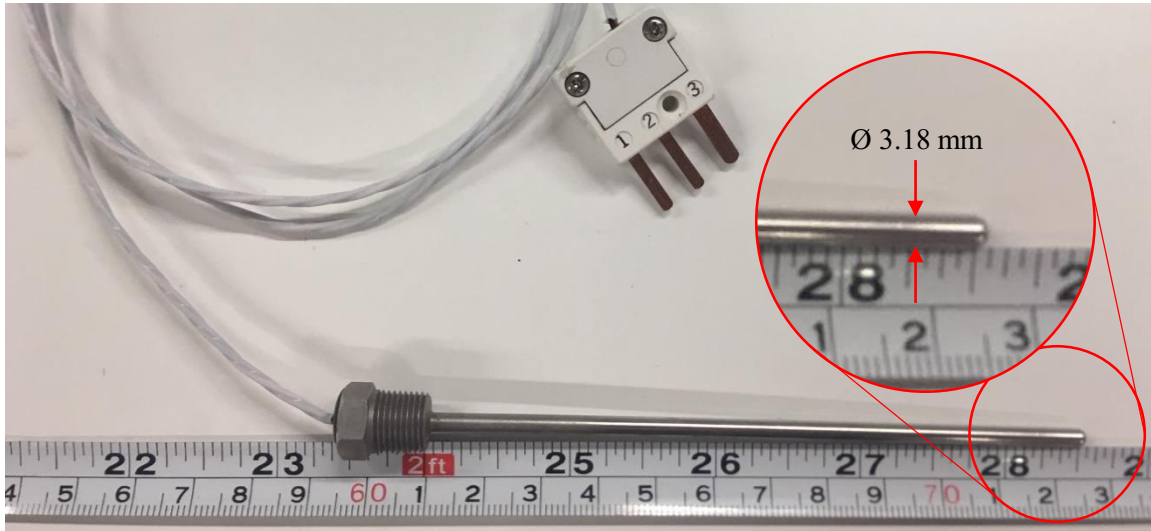


Figure 2-18: Image of a RTD used for coolant temperature measurements.

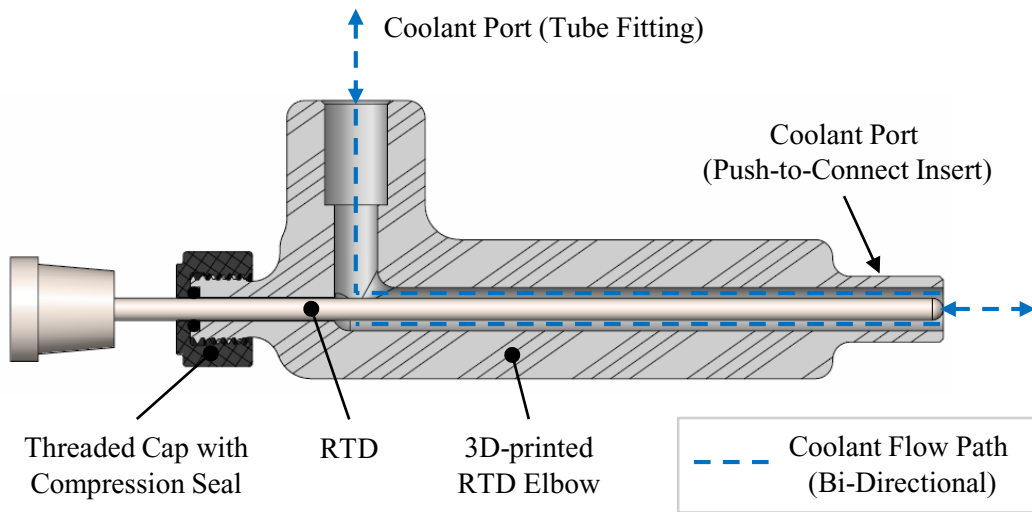


Figure 2-19: Section view of the RTD elbow assembly.

Figure 2-10 earlier in the chapter is the P&ID for the coolant temperature measurement system. RTDs measured the inlet and outlet temperature for two cooling zones: (1) the cooler and (2) the

power cylinder. An RTD data acquisition module (NI-9217 RTD, National Instruments Inc.) collected coolant temperature data at a rate of 100 Hz and transferred data to the data acquisition computer.

The RTD calibration measurements were conducted simultaneously with the thermocouple calibration measurements. The RTDs were calibrated to the same thermometer. All of the RTDs were taped to the thermometer and placed in the water bath at set points of 5, 20, 40, 60, 80, and 95 °C. After 20 minutes at a stable set point, a 10 s sample of data was collected and the thermometer temperature was manually recorded.

Figure 2-20 (a) is a plot of the un-calibrated RTD temperature measurement error at all six thermometer temperatures recorded. The measurement error peaked at the 60 or 80 °C samples for all RTDs. Four unique cubic polynomial correction functions were calculated. The correction functions were applied during data processing to reduce the error of the RTD measurements. Figure 2-20 (b) is a plot of the calibrated RTD measurement errors. All calibrated RTD measurements were within  $\pm 0.2$  °C of the thermometer temperature.

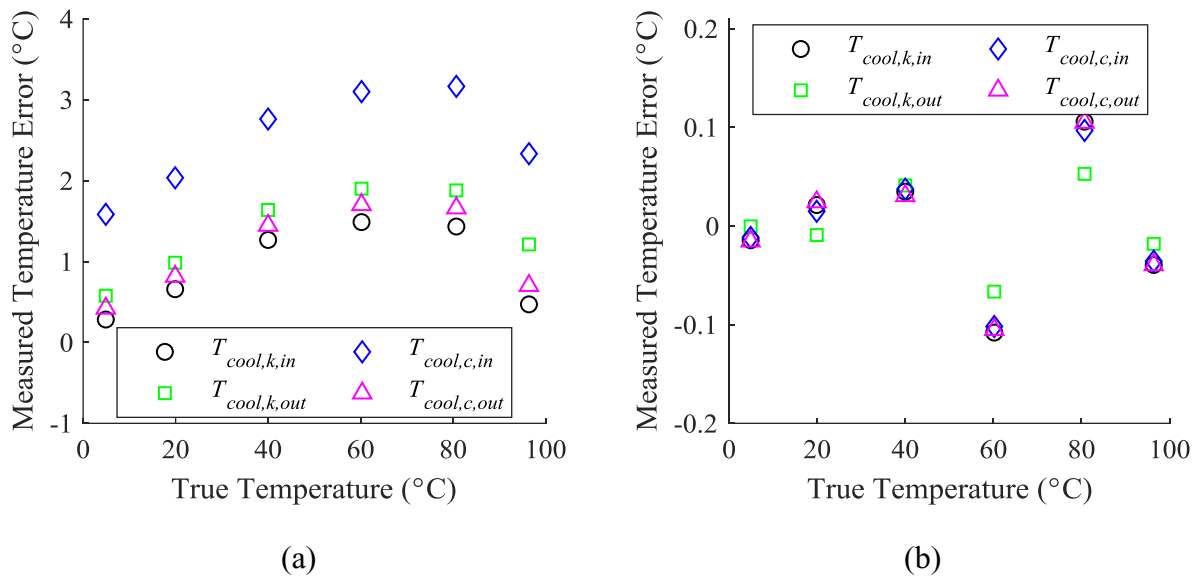


Figure 2-20: Plots of (a) un-calibrated and (b) calibrated RTD measurement error at corresponding thermometer temperatures.

### 2.3.5 Working Gas Pressure

Pressure was measured at two locations in the engine: the power cylinder and the crankcase. Figure 2-21 is a P&ID of the working gas pressure measurement system. A flush-mount, dynamic pressure transducer and an external pressure transducer measured pressure at both locations. Previous experiments found that the external pressure transducers were subject to attenuation and phase lag [79]. Flush-mount, dynamic pressure transducers were introduced to negate those concerns [79]. The dynamic pressure transducers relax, so the external pressure transducers remained in the system to measure mean engine pressure and mean buffer space pressure.



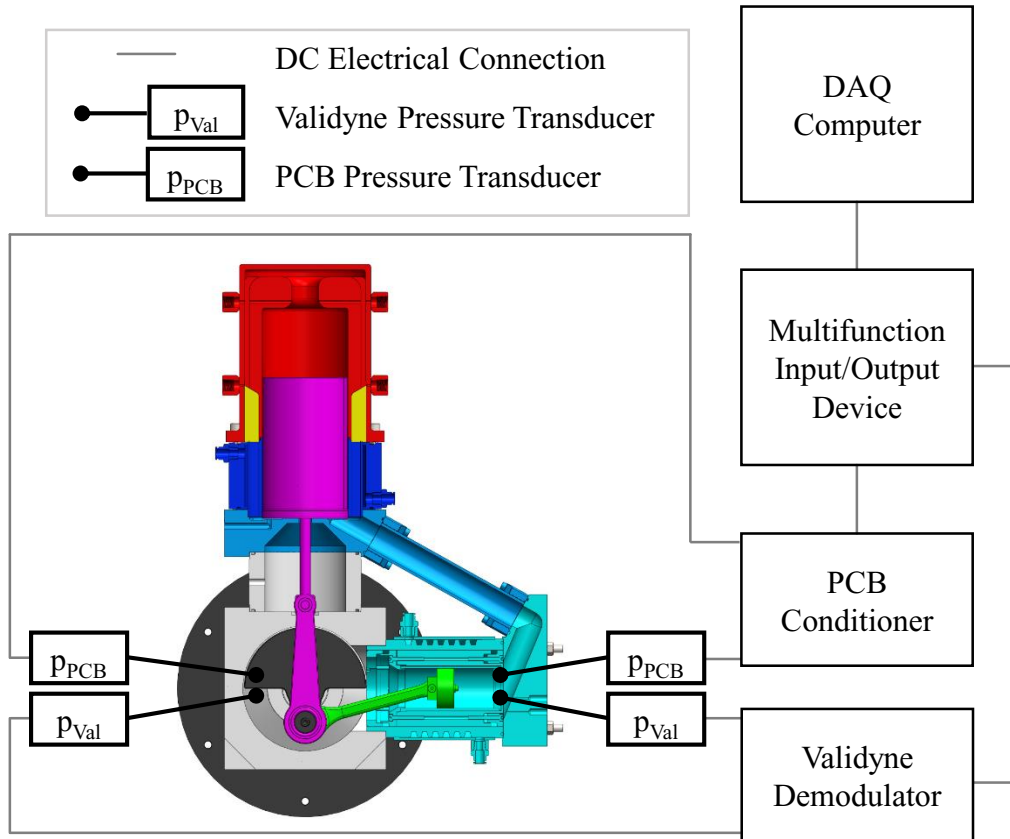
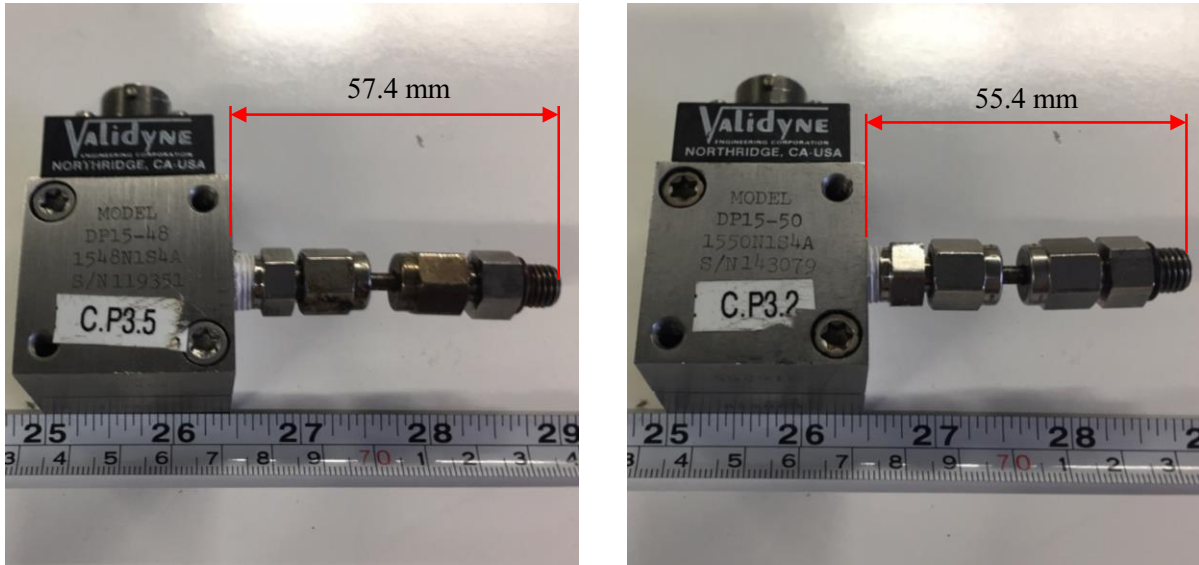


Figure 2-21: P&ID of the working gas pressure measurement system.

### 2.3.5.1 Mean Pressure

Validyne DP15 pressure transducers with diaphragms rated for 860 kPa (125 psi) measured mean pressure in the power cylinder and in the crankcase. Figure 2-22 (a) and (b) are images of the Validyne pressure transducers with scales. Swagelok® fittings on the engine and pressure transducer with a 3.18 mm (0.125”) OD stainless steel tube linked the working space to the pressure transducers. The pressure transducers protruded 89.5 mm and 55.4 mm from the working volume in the power cylinder and the crankcase, respectively. The response time of the power cylinder pressure sensor and tube is 0.016 s, which is equivalent to a phase lag of 0.45 rad at 4.5 Hz [91]. This confirms that the external pressure transducers were not suitable for dynamic pressure measurement.



(a)

(b)

Figure 2-22: Images of the (a) power cylinder and (b) crankcase static pressure transducers.

The Validyne pressure measurement signals were processed and collected with the equipment shown in Figure 2-21. A demodulator (CD280-8, Validyne Engineering) conditioned the signals from the pressure transducers with a gain of 0.01126 V / kPa (0.08 V / psi). A high-speed multifunction I/O device (USB-6211, National Instruments Inc.) sampled the demodulator output at a rate of 30 kHz per channel. Digitized voltage data was passed to the data acquisition computer for collection.

The demodulator has adjustment screws to tune the pressure transducers to a desired zero and span. A pressure calibration device (DPI 603, Druck) provided the reference pressure for tuning. With the calibration device and a pressure transducer open to atmosphere, the demodulator zero was tuned so the digital voltage measurement on the data acquisition computer was 0 V. Then the calibration device and pressure transducer were pressurized to 862 kPa gauge pressure (125 psig) and the demodulator span was tuned so the digital voltage measurement was 10 V. To check the

tuning, the calibration device and pressure transducer were depressurized to 431 kPa gauge pressure (62.5 psig) and a digital voltage measurement near 5 V was confirmed. The voltage data collected in experiments was multiplied by the gain of 86.2 kPa / V during data processing.

The Validyne pressure transducers and calibration device measure pressure relative to the local atmospheric pressure; however, atmospheric pressure changes with weather conditions. Every experiment day barometric pressure was recorded by an iPhone digital pressure sensor (BMP280, Bosch Sensortec) with an absolute pressure accuracy of 0.1 kPa [92]. The daily barometric pressure was added to the gauge pressure measurements to calculate absolute pressure.

Further pressure transducer calibration was performed with the pressure transducers installed on the engine as they would be for experiments. The pressure calibration device was connected to the engine through an extra instrumentation port and its pressure measurement was taken as the true gauge pressure. Engine pressure was charged to roughly 100, 200, 300, 400, 500, 600, and 700 kPa absolute pressure with a pressure regulator and an air compressor. After 10 minutes at the set pressure, a 10 s sample was collected and the calibration device pressure was recorded.

Figure 2-23 (a) is a plot of the un-calibrated Validyne pressure transducer measurement errors. Crankcase pressure error decreased then increased with measured pressure. The power cylinder pressure error increased then decreased with measured pressure. Unique, cubic polynomial correction functions were calculated for each pressure transducer. The correction functions were utilized in data processing to calibrate the Validyne pressure transducer measurements. Figure 2-23 (b) presents the calibrated pressure transducer measurement errors. After calibration, the pressure transducer error was less than  $\pm 0.5$  kPa at all calibration set points.

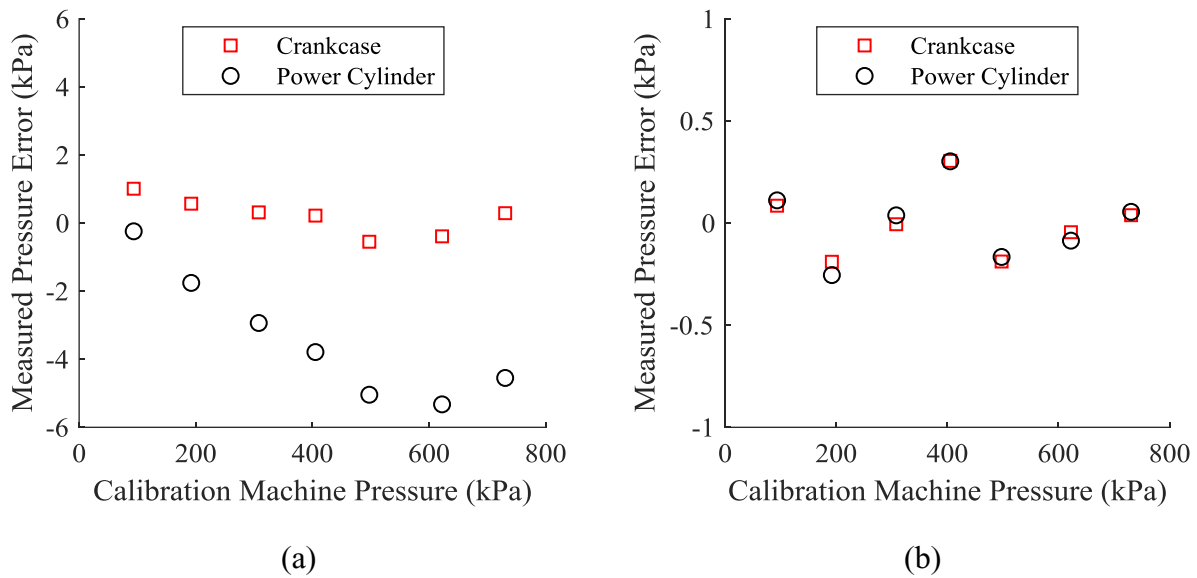
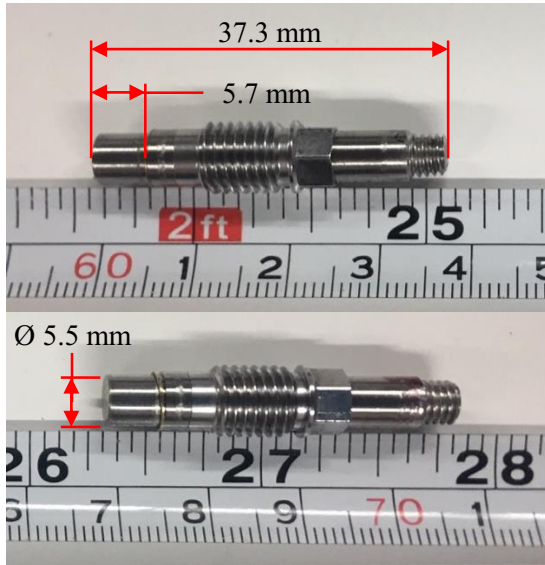


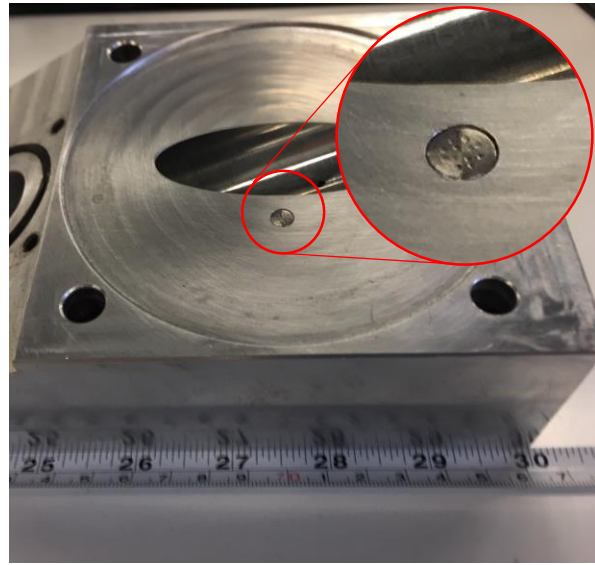
Figure 2-23: Plots of (a) un-calibrated and (b) calibrated Validyne pressure transducer measurement error at corresponding calibration device pressures (absolute pressure).

### 2.3.5.2 Dynamic Pressure

Piezoelectric pressure transducers (113B21, PCB Piezotronics Inc.) measured dynamic pressure in the power cylinder and in the crankcase. Figure 2-24 (a) shows the size of the dynamic pressure transducers. These pressure transducers were mounted flush with the internal engine surfaces (installed in power cylinder head in Figure 2-24 b). The response time of these pressure sensors is less than  $1 \mu\text{s}$  [93]. The manufacturer calibrated the instruments and provided uncertainty and unit corrections specific to the sensor. No further calibration was performed for these instruments.



(a)



(b)

Figure 2-24: (a) Images of both dynamic pressure transducers with dimensions and (b) an image of a dynamic pressure transducer mounted flush in the power cylinder head.

The dynamic pressure signal conditioners and data acquisition devices are shown in Figure 2-21. The voltage signal from the pressure transducers was conditioned with a PCB Piezotronics signal conditioner (113B21, PCB Piezotronics Inc.). The high-speed multifunction I/O device (USB-6211, National Instruments Inc.) sampled the voltage data from the dynamic pressure transducers at a rate of 30 kHz per channel. The data acquisition computer collected the digital voltage measurements.

## 2.4 Data Acquisition

Data was acquired with a program written in LabWindows™ CVI. The program was developed by Speer [79] and was modified for unique file naming and instrumentation changes. Figure 2-25 displays the user interface of the program. It provided live plots of voltage, gas temperature, coolant temperature, engine frequency, load torque, shaft power, and an indicator diagram. The program used thread functions to acquire data from multiple devices with different timing. Voltage data was acquired at 30 kHz for 6 channels, thermocouple data was acquired at 5 kHz for 6 channels, and RTD data was acquired at 1 kHz for 4 channels. The program saved data in three \*.log files. Data sets had unique file name generated from the date and time with additional fields for source temperature, sink temperature, charge pressure, and engine configuration.

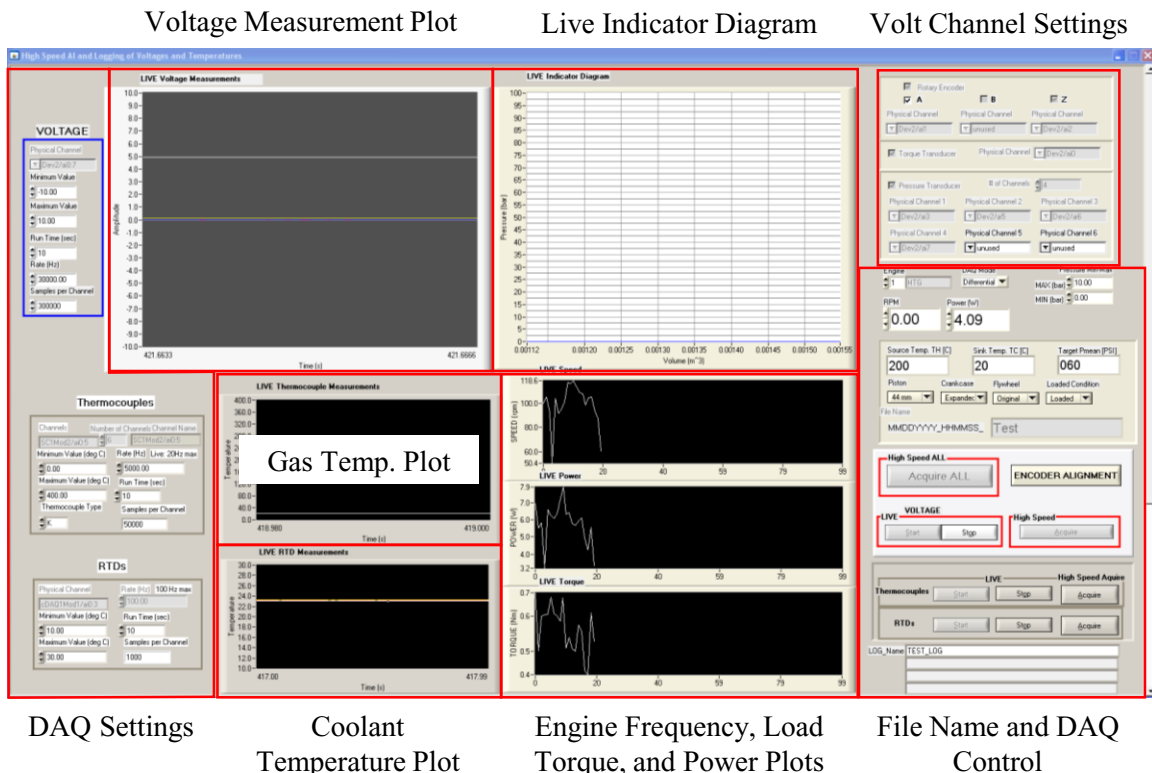


Figure 2-25: Screenshot of the data acquisition program user interface.

### 2.4.1 Transient Experiment Data Acquisition

The goal of the transient experiments was to gather data from engine start to steady-state. The maximum possible acquisition time was used to sample the entire transition. In preliminary experiments, a 180 s acquisition time nearly occupied all the available memory. Figure 2-26 shows the transition of engine frequency and cooler heat transfer rate from engine start to steady-state with the largest flywheel. The engine frequency stabilized near the end of the 180 s sample. Cooler heat transfer rate was within its uncertainty through the entire sample. These show that the engine and heat transfer stabilized in the 180 s sample with the methods used. With 180 s of acquisition time, the transient data sets had 32.4 million voltage samples, 5.4 million thermocouple samples and 720 000 RTD samples.

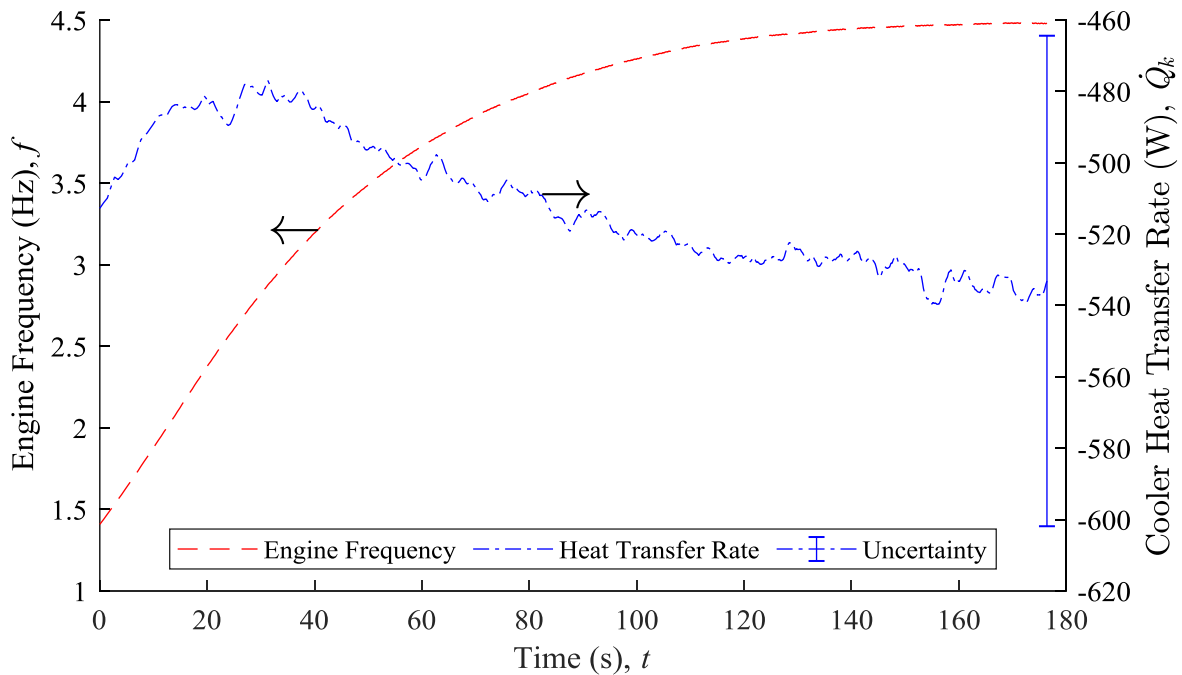


Figure 2-26: Plot of the transient engine frequency and transient cooler heat transfer rate.

### 2.4.2 Steady-State Data Acquisition

Steady-state experiments were performed to evaluate parameters with different operating conditions. Steady-state experiments had a 30 s acquisition time to collect data for 30 rotations at frequencies near 1 Hz (the lowest engine frequency in preliminary experiments). Consequently, the steady-state data sets included 5.4 million voltage samples, 900 000 thermocouple samples and 120 000 RTD samples.



## 2.5 Experiment Procedures

---

Experiments occurred in three stages: start-up, data collection and cool down. The start-up and cool-down stages were standard for all experiments. The data collection stage changed for transient experiments and steady-state experiments. The engine was under continuous supervision during the start-up and data collection stages of experiments. Intermittent supervision was permitted under certain conditions during the cool-down stage. This section describes the experiment procedures in stages.

### 2.5.1 Experiment Start-Up

The experiment start-up stage includes all the actions necessary before data collection begins. The actions were executed as follows:

1. Inform lab users of experiment hazards.
2. Check engine to ensure wires and tubes are clear of mechanical components, coolant tubes are secured in fittings, electrical connections are sound, and potential spills will not interact with electrical connections.
3. Start water bath set to 21 °C.
4. Ensure tubes fill with water and check for leaks.
5. Start the data acquisition devices, signal conditioners, instrument power supplies, data acquisition program and live measurement display.
6. Start the temperature controller and energize the heater power supply.
7. Change temperature controller set point in 100 °C increments with a minimum 10 minute wait period at each set point before advancing to the next set point. Maintain at desired set point for one hour before data collection.

8. While engine is heating, remove cylinder head to expose piston for rotary encoder alignment or alignment confirmation.
9. Reassemble cylinder head, reattach remaining instruments and turn on live measurement displays on data acquisition software user interface.
10. Check charge pressure supply hoses and connections, and close all valves and regulators.
11. Turn on air compressor and introduce the vessel and hoses to 860 kPa (gauge) in stages by sequentially opening valves. Do not charge the engine.
12. Open bypass and charge the engine to a pressure near 35 kPa (gauge) and confirm the engine is sealed.
13. Charge the engine in 100 kPa increments and wait for 1 minute between increases. Once at desired set point, allow pressure to stabilize for 10 minutes.
14. Turn on peristaltic pump to control flow rate and confirm coolant is not contaminated with air.
15. Confirm all wait times are complete and check live measurement display that the operating condition has achieved steady-state.
16. Proceed to transient experiment or steady-state experiment data collection stages.

### 2.5.2 Transient Experiments

The goal of the transient experiments was to collect data from engine start to free-running steady-state. The procedures for the data collection stage of the transient experiments are as follows:

1. Confirm bypass is closed, start engine and wait until engine reaches steady-state (10 minutes). Confirm by checking live measurement display.
2. Set data collection time to 180 seconds.

3. Stop the engine and live measurements.
4. Start data collection.
5. After 4 seconds, restart the engine.
6. Wait for data collection to complete and for the \*.log files to save (near 5 minutes).
7. Restart live measurements and confirm measurements were similar to pre-collection values.
8. For replicates, repeat steps 3 to 7.
9. For operating condition changes:
  - a. Open bypass and apply insurmountable load on friction brake to prevent engine start.
  - b. Execute step 7 from the experiment start-up stage for thermal source temperature change or execute step 13 from the experiment start-up stage for charge pressure change.
  - c. Return to step 1.
10. For flywheel configuration changes:
  - a. Open bypass and apply insurmountable load on friction brake to prevent engine start.
  - b. Change the flywheel configuration.
  - c. Return to step 1.
11. When complete data collection, proceed to cool-down stage.

### 2.5.3 Steady-State Experiments

Steady-state experiments were performed to for measurements at a range of engine frequencies. Ten load conditions were applied for each flywheel configuration, thermal source temperature, and charge pressure. The following list is the data collection procedure for steady-state experiments.

1. Confirm bypass is closed, start engine and wait until engine reaches steady-state (10 minutes). Confirm by checking live measurement display.
2. Set data collection time to 30 seconds.
3. Change mass in load basket to apply new torque load to engine.
4. Let engine stabilize at new load (5 minutes)
5. Stop live measurement display and start data collection.
6. Once data collection is complete, restart live measurement display.
7. Return to step 3 for additional load conditions.
8. For operating condition changes:
  - a. Open bypass and apply insurmountable load on friction brake to prevent engine start.
  - b. Execute step 7 from the experiment start-up stage for thermal source temperature change or execute step 13 from the experiment start-up stage for charge pressure change.
  - c. Return to step 1.
9. For flywheel configuration changes:
  - a. Open bypass and apply insurmountable load on friction brake to prevent engine start.
  - b. Change the flywheel configuration.
  - c. Return to step 1.
10. When complete data collection, proceed to cool-down stage.

#### 2.5.4 Experiment Cool-Down

The experiment cool-down procedure mitigated hazards after the experiment process was complete. The thermal capacity of heater cap stored heat capable of fueling the engine for over an hour and was at temperatures unsafe for contact for several more hours after. Running the engine

at high frequency, increasing the charge pressure, decreasing the coolant temperature, and increasing coolant flow rate all facilitated engine cooling. These were employed when possible during the cool-down stage. The cool-down procedures are as follows:

1. Start live measurement display and, if possible, start engine. Apply a small load if free running frequency exceeds 4.6 Hz (276 rpm).
2. Set thermal source temperature to 10 °C and turn off power supply for the cartridge heaters.
3. Turn off peristaltic pump and remove tubing for unrestricted coolant flow.
4. Set water bath set point to 5 °C to increase heat rejection.
5. Remove load after thermal source temperature cools below 250 °C.
6. Allow the engine to run until it stalls.
7. Open the bypass and depressurize the engine to ambient pressure in 100 kPa intervals at a rate less than 50 kPa / minute.
8. Depressurize the charge pressure supply hoses and pressure vessel.
9. After thermal source temperature cools below 100 °C, turn off the data acquisition devices, signal conditioners, instrument power supplies and the data acquisition program.
10. Turn off the temperature controller and water bath.
11. Check workspace for energized equipment and hazards. Turn of energized equipment and mitigate hazards.
12. Allow remaining cooling to proceed unsupervised.

Intermittent supervision during the cool-down stage was permitted if: (1) the thermal source temperature was below 200 °C, (2) the engine and charge pressure supply were depressurized, and

(3) the engine could not run. The engine was checked every 30 minutes for cooling progress, coolant leaks, and hazards.

## 2.6 Data Processing

---

A data processing code was written in MATLAB® to convert raw data from \*.log files into valuable measurements saved in a standard format. Figure 2-27 is the data processing flow chart. Appendix C. presents the data processing code. The program determined discrete angular position from rotary encoder voltage measurements then averaged data within the discrete angular positions. Instantaneous angular velocity was derived from the angular positions and times. Data was cropped to a global start time to correct for different data acquisition start times. With synchronized data, thermocouple and RTD data were averaged in angular increments. The program reorganized all data in columns for individual rotations. Voltage data required conversion into physical units. The program applied the unique correction functions to the thermocouples, RTDs, and Validyne pressure transducers. Next, the volumes, volume changes, indicated work, shaft power, and uncertainties were calculated. These results were input into the 2<sup>nd</sup> order model before the program saved the processed data, uncertainties, and model results in a standard data structure.

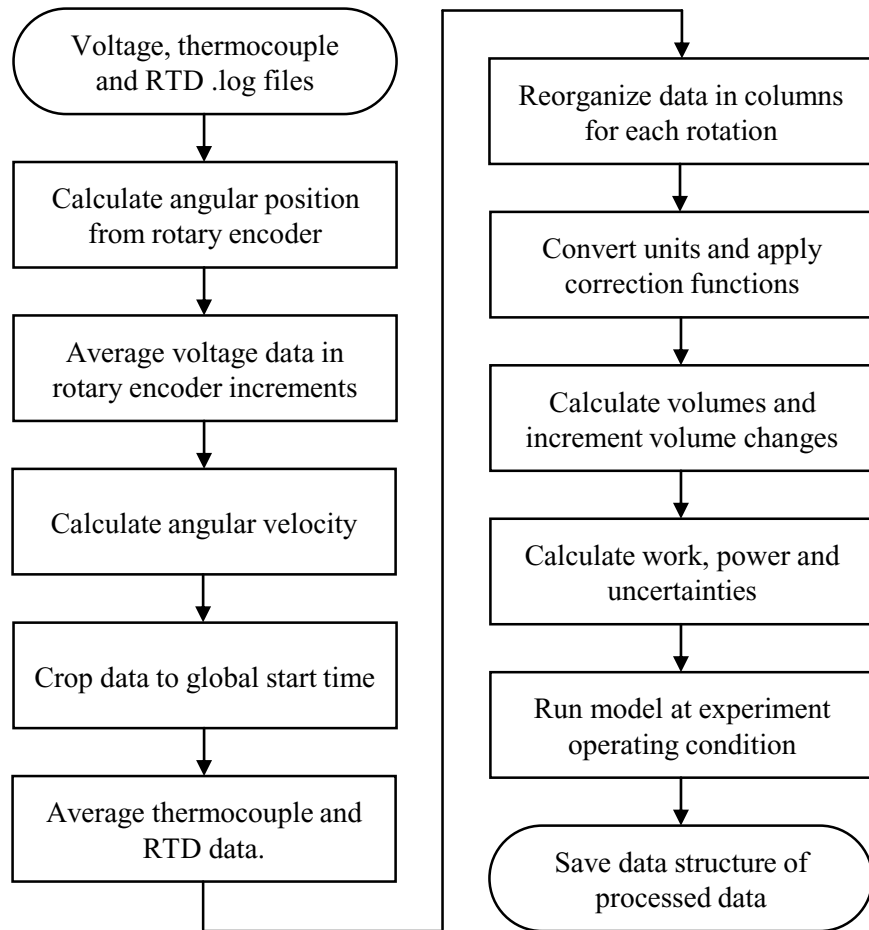


Figure 2-27: Data processing program flow chart.



### 2.6.1 Angular position from rotary encoder

Angular position was calculated from the counts of A and Z rotary encoder pulses. Figure 2-28 presents a sample of raw data from the rotary encoder. Voltage data from the rotary encoder was measured as 0 V or 5 V. Rotary encoder pulses were counted when the voltage measurement exceeded the threshold of 2.5 V. The next pulse was counted the next time the voltage increased above the threshold. The first Z-pulse detected was established as the reference angle ( $\theta = 0$  rad). Backwards and forwards counts of the A-pulse ( $Count_A$ ) were converted to discrete angular positions with Equation 2-1 for the complete data set.

$$\theta = Count_A \cdot \left( \frac{2\pi}{500} \right) \quad 2-1$$

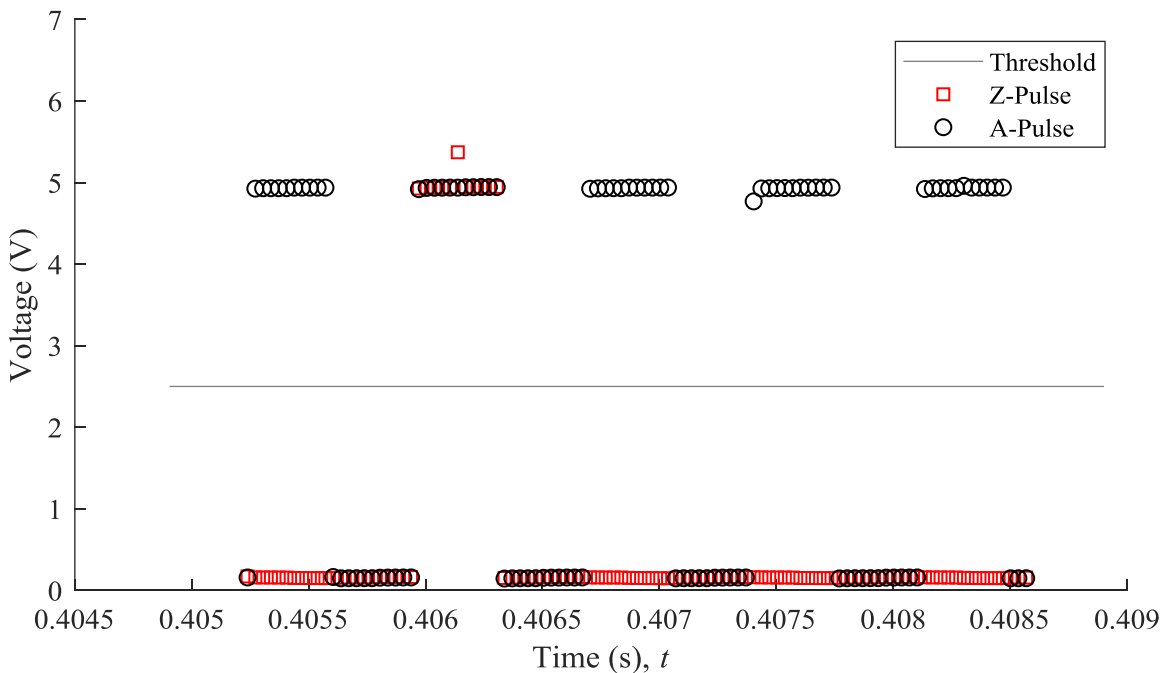


Figure 2-28: Plot of raw voltage data from the rotary encoder.

## 2.6.2 Voltage Data Averaging

Voltage measurements were averaged in each discrete angular position. Figure 2-29 presents the raw voltage data from the torque transducer and pressure sensors in a discrete angular position. Measurements were assumed to be constant in each discrete angular position. The mean torque and pressures were calculated with all the samples in a discrete angular position (between grey lines in Figure 2-29). Random uncertainty of the torque and pressure samples was calculated simultaneously with the averaging. The midpoint sample time was assigned to each discrete angular position.

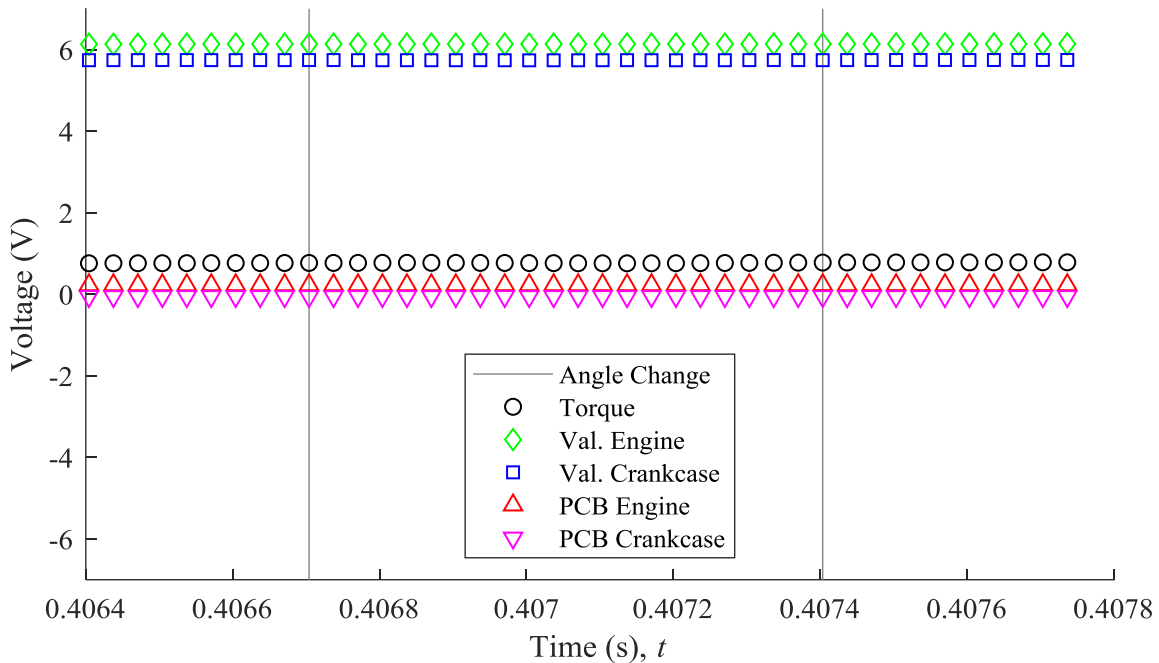


Figure 2-29: Plot of raw voltage data averaged from the torque transducer and pressure sensors.

### 2.6.3 Instantaneous Angular Velocity Calculation

The instantaneous angular velocity was calculated from the angular position measurements and time. Both the angular position and time were discrete measurements. To calculate angular velocity, a quadratic curve was fit to 35 discrete angular positions and the corresponding time. Figure 2-30 provides an example of the data points and fit curve zeroed at the center point. The angular velocity at the center of the fit was the derivative of the quadratic curve evaluated at the center point of the fit. The angular velocity at the first and last 17 angular positions were calculated from quadratic fits of the first 35 and last 35 samples, respectively. The angular velocity at these first and last 17 points may be less accurate but these samples were often cropped later in data processing.

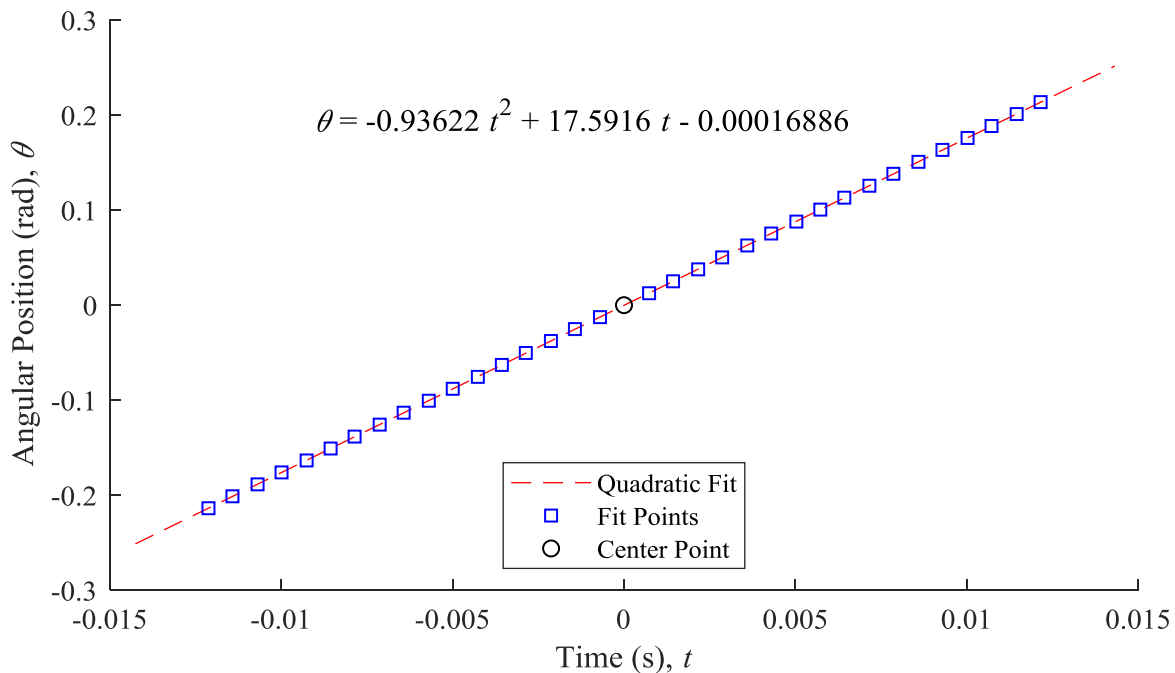


Figure 2-30: Plot of the angular position with time and the fit quadratic polynomial curve used to calculate angular velocity.

## 2.6.4 Data Cropping

Simultaneous data acquisition was performed by three thread functions (one for voltage data, one for thermocouples and one for RTDs). However, the start time of the thread functions were asynchronous, as shown in Table 2-3. A method was developed to synchronize the start time of the data. The last thread function start time was found. Then the time of the first Z-pulse after the last start time was found. Finally, the data collected by all three thread functions were cropped to this time by finding the index with the nearest time. As a result, the incomplete, first rotation was cropped from the data and a common start time was established.

Table 2-3: List of data acquisition start times.

Thread Function or Z-Pulse	Start Time (s)
Voltage	0.081
Thermocouple	0.217
RTD	0.493
1 <sup>st</sup> Z-Pulse	0.764

### 2.6.5 Thermocouple Data Averaging

As mentioned in section 2.3.3, the thermocouple response time was insufficient for time resolved gas temperature measurements yet temperature fluctuations were observed. Thermocouple data was averaged in intervals of 10 discrete angular positions. The time of the angular position data and the time thermocouple data was used to define the averaging intervals from data with different sample timing. Figure 2-31 presents an example of raw thermocouple data that was averaged. Thermocouple random uncertainty was calculated simultaneously with the averaging. The resulting thermocouple data after averaging had 50 samples per rotation.

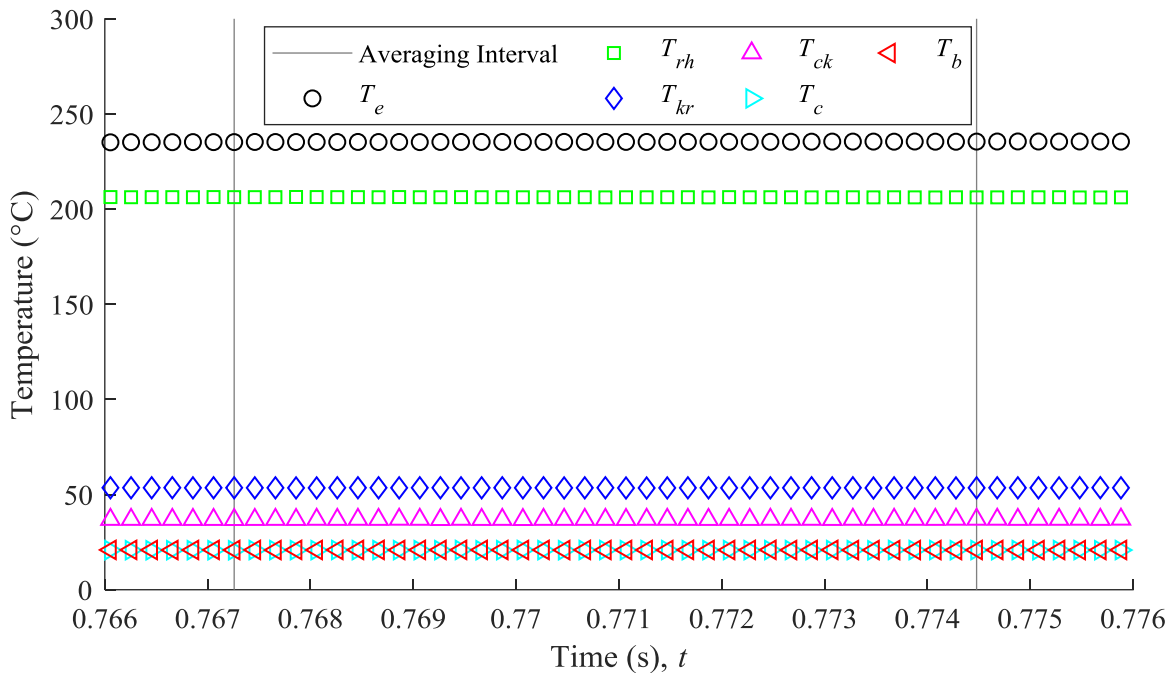


Figure 2-31: Plot of raw thermocouple data averaged in intervals of 10 discrete angular positions.

### 2.6.6 RTD Data Averaging

The coolant temperature was not sensitive to intra-cyclic heat transfer rate fluctuations. Therefore, RTD data was averaged over one complete cycle. Sample time was used to synchronize

the RTD samples and timing of the revolutions. Figure 2-32 shows an example of the raw RTD data over a complete rotation. Like the thermocouple and voltage data, random uncertainty of the RTD data was calculated simultaneously with data averaging. Coolant temperature data was reduced to one sample per rotation.

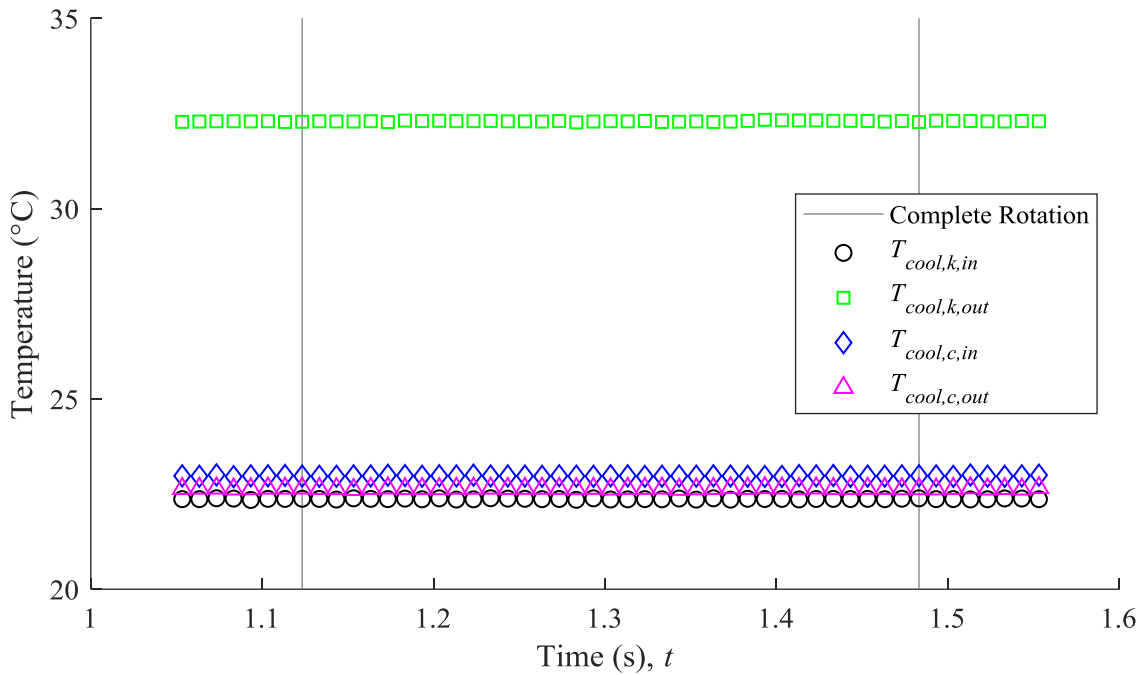


Figure 2-32: Plot of some raw RTD data averaged over a complete rotation.

### 2.6.7 Data Sorting

After averaging, data was sorted into columns by rotation. Time, angular position, angular velocity, torque and pressure data had a value for each discrete angular position and therefore 500 rows per column. Thermocouple data was averaged through 10 discrete angular positions for 50 rows per column. The cyclic mean coolant temperatures had one row per column. Through this process, the incomplete, final rotation was cropped from the data.

### 2.6.8 Engine Volumes and Volume Changes

Engine volumes in the expansion space, compression space, total engine, and buffer space were calculated at each discrete angular position with the equations defined in section 1.3.2. The volume change in each discrete angular position was the product of the crank angle derivatives of the volumes and the angular position change. The volume uncertainty and volume change uncertainty was calculated with the methods in section 2.7.5.

### 2.6.9 Indicated Work

Indicated work is the integral of the engine pressure function with volume. This corresponds to the area enclosed by the pressure volume function. The data processing program calculated this as the area within a polygon created by the phase-averaged engine pressure and corresponding engine volume data points. Section 2.7.7 presents the uncertainty of indicated work calculated from this method. Due to the phase-average pressure, this calculation is valid for the steady-state data sets but not the transient data sets.

### 2.6.10 Shaft Power

The program calculated experiment shaft power as the product of the data set mean torque and mean angular velocity. Similar to indicated work, this shaft power calculation is valid for steady-state data sets but not transient data sets.

### 2.6.11 Modelling of Experiment Results

The last step of data processing program conducted a simulation of the engine with the 2<sup>nd</sup> order thermodynamic model described in Chapter 3. The model simulated the engine with the mean operating condition of an experimental data set. Consequently, the modelled results were valid for steady-state experiments only. The addition the modelling step ensured each steady-state experimental data set had a corresponding modelled data set.

## 2.7 Experimental Uncertainty

---

Measured and calculated values presented in this work have a level of uncertainty associated with them. Most uncertainty calculations followed a general method for random uncertainty, systematic uncertainty, and propagation of uncertainty. However, there were special cases for angular velocity uncertainty, spatial pressure uncertainty, volume uncertainty, volume change uncertainty and indicated work uncertainty. This section outlines the general methods and special methods used to calculate uncertainty. Appendix A. contains example uncertainty calculations for all measurements and propagated uncertainties.

### 2.7.1 Random Uncertainty

Random uncertainty stems from the standard deviation in a group of samples that are expected to share a common value [94]. Noise in measured values and system inconsistencies contribute to the random uncertainty. This analysis assumed data averaged in angular increments are expected to share a common value. This applies to voltage data in every discrete angular position, thermocouple data in groups of 10 discrete angular positions and RTD data in every rotation. Random uncertainty was calculated with the 95 % confidence interval procedure from Wheeler and Ghanji (Equation 2-2) [94]. The standard deviation ( $\sigma_x$ ), number of samples ( $n_x$ ) and students t-value ( $t_{0.05/2, n_x-1}$ ) were unique to every averaged group of samples.

$$U_{random,x} = \pm t_{0.05/2, n_x-1} \cdot \frac{\sigma_x}{\sqrt{n_x}} \quad 2-2$$

### 2.7.2 Systematic Uncertainty

Systematic uncertainty was unique to each instrument. Instruments, signal conditioners, data acquisition devices and calibrations all contributed to the systematic uncertainty. Uncertainties



from all sources were converted to the measurement units and combined with the root-sum-of-squares, Equation 2-3, for the total systematic uncertainty of a measurement as per Wheeler and Ganji [94]. Here the systematic uncertainty of measurement  $x$  is the root-sum-of-squares of the uncertainty components from the equipment and procedures ( $U_{xj}$ ).

$$U_{systematic,x} = \sqrt{\sum_{j=1}^n (U_{xj}^2)} \quad 2-3$$

### 2.7.3 Angular Velocity Uncertainty

The uncertainty from the quadratic fit of angular position and time was lost in the derivative. The uncertainty of instantaneous angular velocity ( $U_{\dot{\theta}_i}$ ) was determined from the slope uncertainty ( $U_B$ ) of a straight line between the first and last fit points. Equation 2-4 calculates for the slope of a line ( $B$ ) between the first and last fit points from the discrete angular position change ( $\Delta\theta$ ) and time ( $t_i$ ). The uncertainty of instantaneous angular velocity ( $U_{\dot{\theta}_i}$ ) was calculated with Equation 2-5 from the angular position change, time, and their uncertainties.

$$B = \frac{34 \cdot \Delta\theta}{t_{i+17} - t_{i-17}} \quad 2-4$$

$$U_{\dot{\theta}_i} = U_B = \frac{U_{\Delta\theta}}{t_{i+17} - t_{i-17}} + \frac{34 \cdot \Delta\theta \cdot U_{t_{i+17}}}{(t_{i+17} - t_{i-17})^2} + \frac{34 \cdot \Delta\theta \cdot U_{t_{i-17}}}{(t_{i+17} - t_{i-17})^2} \quad 2-5$$

### 2.7.4 Pressure Wave Transport Uncertainty

Pressure wave transport uncertainty accounts for the unknown spatial and temporal pressure gradients in both the engine and buffer space. Pressure acting on the piston face is the target of working gas pressure measurements but the pressure sensors are not on the piston face. Volume

changes from the piston, heat transfer in the heat exchangers, and heat transfer with the crankcase walls are some of the processes that change pressure in the engine and buffer space. Pressure waves induced by these processes require time to travel throughout the engine and, more specifically, require time to travel between the piston face and pressure sensor. The pressure wave transport uncertainty is the worst-case estimate of the instantaneous difference between the pressure acting on the sensor and the pressure acting on the piston face.

Pressure wave transport uncertainty was calculated with the worst case parameters. Table 2-4 provides an example calculation. The maximum distances between the piston and dynamic pressure sensor ( $l_{i, max}$ ) were measured in SOLIDWORKS®. The time for a pressure wave to travel between sensor and piston at their greatest separation ( $t_{i, transport, max}$ ) was calculated with Equation 2-6 from the maximum distance between the piston and sensor, and the speed of sound ( $v_{i, sound}$ ). The speed of sound in the working fluid was calculated with Equation 2-7 from the measured gas temperature ( $T_i$ ), the gas constant ( $R$ ), and the specific heat ratio ( $\gamma$ ) [95]. The pressure wave transport uncertainty ( $U_{p_i, transport}$ ) is the product of the maximum measured rate of pressure change ( $dp_i / dt$ ) and the worst-case pressure wave transport time, as shown in Equation 2-8. In the example case shown in Table 2-4, pressure transport uncertainty was 39.5 % and 41.7 % of the dynamic pressure measurement total uncertainty ( $U_{p_i, dynamic}$ ) in the power cylinder and the crankcase, respectively.

$$t_{i,transport,max} = \frac{l_{i,max}}{v_{i,sound}} \quad 2-6$$

$$v_{sound} = \sqrt{\gamma \cdot R \cdot T_i} \quad 2-7$$

$$U_{p_i,transport} = \pm \left( \frac{dp_i}{dt} \right)_{max} \cdot t_{i,transport,max} \quad 2-8$$

Table 2-4: Example of pressure wave transport uncertainty calculation.

Variable	Power Cylinder	Crankcase
Maximum Distance Between Sensor and Piston (mm), $l_{i, max}$	104.5	505.6
Speed of Sound at Mean Temperature (m / s), $v_{i, sound}$	343.7	343.7
Maximum Rate of Pressure Change (kPa / s), $(d_{pi} / dt)_{max}$	2477	496
Pressure Wave Transport Uncertainty (kPa), $U_{pi, transport}$	0.753	0.728
Dynamic Pressure Measurement Total Uncertainty (kPa), $U_{pi, dynamic}$	1.908	1.745

### 2.7.5 Volume and Volume Change Uncertainty

The uncertainty of the working space volumes ( $U_{Vi}$ ) were not calculated with propagation of uncertainty from the angular position of the crankshaft. Rather, the volume of the working spaces were calculated with the crankshaft angular position leading ( $\theta + U_{\theta}$ ) and lagging ( $\theta - U_{\theta}$ ) by its uncertainty. Then the larger of the absolute difference between the measured volume and either the leading or lagging volume was the uncertainty (Equation 2-9). The resulting volume uncertainties are dependent on the angular position.

$$U_{V_i} = \max\left(\left|V(\theta + U_{\theta})_i - V(\theta)_i\right|, \left|V(\theta - U_{\theta})_i - V(\theta)_i\right|\right) \quad 2-9$$

Similarly, the uncertainty of the volume change in one rotary encoder increment ( $U_{dVi}$ ) was calculated by determining the volume change in leading and lagging crankshaft angular positions. Once again, the larger absolute difference between the measured volume change and either the leading and lagging volume change was the uncertainty (Equation 2-10).

$$U_{dV_i} = \max\left(\left|dV(\theta + U_{\theta})_i - dV(\theta)_i\right|, \left|dV(\theta - U_{\theta})_i - dV(\theta)_i\right|\right) \quad 2-10$$

### 2.7.6 Propagation of Uncertainty

Some variables analyzed in this work, such as load torque and engine speed, are interdependent. Therefore, propagation of uncertainty was calculated with Equation 2-11 from Wheeler and Ganji [94] where parameter  $g$  is a function of known parameters  $x_1$  to  $x_n$  with uncertainties  $U_{x1}$  to  $U_{xn}$ . It calculates the maximum uncertainty and is suitable for interdependent variables [94].

$$U_g = \sum_{j=1}^n \left( U_{x_j} \left| \frac{\partial g(x_1, x_2 \dots x_n)}{\partial x_j} \right| \right) \quad 2-11$$

### 2.7.7 Indicated Work Uncertainty

Indicated work is the integral of engine pressure with engine volume and the data processing program calculated it with a polygon area function. These methods did not allow for simple calculations for indicated work uncertainty. As a result, propagation of uncertainty was performed with the sum definition of the integral in Equation 2-12 where  $i$  is the index of a discrete angular position and  $N$  is the index of a complete rotation. It yielded Equation 2-13 for indicated work uncertainty ( $U_{W_I}$ ) that is dependent on the engine pressure ( $p_{E,i}$ ), volume change ( $dV_{E,i}$ ) and their uncertainties at each discrete angular position.

$$W_I = \oint p_E \cdot dV_E \cong \sum_{i=1}^N (p_{E,i} \cdot dV_{E,i}) \quad 2-12$$

$$U_{W_I} = \sum_{i=1}^N \left( (U_{p_{E,i}} \cdot |dV_{E,i}|) + (U_{dV_{E,i}} \cdot |p_{E,i}|) \right) \quad 2-13$$

## 2.8 Experiment Setup and Procedures Summary

---

This section detailed the devices and methods for experiments performed on the low-temperature ST05G Stirling engine built at the University of Alberta. In experiments, thermal source temperature, charge pressure, and load torque were manipulated to expose the engine to a range of operating conditions. Crankshaft angular position, crankshaft torque, working gas temperature, coolant temperature, and working gas pressure, were measured for two types of experiments—transient experiments and steady-state experiments. A data acquisition software gathered the measurements and saved them in standard \*.log files. Then a data processing software averaged measurements, converted units, applied correction functions, calculated uncertainties, and simulated the engine with a 2<sup>nd</sup> order model. The resulting data sets were suitable for analysis and steady-state data sets had modelled results at an identical operating condition to the experiment.

---

## 3 2<sup>ND</sup> ORDER THERMODYNAMIC MODEL

---

This work uses a 2<sup>nd</sup> order thermodynamic model to estimate the performance of the low-temperature ST05G Stirling engine. Speer [79] initially compiled the model with equations and processes from literature. A temperature correction process was added to the model. Appendix B contains code for the 2<sup>nd</sup> order model that has changed from Speer [79]. This chapter explains the calculations and solution process of this model.

The 2<sup>nd</sup> order model completes three iterative processes to generate solution. Figure 3-1 is a flow chart describing the model solution process. First, experimental measurements or predicted operating conditions are used as input data. Then, the reference cycle of the model is calculated from the adiabatic model with the Simple Analysis for imperfect heat exchangers (enclosed in green dashed line in Figure 3-1). Next, the model simultaneously corrects the heat exchanger wall temperatures and the mass of working gas. After the iterative calculations have converged, the model calculates decoupled losses for flow friction, appendix gap losses, conduction loss, gas spring hysteresis, and mechanical friction. Finally, the power and efficiency are calculated.

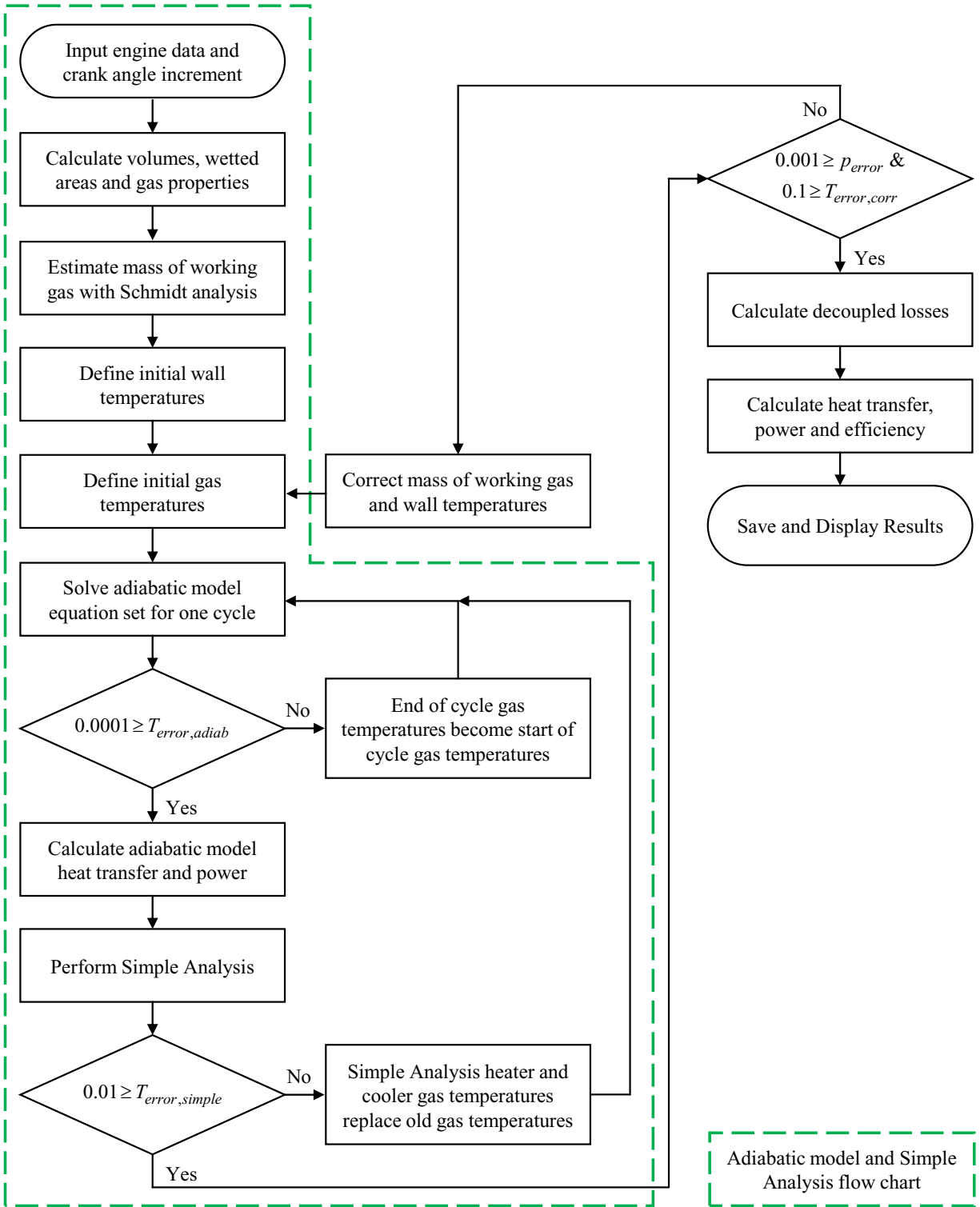


Figure 3-1: Flow chart of the 2<sup>nd</sup> order thermodynamic model.

## 3.1 Volumes and Volume Changes

---

The instantaneous working volume of the engine and the components within it are necessary for accurate modelling. The volumes of the constant volume spaces and variable volume spaces must be calculated to determine the instantaneous working volume. This section describes how the volumes were calculated.

### 3.1.1 Constant Volume Spaces

Constant volume spaces include the heat exchangers, the crankcase excluding the power cylinder, the displacer clearance volume and the power cylinder clearance volume. Speer [79] calculated the volume of working gas in individual engine components with a CAD model of the engine in SOLIDWORKS®. The volume of the displacer was deducted from the internal volume of the engine [79].

The 2<sup>nd</sup> order model calculates working gas volumes in the heat exchangers from geometry inputs. The regenerator geometry inputs are the housing dimensions and the porosity. The heater and cooler geometry inputs are the number of channels, channel width, channel depth, and channel length. The heater is comprised of a bell-mouth entrance to the expansion space, a disc-shaped volume and rectangular slots. The length of the heater slots input into the model was increased so the volume calculated by the thermodynamic model matched the CAD model volume of the heater [79].

### 3.1.2 Variable Volume Spaces

The 2<sup>nd</sup> order model also calculates the instantaneous volumes, and volume changes of the total engine, compression space, expansion space and buffer space. Slider-crank mechanisms govern the motion of the piston and the displacer. Section 1.3.2 presents the derivation and equations for the volume and volume change in the variable volume spaces.



## 3.2 Reference Cycle

---

This 2<sup>nd</sup> order model calculates the reference with the adiabatic model and the Simple Analysis described by Urieli and Berchowitz [29]. Figure 3-2 defines the working gas properties and temperature distribution for the reference cycle calculation. The entire engine has constant mass  $m_E$  and uniform pressure  $p_E$ . The heater, regenerator, and cooler are isothermal (at temperatures  $T_h$ ,  $T_r$ , and  $T_k$ ). The temperatures of the compression space ( $T_c$ ) and expansion space ( $T_e$ ) depend on engine pressure. All cells have a portion of the mass of working gas ( $m_i$ ) that depends on the volume of the cell ( $V_i$ ), the temperature of the cell ( $T_i$ ), and the engine pressure. Mass transfers between engine cells with an angular mass flow rate ( $\dot{m}_{ij}$  with units kg / rad and positive values for flow from the compression space to the expansion space) and a conditional temperature ( $T_{ij}$ ) from the upstream cell. After the adiabatic model and Simple Analysis have converged, heat  $Q_{h,\text{simple}}$  is absorbed from the heater wall at temperature  $T_{w,h}$ . Similarly, heat  $Q_{k,\text{simple}}$  is rejected to the cooler wall at temperature  $T_{w,k}$  (with positive heat transfer into the engine). The engine produces indicated work  $W_I$  that is later subject to decoupled losses. Figure 3-1 earlier in the chapter shows that the model calculates the adiabatic model for one cycle then performs the Simple analysis. The model repeats this process until it converges on a solution.

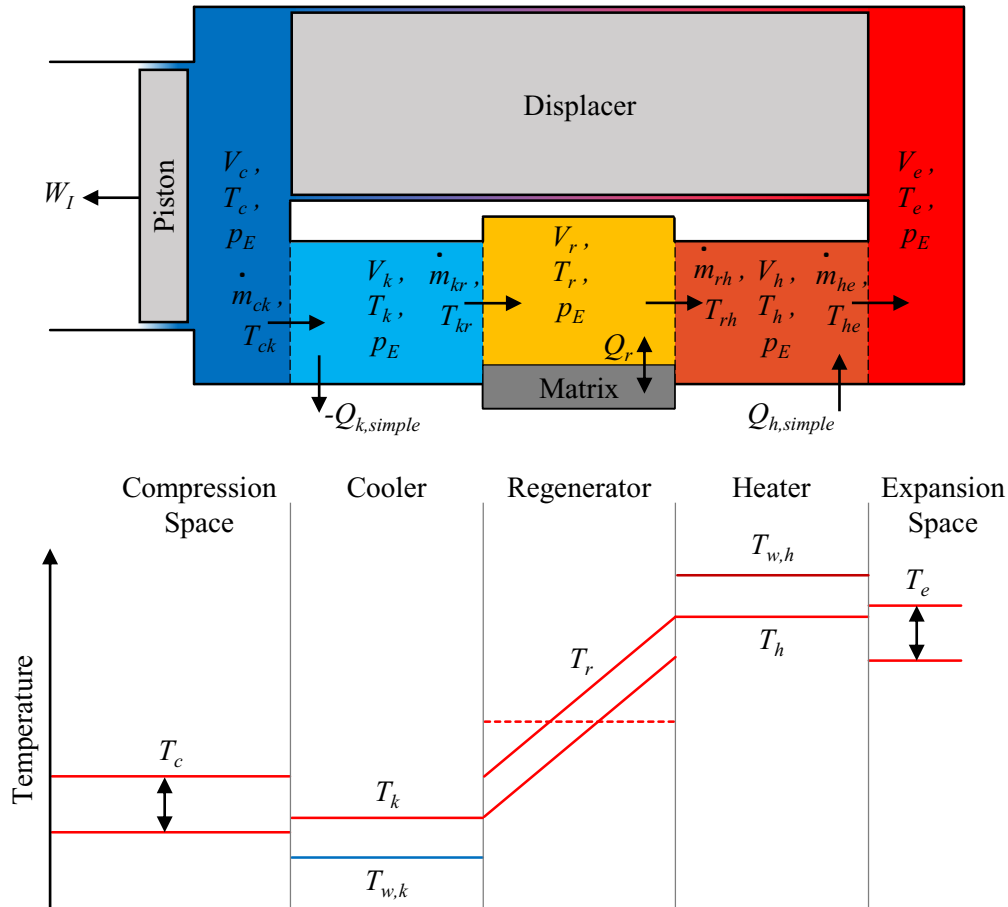


Figure 3-2: Engine schematic and working gas temperature distribution in the adiabatic model with the Simple Analysis after Urieli and Berchowitz [29].

### 3.2.1 Adiabatic Model

Urieli and Berchowitz [29] developed equations and a solution procedure for the adiabatic model. Equation set 3-1 was derived from the conservation of mass, conservation of energy, ideal gas law, and the differential forms of all three equations [29]. The model solves this equation set in order during each step.

$$\frac{dp_E}{d\theta} = \frac{-\gamma \cdot p_E \cdot \left( \left( \frac{dV_c}{d\theta} / T_{ck} \right) + \left( \frac{dV_e}{d\theta} / T_{he} \right) \right)}{(V_c/T_{ck}) + \gamma \cdot [(V_k/T_k) + (V_r/T_r) + (V_h/T_h)] + (V_e/T_{he})}$$

$$\frac{dm_c}{d\theta} = \frac{p_E \cdot (dV_c/d\theta) + V_c \cdot (dp_E/d\theta) \cdot \gamma^{-1}}{R \cdot T_{ck}}$$

$$m_k = \frac{p_E \cdot V_k}{R \cdot T_k}, \quad m_r = \frac{p_E \cdot V_r}{R \cdot T_r}, \quad m_h = \frac{p_E \cdot V_h}{R \cdot T_h}$$

$$m_e = m_E - (m_c + m_k + m_r + m_h)$$

$$T_c = \frac{p_E \cdot V_c}{R \cdot m_c}, \quad T_e = \frac{p_E \cdot V_e}{R \cdot m_e}$$

$$\frac{dm_k}{d\theta} = \frac{m_k}{p_E} \frac{dp_E}{d\theta}, \quad \frac{dm_r}{d\theta} = \frac{m_r}{p_E} \frac{dp_E}{d\theta}, \quad \frac{dm_h}{d\theta} = \frac{m_h}{p_E} \frac{dp_E}{d\theta}$$

3-1

$$\dot{m}_{ck} = -\frac{dm_c}{d\theta}, \quad \dot{m}_{kr} = \dot{m}_{ck} - \frac{dm_k}{d\theta}, \quad \dot{m}_{rh} = \dot{m}_{kr} - \frac{dm_r}{d\theta}, \quad \dot{m}_{he} = \dot{m}_{rh} - \frac{dm_h}{d\theta}$$

$$T_{ck} = \begin{cases} T_c & \text{if } \dot{m}_{ck} > 0 \\ T_k & \text{if } \dot{m}_{ck} \leq 0 \end{cases} \quad \text{and} \quad T_{he} = \begin{cases} T_h & \text{if } \dot{m}_{he} > 0 \\ T_e & \text{if } \dot{m}_{he} \leq 0 \end{cases}$$

$$\frac{dW_I}{d\theta} = p_E \cdot \frac{dV_c}{d\theta} + p_E \cdot \frac{dV_e}{d\theta}$$

$$\frac{dQ_k}{d\theta} = \frac{c_v \cdot V_k \cdot (dp_E/d\theta)}{R - c_p \cdot (\dot{m}_{ck} \cdot T_{ck} - \dot{m}_{kr} \cdot T_k)}$$

$$\frac{dQ_r}{d\theta} = \frac{c_v \cdot V_r \cdot (dp_E/d\theta)}{R - c_p \cdot (\dot{m}_{kr} \cdot T_k - \dot{m}_{rh} \cdot T_h)}$$

$$\frac{dQ_h}{d\theta} = \frac{c_v \cdot V_h \cdot (dp_E/d\theta)}{R - c_p \cdot (\dot{m}_{rh} \cdot T_h - \dot{m}_{he} \cdot T_{he})}$$

The adiabatic model is solved as an initial value problem in increments of crank angle. The Schmidt analysis estimates the initial mass of working gas. Initial expansion space temperature

and compression space temperature are equal to the heater gas temperature and the cooler gas temperatures respectively. This allows for calculation of the remainder of the initial values. The 4<sup>th</sup> order Runge-Kutta method solves the equation set in advancing increments. It continues to solve the equation set until the model converges. The convergence measure is the combined expansion space temperature difference and compression space temperature difference between the start ( $\theta = 0$ ) and end ( $\theta = 2\pi$ ) of a rotation ( $T_{error,adiab}$ ), as defined in Equation 3-2. The adiabatic model converges when this is less than 0.0001 °C, which requires 5 to 10 complete rotations [29].

$$T_{error,adiab} = |T_e(2\pi) - T_e(0)| + |T_c(2\pi) - T_c(0)| < 0.0001 \quad 3-2$$

### 3.2.2 Regenerator Simple Analysis

After the adiabatic model solves, the model performs the regenerator Simple Analysis. The regenerator Simple Analysis calculates the additional heat transfer the heater and cooler must perform due to imperfect regeneration [29]. Figure 3-3 plots the temperature distribution of an ideal regenerator and an imperfect regenerator. The working gas recovers all the heat transferred to the regenerator matrix in both the ideal regenerator and imperfect regenerator [29]. In the ideal regenerator, the outlet temperature is equal to the temperature of the neighboring heat exchanger ( $T_k$  and  $T_h$ ) so the regenerator effectiveness ( $\epsilon_r$ ) is one [29]. The outlet temperature in an imperfect regenerator ( $T_k'$  and  $T_h'$ ) is not equal to the neighboring heat exchanger and the regenerator effectiveness is less than one [29]. As a result, the heater and cooler need to transfer heat at a greater rate ( $Q_{h,simple}$  and  $Q_{k,simple}$ ) to perform the remaining heat exchange, as defined in Equations 3-3 and 3-4 [29]. Variables  $Q_{h,adiab}$ ,  $Q_{r,adiab}$ , and  $Q_{k,adiab}$  are the heat transfer rates in the

heater, regenerator and cooler, respectively, calculated by the adiabatic model [29]. The amount of additional heat transfer depends on how effective the regenerator is.

$$\dot{Q}_{h,simple} = \dot{Q}_{h,adiab} + \dot{Q}_{r,adiab} \cdot (1 - \varepsilon_r) \quad 3-3$$

$$\dot{Q}_{k,simple} = \dot{Q}_{k,adiab} - \dot{Q}_{r,adiab} \cdot (1 - \varepsilon_r) \quad 3-4$$

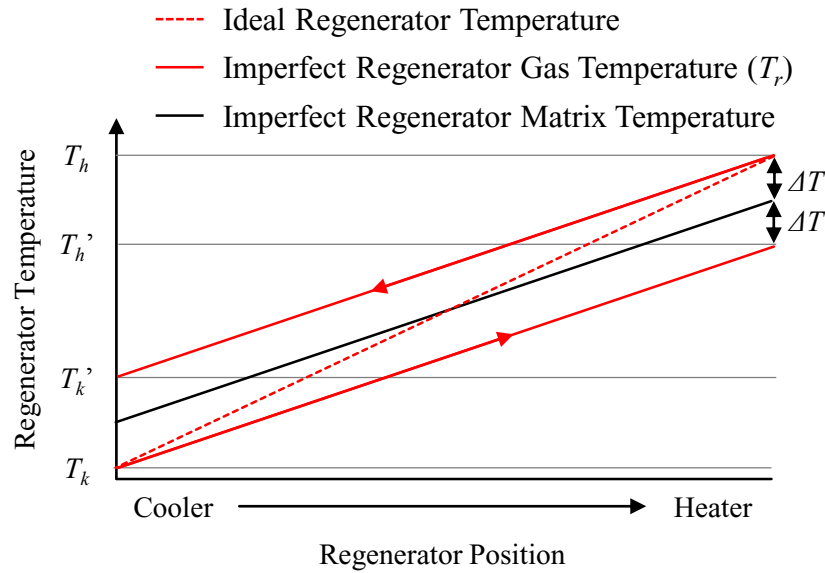


Figure 3-3: Ideal and imperfect regenerator temperature distribution *after Urieli and Berchowitz* [29].

Urieli and Berchowitz [29] use a steady flow correlation to calculate regenerator effectiveness in the Simple Analysis. First, cycle mean Stanton number ( $St_{r,mean}$ ) is calculated from a steady flow correlation—Equation 3-5—that depends on the regenerator cycle mean Reynolds number ( $Re_{r,mean}$ ) and Prandtl number ( $Pr_r$ ). The correlation is specifically for 60.2 % porous wire mesh regenerators with 0.27 mm wires at 2.36 wires/mm (60 mesh). Urieli and Berchowitz [29] used this correlation for 60-70 % porous wire mesh regenerators with wire diameters near 0.04 mm and

wire spacing at 7.87 wires/mm (200 mesh). Speer [79] used the same correlation for the 90 % porous, random-fiber regenerator with wire diameter near 0.05 mm in the low-temperature ST05G.

$$St_{r,mean} = 0.46 \cdot Re_{r,mean}^{-0.4} \cdot Pr_r^{-1} \quad 3-5$$

Urieli and Berchowitz [29] define the effectiveness of a Stirling engine regenerator ( $\epsilon_r$ ) as the heat transferred to the working gas during one blow of the cycle divided by the ideal adiabatic model regenerator heat transfer during the same blow. Equation 3-6 calculates the regenerator effectiveness with the number of transfer units in the regenerator ( $NTU_r$ ), assuming constant specific heats [29]. The number of transfer units in the regenerator, defined by Equation 3-7, depends on the cycle mean Stanton number calculated in Equation 3-5, the wetted area of the regenerator matrix ( $A_{r,wetted}$ ) and the cross-section area of the regenerator ( $A_{r,cross-section}$ ) [29].

$$\epsilon_r = \frac{(T_h - T_k')}{(T_h - T_k)} = \frac{NTU_r}{1 + NTU_r} \quad 3-6$$

$$NTU_r = \frac{St_{r,mean} \cdot A_{r,wetted}}{2 \cdot A_{r,cross-section}} \quad 3-7$$

### 3.2.3 Heater and Cooler Simple Analysis

Additional heat transfer resulting from imperfect regeneration is used to evaluate the heater and cooler gas temperatures ( $T_h$  and  $T_k$ ). The Simple Analysis assumes the heater and cooler wall temperatures ( $T_{w,h}$  and  $T_{w,k}$ ) are constant and uniform [29]. Newton's law of cooling—Equation 3-8—defines the convective heat transfer rate from the heat exchanger to the working gas with a heat transfer coefficient ( $h_{i,mean}$ ), wetted area of the heat exchanger ( $A_{i,wetted}$ ) and the temperature difference between the heat exchanger and working gas [29]. Equation 3-8 was

rearranged to estimate the working gas temperature in the heater with Equation 3-9 and the cooler with Equation 3-10 [29].

$$\dot{Q}_{i,simple} = h_{i,mean} \cdot A_{i,wetted} \cdot (T_{w,i} - T_i) \quad 3-8$$

$$T_h = T_{w,h} - \frac{\dot{Q}_{h,simple}}{h_{h,mean} \cdot A_{h,wetted}} \quad 3-9$$

$$T_k = T_{w,k} - \frac{\dot{Q}_{k,simple}}{h_{k,mean} \cdot A_{k,wetted}} \quad 3-10$$

Urieli and Berchowitz [29] estimate the heat transfer coefficient from correlations for fully-developed, steady, turbulent flow in a smooth, circular pipe. The Blasius correlation (Equation 3-11) calculates Reynolds friction factor ( $f_{Reynolds,i}$ ) with the cycle mean Reynolds number ( $Re_{i,mean}$ ) [29]. Reynolds simple analogy (Equation 3-11) relates the heat transfer coefficient ( $h_{i,mean}$ ) to the Reynolds friction factor, hydraulic diameter of the duct ( $d_i$ ), dynamic viscosity of the working gas ( $\mu_i$ ), isobaric specific heat capacity of the working gas ( $c_{p,i}$ ), and the Prandtl number of the working gas ( $Pr$ ) [29]. Speer [79] estimated heat transfer coefficients in the rectangular ducts of the low-temperature ST05G heater and cooler with this method.

$$f_{Reynolds,i} = 0.0791 \cdot Re_i^{0.75} \quad 3-11$$

$$h_{i,mean} = \frac{f_{Reynolds,i,mean} \cdot \mu_i \cdot c_{p,i}}{2 \cdot d_i \cdot Pr} \quad 3-12$$

### 3.2.4 Combined Adiabatic Model and Simple Analysis Solution

The Simple Analysis calculates the heater and cooler gas temperatures used in the next adiabatic model iteration [29]. After the adiabatic simulation, the model repeats the Simple

Analysis until it converges, as shown in Figure 3-1 earlier in the chapter. The Simple Analysis converges when the cumulative heater and cooler gas temperature change,  $T_{error,simple}$  in Equation 3-13, is less than 0.01 °C.

$$T_{error,simple} = |T_{h,new} - T_{h,old}| + |T_{k,new} - T_{k,old}| < 0.01 \quad 3-13$$



### 3.3 Mass and Temperature Correction

---

Two iterative corrections are used to ensure the model replicates the conditions measured in an experiment. The first correction adjusts the mass of working gas to ensure the mean pressure matches the target. The second correction adjusts the heater and cooler wall temperatures so the modelled expansion space and compression space gas temperatures match the experimental data. This section provides details and results of the correction methods.

#### 3.3.1 Mass of Working Gas Correction

The mass of working gas in the model must be estimated and corrected for the mean pressure to match the specified value. Working gas charge pressure is used to control the mass of working gas in a Stirling engine; whereas, the model requires a constant mass of working gas as an input parameter [29]. The Schmidt analysis is often used to estimate the mass of working gas from charge pressure. Paul and Engeda [96] found a 10 % error in mass of working gas using this method. Their solution to this problem is an iterative method to solve for the correct mass of working gas [96]. The reference cycle of the 2<sup>nd</sup> order model is calculated with an estimate of the mass of working gas [96]. Then the relative error of the modelled mean pressure ( $p_{mean}$ ) and the target mean pressure ( $p_{target}$ ) are used to correct the mass of working gas ( $m_{new}$  from  $m_{old}$ ) with Equation 3-14 [96]. The corrected mass is used in the next iteration of the model until the relative error of mean pressure and target pressure ( $p_{error}$ ) is less than 0.1 % (Equation 3-15) [79,96].

$$m_{new} = \left( 1 - \frac{p_{target} - p_{mean}}{p_{target}} \right) \cdot m_{old} \quad 3-14$$

$$p_{error} = \left| \frac{p_{target} - p_{mean}}{p_{target}} \right| \leq 0.001 \quad 3-15$$

### 3.3.2 Heat Exchanger Wall Temperature Correction

The Simple Analysis requires an estimate of the heat exchanger wall temperatures [29]. Speer [79] estimated the heat exchanger wall temperatures as the average measured gas temperature in the heat exchangers. The resulting mean expansion and compression space gas temperatures varied significantly from the experimental data. Additionally, the ideal adiabatic model generates the maximum possible cyclic pressure change in a Stirling engine [34]; yet the pressure change in the mass corrected model (MCM) is less than the measured pressure change. This suggests that the model was not performing simulations at equivalent operating conditions to the experiments.

A scheme was derived to correct for the expansion space and compression space gas temperature discrepancy. The method used to correct the mass of working gas, described above, was expanded to iteratively adjust the heater and cooler wall temperatures. In each iteration, the expansion and compression space mean gas temperature discrepancies are subtracted from the heater and cooler wall temperatures of the previous iteration as shown in Equations 3-16 and 3-17, respectively. The correction converges when the cumulative, mean gas temperature discrepancy ( $T_{error,corr}$ ) is less than 0.1 °C, as governed by Equation 3-18.

$$T_{w,h,new} = T_{w,h,old} - (T_{e,mean,md} - T_{e,mean,xp}) \quad 3-16$$

$$T_{w,k,new} = T_{w,k,old} - (T_{c,mean,md} - T_{c,mean,xp}) \quad 3-17$$

$$T_{error,corr} = |T_{e,mean,md} - T_{e,mean,xp}| + |T_{c,mean,md} - T_{c,mean,xp}| \leq 0.1 \quad 3-18$$

The goal of the mass and temperature corrected model (M&TCM) was to replicate the operating conditions of an experimental data set. Table 3-1 reports the temperatures and

performance indicators of an experiment, the MCM and the M&TCM. The M&TCM brings the modelled expansion and compression space mean gas temperatures within the uncertainty of the experiment values. The cooler wall temperature of the M&TCM is less than the thermal sink temperature. This impossible outcome is likely the result of the model excluding heat rejection in the connecting pipe and power cylinder. The M&TCM has a larger pressure change than the experimental result. This is reasonable because the adiabatic model is the upper limit of pressure change in Stirling engines [34]. The indicated work of the MCM is closer to the experimental indicated work than the M&TCM, which significantly exceeds it (Table 3-1). Figure 3-4 displays the dimensionless indicator diagrams of the experiment, mass corrected model and temperature corrected model. The MCM indicator diagram is in better agreement with the experiment indicator diagram compared to the M&TCM. The simplified treatment used to calculate the reference cycle in the model should not match the experimental data because it neglects all loss mechanisms beyond imperfect heat transfer. Although the M&TCM indicator diagram and indicated work discrepancy is larger, it simulates the performance of an engine with similar operating conditions to the experiment.

Table 3-1: List of temperatures and performance metrics from an experiment, the MCM, and the M&TCM (used in this work).

Parameter	Experiment	MCM	M&TCM	Unit
Thermal Source Temperature ( $T_H$ )	300	300	300	°C
Thermal Sink Temperature ( $T_C$ )	21	21	21	°C
Mean Expansion Space Temperature ( $T_{e,mean}$ )	$249.0 \pm 3.5$	205.3	248.9	°C
Mean Compression Space Temperature ( $T_{c,mean}$ )	$24.0 \pm 3.5$	65.1	24.0	°C
Heater Wall Temperature ( $T_{w,h}$ )	-	219.2	264.6	°C
Cooler Wall Temperature ( $T_{w,k}$ )	-	58.4	17.7	°C
Cycle Pressure Change ( $p_{E,max} - p_{E,min}$ )	$150.8 \pm 3.9$	127.5	181.1	kPa
Indicated Work ( $W_I$ )	$8.66 \pm 0.22$	8.98	14.33	J

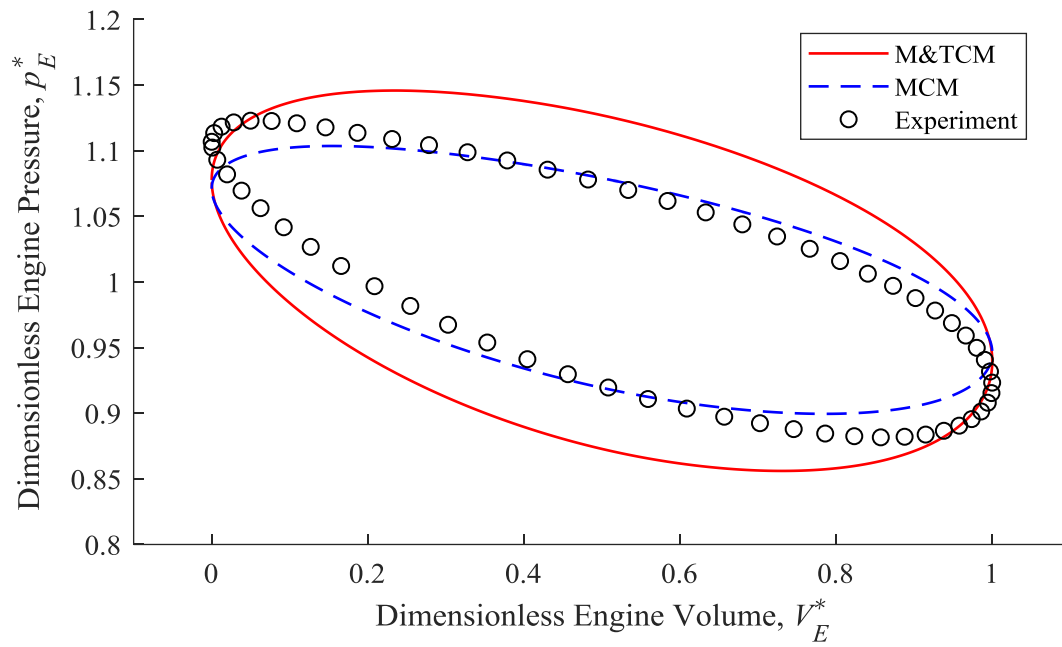


Figure 3-4: Experimental, MCM, and M&TCM dimensionless indicator diagrams.

## 3.4 Decoupled Losses

---

The 2<sup>nd</sup> order model adds flow friction, appendix gap losses, conduction loss, gas spring hysteresis, and mechanical losses to the thermodynamic solution of the model. Section 1.4.3 introduced the loss mechanisms. This section describes how each loss was calculated and how they altered the thermodynamic solution of the model.

### 3.4.1 Heat Exchanger Flow Friction

The model calculates quasi-steady flow friction with the equations presented by Urieli and Berchowitz [29]. The incremental Reynolds friction factor is calculated for each crank angle increment to estimate flow friction, unlike the mean heat transfer coefficient in the Simple Analysis. Equation 3-19 calculates the regenerator Reynolds friction factor ( $f_{Reynolds,r}$ ) and the Blasius correlation—Equation 3-11 from earlier in the chapter—calculates the heater and cooler Reynolds friction factors ( $f_{Reynolds,h}$  and  $f_{Reynolds,k}$ ) [29]. Both equations use the instantaneous, quasi-steady Reynolds number ( $Re_i$ ). Equation 3-20 calculates pressure drop ( $\Delta p_i$ ) in each crank angle increment with Reynolds friction factor, dynamic viscosity ( $\mu_i$ ), instantaneous mass flow rate ( $\dot{m}_i$ ), instantaneous mass of gas in the heat exchanger ( $m_i$ ), hydraulic diameter ( $d_i$ ) and heat exchanger length ( $L_i$ ). [29]. Power lost to flow friction ( $\dot{W}_{\Delta p,i}$ ) is calculated by Equation 3-21 with engine frequency ( $f$ ) and expansion space volume change ( $dV_e$ ). All components of flow friction deduct from the shaft power.

$$f_{Reynolds,r} = 54 + 1.43 \cdot Re_r^{-0.48} \quad 3-19$$

$$\Delta p_i = \frac{2 \cdot f_{Reynolds,i} \cdot \mu_i \cdot \dot{m}_i \cdot L_i^2}{m_i \cdot d_i^2} \quad 3-20$$

$$\dot{W}_{\Delta p,i} = f \cdot \oint \Delta p_i \cdot dV_e \quad 3-21$$

The power lost to flow friction is converted to heat in the heat exchangers and impacts the modelled heat absorption and rejection [29]. The heater flow friction and 50 % of the regenerator flow friction reduce the amount of heat absorbed in the heater. The cooler flow friction and the other 50 % of regenerator flow friction increase the amount of heat rejected in the cooler.

### 3.4.2 Appendix Gap Losses

Appendix gap losses act as a thermal shortcut and increase the heating and cooling requirements of the heater and cooler, respectively. The model includes both shuttle transfer and gas enthalpy transfer as described by Urieli and Berchowitz [29]. Section 1.4.3.3 describes both losses. Shuttle transfer is calculated with Equation 1-34 and gas enthalpy transfer is calculated with Equation 1-35 where the appendix gap width ( $b$ ) is 1 mm and the displacer cylinder length ( $l_{cylinder}$ ) is 220 mm.

### 3.4.3 Conduction Loss

Conduction loss also acts as a thermal shortcut from the heater to the cooler [79]. It increases the heat transfer into the heater and the heat rejection in the cooler. Conduction along the regenerator housing, through the regenerator and through the displacer are considered in this model. The heat transfer through all three pathways are calculated using Fourier's law in one dimension (Equation 1-36 from chapter one). Table 3-2 lists the variables to calculate conduction loss along the three pathways. The following paragraphs describe how the conduction loss parameters were determined by Speer [79].

Table 3-2: List of conduction loss parameters [79].

Conduction Path	Thermal Conductivity (W / m K), $k$	Cross-Section Area (m <sup>2</sup> ), $A_{cross-section}$	Length (m), $L$	Temperature Difference (K), $\Delta T$
Regenerator Housing	47	0.0036	0.055	$T_{w,h} - T_{w,k}$
Regenerator	1.94	0.0061	0.055	$T_h - T_k$
Displacer	0.684	0.0069	0.151	$T_{e,mean} - T_{c,mean}$

Conduction loss along the regenerator housing is the heat transfer through of two annular AISI 1020 steel walls that enclose the regenerator. The external wall has dimensions: 146.5 mm OD, 135.5 mm ID and 55 mm long. The internal wall has dimensions: 103 mm OD, 95.6 mm ID and 55 mm long. The regenerator housing separates the heater and cooler walls. As a result, the temperature difference across the regenerator is the difference between the heater and cooler wall temperatures ( $T_{w,h} - T_{w,k}$ ).

The working gas and regenerator matrix both conduct heat in the regenerator. The annular regenerator has dimensions: 135.5 mm OD, 103 mm ID and 55 mm long. The regenerator is comprised of 90 % working fluid and 10 % AISI 316 stainless steel by volume. The volume-weighted-average thermal conductivity is 1.94 W/m K [79]. The temperature difference between the heater and cooler working gas ( $T_h - T_k$ ) is used for regenerator conduction calculations.

Like the regenerator, the displacer body and working gas in the displacer conduct heat along the displacer. The overall dimensions of the displacer body are 94 mm OD and 151 mm long. It is constructed with 0.8 mm thick, AISI 316 stainless steel walls and the hollow internals contain working gas. The cross-section-area-weighted-average thermal conductivity of the displacer is 0.684 W/m K [79]. The temperature difference across the displacer is the difference between the mean expansion and compression space temperatures ( $T_{e,mean} - T_{c,mean}$ ).

### 3.4.4 Gas Spring Hysteresis

Speer [79] created an empirical model of gas spring hysteresis to use in this 2<sup>nd</sup> order model. Equation 3-22 is a polynomial surface fit to experimental data of the indicated gas spring hysteresis power ( $\dot{W}_{GSH}$ ) with variables of mean pressure ( $p_{mean}$  in kPa) and engine frequency ( $f$  in Hz). The R-squared value of this fit is 0.999 with a range of 200-1000 kPa and 0-2.5 Hz. The gas spring hysteresis loss is deducted from the shaft power of the engine.

$$\begin{aligned} \dot{W}_{GSH} = & 2.29 \times 10^{-13} \cdot p_{mean}^2 + 0.0953 \cdot f^2 + 5.67 \times 10^{-7} \cdot p_{mean} \cdot f \dots \\ & \dots + 2.50 \times 10^{-7} \cdot p_{mean} - 0.204 \cdot f + 0.163 \end{aligned} \quad 3-22$$

### 3.4.5 Mechanical Losses

The model uses Senft's [32] Fundamental Efficiency Theorem (Equation 1-39 from chapter one) to calculate mechanical losses. Forced work is calculated with the model pressure-volume function and the pressure-volume function of an ideal adiabatic buffer space [79]. The mechanism effectiveness is 0.7, which is the lower bound of values used by Senft [27]. The mechanical losses are deducted from the output power of the modelled engine.

### 3.4.6 Decoupled Loss Inclusion

The decoupled power losses are subtracted from the reference cycle results after the mass and temperature corrections are complete. Equation 3-23 calculates the shaft power ( $\dot{W}_S$ ) with the engine frequency ( $f$ ), reference cycle indicated work ( $W_I$ ), forced work ( $W_F$ ), gas spring hysteresis loss ( $\dot{W}_{GSH}$ ), heater flow friction ( $\dot{W}_{\Delta p,h}$ ), regenerator flow friction ( $\dot{W}_{\Delta p,r}$ ) and cooler flow friction ( $\dot{W}_{\Delta p,k}$ ).



$$\dot{W}_S = f \cdot \left( E \cdot W_I - \left( \frac{1}{E} - E \right) \cdot W_F \right) - \dot{W}_{GSH} - \dot{W}_{\Delta p, h} - \dot{W}_{\Delta p, r} - \dot{W}_{\Delta p, k} \quad 3-23$$

The heater must absorb extra heat to overcome the thermal losses. Equation 3-24 solves for the heat absorption rate from the heater ( $\dot{Q}_h$ ). The heat transfer rate calculated by the Simple Analysis ( $\dot{Q}_{h, simple}$ ) is supplemented by the appendix gap losses ( $\dot{Q}_{shuttle}$  and  $\dot{Q}_{pump}$ ) and conduction loss ( $\dot{Q}_{cond}$ ). The flow friction in the heater and half of the flow friction in the regenerator are converted to heat that reduces the heat absorption.

$$\dot{Q}_h = \dot{Q}_{h, simple} + \dot{Q}_{shuttle} + \dot{Q}_{pump} + \dot{Q}_{cond} - \dot{W}_{\Delta p, h} - \frac{\dot{W}_{\Delta p, r}}{2} \quad 3-24$$

The cooler must reject extra heat to overcome thermal shortcuts and flow friction. The heat rejection rate in the cooler is calculated with Equation 3-25. It includes the heat transfer rate in the cooler from the Simple Analysis ( $\dot{Q}_{k, simple}$ ), the appendix gap losses and conduction loss. The heat generated by cooler flow friction and half of the heat generated by regenerator flow friction increase the necessary heat rejection.

$$\dot{Q}_k = -\dot{Q}_{k, simple} + \dot{Q}_{shuttle} + \dot{Q}_{pump} + \dot{Q}_{cond} + \dot{W}_{\Delta p, k} + \frac{\dot{W}_{\Delta p, r}}{2} \quad 3-25$$

## 3.5 Summary

---

A 2<sup>nd</sup> order thermodynamic model was modified to estimate the experimental performance of the low-temperature ST05G-CNC. Speer [79] compiled the model with the exception of the temperature correction. The reference cycle was generated from the adiabatic model with Urieli and Berchowitz' [29] Simple Analysis for imperfect heat exchange. Mass of working gas and the heat exchanger wall temperatures were simultaneously corrected for the model to reflect the experimental operating condition. The model included decoupled losses for heat exchanger flow friction, appendix gap losses, conduction loss, gas spring hysteresis, and mechanical losses.

A temperature correction was added to the model to estimate engine performance with identical operating conditions to corresponding experiments. The MCM did not estimate engine performance with the same operating conditions as the experiments. A temperature correction adjusted the heater and cooler wall temperatures so the modelled expansion and compression space temperatures matched the measured values. The M&TCM more correctly replicated the experimental operating conditions compared to the MCM but it increased the difference between modelled and experimental indicated work.

---

## 4 THE INFLUENCE OF FLYWHEEL SIZE ON STIRLING ENGINE PERFORMANCE

---

Many thermodynamic models of kinematic Stirling engines assume that the angular velocity of the crankshaft is constant. In reality, the angular velocity fluctuates at a cyclic steady-state and the magnitude of the fluctuations are dependent on the flywheel polar moment of inertia [33]. This chapter presents an experimental analysis of the low-temperature ST05G with several different flywheel configurations to determine the effects of flywheel polar moment of inertia on a Stirling engine. It is divided into three parts. The first part studies the transient engine frequency from engine start with different flywheel sizes. The second part evaluates the influence of flywheel size on the steady-state performance of the engine. The third part describes and validates a general method to calculate the appropriate flywheel polar moment of inertia. The chapter ends with a summary of the findings of all three parts.

## 4.1 Flywheel Size Influence on Transient Engine Frequency

Some studies with dynamic models described contradicting changes in the transient engine frequency when simulating Stirling engines with different flywheel sizes [35,53,55,82]. Transient experiments were performed on the low-temperature ST05G with four flywheel configurations to measure changes in the transient engine frequency with different flywheel sizes. This section begins with a brief description of the methods specific to the transient experiments. Then it presents the influence of flywheel polar moment of inertia on the transient engine frequency, steady-state engine frequency, settling time, and overshoot frequency.

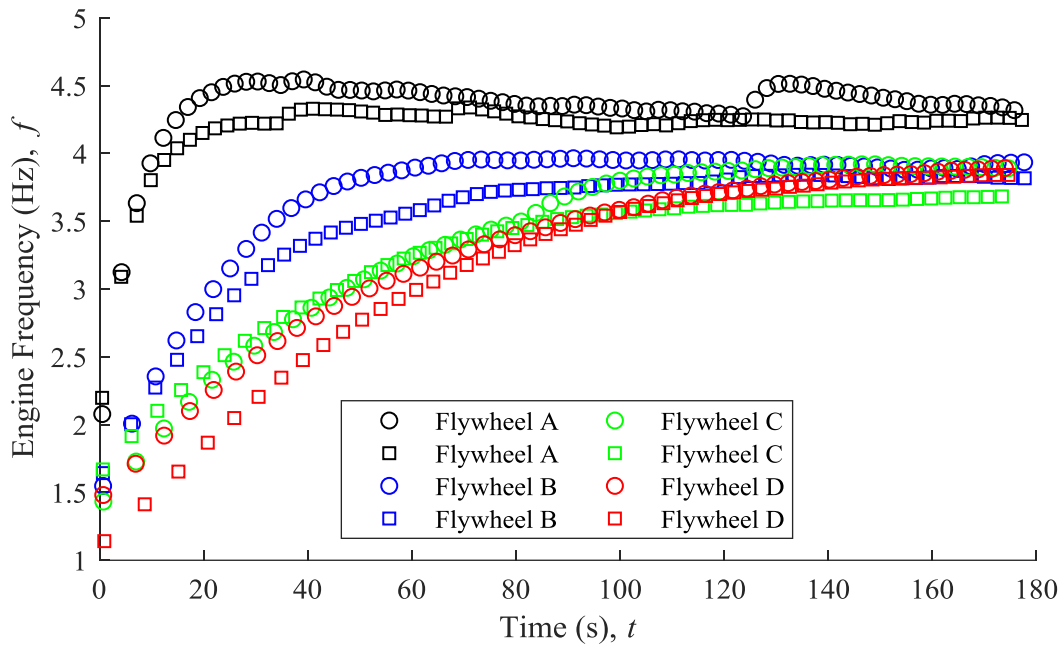
Four flywheel configurations, described in section 2.1.9, were used to evaluate the transient engine frequency of the low-temperature ST05G. Data was collected as the engine transitioned from start to free-running steady-state, as section 2.5.2 explains. Table 4-1 defines the constant and manipulated parameters of these experiments. The experiments were performed at two charge pressures and without a torque load (free-running). Two data sets with arbitrary starting pull velocities were collected at each condition studied to provide a replicate for every experiment.

Table 4-1: List of the constant and manipulated parameters of the transient experiments.

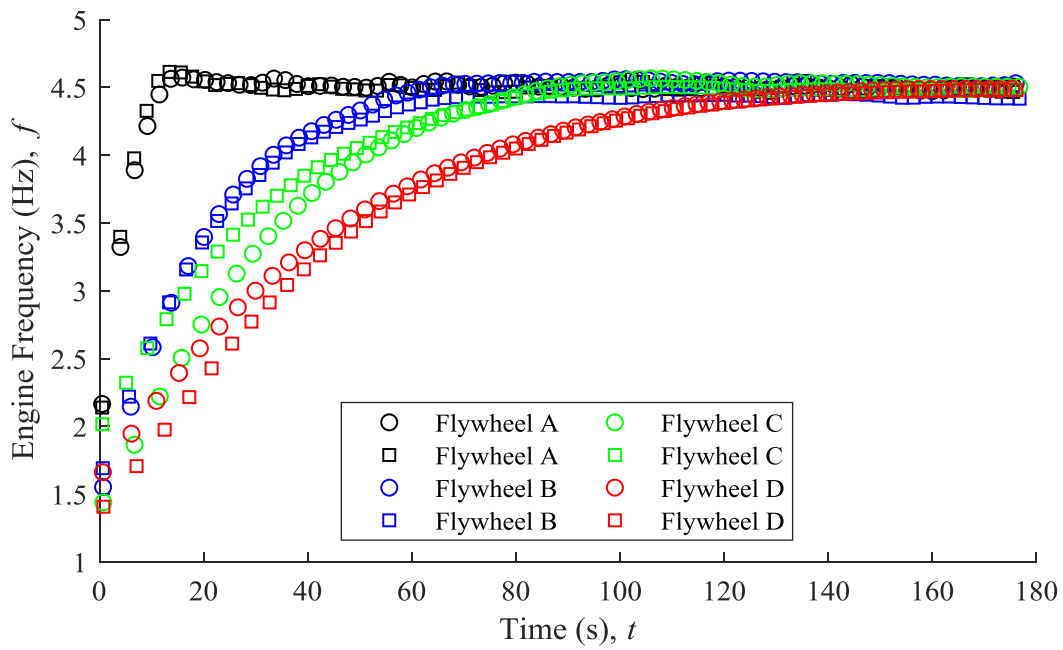
Parameter	Value(s)	Constant or Manipulated
Thermal Source Temperature ( $^{\circ}\text{C}$ ), $T_H$	300	Constant
Thermal Sink Temperature ( $^{\circ}\text{C}$ ), $T_C$	21	Constant
Flywheel Moment of Inertia ( $\text{kg m}^2$ ), $I_{fly}$	(A) 0.0641, (B) 0.2539, (C) 0.4292, and (D) 0.5995	Manipulated
Charge Pressure (kPa), $p_{charge}$	517 and 621	Manipulated
Torque Load (N m), $\tau_E$	No load	Constant

### 4.1.1 Transient Engine Frequency

A transient change in engine frequency was observed. Figure 4-1 illustrates the influence of flywheel polar moment of inertia on the evolution of engine frequency from start to steady-state. Transient experiments with a charge pressure of 517 kPa are in Figure 4-1 (a) and experiments with a charge pressure of 621 kPa are in Figure 4-1 (b). Two experiments were conducted for each flywheel configuration at both charge pressures. The markers presented in Figure 4-1 are the mean frequency from every tenth rotation. The uncertainty of the mean frequency is within the markers and therefore excluded from the plots. Engine frequency stabilizes when the engine has reached steady-state. The following sub-sections break down the influence of flywheel polar moment of inertia on the transient engine frequency into steady-state frequency, settling time, and overshoot. These comments are all in reference to Figure 4-1.



(a)



(b)

Figure 4-1: Plots of the free, transient engine frequency from start for all flywheels with (a) 517 kPa and (b) 621 kPa charge pressure.

### 4.1.2 Steady-State Engine Frequency

The steady-state engine frequency was examined to check if flywheel polar moment of inertia affected the steady-state frequency of the engine. The steady-state engine frequency is the mean frequency of the last ten rotations of the transient data set. Table 4-2 presents the steady-state engine frequency for all flywheel configurations and both charge pressures. When charged to 517 kPa, flywheels B, C, and D converged on steady-state frequencies in the range of 3.68 Hz to 3.93 Hz, whereas flywheel A approached a steady-state frequencies of 4.26 Hz and 4.32 Hz (Figure 4-1 a). All flywheel configurations converged on steady-state frequencies within a range of 4.42 Hz to 4.53 Hz when charged to 621 kPa (Figure 4-1 b).

Table 4-2: The steady-state engine frequency of the transient experiments for all flywheels at both charge pressures.

Flywheel	Flywheel Polar Moment of Inertia (kg m <sup>2</sup> ), $I_{fly}$	Steady-State Frequency (Hz), $f_{steady-state}$				Maximum Uncertainty (Hz)
		517 kPa		621 kPa		
A	0.0641	4.32	4.26	4.50	4.47	± 0.01
B	0.2539	3.93	3.82	4.53	4.42	
C	0.4292	3.89	3.68	4.50	4.48	
D	0.5995	3.89	3.84	4.49	4.47	

Multiple dynamic model studies concluded that flywheel polar moment of inertia did not influence steady-state engine frequency [53,55,82]. The results here agree that all flywheel sizes converge on the same steady-state engine frequency, with one exception. The higher steady-state frequency for flywheel A at 517 kPa charge pressure was examined further. Table 4-3 shows the mean pressure and gas temperature difference (mean expansion space temperature minus mean compression space temperature,  $T_{e,mean} - T_{c,mean}$ ) of the transient experiments charged to 517 kPa. The experiments with flywheel A at 517 kPa charge pressure had similar mean pressures and gas

temperature differences as the other experiments. Therefore, the higher steady-state frequency in this case is not the result of the engine operating at a different condition.

Table 4-3: The steady-state engine frequency, gas temperature difference, and mean pressure of the transient experiments for all flywheels at the 517 kPa charge pressure.

Parameter	Flywheel								Maximum Uncertainty
	A		B		C		D		
Steady-State Frequency (Hz), $f_{steady-state}$	4.32	4.26	3.93	3.82	3.89	3.68	3.89	3.84	$\pm 0.01$
Gas Temperature Difference ( $^{\circ}\text{C}$ ), $T_{e,mean} - T_{c,mean}$	217.7	217.4	221.4	220.7	221.5	221.3	222.1	221.4	$\pm 7.0$
Mean Pressure (kPa), $p_{E,mean}$	527.4	526.7	524.6	523.1	525.1	523.4	520.5	521.0	$\pm 4.54$

Higher engine frequency with flywheel configuration A at 517 kPa could result from inconsistent engine performance. This can be seen by the rapid and unpredictable increases in engine frequency visible in Figure 4-1 (a) earlier in this section. However, both experiments with flywheel configuration A at 517 kPa converged on similar steady-state engine frequencies and experiments with the other flywheel configurations did not show evidence of engine frequency increasing to the steady-state frequency of flywheel configuration A. This does not prove that inconsistent engine performance caused higher steady-state engine frequency with flywheel configuration A at 517 kPa. Consequently, more experiments would need to be performed to determine if inconsistent engine performance caused the exception.

Neither the operating condition nor the inconsistent engine performance provide a sound explanation for the higher steady-state engine frequency with flywheel configuration A charged to 517 kPa. Therefore, smaller flywheels may result in higher steady-state, free-running engine



frequencies. More experiments, some with smaller flywheels, should be performed to study the influence of flywheel polar moment of inertia on steady-state engine frequency.

### 4.1.3 Settling Time

Increasing the flywheel polar moment of inertia is expected to increase the time required for the engine to reach steady-state. Figure 4-1 (a) and (b) illustrate that as flywheel polar moment of inertia increases, the time required to approach steady-state frequency increases. The settling time ( $t_{settle}$ ) is the time for the frequency to meet two conditions. The first condition is that the engine frequency must be within the uncertainty of the steady-state frequency. The second condition is the engine frequency in consecutive rotations has not changed by more than 2 % of the free-running engine frequency. Table 4-4 presents the frequency settling times of the data sets shown in Figure 4-1. The settling time is not identical for the repeat experiments in part due to the arbitrary starting pull velocities. Regardless, the settling time increases as flywheel polar moment of inertia increases for both charge pressures. Therefore, the time required for the engine to achieve steady-state increases with flywheel polar moment of inertia, as expected.

Table 4-4: List of settling times from engine start for all flywheel configurations and both charge pressures.

Flywheel	Flywheel Polar Moment of Inertia (kg m <sup>2</sup> ), $I_{fly}$	Settling Time (s), $t_{settle}$			
		517 kPa		621 kPa	
A	0.0641	16.0	34.9	12.1	10.1
B	0.2539	65.2	120.6	66.5	63.3
C	0.4292	125.0	163.3	86.1	87.1
D	0.5995	169.6	165.3	149.2	153.2

#### 4.1.4 Frequency Overshoot

The frequency overshoot between engine start and steady-state was investigated. The overshoot frequency ( $f_{overshoot}$ ) is the difference between the maximum engine frequency ( $f_{max}$ ) and steady-state engine frequency ( $f_{steady-state}$ ) calculated by Equation 4-1. Frequency overshoot occurs because the heater gas is hotter and the cooler gas is colder at lower engine frequencies, and thermal change lags behind the frequency change until steady-state is achieved. Smaller flywheels should overshoot more because they can accelerate quicker, which exploits the thermal lag. Table 4-5 lists the overshoot frequencies from the datasets shown in Figure 4-1. The engine frequency of experiments with flywheel A have the largest overshoot. The overshoot quickly diminishes as flywheel size increases and is non-existent with flywheel configuration D. Yang et al. [55] used a dynamic model to show that the engine frequency can overshoot the steady-state frequency with smaller flywheels. The transient experiments agree with the work of Yang et al. [55] that the engine frequency can overshoot steady-state with smaller flywheels.

$$f_{overshoot} = f_{max} - f_{steady-state} \quad 4-1$$

Table 4-5: List of overshoot frequencies for all flywheel configurations and both charge pressures.

Flywheel	Flywheel Polar Moment of Inertia (kg m <sup>2</sup> )	Frequency Overshoot (Hz), $f_{overshoot}$				Maximum Uncertainty (Hz)
		517 kPa		621 kPa		
A	0.0641	0.22	0.09	0.08	0.15	± 0.03
B	0.2539	0.03	0.03	0.03	0.04	
C	0.4292	0.03	0.00	0.06	0.02	
D	0.5995	0.00	0.00	0.00	0.00	

#### 4.1.5 Transient Engine Frequency Summary

The low-temperature ST05G was studied in transition from start to steady-state with four flywheel configurations. The steady-state engine frequency, the settling time, and the overshoot frequency were studied. The steady-state engine frequency converged on the same value for all flywheel sizes except for flywheel configuration A at 517 kPa charge pressure. Ignoring the outlier, this matches the results found with dynamic models by Scollo et al. [82], Cheng and Yu [53], and Yang et al. [55]. The settling time increased with the flywheel polar moment of inertia, as shown in most dynamic models [35,53,55,82]. Finally, the frequency overshoot increased as flywheel polar moment of inertia decreased. This agrees with the dynamic model by Yang et al. [55]. The influence of flywheel polar moment of inertia on transient engine frequency of the low-temperature ST05G was shown to follow trends presented by some dynamic models.

## 4.2 Flywheel Size Influence on Steady-State Performance

---

This section determines if angular velocity fluctuations change the performance of the low-temperature ST05G. It starts with a description of the experiment methods specific to the steady-state experiments with different flywheel configurations. Next, the angular velocity fluctuations are quantified by the coefficient of speed fluctuation. Then the shaft power and indicator diagrams are compared to determine influence of angular velocity fluctuations on the engine performance and thermodynamic processes.

The experiments used to evaluate the influence of angular velocity fluctuations on engine performance were performed at steady-state. Table 4-6 lists the constant and manipulated parameters of these experiments. Four flywheel configurations were studied at two charge pressures. Ten torque loads were applied to collect samples at different engine frequencies. Steady-state was achieved five minutes after the engine load was changed. The following results are the entirety or a subset of the data collected with these methods.

Table 4-6: List of the constant and manipulated parameters of the steady-state experiments.

Parameter	Value(s)	Constant or Manipulated
Thermal Source Temperature ( $^{\circ}\text{C}$ ), $T_H$	300	Constant
Thermal Sink Temperature ( $^{\circ}\text{C}$ ), $T_C$	21	Constant
Flywheel Moment of Inertia ( $\text{kg m}^2$ ), $I_{fly}$	(A) 0.0641, (B) 0.2539, (C) 0.4292, and (D) 0.5995	Manipulated
Charge Pressure ( $\text{kPa}$ ), $p_{charge}$	517 and 621	Manipulated
Torque Load ( $\text{N m}$ ), $\tau_E$	Ten unique loads	Manipulated

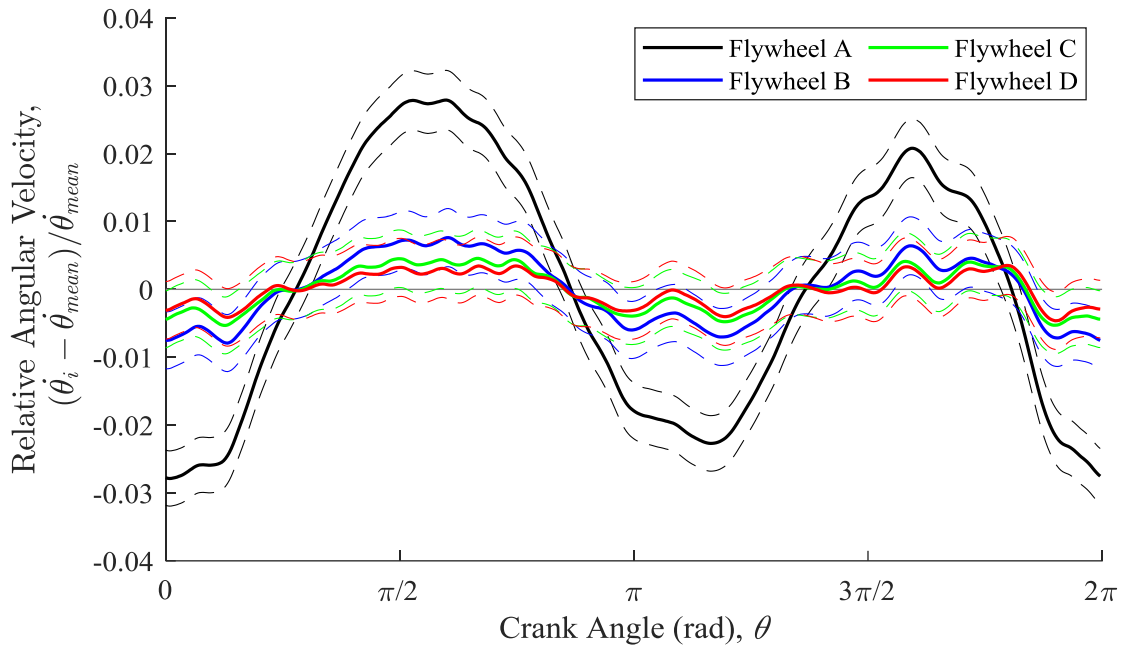
### 4.2.1 Angular Velocity Fluctuations

To compare angular velocity across experiments, the comparison metric must be independent of the mean angular velocity. The relative angular velocity ( $\dot{\theta}^*$ ) accomplishes this. It is the

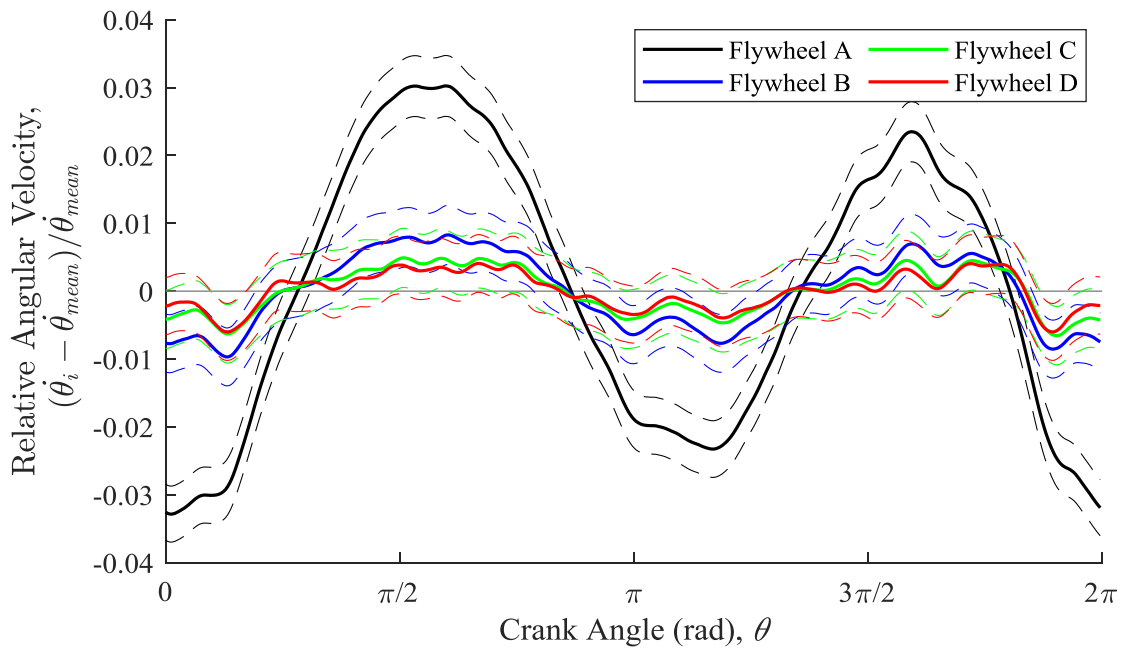
instantaneous angular velocity ( $\dot{\theta}_i$ ) minus the mean angular velocity ( $\dot{\theta}_{mean}$ ) and all divided by the mean angular velocity, as defined in Equation 4-2. If the relative angular velocity is equal to zero, the instantaneous angular velocity is equal to the mean angular velocity. The relative angular velocity is greater than zero when the instantaneous angular velocity is greater than the mean angular velocity. Similarly, the relative angular velocity is negative when the instantaneous angular velocity is less than the mean angular velocity.

$$\dot{\theta}^* = \frac{\dot{\theta}_i - \dot{\theta}_{mean}}{\dot{\theta}_{mean}} \quad 4-2$$

The magnitude of the angular velocity fluctuations were studied. Figure 4-2 presents the relative angular velocity of four flywheel configurations operating near 2.9 Hz at (a) 517 kPa and (b) 621 kPa charge pressures. The solid lines show the relative angular velocity and the dashed lines are the uncertainty bounds of the relative angular velocity. Flywheel configuration A experienced the largest angular velocity fluctuations. The angular velocity fluctuations experienced by flywheel configuration B are the second largest but its relative angular velocity is within the uncertainty of the relative angular velocity of flywheel configurations C and D through most of the cycle. Flywheels C and D configurations have similar relative angular velocity throughout the cycle. The smallest flywheel has the largest angular velocity fluctuations and the largest flywheels have smaller angular velocity fluctuations, as expected.



(a)



(b)

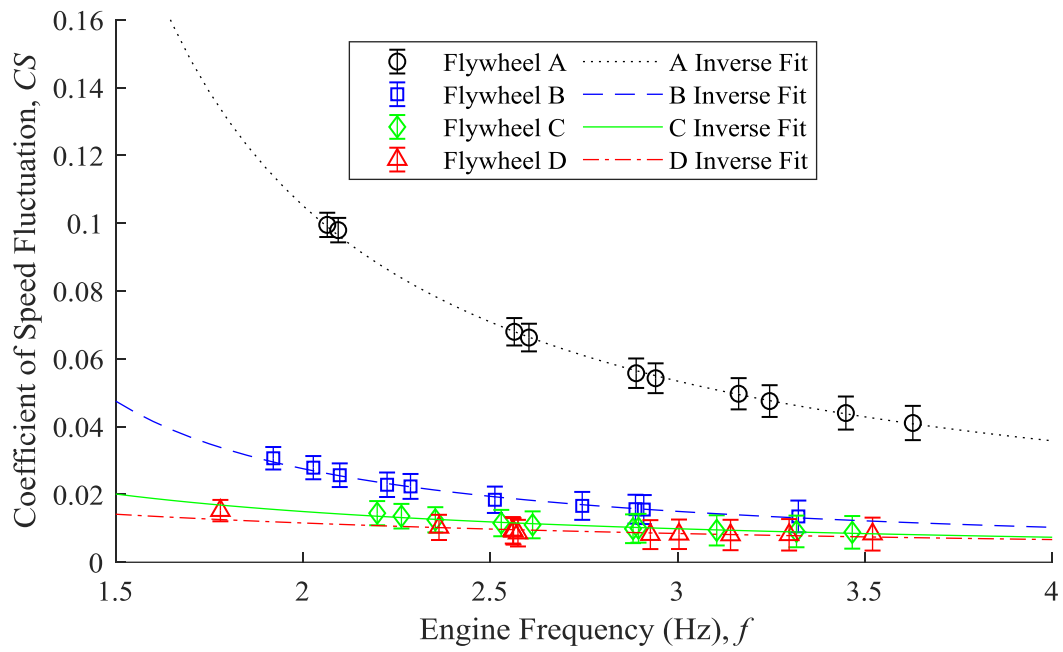
Figure 4-2: Plots of the phase-averaged relative angular velocity with crank angle for four flywheel configurations at (a) 517 kPa and (b) 621 kPa charge pressure.

Figure 4-2 shows that the angular velocity has two primary oscillations per cycle with all flywheel sizes. Angular velocity local minimums are at crank angles near 0 and  $\pi$ , and local maximums are at crank angles near  $\pi/2$  and  $3\pi/2$ . This indicates that the flywheel receives energy at crank angles from about 0 to  $\pi/2$  and from about  $\pi$  to  $3\pi/2$ . This energy transfer is similar to what occurs in a kinematic heat engine with a buffer pressure near the mean engine pressure as described by Senft [27]. Efficacious expansion work and efficacious compression work transfer energy to the flywheel. Forced expansion work and forced compression work remove energy from the flywheel. This suggests that flywheel size could be calculated from the principles of work transfer in Senft's [27,32] Fundamental Efficiency Theorem (FET). Section 4.3 explores this.

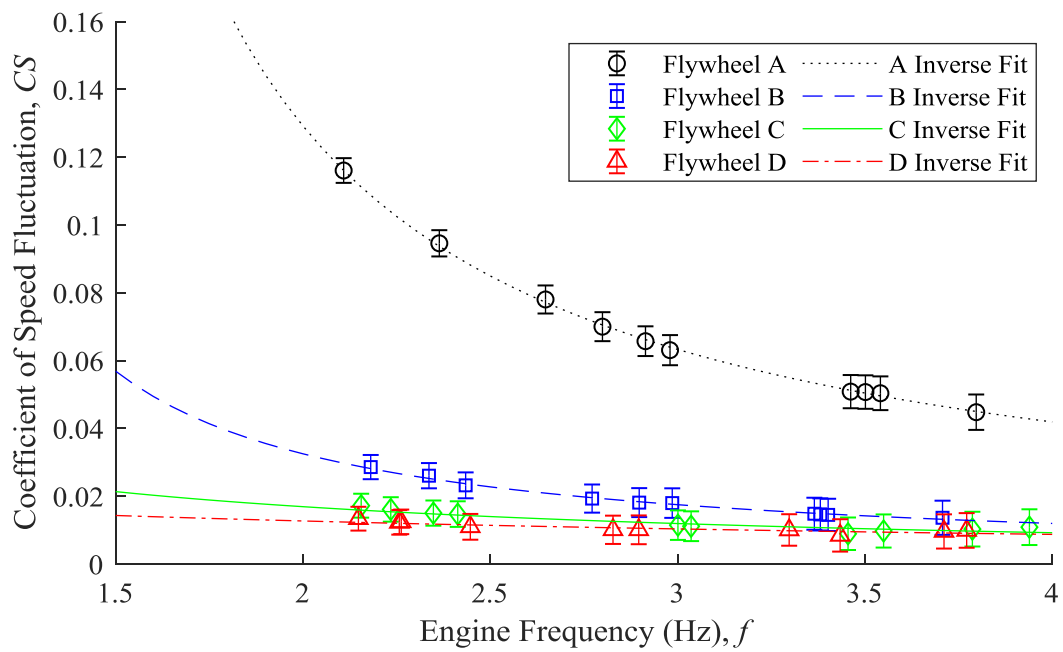
#### 4.2.2 Coefficient of Speed Fluctuation

The coefficient of speed fluctuation ( $CS$ ) is the dimensionless measure of cyclic angular velocity fluctuations. It is calculated with Equation 4-3 from the cycle maximum angular velocity ( $\dot{\theta}_{max}$ ), cycle minimum angular velocity ( $\dot{\theta}_{min}$ ), and cycle mean angular velocity. Figure 4-3 presents plots of the coefficient of speed fluctuation for four flywheel configurations through a range of engine frequencies at (a) 517 kPa and (b) 621 kPa charge pressures. The largest coefficient of speed fluctuation is 0.116 from flywheel configuration A at 617 kPa charge pressure and the lowest engine frequency. This is acceptable for Stirling engines (less than 0.16 from Ipci and Karabulut [84]). Therefore, all flywheel configurations are acceptable for Stirling engine applications.

$$CS = \frac{\dot{\theta}_{max} - \dot{\theta}_{min}}{\dot{\theta}_{mean}} \quad 4-3$$



(a)



(b)

Figure 4-3: Plots of the coefficient of speed fluctuation for four flywheel configurations at (a) 517 kPa and (b) 621 kPa charge pressure with fit curves.



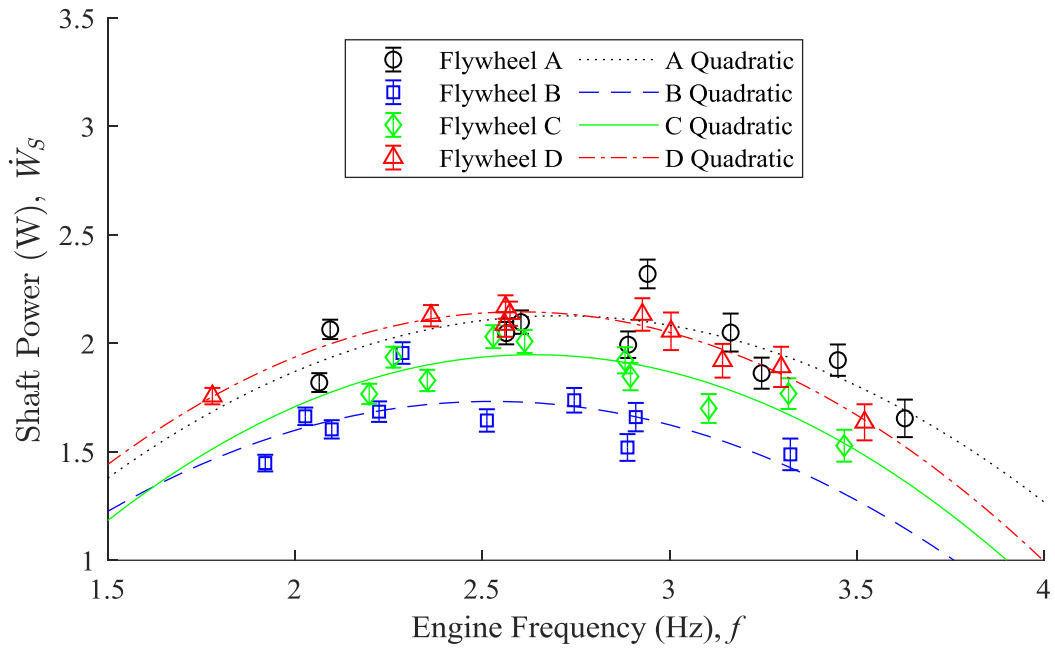
The trend lines in Figure 4-3 show how the coefficient of speed fluctuation changes with engine frequency. The coefficient of speed fluctuation is inversely proportional to engine frequency. This is expected from its definition in Equation 4-3 because mean angular velocity is directly proportional to engine frequency. The coefficient of speed fluctuation has a greater rate of change with frequency for smaller flywheels (configurations A and B). Compared to the larger flywheels (configurations C and D) where the coefficient of speed fluctuation is nearly independent of frequency. As expected, the coefficient of speed fluctuation decreases with increasing engine frequency.

Figure 4-3 also shows the change in coefficient of speed fluctuation with changing flywheel polar moment of inertia. Flywheel configuration A is the smallest flywheel and it has the largest coefficient of speed fluctuation at all engine frequencies. Flywheel configuration B, the second smallest flywheel, has the second largest coefficient of speed fluctuation below 2.5 Hz engine frequency. Flywheel configurations C and D have similar coefficients of speed fluctuation at all engine frequencies. This agrees with flywheel fundamentals where larger flywheels have smaller angular velocity fluctuations [33]. The results here show that small flywheels have the largest coefficient of speed fluctuation and increasing flywheel polar moment of inertia has diminishing returns.

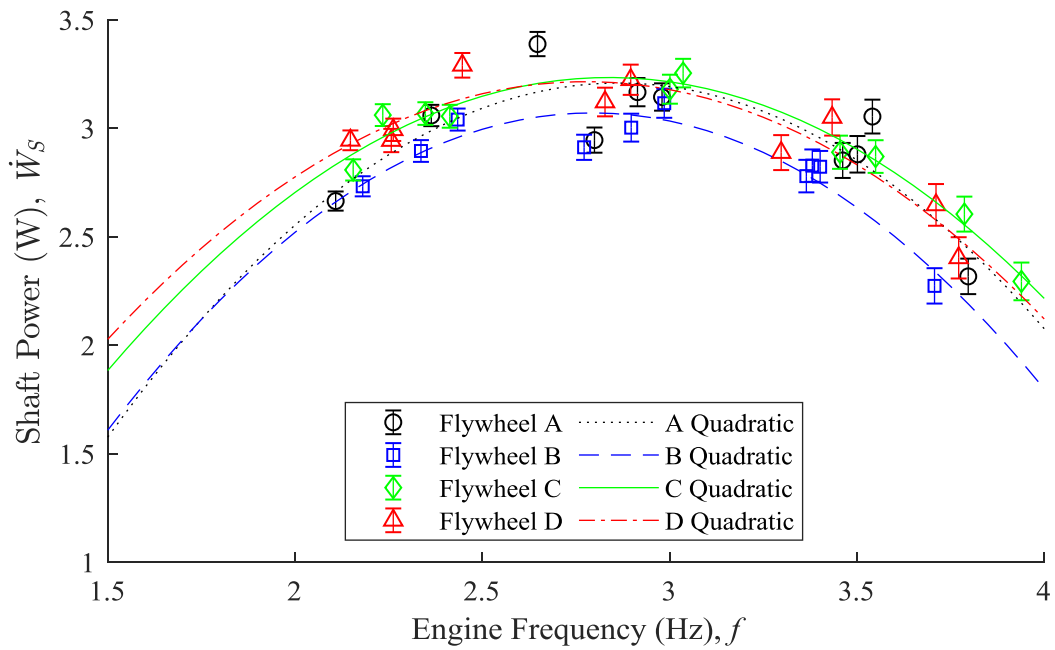
### 4.2.3 Shaft Power

Steady-state experiments were performed to determine if the shaft power curves depended on flywheel polar moment of inertia. Figure 4-4 (a) and (b) display the quadratic shaft power curves for all flywheel configurations at 517 kPa and 621 kPa charge pressures, respectively. At 517 kPa charge pressure, flywheel configurations A and D have similar shaft power curves with the highest maximum shaft powers (Figure 4-4 a). Similarly, at 621 kPa charge pressure, flywheel configurations A, C, and D have similar shaft power curves with the highest maximum shaft power (Figure 4-4 b). In both cases, flywheel configuration B has the lowest shaft power curve. The shaft power curves do not show an optimum flywheel polar moment of inertia for maximum shaft power.

A dynamic model by Cheng and Yu [35] showed that there was an optimal flywheels size for shaft power. However, Yang et al. [55] found that flywheel size did not influence shaft power. These results show that shaft power may depend on flywheel polar moment of inertia, but if there is an optimum flywheel size for shaft power, it is not in the range studied here. Therefore, more flywheel configurations would have to be tested to determine if there is an optimal flywheel polar moment of inertia.



(a)



(b)

Figure 4-4: Experimental shaft power for four flywheel configurations at (a) 517 kPa and (b) 621 kPa charge pressure with fit curves.

#### 4.2.4 Indicator Diagrams

The influence of angular velocity fluctuations on the indicator diagram shape was investigated. Dimensionless indicator diagrams allow for the comparison of experiments with slightly different mean pressures. They illustrate the function of dimensionless engine pressure with dimensionless engine volume. The dimensionless engine pressure ( $p_E^*$ ), defined by Equation 4-4, is the phase-averaged engine pressure ( $p_E$ ) divided by the mean engine pressure ( $p_{E,mean}$ ). The dimensionless engine volume ( $V_E^*$ ) is the instantaneous engine volume ( $V_E$ ) minus the minimum engine volume ( $V_{E,min}$ ) and all divided by swept volume ( $V_{sw}$ ), as shown in Equation 4-5.

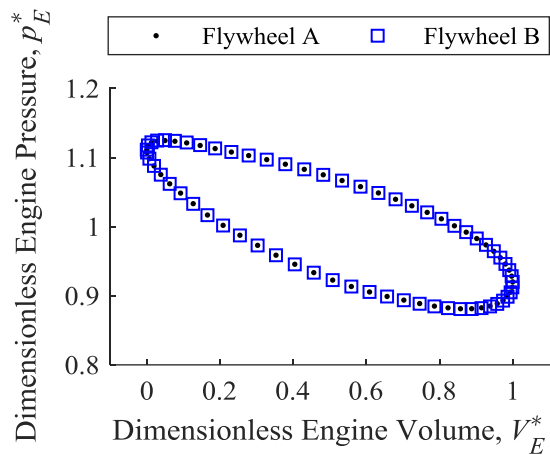
$$p_E^* = \frac{p_E}{p_{E,mean}} \quad 4-4$$

$$V_E^* = \frac{V_E - V_{E,min}}{V_{sw}} \quad 4-5$$

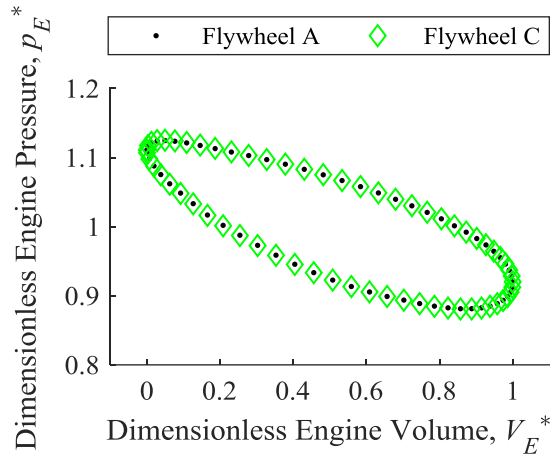
If angular velocity fluctuations change the thermodynamics in the engine, it would be visible in the indicator diagrams. Figure 4-5 presents the dimensionless indicator diagrams for the flywheel configurations and charge pressures defined in Table 4-7. The samples are from the phase-averaged data at every 8<sup>th</sup> rotary encoder increment. The uncertainty of the pressure and volume are near the scale of the markers. The dots of the flywheel A dimensionless indicator diagrams are near the center of the markers for the dimensionless indicator diagrams of other flywheel configurations. This indicates that the dimensionless indicator diagrams of all flywheel configuration are nearly identical at engine frequencies near 2.9 Hz. Therefore, angular velocity fluctuations less 6 % of the mean angular velocity do not influence the indicator diagram. Smaller flywheels with larger angular velocity fluctuations may need to be investigated to observe a change in the indicator diagram shape.

Table 4-7: List of parameters for the dimensionless indicator diagrams presented in Figure 4-5.

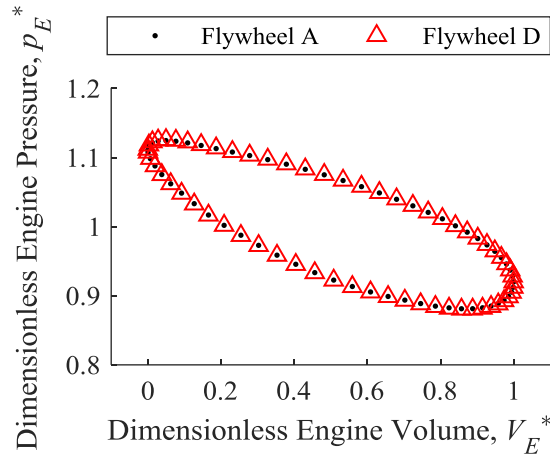
Figure Panel	Charge Pressure (kPa)	Flywheel Configurations	Engine Frequency (Hz), $f$
(a)	517	A and B	2.88 to 3.00
(b)	517	A and C	
(c)	517	A and D	
(d)	621	A and B	
(e)	621	A and C	
(f)	621	A and D	



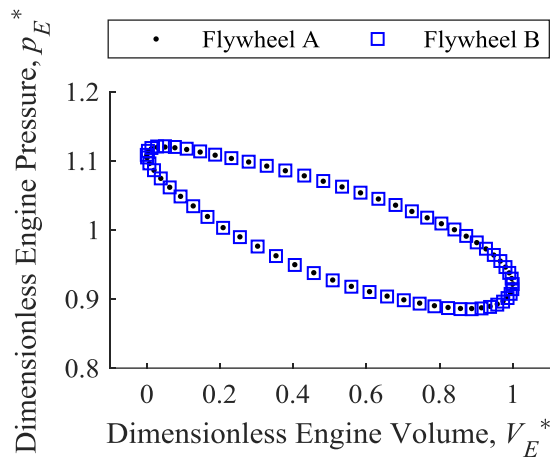
(a)



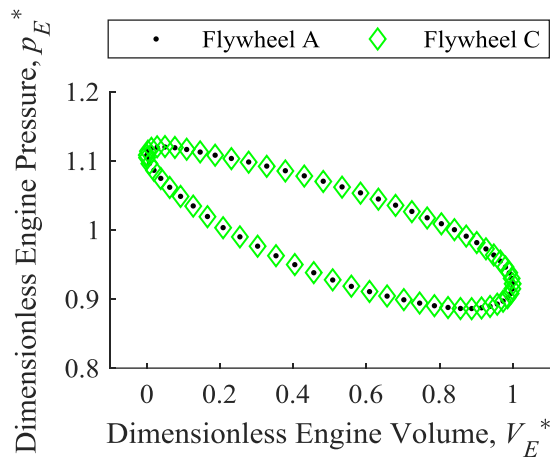
(b)



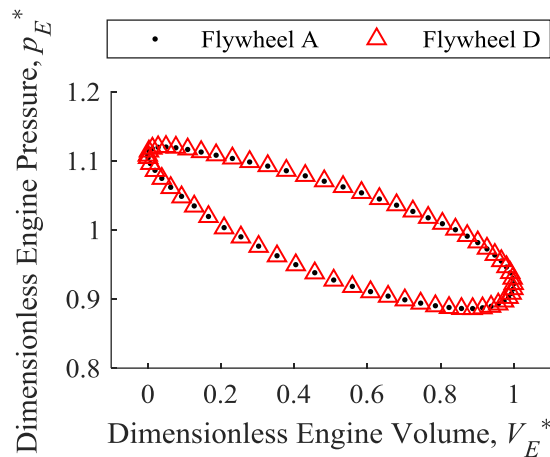
(c)



(d)



(e)



(f)

Figure 4-5: Dimensionless indicator diagrams for flywheel configurations and charge pressures defined in Table 4-7.

#### 4.2.5 Steady-State Performance Summary

Steady-state performance of the low-temperature ST05G was studied with four flywheel configurations. The relative angular velocity and coefficient of speed fluctuation demonstrated how angular velocity fluctuations change with flywheel polar moment of inertia. The shaft power and dimensionless indicator diagrams were checked to determine if engine performance changed with flywheel polar moment of inertia.

The angular velocity oscillates twice per cycle for all flywheel configurations. Therefore, the flywheel receives energy and provides energy twice per cycle. This is similar to the energy transfer described in FET by Senft [27,32] with a buffer pressure near the mean engine pressure. This supports that FET can be used as a general method to calculate flywheel size.

One goal of the steady-state study was to evaluate how flywheel polar moment of inertia changed the angular velocity fluctuations of the engine. The phase-averaged relative angular velocity and the coefficient of speed fluctuation were studied. Increasing flywheel polar moment of inertia decreased the magnitude of the angular velocity fluctuations and reduced the coefficient of speed fluctuation. The influence of flywheel size on the coefficient of speed fluctuation diminished as flywheel size increased. Additionally, the coefficient of speed fluctuation was more sensitive to engine frequency with smaller flywheels. These conclusions match the expectations set by flywheel theory [33].

The shaft power and indicator diagrams were compared across flywheel configurations. The shaft power was similar with the smallest and largest flywheel configurations. The intermediate flywheel configurations produced at most the same shaft power as the extreme flywheel configurations. The dimensionless indicator diagrams were identical for all flywheel sizes studied. Engine performance was not significantly influenced by flywheel polar moment of inertia with the

flywheel configurations studied. All four flywheel configurations had acceptable coefficient of speed fluctuation (less than 0.16). Therefore, smaller flywheels with larger angular velocity fluctuations may need to be studied to determine the influence of flywheel polar moment of inertia on engine performance.



## 4.3 Flywheel Size from the Fundamental Efficiency Theorem

---

A general method to calculate flywheel polar moment of inertia is investigated. The previous section showed that the energy stored in the flywheel of the low-temperature ST05G oscillated twice per cycle. This is similar to the energy transfer with the flywheel described in Senft's [27,32] Fundamental Efficiency Theorem (FET). The sub-sections below develop a method to calculate flywheel polar moment of inertia from FET, then validate it.

### 4.3.1 FET Method Description

Several parameters are required to estimate the size of a flywheel. Equation 4-6 calculates the machine polar moment of inertia ( $I_{fly} + I_{other}$ ) from the parameters: maximum kinetic energy change ( $\Delta KE_{max}$ ), mean angular velocity ( $\dot{\theta}_{mean}$ ), and the coefficient of speed fluctuation ( $CS$ ). In the early stages of Stirling engine design, mean angular velocity is estimated from similar engines and designer intuition. The coefficient of speed fluctuation is selected for the application of the machine. The maximum kinetic energy change must be estimated from thermodynamic and mechanical modelling.

$$I_{fly} + I_{other} = \frac{\Delta KE_{max}}{\dot{\theta}_{mean}^2 \cdot CS} \quad 4-6$$

The piston of the low-temperature ST05G transfers work to the mechanism and receives work from the mechanism twice per cycle. The engine and buffer space indicator diagrams in Figure 4-6 illustrate this. Starting at piston minimum volume, the piston transfers efficacious expansion work ( $W_{Eff,exp}$ ) to the mechanism. Next, the piston receives forced expansion work ( $W_{F,exp}$ ) from the mechanism. Then, efficacious compression work ( $W_{Eff,comp}$ ) transfers to the mechanism. Finally, the piston receives forced compression work ( $W_{F,comp}$ ) to complete the cycle.

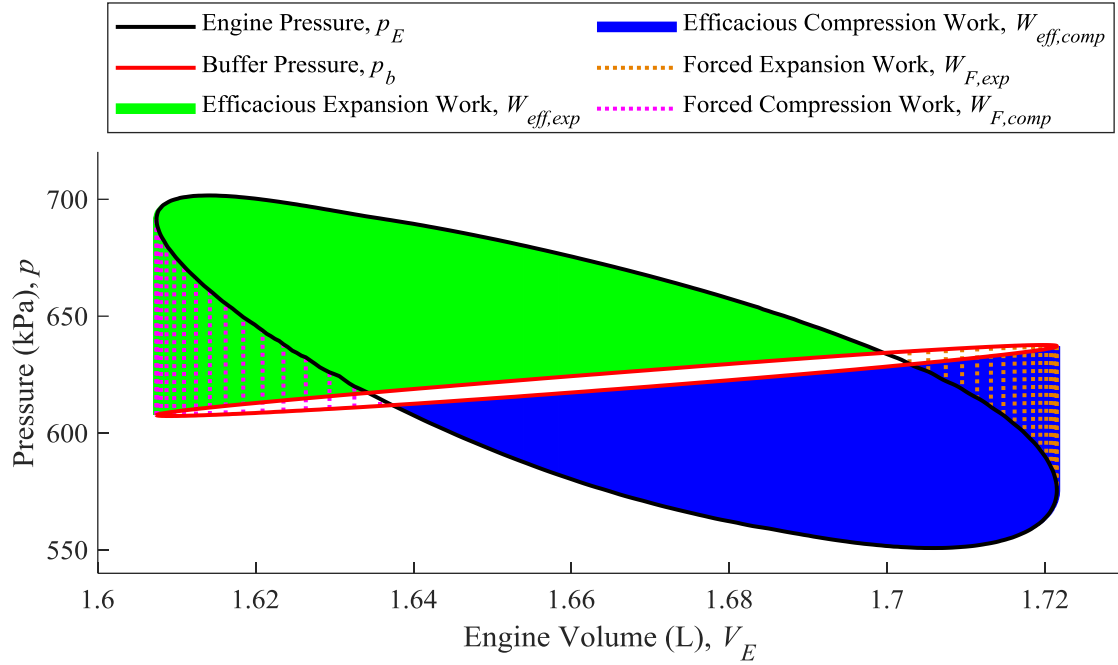


Figure 4-6: Arbitrary indicator diagram with efficacious and forced work areas.

FET provides a method to estimate the maximum kinetic energy change without specific knowledge of the mechanism. The mechanism asynchronously transmits the works defined in the previous paragraph between the flywheel and the piston with effectiveness  $E$ . Figure 4-7 presents the energy transfer to and from the flywheel after the losses to the mechanism. If shaft work ( $W_s$ ) is neglected, the maximum kinetic energy change of the flywheel is the largest of the efficacious or forced work components, as described by Equation 4-7.

$$\Delta KE_{max} = \max \left[ E \cdot W_{Eff,exp} \quad E \cdot W_{Eff,comp} \quad \frac{1}{E} \cdot W_{F,exp} \quad \frac{1}{E} \cdot W_{F,comp} \right] \quad 4-7$$

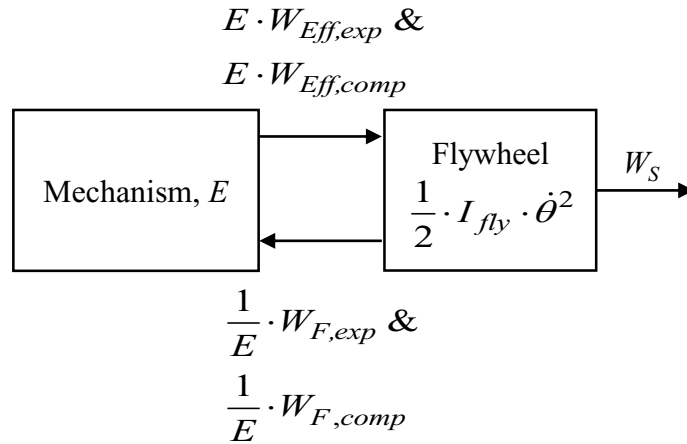


Figure 4-7: Energy transfer diagram of the flywheel in the Fundamental Efficiency Theorem.

The FET method to calculate flywheel size has two requirements for an accurate calculation. First, accurate thermodynamic models of the engine and buffer space must estimate the efficacious and forced works. Second, the mechanism effectiveness must accurately represent the mechanical losses present in the engine. Otherwise, the estimate of maximum kinetic energy change will not match reality.

### 4.3.2 FET Method Validation

The FET method to calculate flywheel polar moment of inertia is validated with two methods. The first method calculates the flywheel polar moment of inertia with the FET method using experimental data and compares it to the flywheel configuration used in the experiment. The second method determines the coefficient of speed fluctuations with the FET method for multiple experimental conditions. These are compared to the corresponding experimental coefficient of speed fluctuation. In both validation procedures, the FET method is calculated with experimental data to remove inaccuracies of a thermodynamic model from the validation. If the FET method proves valid, it may be useful to calculate the required flywheel polar moment of inertia in Stirling engines.

### 4.3.2.1 Flywheel Size Comparison

The first step of this validation is to calculate the flywheel polar moment of inertia with the FET method from experimental data. Table 4-8 lists the variables necessary to calculate flywheel size with the FET method. The coefficient of speed fluctuation and mean angular velocity were calculated from the phase-averaged experimental angular velocity. The efficacious and forced work components were determined from the phase-averaged, experimental engine pressure and buffer pressure. Finally, the experimental mechanism effectiveness was calculated from the experimental efficacious work, forced work, and shaft work in Equation 4-8. These were input into Equation 4-7 to calculate maximum kinetic energy change and Equation 4-6 to calculate flywheel polar moment of inertia.

$$E_{xp} = \frac{W_S + \sqrt{W_S^2 + 4 \cdot W_{Eff} \cdot W_F}}{2 \cdot W_{Eff}} \quad 4-8$$

Table 4-8: List of variables to calculate flywheel polar moment of inertia with the FET method.

Variable	Value
Coefficient of Speed Fluctuation, $CS$	0.018
Mean Angular Velocity (rad / s), $(\dot{\theta}_{mean})$	17.6
Efficacious Expansion Work (J), $W_{Eff,exp}$	5.02
Efficacious Compression Work (J), $W_{Eff,comp}$	4.49
Forced Expansion Work (J), $W_{F,exp}$	0.48
Forced Expansion Work (J), $W_{F,comp}$	1.01
Experimental Mechanism Effectiveness, $E_{xp}$	0.47
Maximum Kinetic Energy Change (J), $\Delta KE_{max}$	2.36

The general method to calculate flywheel polar moment of inertia presented by Scollo et al. [82] is included here for comparison. Section 1.7.2.1 describes the procedure to calculate flywheel polar moment of inertia with this method and Table 4-9 list the variables necessary for the calculation. The mass of working gas in the engine ( $m_E$ ) was estimated by the 2<sup>nd</sup> order model to match the mean engine pressure, as described in section 3.3.1. The thermal sink temperature ( $T_C$ ) is the water bath set point temperature. The maximum and minimum engine volume ( $V_{E,max}$  and  $V_{E,min}$ ) are from the constraints of the kinematic mechanism.

Table 4-9: List of variables to calculate flywheel polar moment of inertia with the method from Scollo et al [82].

Variable	Value
Mass of Working Gas in the Engine (g), $m_E$	7.9
Gas Constant of Air (J / kg K), $R$	287
Thermal Sink Temperature (°C)	21
Maximum Engine Volume (L), $V_{E,max}$	1.721
Minimum Engine Volume (L), $V_{E,min}$	1.607
Maximum Kinetic Energy Change (J), $\Delta KE_{max}$	6.49

Table 4-10 compares the actual flywheel polar moment of inertia to the flywheel polar moment of inertia calculated by the FET method and the method by Scollo et al. [82]. The FET method calculates a flywheel size 65 % larger than the flywheel used in the experiments. This is an improvement on the method from Scollo et al. [82], which over-estimates flywheel size by 352 % in this case. However, the FET method is only useful for an order of magnitude estimate of the flywheel polar moment of inertia.

Table 4-10: Comparison of the flywheel size calculation methods.

Flywheel Size Calculation Method	Flywheel Polar Moment of Inertia (kg m <sup>2</sup> ), $I_{fly}$	Relative Difference
Actual (Experimental)	0.254 (Configuration B)	-
FET Method	0.419	65 %
Scollo et al. [82] Method	1.149	352 %

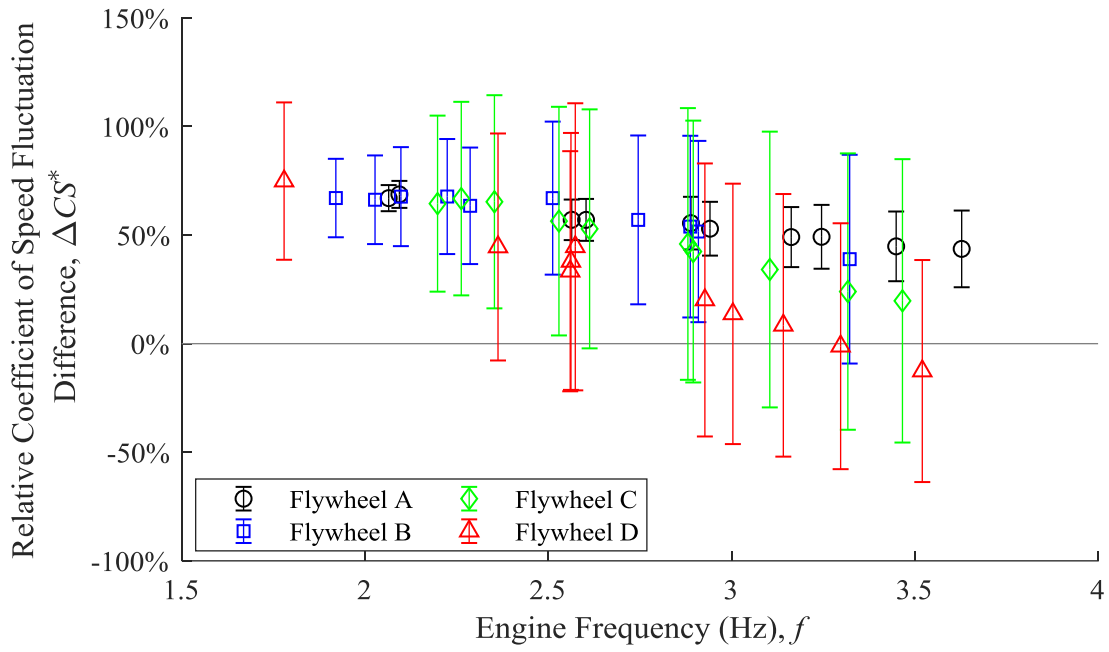
#### 4.3.2.2 Coefficient of Speed Fluctuation Comparison

This method compares the experimental and estimated coefficient of speed fluctuation of four flywheels. The FET method attempts to estimate the coefficient of speed fluctuation shown in Figure 4-3 earlier in the chapter. Similar to the previous validation, the FET method calculated the kinetic energy change from experimental efficacious work, forced work, and mechanism effectiveness. The coefficient of speed fluctuation was then calculated with the actual machine polar moment of inertia, experimental mean angular velocity, and experimental maximum kinetic energy change

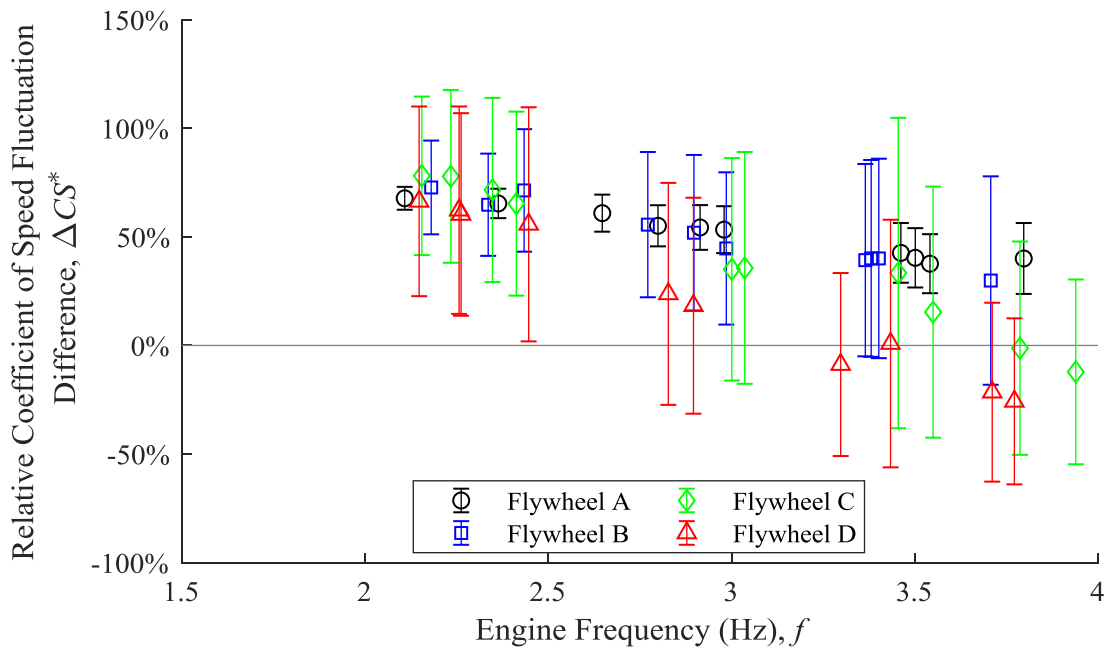
The experiments and FET method are compared with the relative coefficient of speed fluctuation difference ( $\Delta CS^*$ ). It is calculated with Equation 4-9 from the experimental coefficient of speed fluctuation ( $CS_{xp}$ ) and the coefficient of speed fluctuation determined by the FET method ( $CS_{FET}$ ). The relative coefficient of speed fluctuation difference equals zero if the coefficients of speed fluctuation are identical. It is positive if the FET method over-estimates coefficient of speed fluctuation and it is negative if the FET method under-estimates coefficient of speed fluctuation.

$$\Delta CS^* = \frac{CS_{FET} - CS_{xp}}{CS_{xp}} \quad 4-9$$

Figure 4-8 presents the relative coefficient of speed fluctuation as a percent for four flywheel sizes at (a) 517 kPa and (b) 621 kPa charge pressures. In most cases, the relative coefficient of speed fluctuation is between 40 % and 75 %. This indicates that the FET method over-estimates the coefficient of speed fluctuation in most cases. The coefficient of speed fluctuation calculated by the FET method has the correct order of magnitude.



(a)



(b)

Figure 4-8: Plots of the coefficient of speed fluctuation difference for four flywheels at (a) 517 kPa and (b) 621 kPa charge pressures.



### 4.3.3 FET Method Summary

The Fundamental Efficiency Theorem was used to estimate flywheel size. This method was validated by estimating the flywheel size to match the speed fluctuations of an experiment and by estimating the coefficient of speed fluctuation of several experiments. Both validation methods found the FET method had 40 % to 75 % error. The assumption to neglect shaft work may overstep reality because it is a significant energy transfer with the flywheel. The validation methods used experimental results rather than modelled results to isolate the validation to the FET method. Therefore, the accuracy of the FET method for flywheel size is likely to decrease when using a thermodynamic model to estimate flywheel size. In conclusion, the FET method for flywheel size is only valuable for an order of magnitude estimate of flywheel size.

## 4.4 Conclusions

---

This chapter evaluated the influence of flywheel polar moment of inertia on the performance of the low-temperature ST05G. It was divided into three studies. The first study was an evaluation of the transient engine frequency, from start to steady-state, with four flywheel configurations. The second study compared the angular velocity fluctuations and engine performance with the same four flywheel configurations at steady-state. The final study developed and validated of the FET flywheel size calculation method for Stirling engines.

The influence of flywheel polar moment of inertia on the transient engine frequency was investigated. Three metrics were studied: the steady-state engine frequency, the settling time, and the frequency overshoot. The low-temperature ST05G converged on the same steady-state engine frequency with all flywheel sizes, except for the smallest flywheel at 517 kPa charge pressure. The settling time increased with the flywheel polar moment of inertia. Whereas, the frequency overshoot increased with decreasing flywheel polar moment of inertia. These influences of flywheel polar moment of inertia on transient engine frequency agree with some of the dynamic models presented in literature.

The angular velocity fluctuations at steady-state were explored. The relative angular velocity oscillated twice per cycle, which corresponds to the energy transfer with the flywheel in the Fundamental Efficiency Theorem by Senft [32]. The relative angular velocity plots and the coefficient of speed fluctuation showed that the magnitude of the angular velocity fluctuations decreased as flywheel polar moment of inertia increased. This agrees with the fundamentals of flywheels and the dynamic model studies in literature.

The shaft power and indicator diagrams were compared with four flywheel configurations to measure the influence of angular velocity fluctuations on engine performance. The shaft power

was similar with the smallest and largest flywheel configurations. The shaft power had a minimum with an intermediate flywheel size. The indicator diagrams were identical for all flywheel configuration. Therefore, angular velocity fluctuations less than  $CS = 0.12$  do not influence the performance of the low-temperature ST05G. Smaller flywheel configurations may need to be studied to observe any change in performance. This is important because many thermodynamic models, excluding dynamic models, assume that the angular velocity of the engine is constant.

A method to calculate flywheel polar moment of inertia from the results of a thermodynamic model was derived from the energy transfer with the flywheel in the Fundamental Efficiency Theorem by Senft [32]. This method was found to have 65 % error when calculating the flywheel polar moment of inertia to match a measured coefficient of speed fluctuation. Additionally, this method had 40 % to 75 % error in most cases when calculating the coefficient of speed fluctuation for experiments with multiple flywheel sizes. An assumption to neglect the shaft work likely contributes to this error. The accuracy of the FET method for flywheel size is likely to decrease when thermodynamic models are used to estimate flywheel size because the indicator diagrams and mechanism effectiveness will not be exact. Consequently, the FET method for flywheel size is only valuable as an order of magnitude estimate of flywheel polar moment of inertia.

---

## 5 THE ACCURACY OF A 2<sup>ND</sup> ORDER THERMODYNAMIC MODEL AT REDUCED THERMAL SOURCE TEMPERATURE

---

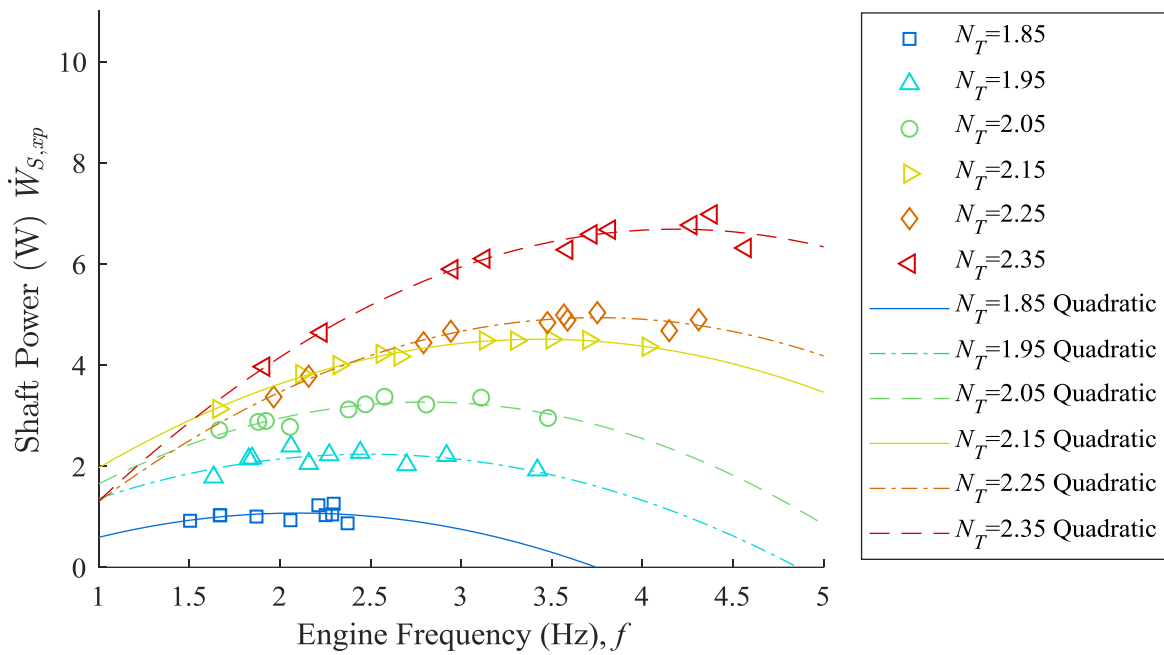
Thermodynamic models must be validated to ensure their accuracy. Current Stirling engine thermodynamic models are primarily validated with HTDSEs [16]. The accuracy of these models may degrade when modelling LTDSEs. This chapter studies the accuracy of the 2<sup>nd</sup> order model described in chapter 3 at a range of thermal source temperature. It begins with a description of the specific experimental methods and an introduction to the data used in this chapter. Then the chapter analyzes the overall accuracy, reference cycle accuracy, and decoupled power loss accuracy of the 2<sup>nd</sup> order model with experimental data. The goals of this study are to determine if the 2<sup>nd</sup> order model is suitable to model a LTDSE and to determine how the model could be most effectively improved.

Some experimental methods are specific to the data used in this chapter. Table 5-1 lists the constant and manipulated parameters of these experiments. The low-temperature ST05G operated at seven thermal source temperatures determined from seven evenly distributed temperature ratios ( $N_T = 1.75$  to  $2.35$  in increments of  $0.1$ ). Data was collected at steady-state with ten unique torque loads. The 2<sup>nd</sup> order model simulated the low-temperature ST05G using the experimental engine frequency, mean pressure, and gas temperatures.

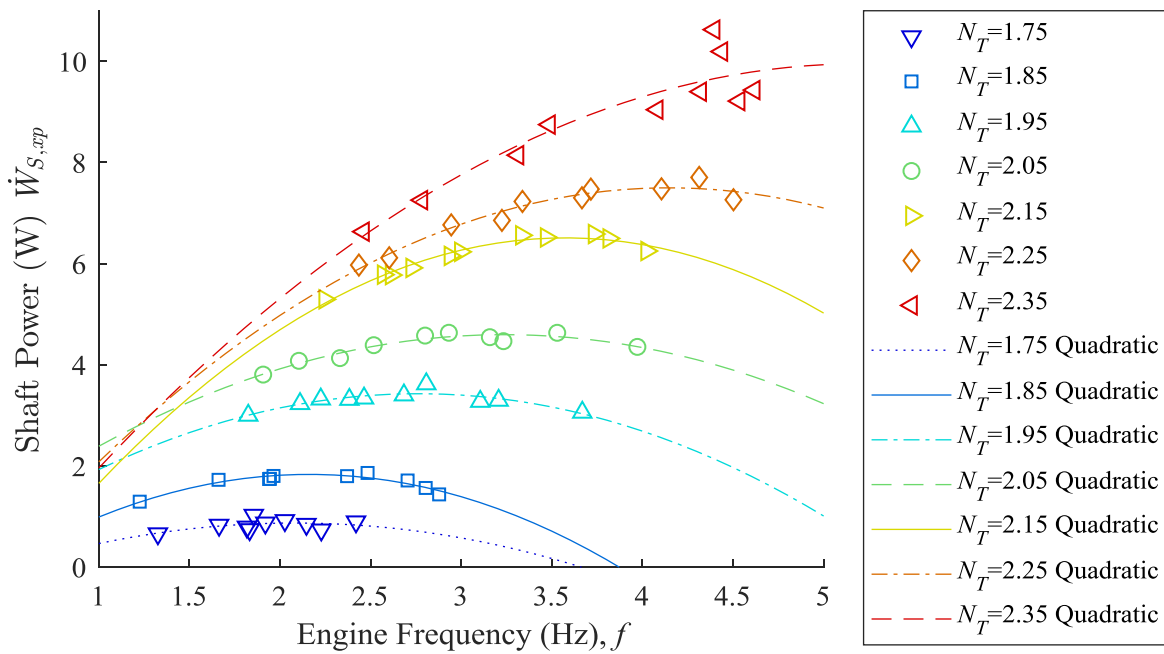
Table 5-1: List of the constant and controlled parameters of the steady-state experiments.

Parameter	Value(s)	Constant or Manipulated
Thermal Source Temperature ( $^{\circ}\text{C}$ ), $T_H$	242, 271, 300, 330, 359, 389, and 418	Manipulated
Thermal Sink Temperature ( $^{\circ}\text{C}$ ), $T_C$	21	Constant
Flywheel Moment of Inertia ( $\text{kg m}^2$ ), $I_{fly}$	(B) 0.2539	Constant
Charge Pressure ( $\text{kPa}$ ), $p_{charge}$	517 and 621	Manipulated
Torque Load ( $\text{N m}$ ), $\tau_E$	Ten unique loads	Manipulated

The experimental data produced the shaft power curves shown in Figure 5-1 (a) and (b). The quadratic trend lines illustrate the trend of shaft power ( $\dot{W}_S$ ) with engine frequency ( $f$ ) and the presence of an optimum frequency for maximum shaft power. Shaft power increases with temperature ratio, with the exception of a few samples. Some shaft power measurements at the  $389^{\circ}\text{C}$  source temperature are less than shaft power measurements at the  $359^{\circ}\text{C}$  source temperature. The engine was disassembled and rebuilt after the experiments with source temperatures at and below  $359^{\circ}\text{C}$  to repair an issue with the displacer seal. This rebuild could have changed the seal or mechanism performance, which may explain the change in shaft power. Consequently, comparisons across source temperatures are restricted to source temperatures from  $242^{\circ}\text{C}$  to  $359^{\circ}\text{C}$ .



(a)



(b)

Figure 5-1: Shaft power curves of the engine charged to (a) 517 kPa and (b) a 621 kPa.

## 5.1 Overall Model Accuracy

---

The primary goal of the 2<sup>nd</sup> order model is to accurately estimate the shaft power produced by the engine. It includes the reference cycle and the decoupled losses. Overall model accuracy is evaluated by comparing the model shaft power and measured shaft power. Shaft power is influenced by the thermal source temperature, thermal sink temperature, mean pressure, and engine frequency. Comparison methods must remove these dependencies because they vary between experiments. Two comparison methods fit this criteria: the relative shaft power difference and the normalized West number difference.

### 5.1.1 Shaft Power Accuracy

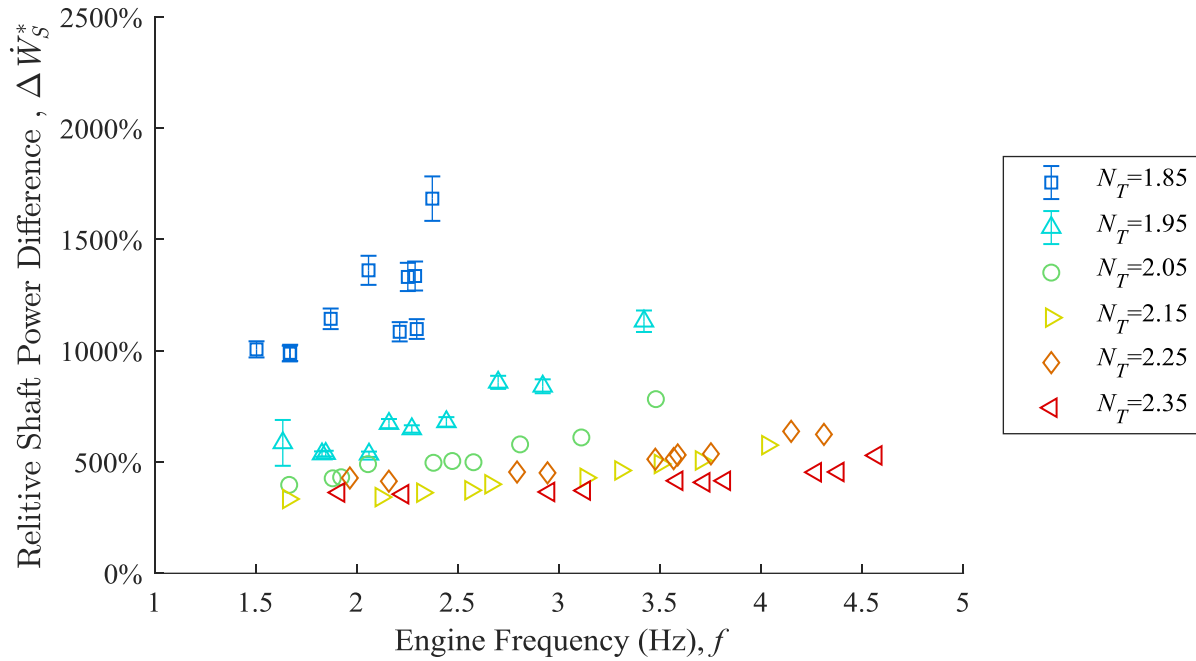
The relative shaft power difference ( $\Delta\dot{W}_S^*$ ) measures how accurately the model estimates shaft power. It is the difference between the modelled and measured shaft power ( $\dot{W}_{S,md}$  and  $\dot{W}_{S,xp}$ ) divided by the measured shaft power, as shown in Equation 5-1. A value of zero corresponds to the modelled shaft power equal to the experimental shaft power. Positive values indicate that the model over-estimates the experimental shaft power.

$$\Delta\dot{W}_S^* = \frac{\dot{W}_{S,md} - \dot{W}_{S,xp}}{\dot{W}_{S,xp}} \quad 5-1$$

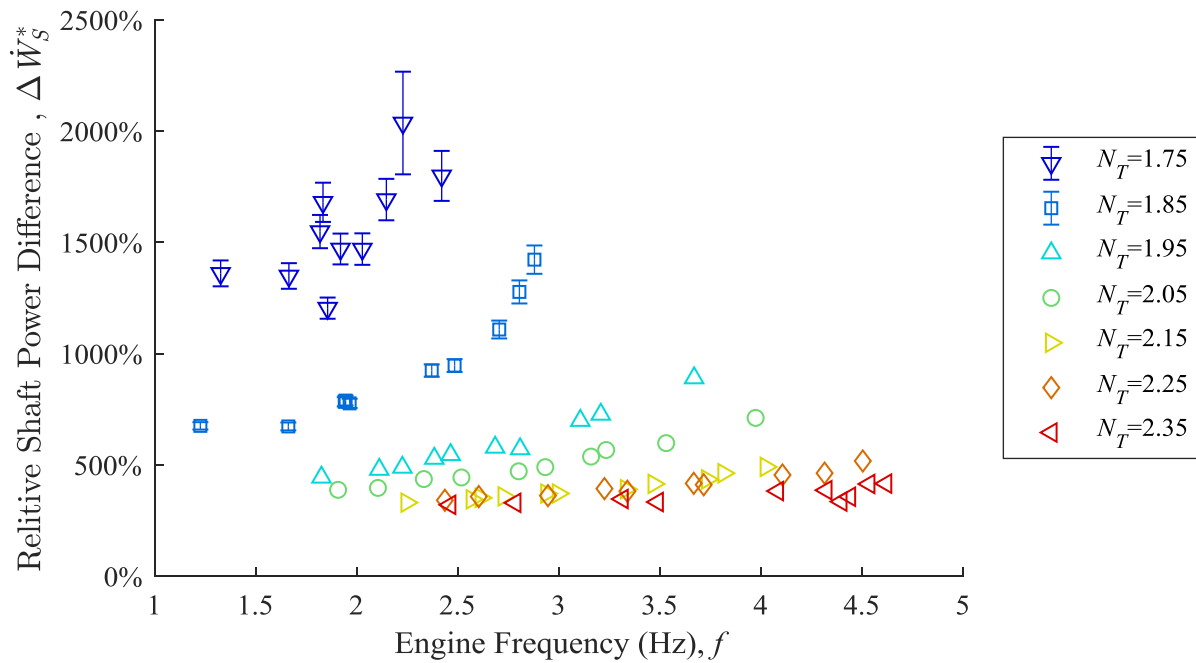
Figure 5-2 presents the relative shaft power difference as a percent for experiments at several temperature ratios and charge pressures of (a) 517 kPa and (b) 621 kPa. Error bars are excluded from data points where the uncertainty is within the marker. The relative shaft power difference ranged from 320 % to 2040 %. This discrepancy is too significant to conclude that the model accurately calculates engine performance. The experiments with the lowest thermal source temperature ( $T_H = 242$  °C and 271 °C) had the largest relative shaft power difference. The relative

shaft power difference decreased as the source temperature increased, with exceptions for samples after the engine was rebuilt ( $T_H = 389\text{ °C}$  and  $418\text{ °C}$ ). If those samples are omitted, the model trends towards lower accuracy at lower temperature ratios. However, the relative shaft power difference may be exaggerated by the small measured shaft powers at low thermal source temperatures.





(a)



(b)

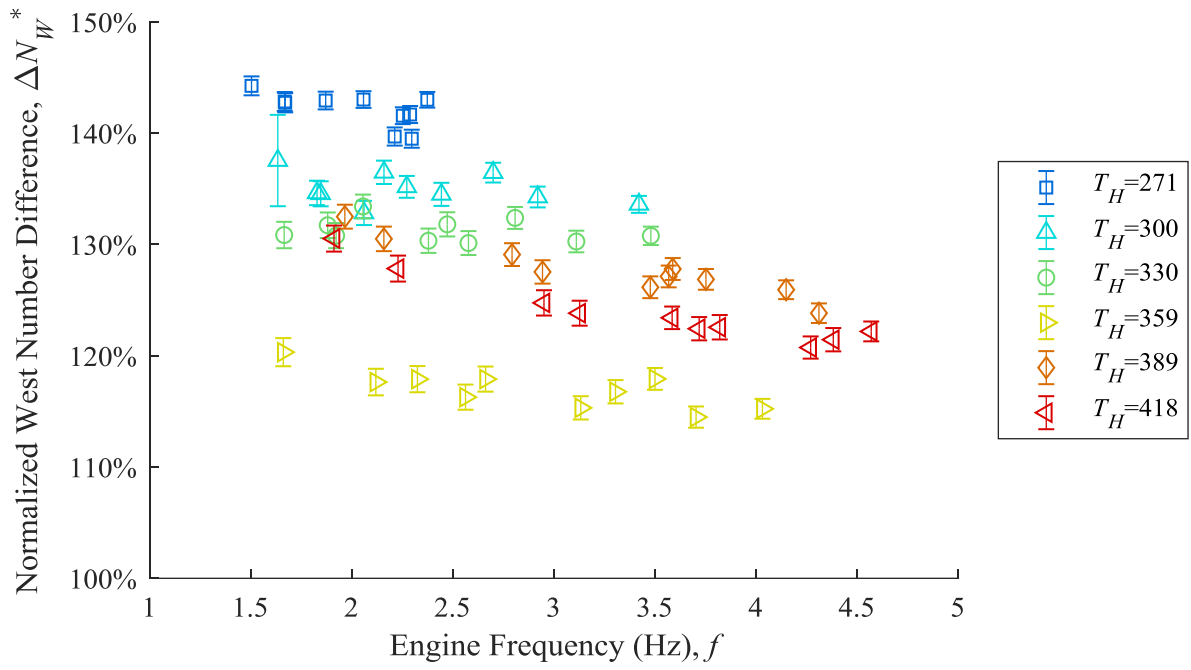
Figure 5-2: Plot of the relative shaft power difference at (a) a 517 kPa charge pressure and (b) a 621 kPa charge pressure.

### 5.1.2 West Number Accuracy

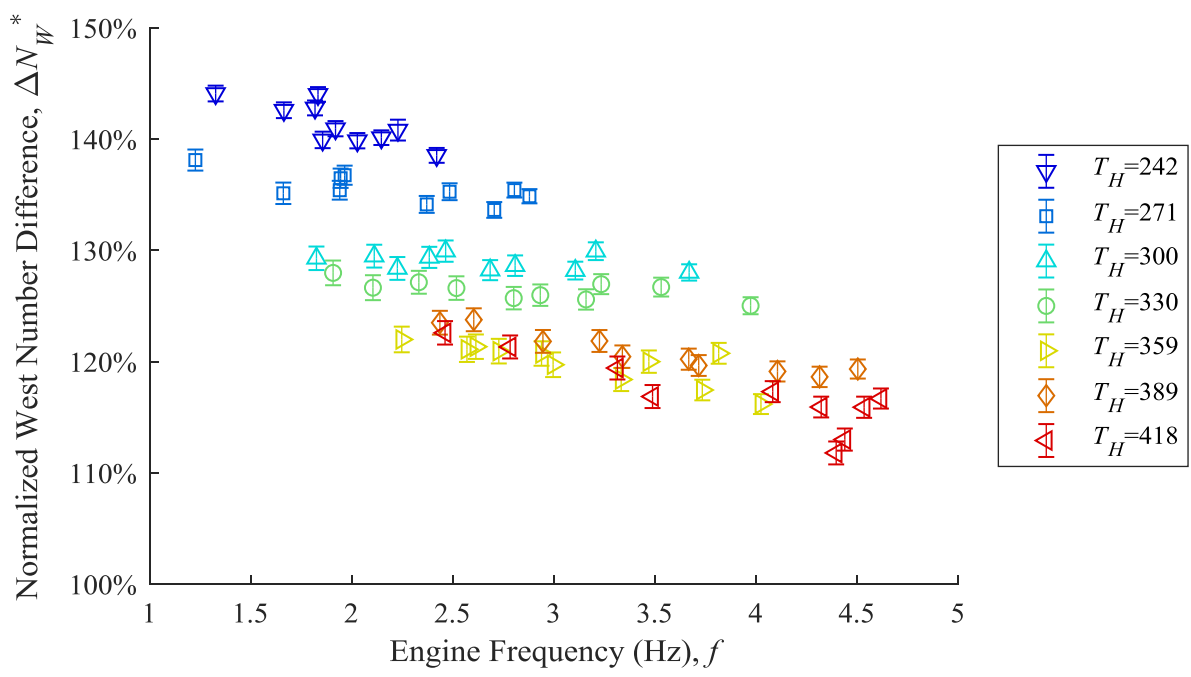
The West number is a dimensionless measure of the overall engine performance that removes the idealized influences of mean pressure, engine frequency, swept volume, thermal source temperature, and thermal sink temperature on shaft power. Therefore, the normalized West number difference ( $\Delta N_W^*$ ) is suitable to draw comparisons of the overall model accuracy at different operating conditions. It is calculated with Equation 5-2 as the difference between the modelled and experimental West numbers ( $N_{W,S,md}$  and  $N_{W,S,xp}$ ) divided by the mean West number determined by West [8] ( $N_W = 0.25$ ). If the normalized West number difference is zero, the model accurately estimates the West number. Positive values correspond to the model over-estimating the experimental West number.

$$\Delta N_W^* = \frac{N_{W,md} - N_{W,xp}}{0.25} \quad 5-2$$

The normalized West number difference was examined at different thermal source temperatures. Figure 5-3 presents the normalized West number difference as a percentage at several source temperatures and charge pressures of (a) 517 kPa and (b) 621 kPa. The West number difference ranges from 112 % to 144 % of the mean West number. Like the relative shaft power difference, this discrepancy is too significant to conclude that the model accurately represents the engine. Figure 5-3 also shows that the normalized West number decreases as source temperature increases from 242 °C to 359 °C. This confirms that the overall model accuracy improves as thermal source temperature increases.



(a)



(b)

Figure 5-3: Plots of the relative West number difference at (a) the 517 kPa charge pressure and (b) the 621 kPa charge pressure.

### 5.1.3 Overall Model Accuracy Summary

The relative shaft power difference and the normalized West number difference measured the overall model accuracy. The calculated values for the relative shaft power difference and the normalized West number difference are large at all conditions studied. These indicate that the complete model does not accurately calculate the performance of the low-temperature ST05G. These metrics do not identify the potential sources of the discrepancy, so further analysis is necessary to determine how to most effectively improve the 2<sup>nd</sup> order model.

The overall model accuracy was studied across thermal source temperatures. Both the relative shaft power difference and the normalized West number difference indicated that the model accuracy declined as source temperature decreased from 359 °C to 242 °C. The reference cycle, decoupled losses, and excluded loss mechanisms in the 2<sup>nd</sup> order model could all potentially contribute to this trend. These are explored in the following sections.

## 5.2 Reference Cycle Accuracy

---

The previous section identified that the 2<sup>nd</sup> order model is inaccurate at all conditions and less accurate at lower thermal source temperatures. The reference cycle can influence the accuracy of the 2<sup>nd</sup> order model in two ways. The first is the direct use of indicated work in the estimate of shaft power. The second is the use of the reference cycle to estimate decoupled losses in the engine. The reference cycle accuracy describes how well the reference cycle reflects the engine thermodynamics. This section evaluates the reference cycle accuracy with the indicated work, the dimensionless indicator diagrams, and a measure of the indicator diagram shape fidelity.

### 5.2.1 Indicated Work Accuracy

Indicated work is the primary measure of the thermodynamic performance of a Stirling engine. The relative indicated work difference ( $\Delta W_I^*$ ) evaluates how well a thermodynamic model estimates the experimental indicated work. It is the difference between the modelled indicated work ( $W_{I,md}$  shown in Figure 5-4 a) and experimental indicated work ( $W_{I,xp}$  shown in Figure 5-4 b) divided by the experimental indicated work, as defined in Equation 5-3. The model perfectly estimates the indicated work when relative indicated work difference is equal to zero. Positive values show that the model over-estimates the experimental indicated work.

$$\Delta W_I^* = \frac{W_{I,md} - W_{I,xp}}{W_{I,xp}} \quad 5-3$$

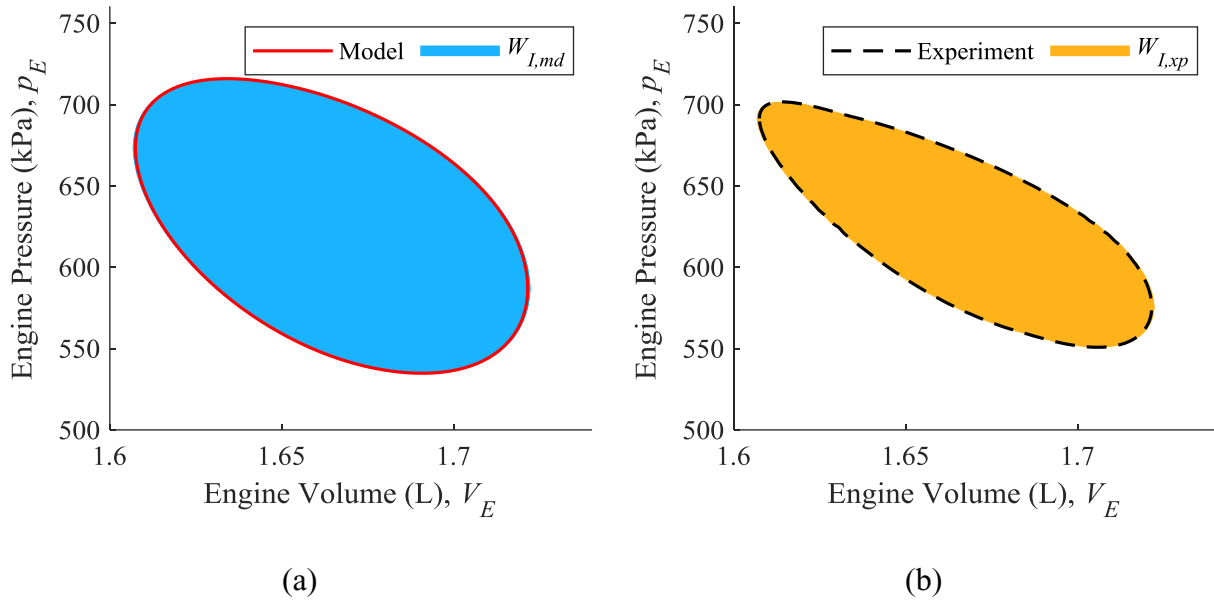
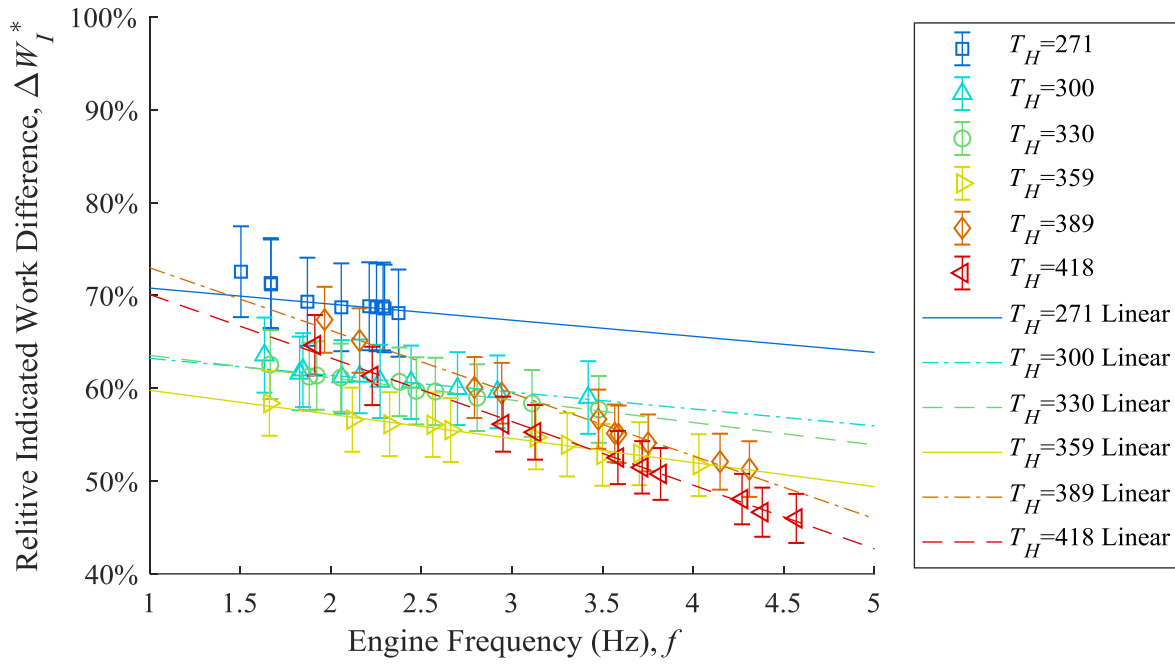


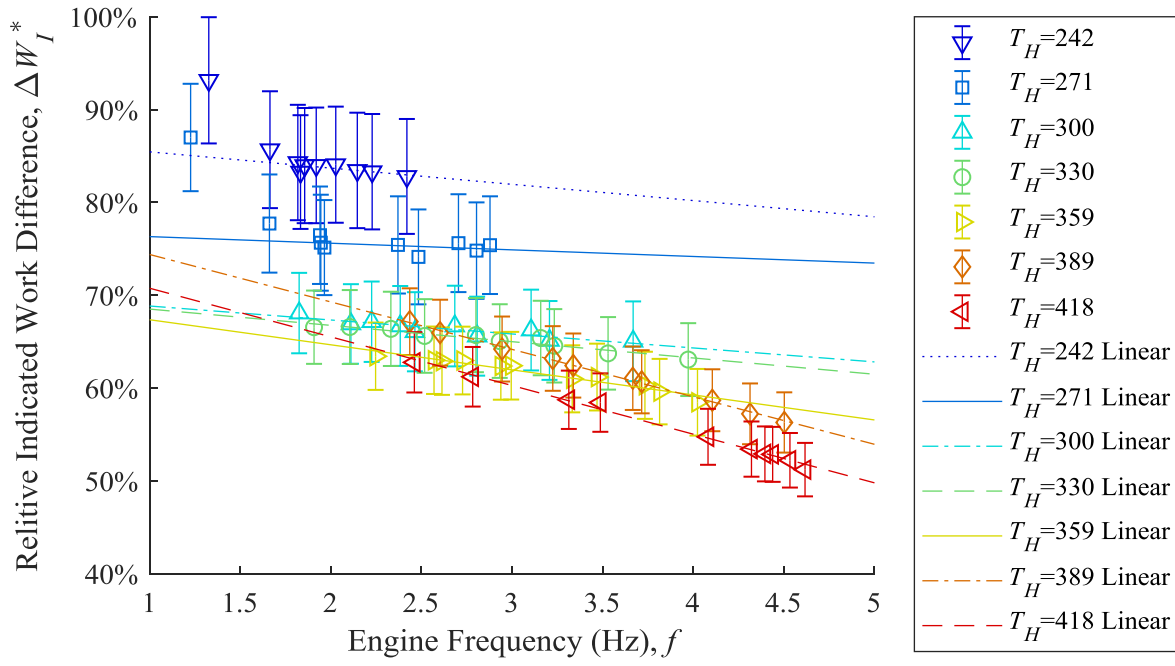
Figure 5-4: Modelled (a) and experimental (b) indicator diagrams with indicated work filled.

Figure 5-5 presents plots of the relative indicated work difference as a percentage for experiments at (a) 517 kPa and (b) 621 kPa charge pressures. The relative indicated work difference ranges from 46 % and 93 %. This shows that the modelled reference cycle overestimates indicated work at all operating conditions studied. Therefore, the reference cycle calculation of the model can improve.

The relative indicated work difference was calculated at seven thermal source temperatures. Figure 5-5 shows that it decreases as thermal source temperature increases from 242 °C to 359 °C. This indicates that the reference cycle accuracy improves as source temperature increases. The relative indicated work difference decreases more significantly as thermal source temperature increases from 242 °C to 300 °C compared to 300 °C to 359 °C. Consequently, changes to the reference cycle calculation must have a greater influence at lower thermal source temperatures to render the reference cycle accurate at all operating conditions.



(a)



(b)

Figure 5-5: Plot of the relative indicated work difference at (a) the 517 kPa charge pressure and (b) the 621 kPa charge pressure with fit curves.

The trend of indicated work accuracy with engine frequency was examined. Under certain conditions the relative indicated work difference shows an increased frequency dependence. This is shown in Figure 5-5 by the trend lines generated from samples with an engine frequency above 1.75 Hz. As engine frequency decreases below 1.75 Hz the relative indicated work difference increases. Further, samples with engine frequency below 1.5 Hz have relative indicated work differences significantly above their trend lines. The slope of the trend lines decreases after the engine was rebuilt ( $T_H = 389\text{ }^\circ\text{C}$  and  $418\text{ }^\circ\text{C}$ ), indicating that the accuracy of the modelled indicated work is more sensitive to engine frequency after the engine was rebuilt. These changes to the accuracy of the modelled indicated work may help identify methods to improve the reference cycle calculation of the model.

### 5.2.2 Cumulative Indicator Diagram Difference

The cumulative indicator diagram difference ( $\Delta pV^*$ ) quantifies the fidelity of the reference cycle indicator diagram. It is the area between the modelled and experimental indicator diagrams, shown in Figure 5-6, divided by the experimental indicated work. It is calculated with Equation 5-4 through a complete rotation ( $i$  from 1 to  $N$ ) with the modelled engine pressure ( $p_{E,md,i}$ ), experimental engine pressure ( $p_{E,xp,i}$ ), incremental engine volume change ( $dV_{E,i}$ ), and experimental indicated work. The cumulative indicator diagram difference is equal to zero when the model indicator diagram is identical to the measured indicator diagram. It increases as the modelled indicator diagram shape varies further from the experimental indicator diagram.

$$\Delta pV^* = \frac{\sum_{i=1}^N |(p_{E,md,i} - p_{E,xp,i}) \cdot dV_{E,i}|}{W_{I,xp}} \quad 5-4$$



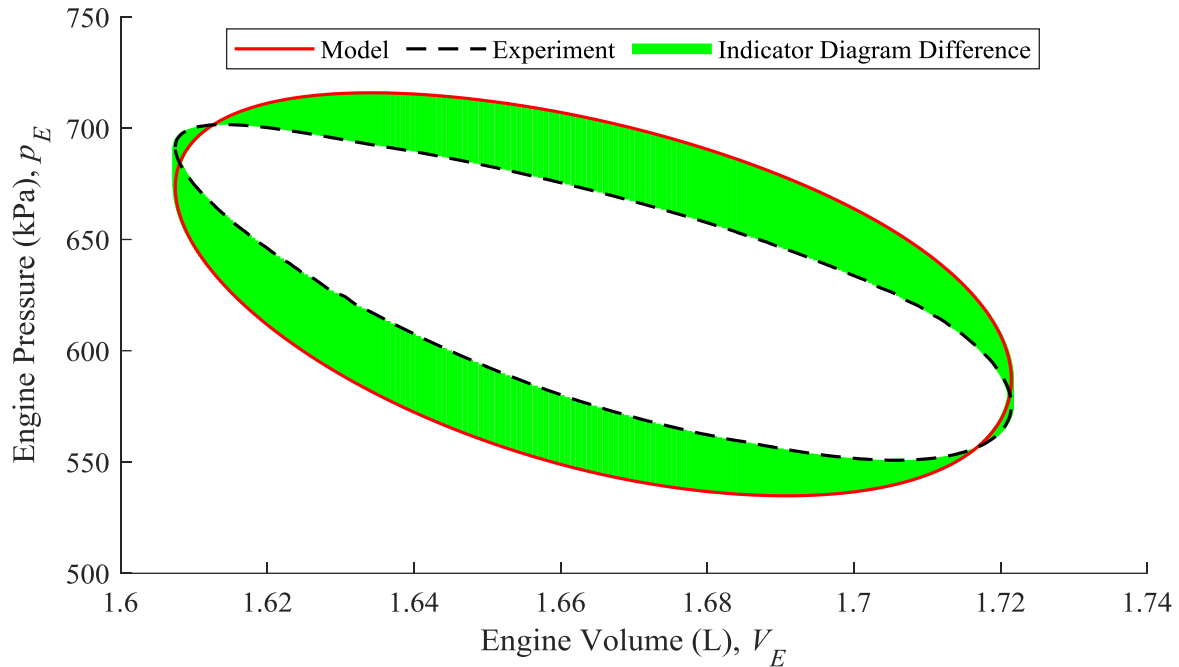
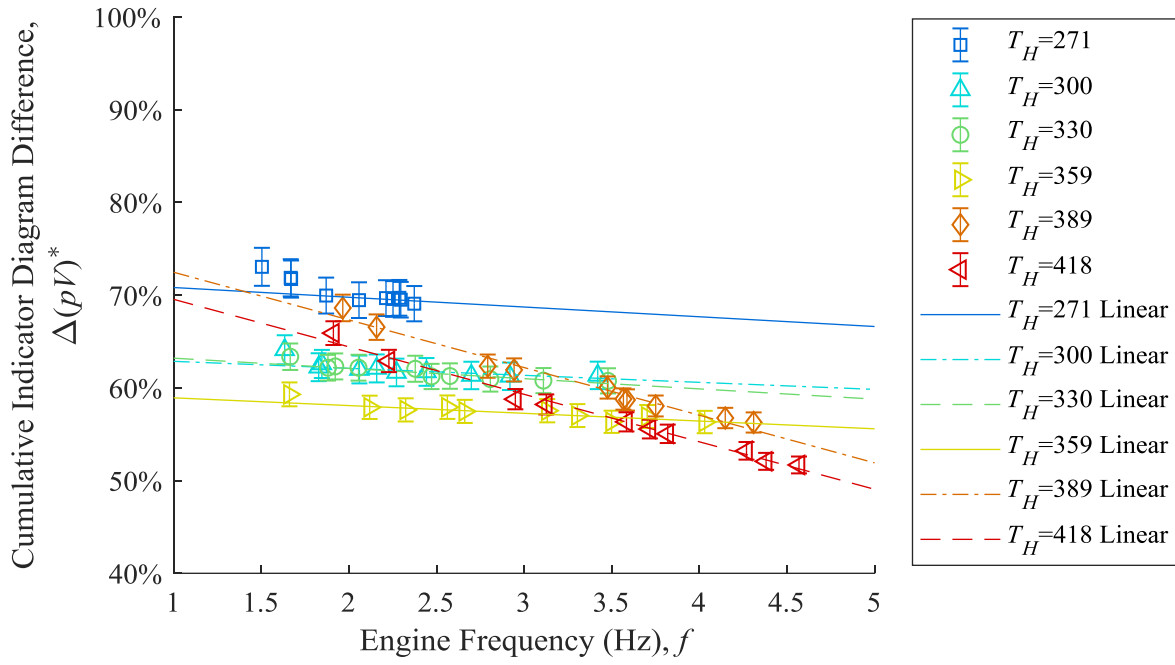


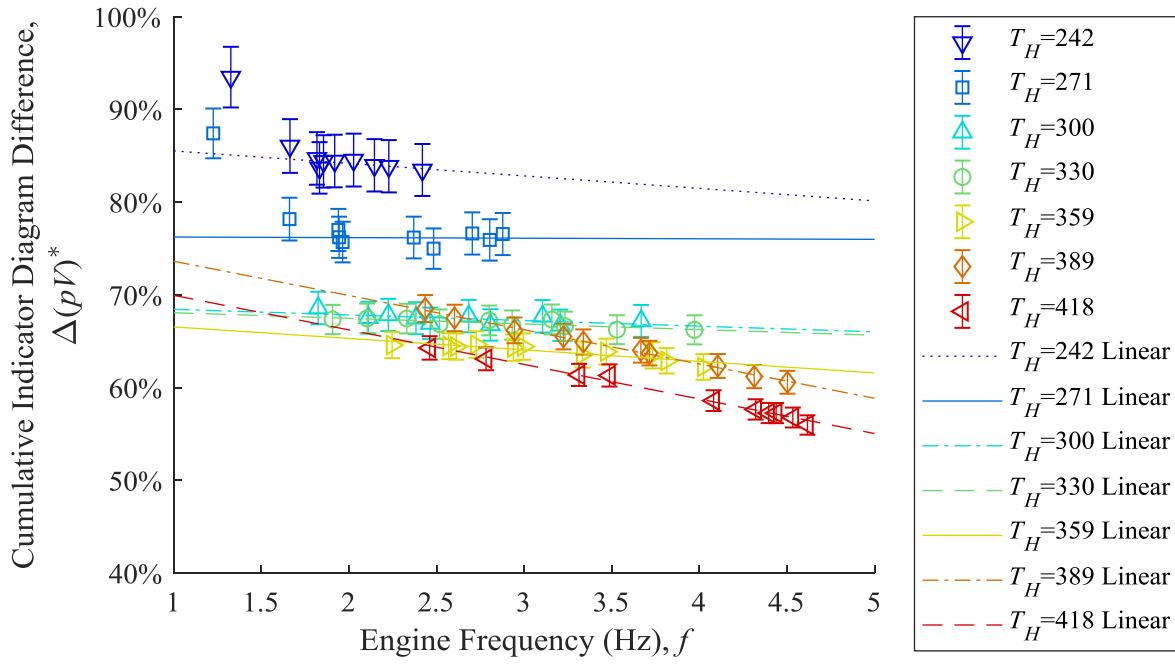
Figure 5-6: Arbitrary indicator diagram with the indicator diagram difference area filled.

Figure 5-7 presents plots of the cumulative indicator diagram difference as a percent at (a) 517 kPa and (b) 621 kPa charge pressures. The cumulative indicator diagram difference ranges from 53 % to 93 % of the indicated work. Therefore, the indicator diagram shape is inaccurate at all operating conditions studied. This supports the conclusion that the 2<sup>nd</sup> order model did not accurately calculate the reference cycle at any of the operating conditions.

The cumulative indicator diagram difference was evaluated at different thermal source temperatures. Figure 5-7 shows that the cumulative indicator diagram difference decreases as the source temperature increases from 242 °C to 359 °C. This indicates that the reference cycle is more accurate at higher temperature ratios.



(a)



(b)

Figure 5-7: Plot of the cumulative indicator diagram difference at (a) the 517 kPa charge pressure and (b) the 621 kPa charge pressure with fit curves.

The influence of engine frequency on the indicator diagram accuracy was studied. Trend lines in Figure 5-7 from samples with engine frequencies above 1.75 Hz show the dependence of indicator diagram accuracy on engine frequency. The accuracy of the indicator diagram strays from the trends in specific cases. The cumulative indicator diagram difference is more sensitive to engine frequencies at engine frequencies below 1.75 Hz. After the engine was rebuilt, the cumulative indicator diagram difference decreases at a greater rate as frequency increases. Similar to the indicated work, low engine frequencies and the engine rebuild increase the indicator diagram accuracy sensitivity to engine frequency.

### 5.2.3 Dimensionless Indicator Diagrams

The indicator diagram of a Stirling engine illustrates the pressure-volume function of the engine. An accurate reference cycle pressure would match the experimental pressure at every instance and the modelled and measured indicator diagrams would be identical. Dimensionless indicator diagrams are independent of mean pressure, which was not repeatable in experiments, and swept volume. They display the dimensionless engine pressure ( $p_E^*$ ) with respect to dimensionless engine volume ( $V_E^*$ ). The dimensionless engine pressure is the instantaneous engine pressure ( $p_E$ ) divided by the mean engine pressure ( $p_{E,mean}$ ), as shown in Equation 5-5. It is equal to one when the instantaneous engine pressure is equal to the mean pressure. The dimensionless engine volume is calculated with Equation 5-6 as the instantaneous engine volume ( $V_E$ ) minus the minimum engine volume ( $V_{E,min}$ ), and all divided by the swept volume ( $V_{sw}$ ). The dimensionless engine volume is equal to zero at the minimum engine volume and equal to one at the maximum engine volume. The area within the dimensionless indicator diagram is the indicated work normalized to mean pressure and swept volume.

$$p_E^* = \frac{P_E}{P_{E,mean}} \quad 5-5$$

$$V_E^* = \frac{V_E - V_{E,min}}{V_{sw}} \quad 5-6$$

Four dimensionless indicator diagrams are presented in Figure 5-8. They are from the maximum power experiments at the operating conditions shown in Table 5-2. The experimental dimensionless indicator diagrams display the phase-averaged pressure at every 8<sup>th</sup> discrete angular position. The uncertainty of the experimental dimensionless engine pressure and dimensionless engine volume are within the markers. The modelled dimensionless indicator diagrams encircle a larger area than the measured dimensionless indicator diagrams in all cases. Further, the modelled dimensionless indicator diagrams are not within the uncertainty of the experimental dimensionless indicator diagrams through most of the cycle.

Table 5-2: List of operating conditions for the dimensionless indicator diagrams in Figure 5-8.

Operating Condition	Figure Panel			
	(a)	(b)	(c)	(d)
Thermal Source Temperature (°C), $T_H$	271	271	359	359
Thermal Sink Temperature (°C), $T_C$	21	21	21	21
Charge Pressure (kPa), $p_{charge}$	517	621	517	621
Engine Frequency (Hz), $f$	2.30	2.48	3.50	3.37
Experimental Shaft Power (W), $\dot{W}_{S,xp}$	1.26	1.86	4.51	6.59

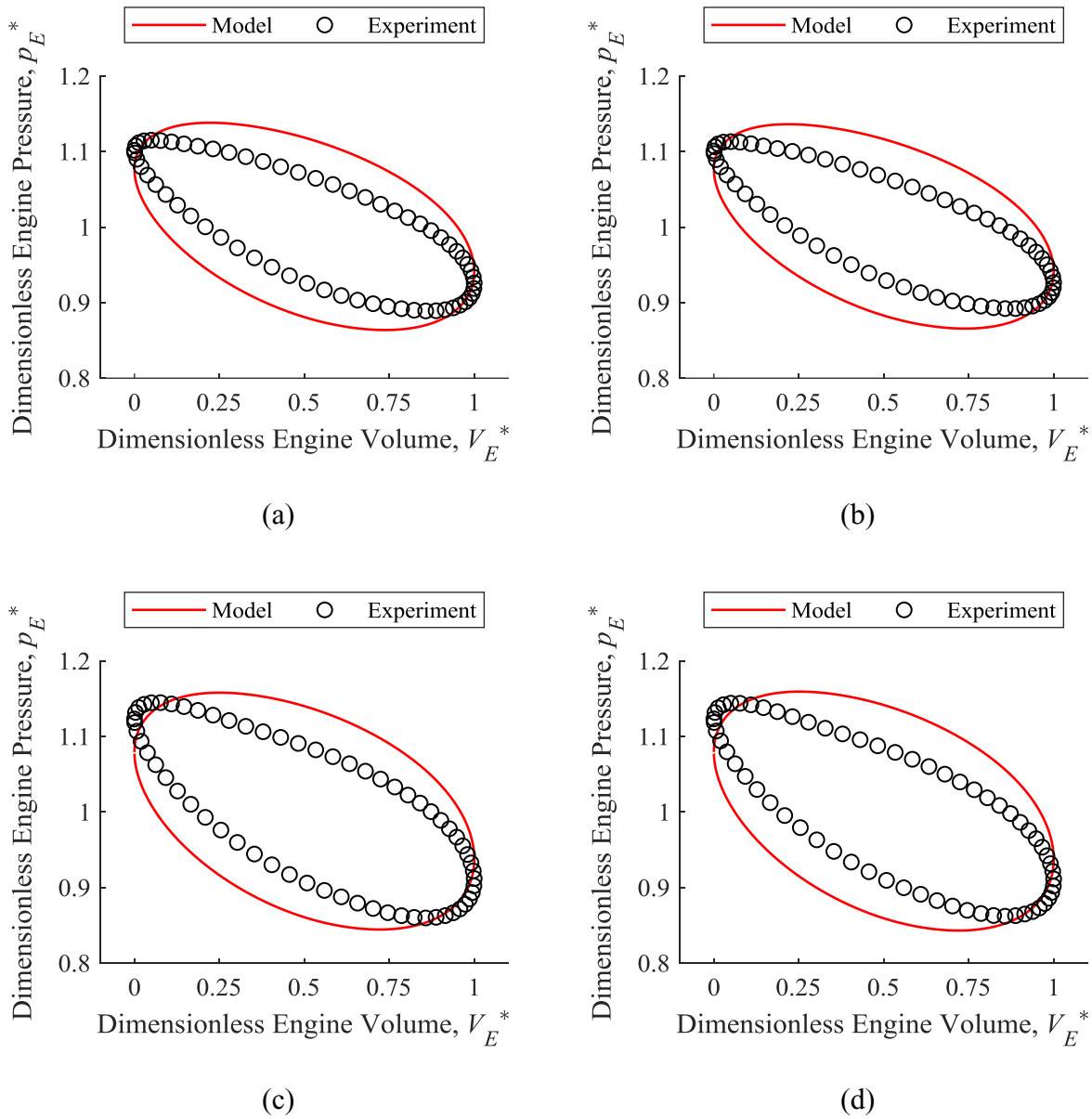


Figure 5-8: Dimensionless indicator diagrams for the maximum power experiments at the operating conditions: (a)  $T_H = 271$  °C and  $p_T = 517$  kPa, (b)  $T_H = 271$  °C and  $p_T = 620$  kPa, (c)  $T_H = 359$  °C and  $p_T = 517$  kPa, and (d)  $T_H = 359$  °C and  $p_T = 620$  kPa.

The dimensionless indicator diagrams are useful for identifying how the model incorrectly represents the engine. Several differences between the model and experiments are visible at all conditions presented in Figure 5-8. The most apparent difference is the modelled expansion

process occurs at higher pressures than the experimental expansion process and the modelled compression process occurs at lower pressures than the modelled compression process. The second difference is a phase shift of the maximum and minimum pressure. The maximum pressure of the model occurs later in the expansion process than the experimental maximum pressure. Similarly, the modelled minimum pressure occurs later in the compression process than the experimental minimum pressure. Changes to the reference cycle calculation that address these discrepancies should show the greatest improvement in reference cycle accuracy.

#### 5.2.4 Reference Cycle Accuracy Summary

The accuracy of the reference cycle in the thermodynamic model was evaluated with the relative indicated work difference, cumulative indicator diagram difference, and dimensionless indicator diagrams. All these measures show that the model does not accurately calculate the reference cycle. The dimensionless indicator diagrams show that the modelled expansion pressure is higher than the experimental expansion pressure and the modelled compression pressure is lower than the experimental compression pressure. Additionally, the modelled maximum and minimum pressures occur later in the cycle than the experimental maximum and minimum pressure. Changes to the reference cycle calculation should target these discrepancies.

The accuracy of the reference cycle was examined at several thermal source temperatures. The relative indicated work difference and the cumulative indicator diagram difference decrease with increasing thermal source temperature. Therefore, the 2<sup>nd</sup> order model more accurately calculates the reference cycle at higher source temperatures. Any loss mechanisms added to the reference cycle calculation should have a greater influence on the performance of engines operating at lower thermal source temperatures.

The first of two potential improvements to the reference cycle calculation is to use a reference cycle with irreversible heat transfer in all engine components. The heat transfer hysteresis loss accounts for the work lost to irreversible heat transfer as a decoupled loss. Yang and Gschwendtner [18] stated that heat transfer hysteresis has a greater influence on the performance of LTDSEs. However, heat transfer hysteresis is a decoupled loss and does not improve the reference cycle calculation. A semi-adiabatic reference cycle includes finite, irreversible heat transfer in the expansion space and compression space. Work lost to irreversible heat transfer in these cells would show in the indicator diagram, and indicated work accuracy could improve. Consequently, it is recommended that the model use a semi-adiabatic reference cycle calculation to improve its accuracy.

The other potential improvement to the 2<sup>nd</sup> order model reference cycle calculation is to include seal leakage. In the low-temperature ST05G, seal leakage occurs between the engine and crankcase. The engine loses gas when its pressure is higher than the crankcase pressure and regains the same mass of gas when its pressure is lower than the crankcase pressure. Li et al. [49] showed that seal leakage decreased expansion pressure, increased compression pressure, and caused maximum and minimum pressure to occur earlier in the cycle. This is similar to the differences between the modelled and experimental dimensionless indicator diagrams. Kolin [17] stated that seal leakage has a greater influence on the performance of LTDSEs. This suggests that including seal leakage in the model can improve its accuracy to a greater extent at lower source temperatures. Therefore, seal leakage shows significant potential to improve the accuracy of the reference cycle calculation.

## 5.3 Decoupled Power Losses Accuracy

---

The decoupled loss mechanisms in the model influence the heat transfer rates and the shaft power. All the heat losses, flow friction, and mechanical losses could not be measured independently with the experiment setup used. However, the total power losses, gas spring hysteresis loss, and forced work can be determined from measurements. This section evaluates the accuracy of the decoupled power losses estimated by the model.

### 5.3.1 Mechanical Efficiency

The mechanical efficiency ( $\eta_{mec}$ ) is the ratio of shaft power ( $\dot{W}_S$ ) to the indicated power ( $\dot{W}_I$ ) described by Equation 5-7. It includes all decoupled power loss mechanisms in the 2<sup>nd</sup> order model. The model calculates decoupled power losses for flow friction, gas spring hysteresis and mechanical losses. The mechanical efficiency difference ( $\Delta\eta_{mec}$  calculated by Equation 5-8) is the difference between the modelled and measured mechanical efficiency ( $\eta_{mec,md}$  and  $\eta_{mec,xp}$ ). If the mechanical efficiency difference is zero, the modelled and measured mechanical efficiency are identical. The mechanical efficiency difference is greater than zero if the model over-estimates mechanical efficiency. The mechanical efficiency difference cannot exceed one, the case when the model calculates zero power losses and the measured shaft power is zero.

$$\eta_{mec} = \frac{\dot{W}_S}{\dot{W}_I} \quad 5-7$$

$$\Delta\eta_{mec} = \eta_{mec,md} - \eta_{mec,xp} \quad 5-8$$

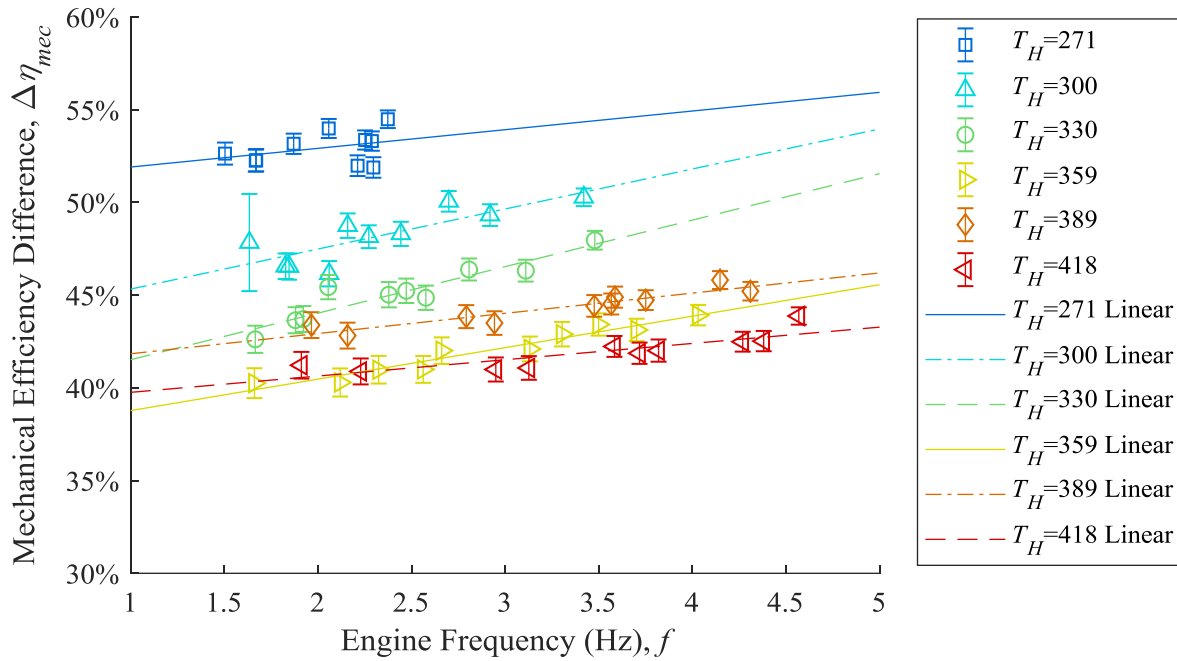
Figure 5-9 presents the mechanical efficiency difference as a percentage with the engine charged to (a) 517 kPa and (b) 621 kPa. The maximum mechanical efficiency difference is 55 % and the minimum is 38 %. Therefore, if the reference cycle accurately estimated indicated power,



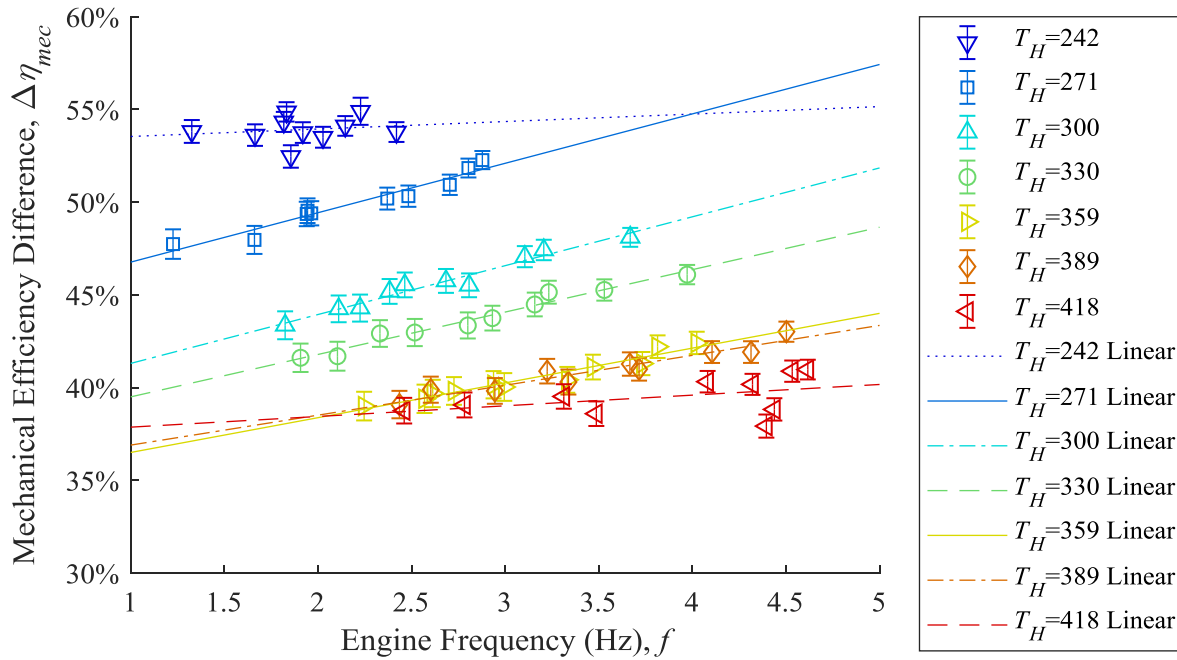
the 2<sup>nd</sup> order model would not accurately estimate the shaft power. The decoupled power loss calculations in the 2<sup>nd</sup> order model require improvement.

The mechanical efficiency difference was studied with different thermal source temperatures. Figure 5-9 shows the mechanical efficiency difference decreases as source temperature increases from 242 °C to 359 °C. This indicates that the decoupled power losses in the 2<sup>nd</sup> order model do not influence engine performance enough at lower source temperatures.

The trend of mechanical efficiency difference with engine frequency is shown in Figure 5-9. The mechanical efficiency difference trends upward as engine frequency increases. This indicates that the model does not properly estimate the frequency dependence of the loss mechanisms. The accuracy of the existing loss mechanisms could decrease with increasing engine frequency. Alternately, loss mechanisms excluded from the 2<sup>nd</sup> order model could have a greater influence on engine performance at higher frequencies.



(a)



(b)

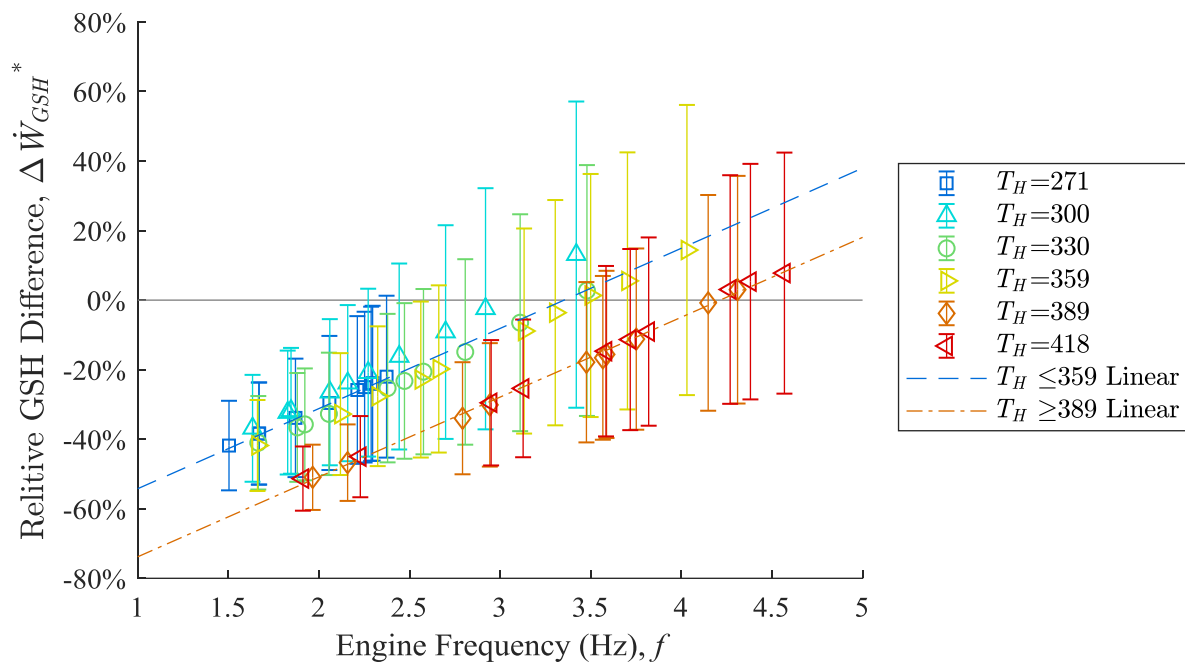
Figure 5-9: Plot of the mechanical efficiency difference at (a) the 517 kPa charge pressure and (b) the 621 kPa charge pressure with fit curves.

### 5.3.2 Gas Spring Hysteresis

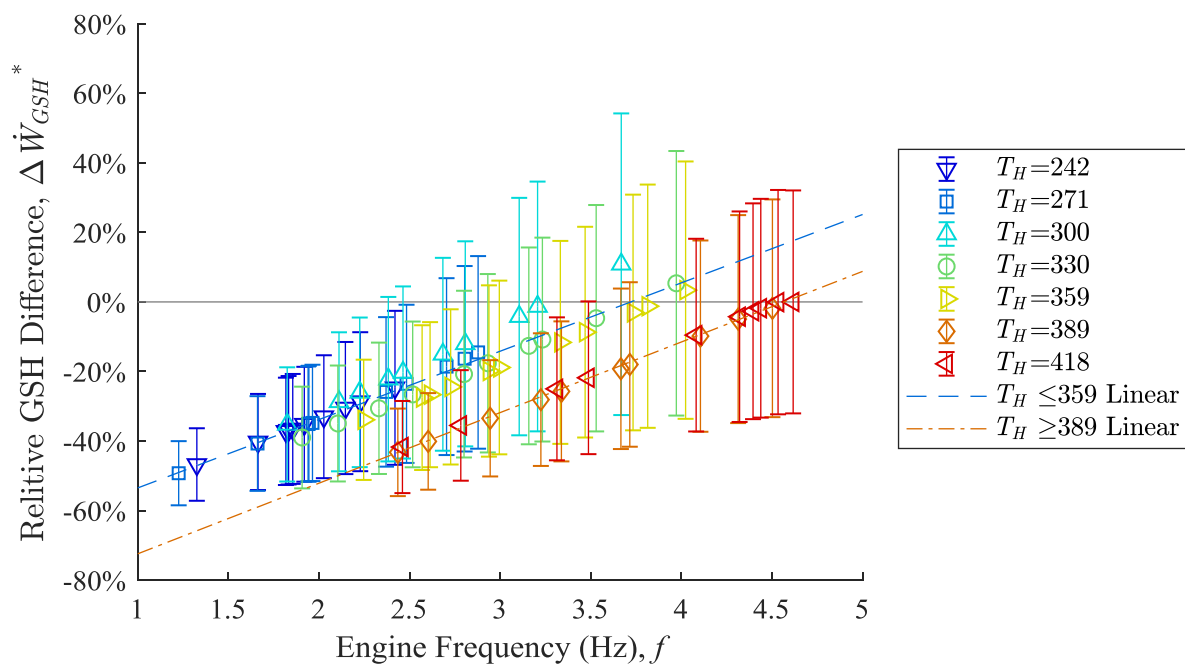
Gas spring hysteresis (GSH) was modelled with an empirical correlation by Speer [79], described in section 3.4.4. The correlation depends on mean pressure and engine frequency [79]. The relative GSH difference provides a metric for the accuracy of the GSH estimate. It is calculated by Equation 5-9 with the modelled ( $\dot{W}_{GSH,md}$ ) and experimental ( $\dot{W}_{GSH,xp}$ ) GSH loss. The model is accurate if the relative GSH difference equals zero. Positive values show the model over-estimates GSH and negative values show the model under-estimates GSH.

$$\Delta\dot{W}_{GSH}^* = \frac{\dot{W}_{GSH,md} - \dot{W}_{GSH,xp}}{\dot{W}_{GSH,xp}} \quad 5-9$$

Figure 5-10 shows the relative GSH difference as a percentage at (a) 517 kPa and (b) 621 kPa charge pressure. The GSH correlation is inaccurate at engine frequencies below 2.5 Hz. This shows that the GSH correlation was inaccurate in its intended frequency range (0-2.5 Hz [79]). Further, the GSH correlation is less accurate after the engine was rebuilt ( $T_H = 389^\circ\text{C}$  and  $418^\circ\text{C}$ ). The trend lines show that the relative GSH difference increases linearly. Therefore, the GSH correlation transitions from under-estimating GSH to over-estimating GSH. This shows that correlation inaccurately calculated the influence of engine frequency on GSH. Consequently, the current GSH correlation should be replaced.



(a)



(b)

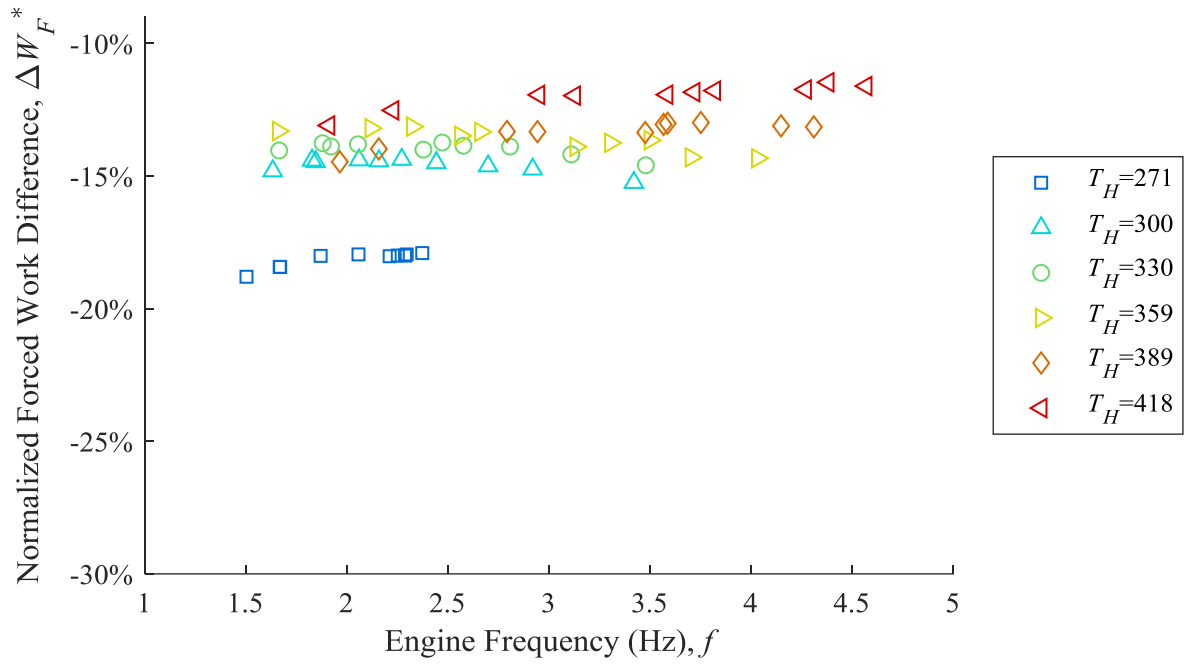
Figure 5-10: Plot of the relative GSH difference at (a) the 517 kPa charge pressure and (b) the 621 kPa charge pressure with fit curves.

### 5.3.3 Forced Work

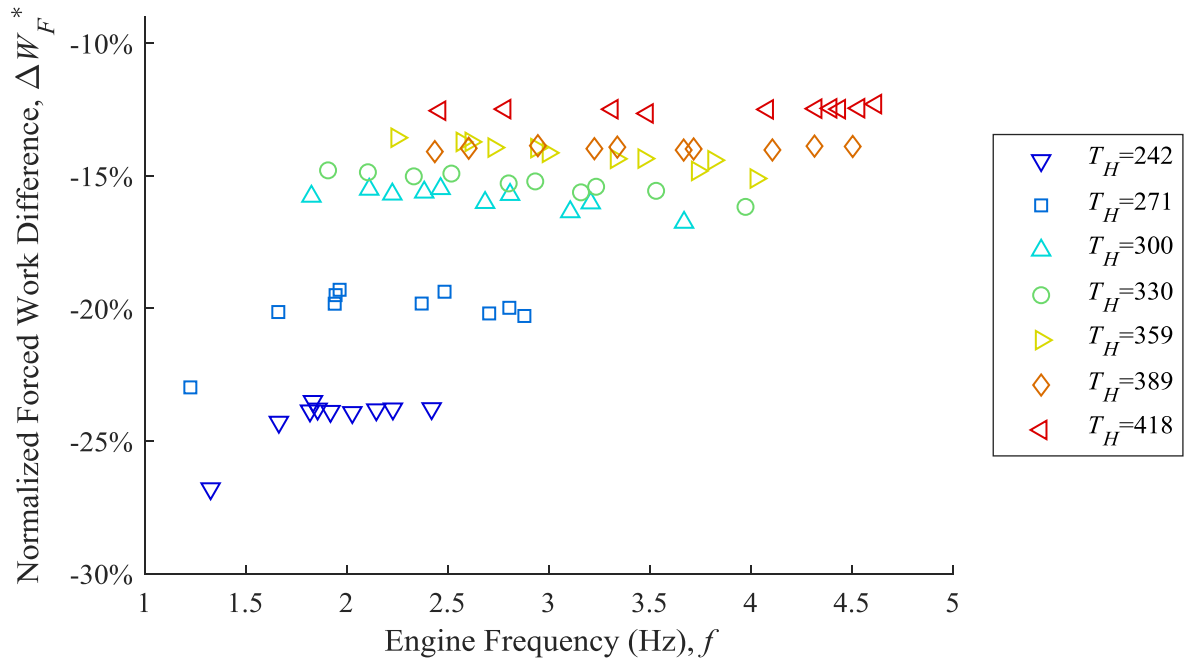
Forced work ( $W_F$ ) is used to calculate mechanical losses in Senft's [32] Fundamental Efficiency Theorem. It is the work transmitted to the piston when it is moving against the net pressure acting on it [27]. Forced work is calculated with the pressure-volume functions of the engine and buffer space [27]. The model assumes the buffer space is adiabatic to calculate forced work. The normalized forced work ( $\Delta W_F^*$ ) difference is the difference between the modelled and experimental forced work ( $W_{F,md} - W_{F,xp}$ ) divided by the experimental indicated work, as defined by Equation 5-10. It is equal to zero if the forced work estimate is accurate. Negative values translate to the model under-estimating forced work. Integer increases of the normalized forced work difference equate to a forced work difference equal to the experimental indicated work.

$$\Delta W_F^* = \frac{W_{F,md} - W_{F,xp}}{W_{I,xp}} \quad 5-10$$

Figure 5-11 presents the normalized forced work as a percentage for samples charged to (a) 517 kPa and (b) 621 kPa. It ranges from  $-27\%$  to  $-12\%$ . Therefore, the modelled forced work is less than the experimental forced work at all operating conditions. Forced work has a greater influence on mechanical loss estimates than indicated work because it transfers through the mechanism twice [27]. The accuracy of the forced work estimate depends on the accuracy of the modelled engine pressure and modelled buffer pressure. Consequently, the estimate of mechanical losses could be more accurate with a more accurate reference cycle.



(a)



(b)

Figure 5-11: Plot of the normalized forced work difference at (a) the 517 kPa charge pressure and (b) the 621 kPa charge pressure.

Figure 5-11 shows that the normalized forced work difference is closer to zero at higher thermal source temperatures. This indicates that the estimate of forced work is more accurate at higher source temperatures. As a result, the estimate of mechanical losses may be more accurate at higher source temperatures. The accuracy of the mechanical losses are tied to the accuracy of reference cycle calculation, which is more accurate at higher source temperatures. Therefore, if the reference cycle accuracy improves at lower temperature ratios, the mechanical loss accuracy could improve with it.

### 5.3.4 Decoupled Loss Summary

The mechanical efficiency and forced work were estimated more accurately at higher thermal source temperatures. Most power loss mechanisms, included or excluded from the model, do not depend on source temperature. However, the mechanical loss estimate requires an accurate reference cycle calculation. The model over-estimated indicated work and under-estimated forced work. This leads to under-estimated mechanical losses. As the accuracy of the indicated work and forced work estimates improve, the mechanical loss estimate could improve. A more accurate reference cycle calculation is likely to improve the mechanical loss estimate at all temperature ratios.

The 2<sup>nd</sup> order model may not properly calculate the frequency dependence of the power loss mechanisms included in it. The GSH correlation accuracy increases with increasing frequency. This shows that its accuracy is dependent on engine frequency and that the correlation should be recalculated or replaced. However, this does not explain the decrease in mechanical efficiency accuracy when engine frequency increases. The flow friction calculations could be inaccurate but these could not be investigated with the instruments used. Another potential source of error is the constant mechanism effectiveness used to calculate mechanical losses with the Fundamental

Efficiency Theorem. The mechanism may be less effective at transmitting energy as the shaking forces and inertial loads increase with engine frequency. This could be corrected with more sophisticated mechanical loss calculations that depend on engine frequency.

Adding losses excluded from the 2<sup>nd</sup> order model can improve its accuracy. Two decoupled power losses were excluded from the model—heat transfer hysteresis and finite piston speed loss. Heat transfer hysteresis accounts for the work lost to irreversible heat transfer in the engine. Ideally, this loss mechanism is included in the reference cycle calculation. Finite piston speed loss accounts for increased resistance on the piston due to higher and lower pressure acting on the piston face as it compresses and expands the working space, respectively. Its validity is unknown because both Speer [79] and the author were unable to find or recreate its derivation. The decoupled losses excluded from the model are either better included in the reference cycle calculation or of unknown validity. Therefore, model improvements should be made to the existing power loss mechanisms and the reference cycle calculation, rather than adding new decoupled loss mechanisms.



## 5.4 Model Accuracy Summary

---

The accuracy of a 2<sup>nd</sup> order model was analyzed at seven thermal source temperatures, two charge pressures, and engine frequencies ranging from 1.2 to 4.6 Hz. The study was divided into three sections—overall model accuracy, reference cycle accuracy, and decoupled power loss accuracy. The goal of the analysis was to determine if the model would be appropriate to model a LTDSE and determine how the model could be improved for modelling LTDSEs.

The current 2<sup>nd</sup> order model was not acceptable for modelling LTDSEs. The overall accuracy of the model was poor at all conditions and was worse at lower thermal source temperatures. Similarly, the reference cycle and the decoupled power losses were less accurate at lower thermal source temperatures. This shows that the 2<sup>nd</sup> order model would not accurately model a LTDSE and potentially Stirling engines at any operating conditions.

Two changes to the reference cycle calculation have potential to improve its accuracy. Semi-adiabatic reference cycle calculations include irreversible heat transfer in the expansion space and compression space. Work is lost to the irreversible heat transfer. Hence, a semi-adiabatic reference cycle could improve the estimate of indicated work. Leakage between the engine and crankcase influences the indicator diagram similarly to the discrepancies between the modelled and experimental indicator diagrams. Both of these loss mechanisms have a greater influence on the performance of LTDSEs compared to HTDSEs [17,18]. Replacing the adiabatic reference cycle with a semi-adiabatic reference cycle and adding leakage to the reference cycle calculation are recommended as the first steps to improve the model accuracy.

Improving the existing decoupled loss calculations may best improve the accuracy of the 2<sup>nd</sup> order model accuracy. The gas spring hysteresis correlation calculated by Speer [79] was inaccurate in its intended range. It could be recalculated. Alternately, it could be replaced by a

general method more suitable for design. Mechanical losses are currently estimated with a constant mechanism effectiveness. However, the mechanism could generate more friction with frequency dependent loads, such as shaking forces. Mechanical losses should be calculated with a more sophisticated method to better estimate the power losses of the engine. Improving the mechanical loss calculation and gas spring hysteresis calculation round out the recommended changes to the 2<sup>nd</sup> order model.

---

## 6 CONCLUSIONS

---

This thesis addressed two goals. The first goal was to experimentally determine the influence of flywheel polar moment of inertia on the transient and steady-state performance of a Stirling engine. The second goal was to evaluate the accuracy of a 2<sup>nd</sup> order model at decreasing thermal source temperatures and to determine how the model could best be improved to model LTDSEs.

Flywheel polar moment of inertia changed the transient and steady-state behavior of the low-temperature ST05G. The settling time of the transient engine frequency increased and the overshoot of the engine frequency decreased when the flywheel polar moment of inertia increased. However, changing flywheel polar moment of inertia did not change the engine frequency at free-running steady-state. The engine had smaller angular velocity fluctuations at loaded steady-state with larger flywheels. This did not translate into a significant change in shaft power or thermodynamic performance. The angular velocity fluctuated twice per revolution due to regions of efficacious and forced work. This motivated the creation of a generic flywheel size calculation method from the Fundamental Efficiency Theorem. It was shown to be accurate for an order of magnitude estimate of flywheel size.

The 2<sup>nd</sup> order model investigated was inaccurate at all conditions tested and its accuracy decreased at lower thermal source temperatures. It was identified that the reference cycle calculation and decoupled power loss calculations could improve. The reference cycle may be improved by using a semi-adiabatic reference cycle calculation that includes leakage between engine and crankcase. This can not only improve the accuracy of the reference cycle but also the accuracy of the mechanical loss calculation. A more sophisticated method to estimate mechanical losses should replace the Fundamental Efficiency Theorem. The gas spring hysteresis correlation

should be recalculated or replaced. The updated model would need to be evaluated to confirm that these changes improve the model.

Future work could address the following topics:

1. Evaluate the transient and steady-state performance of Stirling engines with a flywheel polar moment of inertia that causes large angular velocity fluctuations ( $CS > 0.16$ ).
2. Study the accuracy of a Stirling engine thermodynamic model that includes irreversible heat transfer in all engine cells, leakage, and sophisticated mechanical losses at a range of thermal source temperatures.

---

## REFERENCES

---

- [1] Intergovernmental Panel on Climate Change, 2018, IPCC Special Report on the Impacts of Global warming of 1.5°C - Summary for Policymakers, Intergovernmental Panel on Climate Change.
- [2] National Energy Board Canada, 2019, “Provincial and Territorial Energy Profiles – Alberta,” [www.neb-one.gc.ca](http://www.neb-one.gc.ca) [Online]. Available: <https://www.neb-one.gc.ca/nrg/ntgrtd/mrkt/nrgsstmprfls/ab-eng.html>. [Accessed: 07-Feb-2019].
- [3] Government of Alberta, 2019, “Phasing out coal pollution,” [www.alberta.ca](http://www.alberta.ca) [Online]. Available: <https://www.alberta.ca/climate-coal-electricity.aspx>. [Accessed: 07-Feb-2019].
- [4] Alberta Electric System Operator, 2018, AESO 2017 Annual Market Statistics.
- [5] Grasby, S. E., Allen, D. M., Bell, S., Chen, Z., Ferguson, G., Jessop, A., Kelman, M., Ko, M., Majorowicz, J., Moore, M., Raymond, J., and Therrien, R., 2012, Geothermal Energy Resource Potential of Canada, Calgary.
- [6] CMC, AITF, and AIHA, 2014, Community Integrated Energy Mapping Feasibility Study In Alberta’s Industrial Heartland And Strathcona Industrial Area.
- [7] CanGEA, Alberta Favourability Maps, Calgary, Canada.
- [8] West, C. D., 1986, Principles and Applications of Stirling Engines, Van Nostrand Reinhold Company Inc., New York.
- [9] Walker, G., 1973, Stirling-Cycle Machines, Oxford University Press.
- [10] Kolin, I., Koscak-kolin, S., and Golub, M., 2000, “Geothermal Electricity Production By Means Of The Low Temperature Difference Stirling Engine,” World Geothermal Congress

- 2000, Kyushu, pp. 3199–3203.
- [11] Senft, J. R., 1996, *An Introduction to Low Temperature Differential Stirling Engines*, Moriya Press.
- [12] Cool Energy Inc., 2016, “ThermoHeart TM 25 kW e High Performance Stirling Engine,” pp. 1–8.
- [13] Sun Orbit, 2015, “Sun Orbit” [Online]. Available: <https://web.archive.org/web/20170623154430/http://www.sun-orbit.de:80/>. [Accessed: 15-Feb-2019].
- [14] Hargreaves, C. M., 1991, *The Philips Stirling Engine*, Elsevier Science Publishing Company Inc., New York.
- [15] EPRI, 2002, *Stirling Engine Assessment*, Palo Alto.
- [16] Chen, N. C. J., and Griffin, F. P., 1983, *A Review of Stirling Engine Mathematical Models*.
- [17] Kolin, I., 1991, *Stirling Motor: History - Theory - Practice*, Zagreb University Publications, Ltd., Dubrovnik.
- [18] Yang, D., and Gschwendtner, M., 2018, “Hysteresis Loss in Near-Ambient Stirling Refrigerators,” *The 18th International Stirling Engine Conference*, International Stirling Engine Committee, Tainan.
- [19] ElectrTherm, 2015, “Power+ Generator 4200 – Up to 35kWe,” [electratherm.com](http://electratherm.com) [Online]. Available: <https://electratherm.com/products/power-plus-generator-4200-up-to-35kwe/>. [Accessed: 05-Feb-2019].
- [20] GlobalGeothermal, 2019, “GlobalGeothermal-Solutions,” <http://www.globalgeothermal.com> [Online]. Available:

<http://www.globalgeothermal.com/Solutions.aspx>. [Accessed: 02-Feb-2019].

- [21] Vining, C. B., 2009, “An inconvenient truth about thermoelectrics,” *Nat. Mater.*, **8**(2), pp. 83–85.
- [22] Vélez, F., Segovia, J. J., Martín, M. C., Antolín, G., Chejne, F., and Quijano, A., 2012, “A technical, economical and market review of organic Rankine cycles for the conversion of low-grade heat for power generation,” *Renew. Sustain. Energy Rev.*, **16**(6), pp. 4175–4189.
- [23] Borgnakke, C., and Sonntag, R. E., 2013, *Fundamentals of Thermodynamics*, John Wiley & Sons, Ltd.
- [24] Varga, Z., and Palotai, B., 2017, “Comparison of low temperature waste heat recovery methods,” *Energy*, **137**, pp. 1286–1292.
- [25] Walker, G., and Senft, J. R., 1985, *Free Piston Stirling Engines*, Springer-Verlag, Berlin.
- [26] Sparavigna, A. C., 2016, “Teaching Reitlinger Cycles To Improve Students ’ Knowledge And Comprehension Of Thermodynamics,” *Mech. Mater. Sci. Eng.*, (January), pp. 1–6.
- [27] Senft, J. R., 2007, *Mechanical Efficiency of Heat Engines*, Cambridge University Press, New York.
- [28] Craun, M., and Bamieh, B., 2018, “Optimal Periodic Control of an Ideal Stirling Engine Model,” **137**(July 2015), pp. 1–10.
- [29] Urieli, I., and Berchowitz, D. M., 1984, *Stirling Cycle Engine Analysis*, Adam Hilger Ltd, Bristol.
- [30] Reader, G. T., and Hooper, C., 1983, *Stirling Engines*, E. & F. N. Spon, London.
- [31] Curzon, F. L., and Ahlborn, B., 1975, “Efficiency of a Carnot engine at maximum power output,” *Am. J. Phys.*, **43**(1), pp. 22–24.

- [32] Senft, J. R., 1987, "Mechanical Efficiency of Kinematic Heat Engines," *J. Franklin Inst.*, **324**(2), pp. 273–290.
- [33] Cleghorn, W. L., and Dechev, N., 2015, *Mechanics of Machines*, Oxford University Press, New York.
- [34] Martini, W., 1983, *Stirling Engine Design Manual*.
- [35] Cheng, C., and Yu, Y., 2011, "Dynamic simulation of a beta-type Stirling engine with cam-drive mechanism via the combination of the thermodynamic and dynamic models," *Renew. Energy*, **36**(2), pp. 714–725.
- [36] Senft, J. R., 1982, "A simple derivation of the generalized Beale number," *IECEC '82; Proceedings of the Seventeenth Intersociety Energy Conversion Engineering Conference*, pp. 1652–1655.
- [37] Stumpf, C. J. A., 2019, "Parametric Optimization of a Low Temperature Difference Gamma-Type Stirling Engine to Maximize Shaft Power," University of Alberta.
- [38] Sayyaadi, H., and Ghasemi, H., 2018, "A novel second-order thermal model of Stirling engines with consideration of losses due to the speed of the crank system," *Energy Convers. Manag.*, **168**(April), pp. 505–521.
- [39] Organ, A. J., 2014, *Stirling Cycle Engines: Inner Workings and Design*, John Wiley & Sons, Ltd, Chichester.
- [40] Alfarawi, S., Al-Dadah, R., and Mahmoud, S., 2016, "Enhanced thermodynamic modelling of a gamma-type Stirling engine," *Appl. Therm. Eng.*, **106**, pp. 1380–1390.
- [41] Cengel, Y. A., 2007, *Heat and Mass Transfer: A Practical Approach*, McGraw-Hill, New York.



- [42] Gedeon, D., and Wood, J. G., 1996, Oscillating-Flow Regenerator Test Rig: Hardware and Theory With Derived Correlations for Screens and Felts.
- [43] Thomas, B., and Pittman, D., 2000, "Update on the evaluation of different correlations for the flow friction factor and heat transfer of Stirling engine regenerators," 35th Intersociety Energy Conversion Engineering Conference and Exhibit, American Institute of Aeronautics and Astronautics Inc, Las Vegas, pp. 76–84.
- [44] Zhao, T. S., and Cheng, P., 1996, "Experimental investigations of the onset of turbulence and frictional losses in an oscillatory pipe flow," *Int. J. Heat Fluid Flow*, **17**(May 1995), pp. 356–362.
- [45] Barreno, I., Costa, S. C., Cordon, M., Tutar, M., Urrutibeascoa, I., Gomez, X., and Castillo, G., 2015, "Numerical correlation for the pressure drop in Stirling engine heat exchangers," *Int. J. Therm. Sci.*, **97**, pp. 68–81.
- [46] Zhao, T. S., and Cheng, P., 1996, "The friction coefficient of a fully developed laminar reciprocating flow in a circular pipe," *Int. J. Heat Fluid Flow*, **17**(2), pp. 167–172.
- [47] Mabrouk, M. T., Kheiri, A., and Feidt, M., 2015, "Effect of leakage losses on the performance of a  $\beta$  type Stirling engine," *Energy*, **88**, pp. 111–117.
- [48] Huang, Y., 1994, "Leakage calculation through clearances," International Compressor Engineering Conference, Purdue University, pp. 35–40.
- [49] Li, R., Grosu, L., and Queiros-Condé, D., 2016, "Losses effect on the performance of a Gamma type Stirling engine," *Energy Convers. Manag.*, **114**, pp. 28–37.
- [50] Gedeon, D., and Wood, J., 1992, Oscillating-flow regenerator test rig: Woven screen and metal felt results, Athens.
- [51] Pfeiffer, J., and Kuehl, H.-D., 2014, "Review of Models for Appendix Gap Losses in

- Stirling Cycle Machines,” *J. Propuls. Power*, **30**(5), pp. 1419–1432.
- [52] Petrescu, S., Borcila, B., Costea, M., Banches, E., Popescu, G., Boriaru, N., Stanciu, C., and Dobre, C., 2016, “Concepts and fundamental equations in Thermodynamics with Finite Speed,” 7th International Conference on Advanced Concepts in Mechanical Engineering, IOP Publishing Ltd.
- [53] Cheng, C. H., and Yu, Y. J., 2012, “Combining dynamic and thermodynamic models for dynamic simulation of a beta-type Stirling engine with rhombic-drive mechanism,” *Renew. Energy*, **37**(1), pp. 161–173.
- [54] Millington, B. W., and Hartles, E. R., 1968, “Frictional Losses in Diesel Engines.”
- [55] Yang, H., Cheng, C., and Huang, S., 2018, “A complete model for dynamic simulation of a 1-kW class beta-type Stirling engine with rhombic-drive mechanism,” *Energy*, **161**, pp. 892–906.
- [56] Egas, J., and Clucas, D. M., 2018, “Stirling engine configuration selection,” *Energies*, **11**(3), pp. 1–22.
- [57] Kongtragool, B., and Wongwises, S., 2003, “A review of solar-powered Stirling engines and low temperature differential Stirling engines,” *Renew. Sustain. Energy Rev.*, **7**(2), pp. 131–154.
- [58] Hoegel, B., Pons, D., Gschwendtner, M., Tucker, A., and Sellier, M., 2014, “Thermodynamic peculiarities of alpha-type Stirling engines for low-temperature difference power generation: Optimisation of operating parameters and heat exchangers using a third-order model,” *J. Mech. Eng. Sci.*, **228**(11), pp. 1936–1947.
- [59] Berchowitz, D. M., 1978, “A computer and experimental simulation of Stirling cycle machines,” University of Witwatersrand.

- [60] Urieli, I., 1977, “A Computer Simulation of Stirling Cycle Machines,” University of the Witwatersrand.
- [61] Robson, A., Grassie, T., and Kubie, J., 2007, “Modelling of a low-temperature differential Stirling engine,” *J. Mech. Eng. Sci.*, **221**, pp. 927–944.
- [62] Chen, W. L., 2017, “A study on the effects of geometric parameters in a low-temperature-differential  $\gamma$ -type Stirling engine using CFD,” *Int. J. Heat Mass Transf.*, **107**, pp. 1002–1013.
- [63] Kato, Y., 2016, “Indicated diagrams of a low temperature differential Stirling engine using flat plates as heat exchangers,” *Renew. Energy*, **85**, pp. 973–980.
- [64] VE-Ingenieure, “The ST05G Stirling Engine Project,” [www.ve-ingenieure.de](http://www.ve-ingenieure.de) [Online]. Available: [https://web.archive.org/web/20160410112244/http://www.ve-ingenieure.de/projekt\\_st05g\\_cnc\\_engl.html](https://web.archive.org/web/20160410112244/http://www.ve-ingenieure.de/projekt_st05g_cnc_engl.html). [Accessed: 29-Nov-2018].
- [65] VE-Ingenieure, 2009, “ST05G-CNC Mechanical Drawings.”
- [66] VE-Ingenieure, “ST05G Technical Specifications,” [www.ve-ingenieure.de](http://www.ve-ingenieure.de) [Online]. Available: [https://web.archive.org/web/20150915094555fw\\_/http://www.ve-ingenieure.de:80/viebachstirling/technischdaten.htm](https://web.archive.org/web/20150915094555fw_/http://www.ve-ingenieure.de:80/viebachstirling/technischdaten.htm). [Accessed: 29-Nov-2018].
- [67] Gheith, R., Aloui, F., Tazerout, M., and Ben Nasrallah, S., 2012, “Experimental investigations of a gamma Stirling engine,” *Int. J. Energy Res.*, **36**(12), pp. 1175–1182.
- [68] Gheith, R., Aloui, F., and Nasrallah, S. Ben, 2012, “Study of the regenerator constituting material influence on a gamma type Stirling engine,” *J. Mech. Sci. Technol.*, **26**(4), pp. 1251–1255.
- [69] Gheith, R., Aloui, F., and Ben Nasrallah, S., 2014, “Study of temperature distribution in a Stirling engine regenerator,” *Energy Convers. Manag.*, **88**, pp. 962–972.

- [70] Gheith, R., Hachem, H., Aloui, F., and Ben Nasrallah, S., 2015, “Experimental and theoretical investigation of Stirling engine heater: Parametrical optimization,” *Energy Convers. Manag.*, **105**, pp. 285–293.
- [71] Gheith, R., Aloui, F., and Ben Nasrallah, S., 2015, “Determination of adequate regenerator for a Gamma-type Stirling engine,” *Appl. Energy*, **139**, pp. 272–280.
- [72] Hachem, H., Gheith, R., Aloui, F., and Ben Nasrallah, S., 2015, “Numerical characterization of a gamma-Stirling engine considering losses and interaction between functioning parameters,” *Energy Convers. Manag.*, **96**, pp. 532–543.
- [73] Hachem, H., Creyx, M., Gheith, R., Delacourt, E., Morin, C., Aloui, F., and Nasrallah, S. Ben, 2015, “Comparison based on exergetic analyses of two hot air engines: A Gamma type Stirling engine and an open joule cycle Ericsson engine,” *Entropy*, **17**(11), pp. 7331–7348.
- [74] Bert, J., Chrenko, D., Sophy, T., Le Moyne, L., and Sirot, F., 2014, “Simulation, experimental validation and kinematic optimization of a Stirling engine using air and helium,” *Energy*, **78**, pp. 701–712.
- [75] Alfarawi, S., AL-Dadah, R., and Mahmoud, S., 2016, “Influence of phase angle and dead volume on gamma-type Stirling engine power using CFD simulation,” *Energy Convers. Manag.*, **124**, pp. 130–140.
- [76] Alfarawi, S., AL-Dadah, R., and Mahmoud, S., 2017, “Potentiality of new miniature-channels Stirling regenerator,” *Energy Convers. Manag.*, **133**, pp. 264–274.
- [77] Hooshang, M., Askari Moghadam, R., Alizadeh Nia, S., and Masouleh, M. T., 2015, “Optimization of Stirling engine design parameters using neural networks,” *Renew. Energy*, **74**, pp. 855–866.
- [78] Hooshang, M., Askari Moghadam, R., and AlizadehNia, S., 2016, “Dynamic response

- simulation and experiment for gamma-type Stirling engine,” *Renew. Energy*, **86**, pp. 192–205.
- [79] Speer, C. P., 2018, “Modifications to Reduce the Minimum Thermal Source Temperature of the ST05G-CNC Stirling Engine,” University of Alberta.
- [80] Miller, D. A., Speer, C., and Nobes, D. S., 2018, “Performance of ST05G-CNC Stirling Engine Modified for Operation with Reduced Source Temperature,” *The 18th International Stirling Engine Conference*, International Stirling Engine Committee, Tainan.
- [81] Jadon, V. K., and Verma, S., 2010, *Analysis and Design of Machine Elements*, I. K. International Pvt Ltd., New Delhi.
- [82] Scollo, L. S., Valdez, P. E., Santamarina, S. R., Chini, M. R., and Baro, J. H., 2012, “Twin cylinder alpha stirling engine combined model and prototype redesign,” **8**, pp. 2–10.
- [83] Cheng, C. H., and Yu, Y. J., 2010, “Numerical model for predicting thermodynamic cycle and thermal efficiency of a beta-type Stirling engine with rhombic-drive mechanism,” *Renew. Energy*, **35**(11), pp. 2590–2601.
- [84] Ipci, D., and Karabulut, H., 2018, “Thermodynamic and dynamic analysis of an alpha type Stirling engine and numerical treatment,” *Energy Convers. Manag.*, **169**(December 2017), pp. 34–44.
- [85] Altin, M., Okur, M., Ipci, D., Halis, S., and Karabulut, H., 2018, “Thermodynamic and dynamic analysis of an alpha type Stirling engine with Scotch Yoke mechanism,” *Energy*, **148**, pp. 855–865.
- [86] Cole Parmer Instrument Company LLC., “Masterflex L/S Tubing Options,” [www.masterflex.com](http://www.masterflex.com) [Online]. Available: <https://www.masterflex.com/tech-article/masterflex-ls-tubing-options>. [Accessed: 31-Jan-2018].

- [87] Omega Engineering Inc., 2017, “Temperature & Process Controllers User’s Guide.”
- [88] ASHRAE, 2013, 2013 ASHRAE Handbook - Fundamentals, ASHRAE, Atlanta.
- [89] McMaster-Carr Supply Company, “Vibrate-Damping Precision Flexible Shaft Coupling,” [www.mcmaster.com](http://www.mcmaster.com) [Online]. Available: <https://www.mcmaster.com/9845t5>. [Accessed: 01-Feb-2019].
- [90] Microsoft, 2018, “Memory Limits for Windows and Windows Server Releases,” [docs.microsoft.com](https://docs.microsoft.com/en-gb/windows/desktop/Memory/memory-limits-for-windows-releases#physical-memory-limits-windows-xp) [Online]. Available: <https://docs.microsoft.com/en-gb/windows/desktop/Memory/memory-limits-for-windows-releases#physical-memory-limits-windows-xp>. [Accessed: 18-Jan-2019].
- [91] Validyne Engineering, “Resolution and Frequency Response in Pressure Transducers,” [www.validyne.com](http://www.validyne.com/blog/resolution-and-frequency-response-in-pressure-transducers/) [Online]. Available: <http://www.validyne.com/blog/resolution-and-frequency-response-in-pressure-transducers/>. [Accessed: 01-Feb-2019].
- [92] Bosch Sensortec, 2018, “BMP 280: Data Sheet.”
- [93] PCB Piezotronics Inc., 2018, “Dynamic Pressure Sensors for High Frequency Measurements,” pp. 1–4.
- [94] Wheeler, A. J., Ghanji, A. R., Krishnan, V. V., and Thurow, B. S., 2010, Introduction to Engineering Experimentation, Pearson Higher Education, Upper Saddle River.
- [95] Cengel, Y. A., and Cimbala, J. M., 2014, Fluid Mechanics, McGraw-Hill, New York.
- [96] Paul, C. J., and Engeda, A., 2015, “Modeling a complete Stirling engine,” *Energy*, **80**, pp. 85–97.

---

## APPENDIXES

---

This thesis has four appendixes as follows:

Appendix A. provides sample calculations for uncertainty.

Appendix B. contains the changes to the 2<sup>nd</sup> order model.

Appendix C. contains the data processing MATLAB® code.

Appendix D. contains mechanical drawings of the changes to the low-temperature ST05G.

---

## A. UNCERTAINTY

---

This appendix presents example calculations for all values presented in this thesis. It is divided into three sections: (1) uncertainty of measurements, (2) uncertainty of calculations, and (3) propagation of uncertainty. The uncertainty of measurements defines the uncertainty of data measured with the instruments and equipment installed on the engine. The uncertainty of calculations section presents the parameters derived from measurements that do not follow propagation of uncertainty. Finally, the propagation of uncertainty determines the uncertainty of most parameters derived from measurements.

All uncertainty calculations presented here are from a single data set. Appendix Table A-1 defines the operating condition and engine performance at the data set examined. Many parameters are from a sample within the data set rather than representative of the entire dataset.

Appendix Table A-1: Sample experiment operating condition and performance.

Parameter	Value(s)
Thermal Source Temperature ( $^{\circ}\text{C}$ ), $T_H$	300
Thermal Sink Temperature ( $^{\circ}\text{C}$ ), $T_C$	21
Flywheel Moment of Inertia ( $\text{kg m}^2$ ), $I_{fly}$	(B) 0.2539
Charge Pressure ( $\text{kPa}$ ), $p_{charge}$	621
Torque Load ( $\text{N m}$ ), $\tau_E$	Maximum Power Load
Shaft Power ( $\text{W}$ ), $\dot{W}_S$	3.62



## Uncertainty of Measurements

---

This section presents sample calculations of the uncertainty of measurements. Measured quantities are the thermal source temperature, thermal sink temperature, coolant flow rate, crankshaft angular position, dynamic torque, working gas temperature, coolant temperature, static working gas pressure, and dynamic working gas pressure. Some of these measurements have an uncertainty component from measurement noise. This is calculated with the 95 % confidence interval methods from Wheeler and Ganji [1].

### Thermal Source Temperature Control

Uncertainty of the temperature displayed on the temperature controller (CN8DPT-440-C24, Omega Engineering Inc.).

Appendix Table A-2: Thermal source temperature uncertainty.

Uncertainty Source	Type	Value (°C)	Comment
Observed range	Systematic	2	Observed during experiments.
Feedback Sensor Accuracy	Systematic	0.4	Type-K Thermocouple Uncertainty [2]
Display Resolution	Systematic	0.1	Temperature Controller Display Resolution
Total Uncertainty		2.04	

## Thermal Sink Temperature Control

Uncertainty of the temperature displayed on the water bath (12101-41, Cole-Parmer Instrument Company, LLC.).

Appendix Table A-3: Thermal sink temperature uncertainty.

Uncertainty Source	Type	Value (°C)	Comment
Observed range	Systematic	2	Observed during experiments.
Readout Accuracy	Systematic	0.25	Readout accuracy [3].
Display Resolution	Systematic	0.1	Water bath display resolution
Total Uncertainty		2.01	

## Coolant Flow Rate

Uncertainty of the flow rate set on the peristaltic pump (12101-41, Cole-Parmer Instrument Company, LLC.).

Appendix Table A-4: Coolant flow rate uncertainty.

Uncertainty Source	Type	Value (L/min)	Comment
Contamination and calibration.	Systematic	0.01	Observed during calibration.
Display Resolution	Systematic	0.001	Peristaltic pump display resolution
Spatial Variation	Systematic	-	Ignored because no alternate flow path.
Time Constant	Systematic	-	Ignored because pump operation is continuous.
Total Uncertainty		0.01	

## Crankshaft Angular Position Measurements

Uncertainty of the angular position measurements from the rotary encoder (15S 19M1 0500NV1ROC F03 S1, Encoder Products Company).

Appendix Table A-5: List of Crankshaft Angular Position Instrument Specifications

Specification	Value (cite)	Unit
Model	15S 19M1 0500NV1ROC F03 S1	-
A-Pulses Per Revolution	500	-
Z-Pulses Per Revolution	1	-
Pulse Count Threshold	2.5	V
Angular Division	0.0126	rad

Appendix Table A-6: Absolute Crankshaft Angular Position Uncertainty

Uncertainty Source	Type	Value (rad)	Comment
Random Uncertainty	Random	-	Negligible because noise does not exceed 2.5 V threshold
Mechanical Communication Accuracy	Systematic	0.017	1 ° mechanical play
Mechanical Accuracy	Systematic	0.0003	0.017 ° manufacturer accuracy [4]
Alignment Procedure Uncertainty	Systematic	0.0232 <sup>1</sup>	0.0127 mm piston position uncertainty converted to crankshaft angle with cosine law.
I/O Device Accuracy	Random & Systematic	-	Negligible because uncertainty does not exceed 2.5 V threshold
Total Uncertainty		0.0407	

$$^1 u_{\theta,alignment} = \cos^{-1} \left( \frac{r_3^2 - r_2^2 - r_4^2}{2 \cdot r_2 \cdot r_4} \right), \text{ where: } r_4 = r_2 + r_3 - 0.0127\text{mm}$$

Appendix Table A-7: Relative Crankshaft Angular Position Uncertainty

Uncertainty Source	Type	Value (rad)	Comment
Random Uncertainty	Random	-	Negligible because noise does not exceed 3 V threshold
Mechanical Accuracy	Systematic	0.0003	0.017 ° manufacturer accuracy [4]
I/O Device Accuracy	Random & Systematic	-	Negligible because uncertainty does not exceed 3 V threshold
Total Uncertainty		0.0003	

## Dynamic Torque Measurements

Uncertainty of the dynamic torque measurements by the 1 N m torque transducer (TRS600-1Nm, Futek Advanced Sensor Technology Inc.).

Appendix Table A-8: List of Dynamic Torque Instrument Specifications

Specification	Value [5]	Unit
Model	TRS600-1Nm, Futek Advanced Sensor Technology Inc.	-
Measurement Range	$\pm 1$	N m
Full Scale	1	N m

Appendix Table A-9: Dynamic Torque Uncertainty

Uncertainty Source	Type	Value (N m)	Comment
Random Uncertainty	Random	0.0018	From experiment data and unique to each averaged group of samples.
Instrument nonrepeatability	Random	0.002	0.2 % full scale [5]
Instrument nonlinearity	Systematic	0.002	0.2 % full scale [5]
Instrument hysteresis	Systematic	0.001	0.1 % full scale [5]
I/O Device Accuracy	Random & Systematic	0.0003	NI-6211 absolute accuracy at 10 V full scale. (0.00269 V)*(1 N m/10 V) [6]
Time Constant	Systematic	-	Unnecessary for steady-state mean value.
Total Uncertainty		0.0035	

## Working Gas Temperature Measurements

Uncertainty of the gas temperature measurements by type-K thermocouples (HKMTSS-062E-6, Omega Engineering Inc.).

Appendix Table A-10: List of Working Gas Temperature Instrument Specifications

Specification	Value	Unit
Model	HKMTSS-062E-6, Omega Engineering Inc.	-
Measurement Range	21-418	°C
Full Scale	418	°C
Instrument Uncertainty	3.135	°C

Appendix Table A-11: Working Gas Temperature Uncertainty

Uncertainty Source	Type	Value (°C)	Comment
Random Uncertainty	Random	0.0016	From experiment data and unique to averaged group of samples.
Instrument Uncertainty	Random & Systematic	3.135	0.75 % of 400 °C (greater of 2.2 °C or 0.75 %) [7]
Cold Junction Repeatability	Random	0.35	Cold junction repeatability from 15 to 35 °C [8]
Digitization Module Error	Random & Systematic	1.488	SCXI-1600 absolute accuracy at 0.05 V full scale. (0.061 mV)*(418 °C/17.158 mV) [9,10]
Calibration Thermometer Resolution	Systematic	0.1	ERTCO 1005-3S thermometer resolution [11]
Spatial Variation	Systematic	-	Ignored because sensor size is small (0.76 mm).
Time Constant	Systematic	-	Unnecessary for steady-state mean value.
Total Uncertainty		3.489	

## Coolant Temperature Measurements

Uncertainty of the coolant temperature measured by RTDs (RTD-810, Omega Engineering Inc.).

Appendix Table A-12: List of Coolant Temperature Instrument Specifications

Specification	Value	Unit
Model	RTD-810, Omega Engineering Inc.	-
Measurement Range	5-50	°C
Full Scale	50	°C
Instrument Uncertainty	0.35 [12]	°C

Appendix Table A-13: Coolant Temperature Uncertainty

Uncertainty Source	Type	Value (°C)	Comment
Random Uncertainty	Random	0.005	From experiment data and unique to averaged group of samples.
Instrument Uncertainty	Random & Systematic	0.35	Class A RTD within 0-100 °C range [12].
RTD Module Accuracy	Random & Systematic	0.50	NI-9217 RTD module maximum accuracy for measurements within -200-150 °C [13]
Calibration Thermometer Resolution	Systematic	0.1	ERTCO 1005-3S thermometer resolution [11]
Spatial Variation	Systematic	-	Ignored because sensor in small cross-sectional area stream.
Time Constant	Systematic	-	Unnecessary for steady-state mean value.
Total Uncertainty		0.619	

## Mean Pressure Measurements

Uncertainty of the Validyne pressure transducer (DP-15, Validyne Engineering) measurements.

Appendix Table A-14: List of Mean Pressure Instrument Specifications

Specification	Value [14]	Unit
Model	DP-15, Validyne Engineering	-
Measurement Range	0-862	kPa (gauge)
Full Scale	862	kPa
Instrument Uncertainty	4.31	kPa

Appendix Table A-15: Mean Pressure Uncertainty

Uncertainty Source	Type	Value (kPa)	Comment
Random Uncertainty	Random	0.05	From experiment data and unique to averaged group of samples.
Instrument Uncertainty	Random & Systematic	4.31	0.5 % full scale [14]
Demodulator Linearity	Systematic	0.43	Validyne CD280 linearity. 0.05 % full scale [15]
Demodulator Stability	Systematic	0.86	Validyne CD280 stability. 0.1 % full scale [15]
I/O Device Accuracy	Random & Systematic	0.23	NI-6211 absolute accuracy at 10 V full scale. $(0.00269 \text{ V}) \cdot (862 \text{ kPa}/10 \text{ V})$ [6]
Calibration Device Resolution	Systematic	0.69	Druck DPI 603 display capability (125.0 psi) with unit conversion [16]
Spatial Variation	Systematic	-	Ignored for steady-state mean value
Time Constant	Systematic	-	Unnecessary for steady-state mean value.
Total Uncertainty		4.47	



## Dynamic (Relative) Pressure Measurements

Uncertainty of the flush-mount PCB pressure transducer (113B21, PCB Piezotronics Inc.) measurements.

Appendix Table A-16: List of Dynamic Pressure Instrument Specifications

Specification	Value [17]	Unit
Model	113B21, PCB Piezotronics Inc.	-
Measurement Range	$\pm 1420.5$	kPa (relative)
Full Scale	1421	kPa
Instrument Uncertainty	1 % of measurement	-

Appendix Table A-17: Dynamic Pressure Uncertainty

Uncertainty Source	Type	Value (kPa)	Comment
Random Uncertainty	Random	0.10	From experiment data and unique to averaged group of samples.
Instrument Uncertainty	Random & Systematic	0.68	1 % measurement ( $67.87 \text{ kPa}^{-1}$ ) [17]
I/O Device Accuracy	Random & Systematic	0.40	NI-6211 absolute accuracy at 5 V full scale. $(0.00269 \text{ V}) \cdot (1421 \text{ kPa}/5 \text{ V})$ [6]
Spatial Variation	Systematic	0.75	Pressure wave transport uncertainty. Pressure on piston face not equal to pressure at sensor.
Time Constant	Systematic	-	Constant mean pressure measured by other sensors negates relaxation time. Rise time less than $1 \mu\text{s}$ [18].
Total Uncertainty		1.91	

## Uncertainty Calculations

---

This section presents the sample calculations of uncertainty that does not follow the propagation of uncertainty. Parameters in this category are the angular velocity, non-constant volumes, and volume changes.

### Angular Velocity

The angular velocity uncertainty is the uncertainty of the slope between the first and last fit points.

$$B = \frac{34 \cdot \Delta\theta}{t_{i+17} - t_{i-17}} \quad \text{A-1}$$

$$U_{\dot{\theta}_i} = U_B = \frac{U_{\Delta\theta}}{t_{i+17} - t_{i-17}} + \frac{34 \cdot \Delta\theta \cdot U_{t_{i+17}}}{(t_{i+17} - t_{i-17})^2} + \frac{34 \cdot \Delta\theta \cdot U_{t_{i-17}}}{(t_{i+17} - t_{i-17})^2} \quad \text{A-2}$$

Appendix Table A-18: Angular Velocity Uncertainty

Variable	Symbol	Value	Units
Crank Angle Change	$\Delta\theta$	0.0126	rad
Relative Crank Angle Uncertainty	$U_{\Delta\theta}$	$\pm 0.0003$	rad
First fit point time	$t_{i-17}$	3.7547	s
First fit point time uncertainty	$Ut_{i-17}$	$\pm 1.67 \times 10^{-5}$	s
Last fit point time	$t_{i+17}$	3.7790	s
Last fit point time uncertainty	$Ut_{i+17}$	$\pm 1.67 \times 10^{-5}$	s
Angular Velocity Uncertainty	$U_{\dot{\theta}_i}$	$\pm 0.0364$	rad / s

## Volume Uncertainty

The volume uncertainty is the more deviant of the volumes leading and lagging by the crank angle uncertainty.

$$U_{V_i} = \max\left(\left|V(\theta+U_\theta)_i - V(\theta)_i\right|, \left|V(\theta-U_\theta)_i - V(\theta)_i\right|\right) \quad \text{A-3}$$

Appendix Table A-19: Maximum Engine Volume Uncertainty

Variable	Symbol	Value	Units
Crank Angle	$\theta$	1.332	rad
Crank Angle Uncertainty	$U_\theta$	$\pm 0.0407$	rad
Engine Volume	$V_E(\theta)$	1.6573	L
Leading Engine Volume	$V_E(\theta+U_\theta)$	1.6589	L
Lagging Engine Volume	$V_E(\theta-U_\theta)$	1.6555	L
Engine Volume Uncertainty	$U_{VE}$	$\pm 0.0017$	L

## Volume Change Uncertainty

Uncertainty of the engine volume changes is the more deviant of the volume changes leading and lagging by the angular position uncertainty.

$$U_{dV_i} = \max\left(\left|dV(\theta+U_\theta)_i - dV(\theta)_i\right|, \left|dV(\theta-U_\theta)_i - dV(\theta)_i\right|\right) \quad \text{A-4}$$

Appendix Table A-20: Maximum Engine Volume Change Uncertainty

Variable	Symbol	Value	Units
Crank Angle	$\theta$	0.025	rad
Crank Angle Uncertainty	$U_\theta$	$\pm 0.0407$	rad
Engine Volume Change	$dV_E(\theta)$	0.011	mL
Leading Engine Volume Change	$dV_E(\theta+U_\theta)$	0.037	mL
Lagging Engine Volume Change	$dV_E(\theta-U_\theta)$	-0.015	mL
Engine Volume Change Uncertainty	$U_{dVE}$	$\pm 0.026$	mL

## Propagation of Uncertainty

---

This section presents the sample propagation of uncertainty for calculated parameters in this thesis. The calculations follow the maximum uncertainty method from Wheeler and Ganji [1].

### Indicated Work

The propagation of uncertainty for phase-averaged indicated work.

$$W_I = \oint p_E \cdot dV_E \cong \sum_{i=1}^N (p_{E,i} \cdot dV_{E,i})$$

$$U_{W_I} = \sum_{i=1}^N \left( (U_{p_{E,i}} \cdot |dV_{E,i}|) + (U_{dV_{E,i}} \cdot |p_{E,i}|) \right)$$

A-5

Appendix Table A-21: Indicated work uncertainty.

Variable	Symbol	Value	Uncertainty	Units
Engine Pressure (1 <sup>st</sup> index)	$p_{E,1}$	691.5	± 1.91	kPa
Engine Volume Change (1 <sup>st</sup> index)	$dV_{E,1}$	0	± 0.0261	mL
Indicated Work	$W_I$	8.655	± 0.222	J

## Shaft Power

The propagation of uncertainty for sample averaged shaft power.

$$\dot{W}_S = \tau_{mean} \cdot \dot{\theta}_{mean}$$

$$U_{\dot{W}_S} = \left( U_{\tau_{mean}} \cdot |\dot{\theta}_{mean}| \right) + \left( U_{\dot{\theta}_{mean}} \cdot |\tau_{mean}| \right)$$

A-6

Appendix Table A-22: Shaft power uncertainty.

Variable	Symbol	Value	Uncertainty	Units
Mean Torque	$\tau_{mean}$	0.2053	$\pm 0.0035$	Nm
Mean Angular Velocity	$\dot{\theta}_{mean}$	17.649	$\pm 0.037$	rad/s
Shaft Power	$\dot{W}_S$	3.6207	$\pm 0.0625$	W

## Engine Frequency

The propagation of uncertainty for cycle average engine frequency.

$$f = \frac{\dot{\theta}_{mean}}{2 \cdot \pi}$$

$$U_f = \frac{U_{\dot{\theta}_{mean}}}{2 \cdot \pi}$$

A-7

Appendix Table A-23: Engine frequency uncertainty.

Variable	Symbol	Value	Uncertainty	Units
Mean Angular Velocity	$\dot{\theta}_{mean}$	17.649	$\pm 0.037$	rad/s
Engine Frequency	$f$	2.807	$\pm 0.0058$	Hz

## Gas Temperature Difference

The propagation of uncertainty for gas temperature difference.

$$\Delta T_{gas} = T_e - T_c$$

$$U_{\Delta T_{gas}} = U_{T_e} + U_{T_c}$$

A-8

Appendix Table A-24: Gas temperature difference uncertainty.

Variable	Symbol	Value	Uncertainty	Units
Expansion Space Temperature	$T_e$	248.96	$\pm 3.49$	$^{\circ}\text{C}$
Compression Space Temperature	$T_c$	23.98	$\pm 3.49$	$^{\circ}\text{C}$
Gas Temperature Difference	$\Delta T_{gas}$	3.6207	$\pm 6.97$	$^{\circ}\text{C}$



## Frequency Overshoot

The propagation of uncertainty for frequency overshoot calculated with transient experiment data.

$$f_{overshoot} = f_{max} - f_{steady-state}$$

$$U_{f_{overshoot}} = U_{f_{max}} + U_{f_{steady-state}}$$

A-9

Appendix Table A-25: Overshoot frequency uncertainty.

Variable	Symbol	Value	Uncertainty	Units
Maximum Frequency	$f_{max}$	4.546	$\pm 0.013$	Hz
Steady-State Frequency	$f_{steady-state}$	4.322	$\pm 0.012$	Hz
Shaft Power	$f_{overshoot}$	0.223	$\pm 0.025$	Hz

## Relative Angular Velocity

The propagation of uncertainty for phase-averaged relative angular velocity.

$$\dot{\theta}^* = \frac{\dot{\theta}_i - \dot{\theta}_{mean}}{\dot{\theta}_{mean}}$$

$$U_{\dot{\theta}^*} = \left( U_{\dot{\theta}_i} \cdot \left| \frac{1}{\dot{\theta}_{mean}} \right| \right) + \left( U_{\dot{\theta}_{mean}} \cdot \left| \frac{-\dot{\theta}_i}{\dot{\theta}_{mean}^2} \right| \right)$$

A-10

Appendix Table A-26: Relative angular velocity uncertainty.

Variable	Symbol	Value	Uncertainty	Units
Phase Averaged Angular Velocity	$\dot{\theta}_i$	17.57	$\pm 0.036$	rad/s
Mean Angular Velocity	$\dot{\theta}_{mean}$	17.64	$\pm 0.037$	rad/s
Relative Angular Velocity	$\dot{\theta}^*$	-0.0041	$\pm 0.0041$	-

## Coefficient of Speed Fluctuation

The propagation of uncertainty for phase-averaged coefficient of speed fluctuation.

$$CS = \frac{\dot{\theta}_{max} - \dot{\theta}_{min}}{\dot{\theta}_{mean}}$$

A-11

$$U_{CS} = \left( U_{\dot{\theta}_{max}} \cdot \left| \frac{1}{\dot{\theta}_{mean}} \right| \right) + \left( U_{\dot{\theta}_{min}} \cdot \left| \frac{-1}{\dot{\theta}_{mean}} \right| \right) + \left( U_{\dot{\theta}_{mean}} \cdot \left| \frac{-CS}{\dot{\theta}_{mean}} \right| \right)$$

Appendix Table A-27: Coefficient of speed fluctuation uncertainty.

Variable	Symbol	Value	Uncertainty	Units
Maximum Angular Velocity	$\dot{\theta}_{max}$	17.80	$\pm 0.037$	rad/s
Minimum Angular Velocity	$\dot{\theta}_{min}$	17.48	$\pm 0.036$	rad/s
Mean Angular Velocity	$\dot{\theta}_{mean}$	17.64	$\pm 0.037$	rad/s
Coefficient of Speed Fluctuation	$CS$	0.223	$\pm 0.025$	-

## Dimensionless Engine Pressure

The propagation of uncertainty for dimensionless engine pressure.

$$p_E^* = \frac{p_E}{p_{E,mean}}$$

$$U_{p_E^*} = \left( U_{p_E} \cdot \left| \frac{1}{p_{E,mean}} \right| \right) + \left( U_{p_{E,mean}} \cdot \left| \frac{-p_E^*}{p_{E,mean}} \right| \right)$$

A-12

Appendix Table A-28: Relative angular velocity uncertainty.

Variable	Symbol	Value	Uncertainty	Units
Phase Averaged Angular Velocity	$p_E$	691.5	$\pm 1.91$	kPa
Mean Angular Velocity	$p_{E,mean}$	624.8	$\pm 4.48$	kPa
Relative Angular Velocity	$p_E^*$	1.107	$\pm 0.011$	-

## Dimensionless Engine Volume

The propagation of uncertainty for dimensionless engine volume.

$$V_E^* = \frac{V_E - V_{E,min}}{V_{sw}}$$

$$U_{V_E^*} = \left( \frac{U_{V_E}}{V_{sw}} \right) + \left( \frac{U_{V_{E,min}}}{V_{sw}} \right)$$

A-13

Appendix Table A-29: Relative angular velocity uncertainty.

Variable	Symbol	Value	Uncertainty	Units
Engine Volume	$V_E$	1.672	$\pm 0.0017$	L
Minimum Volume	$V_{E,min}$	1.607	$\pm 3.01 \times 10^{-5}$	L
Swept Volume	$V_{sw}$	0.114	$\pm 0$	L
Relative Angular Velocity	$V_E^*$	0.565	$\pm 0.015$	-

## Relative Coefficient of Speed Fluctuation Difference

The propagation of uncertainty for relative coefficient of speed fluctuation difference.

$$\Delta CS^* = \frac{CS_{FET} - CS_{xp}}{CS_{xp}} \cdot 100\%$$

$$U_{\Delta CS^*} = \left[ \left( U_{CS_{FET}} \cdot \left| \frac{1}{CS_{xp}} \right| \right) + \left( U_{CS_{xp}} \cdot \left| \frac{-CS_{FET}}{CS_{xp}^2} \right| \right) \right] \cdot 100\%$$

A-14

Appendix Table A-30: Relative coefficient of speed fluctuation difference uncertainty.

Variable	Symbol	Value	Uncertainty	Units
FET Coefficient of Speed Fluctuation	$CS_{FET}$	0.029	$\pm 0$	-
Experiment Coefficient of Speed Fluctuation	$CS_{xp}$	0.018	$\pm 0.004$	-
Coefficient of Speed Fluctuation	$\Delta CS^*$	61.2	$\pm 9.0$	%

## West Number

The propagation of uncertainty for sample mean West number.

$$N_W = \frac{\dot{W}_S}{p_{E,mean} \cdot V_{swp} \cdot f} \cdot \left( \frac{T_H - T_C}{T_H + T_C} \right)^{-1}$$

$$U_{N_W} = \left( U_{\dot{W}_S} \cdot \left| \frac{1}{p_{E,mean} \cdot V_{swp} \cdot f} \left( \frac{T_H - T_C}{T_H + T_C} \right)^{-1} \right| \right) \dots$$

$$+ \left( U_{p_{E,mean}} \cdot \left| \frac{-\dot{W}_S}{p_{E,mean}^2 \cdot V_{swp} \cdot f} \left( \frac{T_H - T_C}{T_H + T_C} \right)^{-1} \right| \right) \dots$$

$$+ \left( U_f \cdot \left| \frac{-\dot{W}_S}{p_{E,mean} \cdot V_{swp} \cdot f^2} \left( \frac{T_H - T_C}{T_H + T_C} \right)^{-1} \right| \right) \dots$$

$$+ \left( U_{T_H} \cdot \left| \frac{\dot{W}_S}{p_{E,mean} \cdot V_{swp} \cdot f} \left( \frac{-2 \cdot T_C}{(T_H - T_C)^2} \right) \right| \right) \dots$$

$$+ \left( U_{T_C} \cdot \left| \frac{\dot{W}_S}{p_{E,mean} \cdot V_{swp} \cdot f} \left( \frac{2 \cdot T_H}{(T_H - T_C)^2} \right) \right| \right)$$

A-15

Appendix Table A-31: West number uncertainty.

Variable	Symbol	Value	Uncertainty	Units
Shaft Power	$\dot{W}_S$	3.62	$\pm 0.063$	W
Mean Engine Pressure	$p_{E,mean}$	$624.8 \times 10^3$	$\pm 4.48 \times 10^3$	Pa
Swept Volume	$V_{swp}$	$1.14 \times 10^{-4}$	$\pm 0$	m <sup>3</sup>
Engine Frequency	$f$	2.807	$\pm 0.0058$	Hz
Thermal Source Temperature	$T_H$	573.15	$\pm 2.04$	K
Thermal Sink Temperature	$T_C$	294.15	$\pm 2.01$	K
West Number	$N_W$	0.0563	$\pm 0.0023$	-

## Relative Shaft Power Difference

The propagation of uncertainty for relative shaft power difference.

$$\Delta \dot{W}_S^* = \left( \frac{\dot{W}_{S,md} - \dot{W}_{S,xp}}{\dot{W}_{S,xp}} \right) \cdot 100\%$$

$$U_{\Delta \dot{W}_S^*} = \left( U_{\dot{W}_{S,xp}} \cdot \left| \frac{-\dot{W}_{S,md}}{\dot{W}_{S,xp}^2} \right| \right) \cdot 100\%$$

A-16

Appendix Table A-32: Relative shaft power difference uncertainty.

Variable	Symbol	Value	Uncertainty	Units
Modelled Shaft Power	$\dot{W}_{S,md}$	24.31	$\pm 0$	W
Measured Shaft Power	$\dot{W}_{S,xp}$	3.621	$\pm 0.063$	W
Relative Shaft Power Difference	$\Delta \dot{W}_S^*$	571.4	$\pm 11.6$	%



## Normalized West Number Difference

The propagation of uncertainty for normalized West number difference.

$$\Delta N_{W}^* = \frac{N_{W,md} - N_{W,xp}}{N_{W} = 0.25} \cdot 100\%$$

A-17

$$U_{\Delta N_{W}^*} = \left( U_{N_{W,xp}} \cdot \left| \frac{-1}{0.25} \right| \right) \cdot 100\%$$

Appendix Table A-33: Relative West number uncertainty.

Variable	Symbol	Value	Uncertainty	Units
Modelled West Number	$N_{W,md}$	0.3778	$\pm 0$	-
Experiment West Number	$N_{W,xp}$	0.0563	$\pm 0.0023$	-
Relative West Number Difference	$\Delta N_{W,S}$	128.6	$\pm 0.92$	%

## Relative Indicated Work Difference

The propagation of uncertainty for relative indicated work difference.

$$\Delta W_I^* = \left( \frac{W_{I,md} - W_{I,xp}}{W_{I,xp}} \right) \cdot 100\%$$

$$U_{\Delta W_I^*} = \left( U_{W_{I,xp}} \cdot \left| \frac{-W_{I,md}}{W_{I,xp}^2} \right| \right) \cdot 100\%$$

A-18

Appendix Table A-34: Relative indicated work difference uncertainty.

Variable	Symbol	Value	Uncertainty	Units
Modelled Indicated Work	$W_{I,md}$	14.33	$\pm 0$	J
Measured Indicated Work	$W_{I,xp}$	8.655	$\pm 0.222$	J
Relative Indicated Work Difference	$\Delta W_I^*$	65.59	$\pm 4.25$	%

## Cumulative Indicator Diagram Difference

The propagation of uncertainty for the cumulative indicator diagram difference.

$$\Delta pV^* = \frac{\sum_{i=1}^N \left| (p_{E,md,i} - p_{E,xp,i}) \cdot dV_{E,i} \right|}{W_{I,xp}}$$

$$U_{\Delta pV^*} = \sum_{i=1}^N \left( \left( U_{p_{E,xp,i}} \cdot \left| \frac{-dV_{E,i}}{W_{I,xp}} \right| \right) + \left( U_{dV_{E,i}} \cdot \left| \frac{(p_{E,md,i} - p_{E,xp,i})}{W_{I,xp}} \right| \right) \right) \dots$$

A-19

$$+ \left( U_{W_{I,xp}} \cdot \frac{\Delta pV^*}{W_{I,xp}} \right)$$

Appendix Table A-35: Cumulative indicator diagram difference uncertainty.

Variable	Symbol	Value	Uncertainty	Units
Modelled Engine Pressure (1 <sup>st</sup> index)	$p_{E,md,1}$	673.3	± 0	kPa
Measured Engine Pressure (1 <sup>st</sup> index)	$p_{E,xp,1}$	691.5	± 1.91	kPa
Engine Volume Change (1 <sup>st</sup> index)	$dV_{E,1}$	0	± 0.0261	mL
Experimental Indicated Work	$W_{I,xp}$	8.655	± 0.222	J
Cumulative Indicator Diagram Difference	$\Delta pV^*$	66.76	± 1.69	%

## Indicated Power

The propagation of uncertainty for indicated power.

$$\dot{W}_I = W_I \cdot f$$

$$U_{\dot{W}_I} = (U_{W_I} \cdot f) + (U_f \cdot W_I)$$

A-20

Appendix Table A-36: Indicated power uncertainty.

Variable	Symbol	Value	Uncertainty	Units
Indicated Work	$W_I$	8.655	$\pm 0.222$	J
Engine Frequency	$f$	2.807	$\pm 0.0058$	Hz
Indicated Power	$\dot{W}_I$	24.29	$\pm 0.67$	W

## Mechanical Efficiency

The propagation of uncertainty for mechanical efficiency.

$$\eta_{mec} = \frac{\dot{W}_S}{\dot{W}_I}$$

$$U_{\eta_{mec}} = \left( U_{\dot{W}_S} \cdot \left| \frac{1}{\dot{W}_I} \right| \right) + \left( U_{\dot{W}_I} \cdot \left| \frac{-\dot{W}_S}{\dot{W}_I^2} \right| \right)$$

A-21

Appendix Table A-37: Mechanical efficiency uncertainty.

Variable	Symbol	Value	Uncertainty	Units
Shaft Power	$\dot{W}_S$	3.621	$\pm 0.063$	W
Indicated Power	$\dot{W}_I$	2.807	$\pm 0.0058$	W
Mechanical Efficiency	$\eta_{mec}$	0.1490	$\pm 0.0067$	-

## Mechanical Efficiency Difference

The propagation of uncertainty for the mechanical efficiency difference.

$$\Delta\eta_{mec} = (\eta_{mec,md} - \eta_{mec,xp}) \cdot 100\%$$

$$U_{\Delta\eta_{mec}} = (U_{\eta_{mec,md}} + U_{\eta_{mec,xp}}) \cdot 100\%$$

A-22

Appendix Table A-38: Mechanical efficiency difference uncertainty.

Variable	Symbol	Value	Uncertainty	Units
Modelled Mechanical Efficiency	$\eta_{mec,md}$	0.6042	$\pm 0$	-
Experimental Mechanical Efficiency	$\eta_{mec,xp}$	0.1490	$\pm 0.0067$	-
Mechanical Efficiency Difference	$\Delta\eta_{mec}$	45.51	$\pm 0.67$	%

## Relative Gas Spring Hysteresis Difference

The propagation of uncertainty for the gas spring hysteresis (GSH) difference.

$$\Delta \dot{W}_{GSH}^* = \frac{\dot{W}_{GSH,md} - \dot{W}_{GSH,xp}}{\dot{W}_{GSH,xp}}$$

$$U_{\Delta \dot{W}_{GSH}^*} = \left( \left( U_{\dot{W}_{GSH,md}} \cdot \left| \frac{1}{\dot{W}_{GSH,xp}} \right| \right) + \left( \dot{W}_{GSH,xp} \cdot \left| \frac{-\dot{W}_{GSH,md}}{\dot{W}_{GSH,xp}^2} \right| \right) \right)$$

A-23

Appendix Table A-39: Relative GSH difference uncertainty.

Variable	Symbol	Value	Uncertainty	Units
Modelled GSH	$\dot{W}_{GSH,md}$	1.581	± 0	W
Experimental GSH	$\dot{W}_{GSH,xp}$	1.798	± 0.602	W
Relative GSH Difference	$\Delta \dot{W}_{GSH}^*$	-12.05	± 29.48	%

## Normalized Forced Work Difference

The propagation of uncertainty for the normalized forced work difference.

$$\Delta W_F^* = \left( \frac{W_{F,md} - W_{F,xp}}{W_{I,xp}} \right) \cdot 100\%$$

$$U_{\Delta W_F^*} = \left( \left( U_{W_{F,md}} \cdot \left| \frac{1}{W_{I,xp}} \right| \right) + \left( U_{W_{F,xp}} \cdot \left| \frac{-1}{W_{I,xp}} \right| \right) + \left( U_{W_{I,xp}} \cdot \left| \frac{U_{W_{F,md}} - U_{W_{F,xp}}}{W_{I,xp}^2} \right| \right) \right) \cdot 100\%$$

A-24

Appendix Table A-40: Relative indicated work difference uncertainty.

Variable	Symbol	Value	Uncertainty	Units
Modelled Indicated Work	$W_{F,md}$	0.131	$\pm 0$	J
Measured Indicated Work	$W_{F,xp}$	1.491	$\pm 0.015$	J
Measured Indicated Work	$W_{I,xp}$	8.655	$\pm 0.222$	J
Relative Indicated Work Difference	$\Delta W_F^*$	-15.71	$\pm 0.57$	%



## Appendix A References

---

- [1] Wheeler, A. J., Ghanji, A. R., Krishnan, V. V., and Thurow, B. S., 2010, Introduction to Engineering Experimentation, Pearson Higher Education, Upper Saddle River.
- [2] Omega Engineering Inc., “Omega Temperature , Process and Strain Controllers.”
- [3] Cole Parmer Instrument Company LLC., 2005, “Operators Manual Programmable / Digital Controller Models.”
- [4] Encoder Products Company, 2014, “Model 15S - Incremental Shaft Encoder - Specification Sheet.”
- [5] Futek Advanced Sensor Technology Inc., “Rotary Torque Sensor – Non-Contact Shaft-to-Shaft Model TRS600 - Specification Sheet.”
- [6] National Instruments Corporation, 2017, “USB-6211 Specifications.”
- [7] Omega Engineering Inc., “ANSI and IEC Color Codes for Thermocouples, Wire and Connectors.”
- [8] National Instruments Corporation, 1997, “BNC/TC-2095 Rack-Mount Adapter Installation Guide,” (September).
- [9] National Institute of Standards and Technology, “Revised Thermocouple Reference Tables,” pp. 204–205.
- [10] National Instruments Corporation, 2004, “SCXI-1600 User Manual.”
- [11] Cole Parmer Instrument Company LLC., 2019, “Ertco 1005-3 Celsius Scale Sama Thermometers,” [www.coleparmer.com](http://www.coleparmer.com) [Online]. Available: <https://www.coleparmer.com/i/ertco-1005-3-celsius-scale-sama-thermometers-range-1-101-cimmersion-depth-76mm/0811965>. [Accessed: 18-Jan-2019].

- [12] King, D. J., “Resistance Elements and RTD ’s,” pp. 54–56.
- [13] National Instruments Corporation, 2016, “NI 9217 Datasheet.”
- [14] Validyne Engineering, 2018, “Validyne DP15 Variable Reluctance Differential Pressure Transducer Data Sheet.”
- [15] Validyne Engineering, “Validyne CD280 Four or Eight Channel Carrier Demodulator Data Sheet.”
- [16] GE Industrial Sensing, “DPI 603 Druck Portable Pressure Calibrator.”
- [17] PCB Piezotronics Inc., 2017, “PCB-113B21 Calibration Certificate.”
- [18] PCB Piezotronics Inc., 2018, “Dynamic Pressure Sensors for High Frequency Measurements,” pp. 1–4.

---

## B. 2<sup>ND</sup> ORDER MODEL CODE

---

This appendix contains the 2<sup>nd</sup> order model MATLAB® code that has changed from Speer [1]. Specifically, two functions have changed. A temperature correction was added to the mass correction function. The volume function was changed to start at piston TDC. Those codes are presented below.

### Mass and Temperature Correction Function

---

```
function ENGINE_DATA = mass_temp_correction(ENGINE_DATA,crank_inc,Model_Code)

% Written by Connor Speer and Shahzeb Mirza, October 2017.
% Modified by David Miller - Oct. 2018
%
% This function uses the iterative scheme proposed by "2015(Paul) Modeling a
% complete Stirling engine", to correct the mass of working fluid so that
% the reference cycle simulation has the same mean pressure as the one
% specified by the user in ENGINE_DATA.
%
% Modified to correct for errors between the experimental and simulation
% expansions space and compression space temperature.
%
%%%%%%%%%%%%%%%%%%%%%%%%%%%%%%%%%%%%%%%%%%%%%%%%%%%%%%%%%%%%%%%%%%%%%%%%

% Find pressure as a function of crank angle using the initial mass value
% in the ENGINE_DATA structure, which is calculated in define.m using the
% Schmidt analysis.
if Model_Code == 1
    % Solve the ideal isothermal model
    ISOTHERMAL_DATA = isothermal(ENGINE_DATA,crank_inc);
    REF_CYCLE_DATA = ISOTHERMAL_DATA;
elseif Model_Code == 2
    % Solve the ideal adiabatic model
    ADIABATIC_DATA = adiabatic(ENGINE_DATA,crank_inc);
    REF_CYCLE_DATA = ADIABATIC_DATA;
elseif Model_Code == 3
    % Solve the simple model (no flow friction)
    SIMPLE_DATA = simple(ENGINE_DATA,crank_inc);
    REF_CYCLE_DATA = SIMPLE_DATA;
else
    disp('ERROR: Invalid model code.')
```

```

% Recall the mean pressure specified in the ENGINE_DATA structure.
pmean = ENGINE_DATA.pmean; %(Pa)

% Calculate the mean expansion space and compression space temperature errors
(K)
E_Tge = mean([REF_CYCLE_DATA.Tge])-ENGINE_DATA.Tge;
E_Tgc = mean([REF_CYCLE_DATA.Tgc])-ENGINE_DATA.Tgc;

% recall the wall temperature specified in ENGINE_DATA (K)
Twh_old = ENGINE_DATA.Twh;
Twk_old = ENGINE_DATA.Twk;

% If this 'found' mean pressure is significantly different from the
% 'desired' mean pressure specified in the ENGINE_DATA structure, then
% iteratively loop through an algorithm that changes the mass value until
% the mean pressure calculated by the reference cycle matches the desired
% value.

% Futher, while the expansion space temperature error and compression space
% temperature error are greater than 0.1 K, then wall temperature in the
% heater and cooler will be corrected. Once reference cycle expansion space
% and compression space mean temperature match the experimental or
% specified values then te loop stops.

Mold = ENGINE_DATA.mgas; %(kg)

while( (abs((pmean - pbar)/pmean) > 0.001) || ((abs(E_Tge)+abs(E_Tgc)) >
0.1))

    % Correct mass of gas
    Mnew = (1 + (pmean - pbar)/pmean) * Mold;
    Mold = Mnew;
    ENGINE_DATA.mgas = Mnew;

    % Correct and heater gas temperature
    Twh_new = Twh_old-E_Tge;
    Twh_old = Twh_new;
    ENGINE_DATA.Twh = Twh_new;

    % Correct and cooler gas temperature
    Twk_new = Twk_old-E_Tgc;
    Twk_old = Twk_new;
    ENGINE_DATA.Twk = Twk_new;

    if Model_Code == 1
        % Solve the ideal isothermal model
        ISOTHERMAL_DATA = isothermal(ENGINE_DATA,crank_inc);
        disp(abs((pmean - pbar)/pmean));
        REF_CYCLE_DATA = ISOTHERMAL_DATA;
    elseif Model_Code == 2
        % Solve the ideal adiabatic model
        ADIABATIC_DATA = adiabatic(ENGINE_DATA,crank_inc);
        REF_CYCLE_DATA = ADIABATIC_DATA;
    elseif Model_Code == 3
        % Solve the simple model (no flow friction)

```

```

        SIMPLE_DATA = simple(ENGINE_DATA,crank_inc);
        REF_CYCLE_DATA = SIMPLE_DATA;
    else
        disp('ERROR: Invalid model code.')
    end

    % Find the mean pressure of the reference cycle
    pbar = mean([REF_CYCLE_DATA.p]);

    % Calculate the new expansion space and compression space temperature
    error (K)
    E_Tge = mean([REF_CYCLE_DATA.Tge])-ENGINE_DATA.Tge;
    E_Tgc = mean([REF_CYCLE_DATA.Tgc])-ENGINE_DATA.Tgc;

end

```

# Volume Calculation Function

---

```
function [Vc,Ve,dVc,dVe] = volume(theta, ENGINE_DATA)
% determine working space volume variations and derivatives
% Israel Urieli, 7/6/2002
% Modified 2/14/2010 to include rockerV (rockdrive)
% Modified by Connor Speer October 2017
% Modified by David Miller Dec. 2018
% Modified to gamma workspace minimum volume occurs at theta = 0

% Argument: theta - current cycle angle [radians]
% Returned values:
%   vc, ve - compression, expansion space volumes [m^3]
%   dvc, dve - compression, expansion space volume derivatives

% *** Note: For gamma engines, the total workspace volume is maximum at
% crank angle 0. For alpha engines, the compression space volume is maximum
% at crank angle zero.

engine_type = ENGINE_DATA.engine_type; % Letter indicating engine layout and
drive mechanism

if(strncmp(engine_type,'s',1)) % Sinusoidal alpha
    [Vc,Ve,dVc,dVe] = sinevol(theta, ENGINE_DATA);
elseif(strncmp(engine_type,'y',1)) % Ross yoke mechanism alpha
    [Vc,Ve,dVc,dVe] = yokevol(theta, ENGINE_DATA);
elseif(strncmp(engine_type,'r',1)) % Ross rocker V-drive alpha
    [Vc,Ve,dVc,dVe] = rockvol(theta, ENGINE_DATA);
elseif(strncmp(engine_type,'g',1)) % Sinusoidal gamma
    [Vc,Ve,dVc,dVe] = gammasinvol(theta, ENGINE_DATA);
elseif(strncmp(engine_type,'x',1)) % Slider-crank mechanism gamma
    [Vc,Ve,dVc,dVe] = gammacrankvol(theta, ENGINE_DATA);
elseif(strncmp(engine_type,'a',1)) % Slider-crank mechanism alpha
    [Vc,Ve,dVc,dVe] = alphacrankvol(theta, ENGINE_DATA);
end
%=====

function [Vc,Ve,dVc,dVe] = sinevol(theta, ENGINE_DATA)
% sinusoidal drive volume variations and derivatives
% Israel Urieli, 7/6/2002
% Argument: theta - current cycle angle [radians]
% Returned values:
%   vc, ve - compression, expansion space volumes [m^3]
%   dvc, dve - compression, expansion space volume derivatives

Vclc = ENGINE_DATA.Vclc;
Vcle = ENGINE_DATA.Vcle;
Vswc = ENGINE_DATA.Vswc;
Vswe = ENGINE_DATA.Vswe;
alpha = ENGINE_DATA.alpha;

% Vclc Vcle % compression, expansion clearance vols [m^3]
% Vswc Vswe % compression, expansion swept volumes [m^3]
% alpha % phase angle advance of expansion space [radians]
```

```

Vc = Vclc + 0.5*Vswc*(1 + cos(theta));
Ve = Vcle + 0.5*Vswe*(1 + cos(theta + alpha));
dVc = -0.5*Vswc*sin(theta);
dVe = -0.5*Vswe*sin(theta + alpha);
%=====

function [Vc, Ve, dVc, dVe] = yokevol(theta, ENGINE_DATA)
% Ross yoke drive volume variations and derivatives
% Israel Urieli, 7/6/2002
% Modified by Connor Speer, October 2017.
% Argument: theta - current cycle angle [radians]
% Returned values:
%   Vc, Ve - compression, expansion space volumes [m^3]
%   dVc, dVe - compression, expansion space volume derivatives

% compression, expansion clearance vols [m^3]
Vclc = ENGINE_DATA.Vclc;
Vcle = ENGINE_DATA.Vcle;

b1 = ENGINE_DATA.b1; % Ross yoke length (1/2 yoke base) [m]
b2 = ENGINE_DATA.b2; % Ross yoke height [m]
crank = ENGINE_DATA.crank; % crank radius [m]

% area of compression/expansion pistons [m^2]
acomp = ENGINE_DATA.acomp;
aexp = ENGINE_DATA.aexp;

ymin = ENGINE_DATA.ymin; % minimum yoke vertical displacement [m]

sinh = sin(theta);
costh = cos(theta);
bth = (b1^2 - (crank*costh)^2)^0.5;
ye = crank*(sinh + (b2/b1)*costh) + bth;
yc = crank*(sinh - (b2/b1)*costh) + bth;

Ve = vcle + aexp*(ye - ymin);
Vc = vclc + acomp*(yc - ymin);
dVc = acomp*crank*(costh + (b2/b1)*sinh + crank*sinh*costh/bth);
dVe = aexp*crank*(costh - (b2/b1)*sinh + crank*sinh*costh/bth);
%=====

function [vc, ve, dvc, dve] = rockvol(theta, ENGINE_DATA)
% Ross Rocker-V drive volume variations and derivatives
% Israel Urieli, 7/6/2002 & Martine Long 2/25/2005
% Argument: theta - current cycle angle [radians]
% Returned values:
%   vc, ve - compression, expansion space volumes [m^3]
%   dvc, dve - compression, expansion space volume derivatives

global vclc vcle % compression, expansion clearance vols [m^3]
global crank % crank radius [m]
global acomp aexp % area of compression/expansion pistons [m^2]
global conrodc conrode % length of comp/exp piston connecting rods [m]

```

```

global ycmax yemax % maximum comp/exp piston vertical displacement [m]

sinth = sin(theta);
costh = cos(theta);
beth = (conrode^2 - (crank*costh)^2)^0.5;
bcth = (conrodc^2 - (crank*sinth)^2)^0.5;
ye = beth - crank*sinth;
yc = bcth + crank*costh;

ve = vcle + aexp*(yemax - ye);
vc = vclc + acomp*(ycmax - yc);
dvc = acomp*crank*sinth*(crank*costh/bcth + 1);
dve = -aexp*crank*costh*(crank*sinth/beth - 1);

function [vc,ve,dvc,dve] = gammasinvol(theta, ENGINE_DATA);
% gamma sinusoidal drive volume variations and derivatives
% Added by Connor Speer - January 2017
% Argument: theta - current cycle angle [radians]
% Returned values:
%   vc, ve - compression, expansion space volumes [m^3]
%   dvc, dve - compression, expansion space volume derivatives

global vclp vcld % piston, displacer clearance vols [m^3]
global vswp vswd % compression, expansion swept volumes [m^3]
global beta % phase angle advance of displacer motion over piston [radians]

%*** Total volume is maximum at theta = 0 for gammas.
vc = vcld + vclp + (vswd*0.5)*(1 + ((vswp/vswd)*(1+cos(theta-pi)) -
cos(theta+beta-pi)));
ve = vcld + (vswd*0.5)*(1 + cos(theta+beta-pi));
dvc = -(vswd*0.5)*((vswp/vswd)*sin(theta-pi) - sin(theta+beta-pi));
dve = -(vswd*0.5)*sin(theta+beta-pi);
%=====

function [vc,ve,dvc,dve] = gammacrankvol(theta, ENGINE_DATA)
% gamma crankshaft drive volume variations and derivatives
% Added by Connor Speer - February 2017
% Argument: theta - current cycle angle [radians]
% Returned values:
%   vc, ve - compression, expansion space volumes [m^3]
%   dvc, dve - compression, expansion space volume derivatives

vclp = ENGINE_DATA.Vclp;
vcld = ENGINE_DATA.Vcld;
Dbore = ENGINE_DATA.Dbore;
Pbore = ENGINE_DATA.Pbore;
Dr1 = ENGINE_DATA.Dr1;
Dr2 = ENGINE_DATA.Dr2;
Dr3 = ENGINE_DATA.Dr3;
Pr1 = ENGINE_DATA.Pr1;
Pr2 = ENGINE_DATA.Pr2;
Pr3 = ENGINE_DATA.Pr3;
beta = ENGINE_DATA.beta_deg*(pi/180);

```



```

% vclp vcld % piston, displacer clearance vols [m^3]
% Dbore Pbore % displacer, piston bores [m]
% Dr1 Pr1 % displacer, piston desaxe offset in [m]
% Dr2 Pr2 % displacer, piston crank length (half stroke) in [m]
% Dr3 Pr3 % displacer, piston connecting rod lengths [m]
% beta % phase angle advance of displacer motion over piston [radians]

%*** Total volume is minimum at theta = 0 for gammas.
Ptheta2 = pi - theta-pi;
Dtheta2 = Ptheta2 - beta;

Dtheta3 = pi - asin((-Dr1+(Dr2*sin(Dtheta2)))/Dr3);
Dr4 = Dr2*cos(Dtheta2) - Dr3*cos(Dtheta3);
Dr4max = sqrt(((Dr2+Dr3)^2)-(Dr1^2));
Dr4min = sqrt(((Dr3-Dr2)^2)-(Dr1^2));
ve = (vcld*0.5) + ((pi/4)*(Dbore^2))*(Dr4max-Dr4);
DVc = (((pi/4)*(Dbore^2))*(Dr4max-Dr4min)) - ve;

Ptheta3 = pi - asin((-Pr1+(Pr2*sin(Ptheta2)))/Pr3);
Pr4 = Pr2*cos(Ptheta2) - Pr3*cos(Ptheta3);
Pr4max = sqrt(((Pr2+Pr3)^2)-(Pr1^2));
PVc = (((pi/4)*(Pbore^2))*(Pr4max-Pr4));
vc = (vcld) + vclp + DVc + PVc;

dDtheta3 = (Dr2.*cos(Dtheta2))./(Dr3.*sqrt(1-(((Dr1+(Dr2.*sin(Dtheta2)))/Dr3).^2)));
dDr4 = Dr2.*sin(Dtheta2) + Dr3.*sin(Dtheta3).*dDtheta3;
dve = -(pi/4)*(Dbore^2).*(dDr4);

dPtheta3 = (Pr2.*cos(Ptheta2))./(Pr3.*sqrt(1-(((Pr1+(Pr2.*sin(Ptheta2)))/Pr3).^2)));
dPr4 = Pr2.*sin(Ptheta2) + Pr3.*sin(Ptheta3).*dPtheta3;
dPVc = -(pi/4)*(Pbore^2).*(dPr4);
dDVc = -dve;
dvc = dDVc + dPVc;
%=====

function [vc,ve,dvc,dve] = alphacrankvol(theta, ENGINE_DATA)
% alpha crankshaft drive volume variations and derivatives
% Added by Connor Speer - February 2017
% Argument: theta - current cycle angle [radians]
% Returned values:
% vc, ve - compression, expansion space volumes [m^3]
% dvc, dve - compression, expansion space volume derivatives

vclc = ENGINE_DATA.Vclc;
vcle = ENGINE_DATA.Vcle;
Cbore = ENGINE_DATA.Cbore;
Ebore = ENGINE_DATA.Ebore;
Cr1 = ENGINE_DATA.Cr1;
Cr2 = ENGINE_DATA.Cr2;
Cr3 = ENGINE_DATA.Cr3;
Er1 = ENGINE_DATA.Er1;
Er2 = ENGINE_DATA.Er2;
Er3 = ENGINE_DATA.Er3;

```

```

alpha = ENGINE_DATA.alpha;

% vclc vcle % compression, expansion clearance vols [m^3]
% Cbore Ebore % compression, expansion piston bores [m]
% Cr1 Er1 % compression, expansion desaxe offset in [m]
% Cr2 Er2 % compression, expansion crank length (half stroke) in [m]
% Cr3 Er3 % compression, expansion connecting rod lengths [m]
% alpha % phase angle advance of expansion space [radians]

%*** Compression space volume is maximum at theta = 0 for alphas. Be
% careful defining crank angle 0 if using a desaxe offset.
Ctheta2 = theta - pi;
Etheta2 = Ctheta2 + alpha;

Ctheta3 = pi - asin((-Cr1+(Cr2*sin(Ctheta2)))/Cr3);
Cr4 = Cr2*cos(Ctheta2) - Cr3*cos(Ctheta3);
Cr4max = sqrt(((Cr2+Cr3)^2)-(Cr1^2));
vc = vclc + ((pi/4)*(Cbore^2))*(Cr4max-Cr4);

Etheta3 = pi - asin((-Er1+(Er2*sin(Etheta2)))/Er3);
Er4 = Er2*cos(Etheta2) - Er3*cos(Etheta3);
Er4max = sqrt(((Er2+Er3)^2)-(Er1^2));
ve = vcle + ((pi/4)*(Ebore^2))*(Er4max-Er4);

dCtheta3 = (-Cr2*cos(Ctheta2))/(Cr3*sqrt(1-((( -
Cr1+(Cr2*sin(Ctheta2)))/Cr3).^2)));
dCr4 = -Cr2*sin(Ctheta2) + Cr3*sin(Ctheta3)*dCtheta3;
dvc = -(pi/4)*(Cbore^2)*(dCr4);

dEtheta3 = (-Er2*cos(Etheta2))/(Er3*sqrt(1-((( -
Er1+(Er2*sin(Etheta2)))/Er3).^2)));
dEr4 = -Er2*sin(Etheta2) + Er3*sin(Etheta3)*dEtheta3;
dve = -(pi/4)*(Ebore^2)*(dEr4);
%=====

```

## Appendix B References

---

- [1] Speer, C. P., 2018, “Modifications to Reduce the Minimum Thermal Source Temperature of the ST05G-CNC Stirling Engine,” University of Alberta.

---

## C. DATA PROCESSING CODE

---

This appendix contains the data processing MATLAB® code used for data in this thesis. It is divided into five sections: the user interface function, data processing function, import functions, calibration functions, and support functions.

### User Interface Function

---

```
function varargout = DataProcessingGUI(varargin)
% DATAPROCESSINGGUI MATLAB code for DataProcessingGUI.fig
%   DATAPROCESSINGGUI, by itself, creates a new DATAPROCESSINGGUI or
raises the existing
%   singleton*.
%
%   H = DATAPROCESSINGGUI returns the handle to a new DATAPROCESSINGGUI or
the handle to
%   the existing singleton*.
%
%   DATAPROCESSINGGUI('CALLBACK',hObject,eventData,handles,...) calls the
local
%   function named CALLBACK in DATAPROCESSINGGUI.M with the given input
arguments.
%
%   DATAPROCESSINGGUI('Property','Value',...) creates a new
DATAPROCESSINGGUI or raises the
%   existing singleton*. Starting from the left, property value pairs are
applied to the GUI before DataProcessingGUI_OpeningFcn gets called.
An
%   unrecognized property name or invalid value makes property application
%   stop. All inputs are passed to DataProcessingGUI_OpeningFcn via
varargin.
%
%   *See GUI Options on GUIDE's Tools menu. Choose "GUI allows only one
%   instance to run (singleton)".
%
% See also: GUIDE, GUIDATA, GUIHANDLES

% Edit the above text to modify the response to help DataProcessingGUI

% Last Modified by GUIDE v2.5 05-Nov-2018 16:38:02

% Begin initialization code - DO NOT EDIT
gui_Singleton = 1;
gui_State = struct('gui_Name',       mfilename, ...
                  'gui_Singleton',  gui_Singleton, ...
                  'gui_OpeningFcn', @DataProcessingGUI_OpeningFcn, ...
                  'gui_OutputFcn',  @DataProcessingGUI_OutputFcn, ...
                  'gui_LayoutFcn',  [] , ...
```

```

        'gui_Callback', []);
if nargin && ischar(varargin{1})
    gui_State.gui_Callback = str2func(varargin{1});
end

if nargin
    [varargout{1:nargout}] = gui_mainfcn(gui_State, varargin{:});
else
    gui_mainfcn(gui_State, varargin{:});
end
% End initialization code - DO NOT EDIT

% --- Executes just before DataProcessingGUI is made visible.
function DataProcessingGUI_OpeningFcn(hObject, eventdata, handles, varargin)
% This function has no output args, see OutputFcn.
% hObject    handle to figure
% eventdata  reserved - to be defined in a future version of MATLAB
% handles    structure with handles and user data (see GUIDATA)
% varargin   command line arguments to DataProcessingGUI (see VARARGIN)

% Choose default command line output for DataProcessingGUI
handles.output = hObject;

% Update handles structure
guidata(hObject, handles);

% UIWAIT makes DataProcessingGUI wait for user response (see UIRESUME)
% uiwait(handles.figure1);

% --- Outputs from this function are returned to the command line.
function varargout = DataProcessingGUI_OutputFcn(hObject, eventdata, handles)
% varargout  cell array for returning output args (see VARARGOUT);
% hObject    handle to figure
% eventdata  reserved - to be defined in a future version of MATLAB
% handles    structure with handles and user data (see GUIDATA)

% Get default command line output from handles structure
varargout{1} = handles.output;
set(handles.pushbutton4, 'enable', 'on');

% --- Executes on selection change in ProcessSelector.
function ProcessSelector_Callback(hObject, eventdata, handles)
% hObject    handle to ProcessSelector (see GCBO)
% eventdata  reserved - to be defined in a future version of MATLAB
% handles    structure with handles and user data (see GUIDATA)

% Hints: contents = cellstr(get(hObject, 'String')) returns ProcessSelector
% contents as cell array
%         contents{get(hObject, 'Value')} returns selected item from
ProcessSelector
Processes = cellstr(get(handles.ProcessSelector, 'string'));

```

```

Process = Processes{get(handles.ProcessSelector, 'value')};

if isequal(Process, Processes{2})
    set(handles.LogFolder, 'enable', 'off');
    set(handles.LogFolderSearch, 'enable', 'off');
else
    set(handles.LogFolder, 'enable', 'on');
    set(handles.LogFolderSearch, 'enable', 'on');
end

% --- Executes during object creation, after setting all properties.
function ProcessSelector_CreateFcn(hObject, eventdata, handles)
% hObject    handle to ProcessSelector (see GCBO)
% eventdata  reserved - to be defined in a future version of MATLAB
% handles    empty - handles not created until after all CreateFcns called

% Hint: popupmenu controls usually have a white background on Windows.
%         See ISPC and COMPUTER.
if ispc && isequal(get(hObject, 'BackgroundColor'),
get(0, 'defaultUiControlBackgroundColor'))
    set(hObject, 'BackgroundColor', 'white');
end

% --- Executes on button press in LogFolderSearch.
function LogFolderSearch_Callback(hObject, eventdata, handles)
% hObject    handle to LogFolderSearch (see GCBO)
% eventdata  reserved - to be defined in a future version of MATLAB
% handles    structure with handles and user data (see GUIDATA)
LogFolder = uigetdir('W:\David Miller_W');
set(handles.LogFolder, 'string', LogFolder);

function LogFolder_Callback(hObject, eventdata, handles)
% hObject    handle to LogFolder (see GCBO)
% eventdata  reserved - to be defined in a future version of MATLAB
% handles    structure with handles and user data (see GUIDATA)

% Hints: get(hObject, 'String') returns contents of LogFolder as text
%         str2double(get(hObject, 'String')) returns contents of LogFolder as a
double

% --- Executes during object creation, after setting all properties.
function LogFolder_CreateFcn(hObject, eventdata, handles)
% hObject    handle to LogFolder (see GCBO)
% eventdata  reserved - to be defined in a future version of MATLAB
% handles    empty - handles not created until after all CreateFcns called

% Hint: edit controls usually have a white background on Windows.
%         See ISPC and COMPUTER.

```

```

if ispc && isequal(get(hObject,'BackgroundColor'),
get(0,'defaultUicontrolBackgroundColor'))
    set(hObject,'BackgroundColor','white');
end

% --- Executes on button press in RAWFolderSearch.
function RAWFolderSearch_Callback(hObject, eventdata, handles)
% hObject    handle to RAWFolderSearch (see GCBO)
% eventdata  reserved - to be defined in a future version of MATLAB
% handles    structure with handles and user data (see GUIDATA)
RAWFolder = uigetdir('X:\01_Current_Students\David
Miller\06_DAQAndExperiments\01_ExperimentData');
set(handles.RAWFolder,'string',RAWFolder);

% --- Executes on button press in PROFolderSearch.
function PROFolderSearch_Callback(hObject, eventdata, handles)
% hObject    handle to PROFolderSearch (see GCBO)
% eventdata  reserved - to be defined in a future version of MATLAB
% handles    structure with handles and user data (see GUIDATA)
PROFolder = uigetdir('X:\01_Current_Students\David
Miller\06_DAQAndExperiments\03_ProcessedData');
set(handles.PROFolder,'string',PROFolder);

function RAWFolder_Callback(hObject, eventdata, handles)
% hObject    handle to RAWFolder (see GCBO)
% eventdata  reserved - to be defined in a future version of MATLAB
% handles    structure with handles and user data (see GUIDATA)

% Hints: get(hObject,'String') returns contents of RAWFolder as text
%        str2double(get(hObject,'String')) returns contents of RAWFolder as a
double

% --- Executes during object creation, after setting all properties.
function RAWFolder_CreateFcn(hObject, eventdata, handles)
% hObject    handle to RAWFolder (see GCBO)
% eventdata  reserved - to be defined in a future version of MATLAB
% handles    empty - handles not created until after all CreateFcns called

% Hint: edit controls usually have a white background on Windows.
%        See ISPC and COMPUTER.
if ispc && isequal(get(hObject,'BackgroundColor'),
get(0,'defaultUicontrolBackgroundColor'))
    set(hObject,'BackgroundColor','white');
end

function PROFolder_Callback(hObject, eventdata, handles)
% hObject    handle to PROFolder (see GCBO)

```

```

% eventdata reserved - to be defined in a future version of MATLAB
% handles structure with handles and user data (see GUIDATA)

% Hints: get(hObject,'String') returns contents of PROFolder as text
% str2double(get(hObject,'String')) returns contents of PROFolder as a
double

% --- Executes during object creation, after setting all properties.
function PROFolder_CreateFcn(hObject, eventdata, handles)
% hObject handle to PROFolder (see GCBO)
% eventdata reserved - to be defined in a future version of MATLAB
% handles empty - handles not created until after all CreateFcns called

% Hint: edit controls usually have a white background on Windows.
% See ISPC and COMPUTER.
if ispc && isequal(get(hObject,'BackgroundColor'),
get(0,'defaultUiControlBackgroundColor'))
    set(hObject,'BackgroundColor','white');
end

% --- Executes on button press in pushbutton4.
function pushbutton4_Callback(hObject, eventdata, handles)
% hObject handle to pushbutton4 (see GCBO)
% eventdata reserved - to be defined in a future version of MATLAB
% handles structure with handles and user data (see GUIDATA)
CalibrationFolder = 'X:\01_Current_Students\David
Miller\06_DAQAndExperiments\02_DataProcessing\01_Calibration';
ProcessorFolder = 'X:\01_Current_Students\David
Miller\06_DAQAndExperiments\02_DataProcessing\02_DataSetProcessor';
EngineDataFolder = 'X:\01_Current_Students\David
Miller\06_DAQAndExperiments\02_DataProcessing\03_EngineData';
ImportFolder = 'X:\01_Current_Students\David
Miller\06_DAQAndExperiments\02_DataProcessing\04_ImportFunctions';
SupportFolder = 'X:\01_Current_Students\David
Miller\06_DAQAndExperiments\02_DataProcessing\05_SupportFunctions';
addpath(CalibrationFolder,ProcessorFolder,EngineDataFolder,ImportFolder,SupportFolder);

Processes = cellstr(get(handles.ProcessSelector,'string'));
Process = Processes{get(handles.ProcessSelector,'value')};
LogFolder = get(handles.LogFolder,'string');
RAWFolder = get(handles.RAWFolder,'string');
PROFolder = get(handles.PROFolder,'string');

if isequal(Process,Processes{2})
    set(handles.pushbutton4,'enable','off');
    NDGRawStructureProcessorFx(RAWFolder,PROFolder);
    set(handles.pushbutton4,'enable','on');
else
    set(handles.pushbutton4,'enable','off');
    NDGDataSetProcessorFx(LogFolder,RAWFolder,PROFolder);
    set(handles.pushbutton4,'enable','on');
end

```



# Data Processing Function

---

```
function
NDGDataSetProcessorFx(Log_FileLocation,RAW_FileLocation,PRO_FileLocation)
% NDGDataSetProcessor.m
%
% By David Miller - Oct. 2018
%
% This Function:
% Imports data files from NDG experiments,
% Creates and saves a raw data structure as a .mat file,
% Reorganizes and Averages data within rotary encoder increments,
% Crops data to first rotary encoder Z pulses after the last start time,
% Averages thermocouple data to every 10 encoder A pulses,
% Organizes data into columns for each complete rotation,
% Calibrates and corrects data,
% Calculates systematic uncertainties,
% Calculates instantaneous engine speed and uncertainty,
% Calculates engine volumes and uncertainties,
% Saves calibrated data in an organized data structure .mat file.

%% Import Data From Data Files

% Load Calibration Data
load RTD_FIT.mat
load TC_FIT.mat
load VAL_FIT.mat

% Locate and add model functions to path
ModelFolder = 'X:\01_Current_Students\David
Miller\07_ModelsAndCalculations\01_SEACode\2018-10-16-SEACode-GasTemp\01_SEA
- Rev 5'; % model folder (update if changes are made)
addpath(ModelFolder);
addpath(strcat(ModelFolder, '\4th Order Runge-Kutta'));
addpath(strcat(ModelFolder, '\The adiabatic Function Set'));
addpath(strcat(ModelFolder, '\The define Function Set'));
addpath(strcat(ModelFolder, '\The isothermal Function Set'));
addpath(strcat(ModelFolder, '\The parasitic losses Function Set'));
addpath(strcat(ModelFolder, '\The simple Function Set'));

% % Point to folder with data files to process
% Log_FileLocation = 'X:\01_Current_Students\David
Miller\06_DAQAndExperiments\01_ExperimentData\2018-11-
02_FreeSpeedExperiments';
%
% % Point to folder to save processed data
% RAW_FileLocation = 'X:\01_Current_Students\David
Miller\06_DAQAndExperiments\03_ProcessedData\2018-11-
02_FreeSpeedExperiments';
% PRO_FileLocation = 'X:\01_Current_Students\David
Miller\06_DAQAndExperiments\03_ProcessedData\2018-11-
02_FreeSpeedExperiments';

% Get data file info in folder
FilesInfo = dir(fullfile(Log_FileLocation, '*.log'));
```

```

WaitBar = waitbar(0, 'Processing Data');

% For each data set in the folder
for FileNum = 1:3:length(FilesInfo)

    % General File Name To Process
    FileName = erase(FilesInfo(FileNum).name, '_RTD.log');
    FileName = erase(FileName, '_Temp.log');
    FileName = erase(FileName, '_Volt.log');

    % Individual file names to process
    DATA.Vfilename = strcat(Log_FileLocation, '\', FileName, '_Volt.log'); %
voltage file name
    DATA.Tfilename = strcat(Log_FileLocation, '\', FileName, '_Temp.log'); %
thermocouple file name
    DATA.RTDfilename = strcat(Log_FileLocation, '\', FileName, '_RTD.log'); %
RTD file name

    % Import Voltage Data
    [DATA.VTime, DATA.A, DATA.Z, DATA.TOR, DATA.P1, DATA.P2, DATA.P3, DATA.P4] ...
    = PImport(DATA.Vfilename);
    % VTime -> Time for voltage data [s] (Time0 at aquire start)
    % A -> Rotarty encoder A pulse [V] (500 PPR)
    % Z -> Rotarty encoder Z pulse [V] (1 PPR)
    % TOR -> Torque transducer output [V]
    % P1 -> Validyne crankcase [V]
    % P2 -> Validyne power cylinder [V]
    % P3 -> PCB power cylinder [V]
    % P4 -> PCB crankcase [V]

    % Import Thermocouple Data
    [DATA.TTime, DATA.T0, DATA.T1, DATA.T2, DATA.T3, DATA.T4, DATA.T5] ...
    = TImport(DATA.Tfilename);
    % TTime -> Time for thermocouple data [s] (Time0 at aquire start)
    % T0 -> Expansion space gas temperature [deg. C]
    % T1 -> HH-regen gas temperature [deg. C]
    % T2 -> Regen-cooler bypass side gas temperature [deg. C]
    % T3 -> Diplacer mount gas temperature [deg. C]
    % T4 -> Power cylinder gas temperature [deg. C]
    % T5 -> Crankcase gas temperature [deg. C]

    % Import RTD Data
    [DATA.RTDTime, DATA.RTD0, DATA.RTD1, DATA.RTD2, DATA.RTD3] ...
    = RTDImport(DATA.RTDfilename);
    % RTDTime -> Time for RTD data [s] (Time0 at aquire start)
    % RTD0 -> Cooler inlet water temperature [deg. C]
    % RTD1 -> Cooler outlet water temperature [deg. C]
    % RTD2 -> Power cylinder inlet water temperature [deg. C]
    % RTD3 -> Power cylinder outlet water temperature [deg. C]

    % Extract Data from File Name
    % 'MMDDYYYY_HHMMSS_200_20_060_ABA_L'
    DATA.Date = FileName(1:8);
    DATA.TH = str2double(FileName(17:19));

```

```

DATA.TC = str2double(FileName(21:22));
DATA.PT = 6894.76*str2double(FileName(24:26));
DATA.Piston = FileName(28);
DATA.Crankcase = FileName(29);
DATA.Flywheel = FileName(30);
DATA.LoadCond = FileName(32);

% Determine Engine Configuration
EngineConfig = [DATA.Piston,DATA.Crankcase,DATA.Flywheel];
switch EngineConfig
    case ['A','B','A'] % 44 mm piston, extended crankcase, flywheel A
        ENGINE_DATA = NDG_DATA_44_CE_FA;
    case ['A','A','A'] % TEMP
        ENGINE_DATA = NDG_DATA_44_CE_FA;
    case ['A','B','B'] % 44 mm piston, extended crankcase, flywheel B
        ENGINE_DATA = NDG_DATA_44_CE_FB;
    case ['A','B','C'] % 44 mm piston, extended crankcase, flywheel C
        ENGINE_DATA = NDG_DATA_44_CE_FC;
    case ['A','B','D'] % 44 mm piston, extended crankcase, flywheel D
        ENGINE_DATA = NDG_DATA_44_CE_FD;
    case ['A','B','E'] % 44 mm piston, extended crankcase, flywheel E
        ENGINE_DATA = NDG_DATA_44_CE_FE;
    otherwise % may need to create new engine data file
        error('Invalid Engine Configuration');
end

DATA.ENGINE_DATA = ENGINE_DATA;

% Save raw data structure as .mat file with same base name as log files
RAW_FileName = strcat('RAW_',FileName);
evalc([matlab.lang.makeValidName(RAW_FileName),' = DATA']);
save(strcat(RAW_FileLocation,'/',RAW_FileName,'.mat'),RAW_FileName);
clear(RAW_FileName);

%% Establish Rotary Encoder Positions and Average Data Within Steps

% Calculate crankshaft position
[DATA.Theta] = Encoder_2_Angle(DATA.A,DATA.Z); % crankshaft position
[rad]

% Average voltage data at each rotary encoder step
index = 1; % initialize encoder step count (500 PPR)
uniquecount = length(unique(DATA.Theta)); % total number of unique
encoder steps
TempTheta = zeros(uniquecount,1); % Temporary crankshaft position [rad]
TempTOR = zeros(uniquecount,1); % Temporary torque [V]
TempP1 = zeros(uniquecount,1); % Temporary validyne power cylinder
pressure [V]
TempP2 = zeros(uniquecount,1); % Temporary validyne crankcase pressure
[V]
TempP3 = zeros(uniquecount,1); % Temporary PCB power cylinder pressure
[V]
TempP4 = zeros(uniquecount,1); % Temporary PCB crankcase pressure [V]
TempVTime = zeros(uniquecount,1); % Temporary Voltage DAQ Time [s]

```

```

    Ur_TOR = zeros(uniquecount,1); % torque Random Uncertainty [V]
    Ur_P1 = zeros(uniquecount,1); % validyne power cylinder pressure Random
    Uncertainty [V]
    Ur_P2 = zeros(uniquecount,1); % validyne crankcase pressure Random
    Uncertainty [V]
    Ur_P3 = zeros(uniquecount,1); % PCB power cylinder pressure Random
    Uncertainty [V]
    Ur_P4 = zeros(uniquecount,1); % PCB crankcase pressure Random Uncertainty
    [V]
    U_VTime = zeros(uniquecount,1); % Voltage DAQ Time Random Uncertainty [s]

    VIndexLow = 1;
    VIndexHigh = 2;

    for n = 2:1:length(DATA.Theta) % for every raw datapoint after the 1st

        if DATA.Theta(n) == DATA.Theta(n-1) % if the crankshaft position has
not changed

            VIndexHigh = n; % increase the high volt data index to n

        else % the crankshaft position has changed

            counter = VIndexHigh-VIndexLow; % number of samples in rotary
encoder increment

            TempTheta(index) = DATA.Theta(VIndexLow); % save current crank
angle

            % average all of the data points within encoder increment
            TempTOR(index) = sum(DATA.TOR(VIndexLow:VIndexHigh))/counter;
            TempP1(index) = sum(DATA.P1(VIndexLow:VIndexHigh))/counter;
            TempP2(index) = sum(DATA.P2(VIndexLow:VIndexHigh))/counter;
            TempP3(index) = sum(DATA.P3(VIndexLow:VIndexHigh))/counter;
            TempP4(index) = sum(DATA.P4(VIndexLow:VIndexHigh))/counter;
            TempVTime(index) =
DATA.VTime(floor(mean([VIndexLow,VIndexHigh])));

            t_0025 = tinvt(0.975,counter-1); % inverse 2 tail t-test with 95%
confidence interval

            % Calculate random uncertainty within encoder increment
            Ur_TOR(index) =
t_0025*std(DATA.TOR(VIndexLow:VIndexHigh))/sqrt(counter);
            Ur_P1(index) =
t_0025*std(DATA.P1(VIndexLow:VIndexHigh))/sqrt(counter);
            Ur_P2(index) =
t_0025*std(DATA.P2(VIndexLow:VIndexHigh))/sqrt(counter);
            Ur_P3(index) =
t_0025*std(DATA.P3(VIndexLow:VIndexHigh))/sqrt(counter);
            Ur_P4(index) =
t_0025*std(DATA.P4(VIndexLow:VIndexHigh))/sqrt(counter);

            % Calculate maximum time uncertainty

```

```

        U_VTime(index) = (DATA.VTime(VIndexHigh)-
DATA.VTime(VIndexLow))./counter;

        % move to new encoder increment
        index = index + 1;

%           counter = 1; % reset data point count
        VIndexLow = n;
    end
end

    counter = VIndexHigh-VIndexLow; % number of samples in last encoder
increment

    TempTheta(index) = DATA.Theta(VIndexLow); % save the last crank increment

% average all of the data points within last encoder increment
    TempTheta(index) = DATA.Theta(VIndexLow);
    TempTOR(index) = sum(DATA.TOR(VIndexLow:VIndexHigh))/counter;
    TempP1(index) = sum(DATA.P1(VIndexLow:VIndexHigh))/counter;
    TempP2(index) = sum(DATA.P2(VIndexLow:VIndexHigh))/counter;
    TempP3(index) = sum(DATA.P3(VIndexLow:VIndexHigh))/counter;
    TempP4(index) = sum(DATA.P4(VIndexLow:VIndexHigh))/counter;
    TempVTime(index) = sum(DATA.VTime(VIndexLow:VIndexHigh))/counter;

    t_0025 = tinv(0.975,counter); % inverse 2 tail t-test with 95% confidence
interval

% Calculate random uncertainty within last encoder increment
    Ur_TOR(index) = t_0025*std(DATA.TOR(VIndexLow:VIndexHigh))/sqrt(counter);
    Ur_P1(index) = t_0025*std(DATA.P1(VIndexLow:VIndexHigh))/sqrt(counter);
    Ur_P2(index) = t_0025*std(DATA.P2(VIndexLow:VIndexHigh))/sqrt(counter);
    Ur_P3(index) = t_0025*std(DATA.P3(VIndexLow:VIndexHigh))/sqrt(counter);
    Ur_P4(index) = t_0025*std(DATA.P4(VIndexLow:VIndexHigh))/sqrt(counter);

% Calculate maximum time uncertainty (s)
    U_VTime(index) = 0.5*(DATA.VTime(VIndexHigh)-DATA.VTime(VIndexLow));

% Move temporary data to data structure
    DATA.Theta = TempTheta;
    DATA.TOR = TempTOR;
    DATA.P1 = TempP1;
    DATA.P2 = TempP2;
    DATA.P3 = TempP3;
    DATA.P4 = TempP4;
    DATA.VTime = TempVTime;
    DATA.U_VTime = U_VTime;

%% Crank Angle Uncertainty, Angular Velocity and Uncertainty

% crank angle uncertainty
    U_Theta = sqrt((1*(pi/180))^2+(0.0232)^2+(0.017*pi/180)^2); % (rad)
% Encoder comm. accuracy, dial indicator resolution, Encoder accuracy

```

```

    % relative crank angle uncertainty
    U_ThetaRel = 0.017*pi/180; % relative crank angle uncertainty (rad)
(encoder accuracy)

    % Crankshaft instantaneous velocity and uncertainty [rad/s]
    [DATA.ThetaVel,U_ThetaVel] =
AngularVelocity(DATA.Theta,DATA.VTime,U_ThetaRel,U_VTime);

    %% Crop data to start time and 1st Z-pulse

    % find minimum time indexes

    % if RTD start time is greater than thermocouple start time and volt
    % start time
    if ((DATA.RTDTime(1)>DATA.TTime(1)) && (DATA.RTDTime(1)>DATA.VTime(1)))
        MinTime = min(DATA.RTDTime); % minimum time is RTD start time

    % if thermocouple start time is greater than RTD start time and volt
    % start time
    elseif ((DATA.TTime(1)>DATA.RTDTime(1)) && (DATA.TTime(1)>DATA.VTime(1)))
        MinTime = min(DATA.TTime); % minimum time is thermocouple start time

    % if volt start time is greater than thermocouple start time and RTD
    % start time
    elseif ((DATA.VTime(1)>DATA.TTime(1)) && (DATA.VTime(1)>DATA.RTDTime(1)))
        MinTime = DATA.VTime(1); % minimum time is volt start time

    end

    % Find first Z pulse after all DAQ started
    ZPulse1 = find(DATA.Theta == 0); % find the index of the first Z pulse

    [Temp,VStartI] = min(abs(DATA.VTime-MinTime)); % Volt minimum start time
index

    while ZPulse1<VStartI % while the first Z Pulse index is less than the
Volt minimum time index
        ZPulse1 = ZPulse1+500; % Add 1 rotation to the first Z Pulse index
    end

    StartTime = DATA.VTime(ZPulse1); % Start time is time of first Z pulse

    % find the indexes nearest to the start time
    [Temp,RTDStartI] = min(abs(DATA.RTDTime-StartTime)); % RTD start index
    [Temp,TStartI] = min(abs(DATA.TTime-StartTime)); % Thermocouple start
index
    VStartI = ZPulse1; % Volt start index

    % Crop data to shared start time
    DATA.VTime = DATA.VTime(VStartI:end);
    DATA.Theta = DATA.Theta(VStartI:end);
    DATA.ThetaVel = DATA.ThetaVel(VStartI:end);
    DATA.TOR = DATA.TOR(VStartI:end);
    DATA.P1 = DATA.P1(VStartI:end);

```

```

DATA.P2 = DATA.P2 (VStartI:end);
DATA.P3 = DATA.P3 (VStartI:end);
DATA.P4 = DATA.P4 (VStartI:end);

Ur_TOR = Ur_TOR (VStartI:end);
Ur_P1 = Ur_P1 (VStartI:end);
Ur_P2 = Ur_P2 (VStartI:end);
Ur_P3 = Ur_P3 (VStartI:end);
Ur_P4 = Ur_P4 (VStartI:end);
U_VTime = U_VTime (VStartI:end);
U_ThetaVel = U_ThetaVel (VStartI:end);

DATA.TTime = DATA.TTime (TStartI:end);
DATA.T0 = DATA.T0 (TStartI:end);
DATA.T1 = DATA.T1 (TStartI:end);
DATA.T2 = DATA.T2 (TStartI:end);
DATA.T3 = DATA.T3 (TStartI:end);
DATA.T4 = DATA.T4 (TStartI:end);
DATA.T5 = DATA.T5 (TStartI:end);

DATA.RTDTime = DATA.RTDTime (RTDStartI:end);
DATA.RTD0 = DATA.RTD0 (RTDStartI:end);
DATA.RTD1 = DATA.RTD1 (RTDStartI:end);
DATA.RTD2 = DATA.RTD2 (RTDStartI:end);
DATA.RTD3 = DATA.RTD3 (RTDStartI:end);

%% Sort Volt and RTD data into columns for a single rotation

NumCol = floor(length(DATA.Theta)/500); % total number of columns (number
of complete rotations after start)
NumRow = 500; % total number of rows (number of encoder A pulses)

% initialize temporary volt variables to correct size
TempVTime = zeros (NumRow, NumCol);
TempTheta = zeros (NumRow, NumCol);
TempTOR = zeros (NumRow, NumCol);
TempP1 = zeros (NumRow, NumCol);
TempP2 = zeros (NumRow, NumCol);
TempP3 = zeros (NumRow, NumCol);
TempP4 = zeros (NumRow, NumCol);
TempThetaVel = zeros (NumRow, NumCol);

TempUr_TOR = zeros (NumRow, NumCol);
TempUr_P1 = zeros (NumRow, NumCol);
TempUr_P2 = zeros (NumRow, NumCol);
TempUr_P3 = zeros (NumRow, NumCol);
TempUr_P4 = zeros (NumRow, NumCol);
TempU_VTime = zeros (NumRow, NumCol);
TempU_ThetaVel = zeros (NumRow, NumCol);

% initialize temporary RTD variables to correct size (one point per
% rotation)
TempRTD0 = zeros (1, NumCol);
TempRTD1 = zeros (1, NumCol);
TempRTD2 = zeros (1, NumCol);

```

```

TempRTD3 = zeros(1,NumCol);

% initialize RTD random uncertainty (one point per rotation)
Ur_RTD0 = zeros(1,NumCol);
Ur_RTD1 = zeros(1,NumCol);
Ur_RTD2 = zeros(1,NumCol);
Ur_RTD3 = zeros(1,NumCol);

for Z = 1:NumCol % for rotation count from 1 to last

    A = 1; % reset encoder A pulse count

    % index of RTDTime that is closest to the VTime at the start of the
rotation
    [Temp,RTDIndexLow] = min(abs(DATA.VTime((Z-1)*500+A)-DATA.RTDTime));

    for A = 1:NumRow % for each rotary encoder A pulse from 1 to 500

        index = (Z-1)*500+A; % corresponding index in the Volt data

        % Reorganize volt data into columns for each rotation
        TempVTime(A,Z) = DATA.VTime(index);
        TempTheta(A,Z) = DATA.Theta(index);
        TempTOR(A,Z) = DATA.TOR(index);
        TempP1(A,Z) = DATA.P1(index);
        TempP2(A,Z) = DATA.P2(index);
        TempP3(A,Z) = DATA.P3(index);
        TempP4(A,Z) = DATA.P4(index);
        TempThetaVel(A,Z) = DATA.ThetaVel(index);

        TempUr_TOR(A,Z) = Ur_TOR(index);
        TempUr_P1(A,Z) = Ur_P1(index);
        TempUr_P2(A,Z) = Ur_P2(index);
        TempUr_P3(A,Z) = Ur_P3(index);
        TempUr_P4(A,Z) = Ur_P4(index);
        TempU_VTime(A,Z) = U_VTime(index);
        TempU_ThetaVel(A,Z) = U_ThetaVel(index);

    end

    % index of RTDTime that is closest to the VTime at the end of the
rotation
    [Temp,RTDIndexHigh] = min(abs(DATA.VTime((Z-1)*500+A)-DATA.RTDTime));

    counter = RTDIndexHigh-RTDIndexLow; % number of RTD samples in this
rotation

    % average the RTD data in each rotation
    TempRTD0(1,Z) = mean(DATA.RTD0(RTDIndexLow:RTDIndexHigh));
    TempRTD1(1,Z) = mean(DATA.RTD1(RTDIndexLow:RTDIndexHigh));
    TempRTD2(1,Z) = mean(DATA.RTD2(RTDIndexLow:RTDIndexHigh));
    TempRTD3(1,Z) = mean(DATA.RTD3(RTDIndexLow:RTDIndexHigh));

```



```

        t_0025 = tinv(0.975,counter-1); % inverse 2 tail t-test with 95%
confidence interval

        % RTD data random uncertainty in this rotation
        Ur_RTD0(1,Z) =
t_0025*std(DATA.RTD0(RTDIndexLow:RTDIndexHigh))/sqrt(counter);
        Ur_RTD1(1,Z) =
t_0025*std(DATA.RTD1(RTDIndexLow:RTDIndexHigh))/sqrt(counter);
        Ur_RTD2(1,Z) =
t_0025*std(DATA.RTD2(RTDIndexLow:RTDIndexHigh))/sqrt(counter);
        Ur_RTD3(1,Z) =
t_0025*std(DATA.RTD3(RTDIndexLow:RTDIndexHigh))/sqrt(counter);

end

% Save temporary uncertainties
Ur_TOR = TempUr_TOR;
Ur_P1 = TempUr_P1;
Ur_P2 = TempUr_P2;
Ur_P3 = TempUr_P3;
Ur_P4 = TempUr_P4;
U_VTime = TempU_VTime;
U_ThetaVel = TempU_ThetaVel;

%% Sort Thermocouple data into columns for a single rotation

NumRowT = NumRow/10; % 1 data point for every 10 rotary encoder A pulses

% initialize temporary thermocouple variables to correct size (one
% point per 10 A pulses)
TempTTime = zeros(NumRowT,NumCol);
TempT0 = zeros(NumRowT,NumCol);
TempT1 = zeros(NumRowT,NumCol);
TempT2 = zeros(NumRowT,NumCol);
TempT3 = zeros(NumRowT,NumCol);
TempT4 = zeros(NumRowT,NumCol);
TempT5 = zeros(NumRowT,NumCol);

U_TTime = zeros(NumRowT,NumCol);
Ur_T0 = zeros(NumRowT,NumCol);
Ur_T1 = zeros(NumRowT,NumCol);
Ur_T2 = zeros(NumRowT,NumCol);
Ur_T3 = zeros(NumRowT,NumCol);
Ur_T4 = zeros(NumRowT,NumCol);
Ur_T5 = zeros(NumRowT,NumCol);

TIndexHigh = 1; % initialize the temperature index low (calculated in
loop)

for Z = 1:NumCol % for rotation count from 1 to last

    for AT = 1:NumRowT % for each 10 rotary encoder A pulses to 500

        TIndexLow = TIndexHigh; % the low index is the previous high
index

```

```

        VIndexLow = (Z-1)*500+(AT-1)*10+1; % the lower VTime index to
predict the next high index
        VIndexHigh = (Z-1)*500+(AT)*10; % the higher VTime index to
predict the next high index

        % the new high index is the is the index of TTime nearest to the
average of the low and high VIndexes VTime
        [Temp,TIndexHigh] = min(abs(DATA.TTime-
mean(DATA.VTime(VIndexLow:VIndexHigh)))));

        counter = TIndexHigh-TIndexLow; % number of thermocouple samples
for this interval

        % The thermocouple data in these 10 rotary encoder pulses is
% the mean between the low and high indexes
TempTTime(AT,Z) = sum(DATA.TTime(TIndexLow:TIndexHigh))/counter;
TempT0(AT,Z) = sum(DATA.T0(TIndexLow:TIndexHigh))/counter;
TempT1(AT,Z) = sum(DATA.T1(TIndexLow:TIndexHigh))/counter;
TempT2(AT,Z) = sum(DATA.T2(TIndexLow:TIndexHigh))/counter;
TempT3(AT,Z) = sum(DATA.T3(TIndexLow:TIndexHigh))/counter;
TempT4(AT,Z) = sum(DATA.T4(TIndexLow:TIndexHigh))/counter;
TempT5(AT,Z) = sum(DATA.T5(TIndexLow:TIndexHigh))/counter;

        t_0025 = tinvc(0.975,counter-1); % inverse 2 tail t-test with 95%
confidence interval

        % Thermocouple data random uncertainty in the these 10 rotary
% encoder pulses
        Ur_T0(AT,Z) =
t_0025.*std(DATA.T0(TIndexLow:TIndexHigh))./sqrt(counter);
        Ur_T1(AT,Z) =
t_0025.*std(DATA.T1(TIndexLow:TIndexHigh))./sqrt(counter);
        Ur_T2(AT,Z) =
t_0025.*std(DATA.T2(TIndexLow:TIndexHigh))./sqrt(counter);
        Ur_T3(AT,Z) =
t_0025.*std(DATA.T3(TIndexLow:TIndexHigh))./sqrt(counter);
        Ur_T4(AT,Z) =
t_0025.*std(DATA.T4(TIndexLow:TIndexHigh))./sqrt(counter);
        Ur_T5(AT,Z) =
t_0025.*std(DATA.T5(TIndexLow:TIndexHigh))./sqrt(counter);

        % Thermocouple Time Uncertainty
        U_TTime(AT,Z) = max(DATA.U_VTime(VIndexLow:VIndexHigh));

end

        AT = 1; % reset the rotary encoder 10 pulse count for the next
rotation

end

%% Correct Torque Data and Uncertainty

```

```

switch DATA.Date
case '11012018'
[DATA.TOR, DATA.Ur_TOR, DATA.Us_TOR]...
= Futek_Torque_10Nm_Calibration(TempTOR, Ur_TOR); % torque data
[Nm]

case '11022018'
[DATA.TOR, DATA.Ur_TOR, DATA.Us_TOR]...
= Futek_Torque_10Nm_Calibration(TempTOR, Ur_TOR); % torque data
[Nm]

case '11082018'
[DATA.TOR, DATA.Ur_TOR, DATA.Us_TOR]...
= Futek_Torque_10Nm_Calibration(TempTOR, Ur_TOR); % torque data
[Nm]

case '11092018'
[DATA.TOR, DATA.Ur_TOR, DATA.Us_TOR]...
= Futek_Torque_10Nm_Calibration(TempTOR, Ur_TOR); % torque data
[Nm]

case '11142018'
[DATA.TOR, DATA.Ur_TOR, DATA.Us_TOR]...
= Futek_Torque_1Nm_Calibration(TempTOR, Ur_TOR); % torque data
[Nm]

case '11152018'
[DATA.TOR, DATA.Ur_TOR, DATA.Us_TOR]...
= Futek_Torque_1Nm_Calibration(TempTOR, Ur_TOR); % torque data
[Nm]

case '11162018'
[DATA.TOR, DATA.Ur_TOR, DATA.Us_TOR]...
= Futek_Torque_1Nm_Calibration(TempTOR, Ur_TOR); % torque data
[Nm]

case '11202018'
[DATA.TOR, DATA.Ur_TOR, DATA.Us_TOR]...
= Futek_Torque_1Nm_Calibration(TempTOR, Ur_TOR); % torque data
[Nm]

case '11212018'
[DATA.TOR, DATA.Ur_TOR, DATA.Us_TOR]...
= Futek_Torque_1Nm_Calibration(TempTOR, Ur_TOR); % torque data
[Nm]

case '11232018'
[DATA.TOR, DATA.Ur_TOR, DATA.Us_TOR]...
= Futek_Torque_1Nm_Calibration(TempTOR, Ur_TOR); % torque data
[Nm]

case '11272018'
[DATA.TOR, DATA.Ur_TOR, DATA.Us_TOR]...
= Futek_Torque_1Nm_Calibration(TempTOR, Ur_TOR); % torque data
[Nm]

```

```

    case '12042018'
    [DATA.TOR,DATA.Ur_TOR,DATA.Us_TOR]...
        = Futek_Torque_1Nm_Calibration(TempTOR,Ur_TOR); % torque data
[Nm]

    case '12062018'
    [DATA.TOR,DATA.Ur_TOR,DATA.Us_TOR]...
        = Futek_Torque_1Nm_Calibration(TempTOR,Ur_TOR); % torque data
[Nm]

    case '12112018'
    [DATA.TOR,DATA.Ur_TOR,DATA.Us_TOR]...
        = Futek_Torque_1Nm_Calibration(TempTOR,Ur_TOR); % torque data
[Nm]

    case '02272019'
    [DATA.TOR,DATA.Ur_TOR,DATA.Us_TOR]...
        = Futek_Torque_1Nm_Calibration(TempTOR,Ur_TOR); % torque data
[Nm]

    otherwise
    error('Date Not Specified For Torque Calibration. Line 465');

end

%% Correct and Calibrate Pressure Data and Uncertainty

% Correct PCB Data to [Pa] and calculate uncertainty (Transucer LW35042)
DATA.P3 = TempP3.*(1000000/3.519); % Convert P3 systematic uncertainty
units [Pa]

Us_P3 = sqrt((0.01*TempP3).^2+(0.001*5)^2+0.00269^2); % (V)
% Transucer uncertainty, Transducer nonlinearity, NI-USB-6211 uncertainty
@ 10V.
DATA.Us_P3 = Us_P3.*(1000000/3.519); % Convert P3 systematic uncertainty
units [Pa]
DATA.Ur_P3 = Ur_P3.*(1000000/3.519); % Convert P3 random uncertainty
units [Pa]

% Correct PCB Data to [Pa] and calculate uncertainty (Transucer LW35041)
DATA.P4 = TempP4.*(1000000/3.602); % Convert P4 systematic uncertainty
units [Pa]

Us_P4 = sqrt((0.01*TempP4).^2+(0.001*5)^2+0.00269^2); % (V)
% Transucer uncertainty, Transducer nonlinearity, NI-USB-6211 uncertainty
@ 10V.
DATA.Us_P4 = Us_P4.*(1000000/3.602); % Convert P4 systematic uncertainty
units [Pa]
DATA.Ur_P4 = Ur_P4.*(1000000/3.602); % Convert P4 systematic uncertainty
units [Pa]

% Barometric pressure
[Pbaro] = BarometricPressure(DATA.Date);

```

```

% Validyne pressure transducer systematic uncertainty (+/- Pa)
ValFS = 6894.76*125; % Validyne transducer full scale (Pa)
Us_Val =
sqrt((0.005*ValFS)^2+(0.0005*ValFS)^2+(0.001*ValFS)^2+(0.00269*ValFS/10)^2+(0
.1*6894.75)^2+100^2); % (Pa)
% Pressure transducer accuracy, demodulator nonlinearity, demodulator
stability, NI-USB-6211 uncertainty @ 10V, calibration transducer
resolution, barometric pressure uncertainty.

% Correct Validyne P1 to (Pa)
TempP1 = Pbaro+TempP1.*12.5.*6894.76; % P1 Pressure Conversion (Pa)
DATA.P1 = TempP1+(VAL_FIT.P1(1).*TempP1.^3+VAL_FIT.P1(2).*TempP1.^2+...
VAL_FIT.P1(3).*TempP1+VAL_FIT.P1(4)); % P1 Pressure Correction (Pa)
DATA.Ur_P1 = Ur_P1.*12.5.*6894.76; % P1 random uncertainty pressuer
conversion (Pa)
DATA.Us_P1 = Us_Val; % P1 systematic uncertainty (Pa)

% Correct Validyne P2 to (Pa)
TempP2 = Pbaro+TempP2.*12.5.*6894.76; % P1 Pressure Conversion (Pa)
DATA.P2 = TempP2+(VAL_FIT.P2(1).*TempP2.^3+VAL_FIT.P2(2).*TempP2.^2+...
VAL_FIT.P2(3).*TempP2+VAL_FIT.P2(4)); % P2 Pressure Correction (Pa)
DATA.Ur_P2 = Ur_P2.*12.5.*6894.76; % P2 random uncertainty pressuer
conversion (Pa)
DATA.Us_P2 = Us_Val; % P2 systematic uncertainty (Pa)

%% Pressure Wave Transport Uncertainty

L_b_Piston_Max = 0.5056; % max distance from crankcase pressure sensor to
piston[m]
L_PC_Piston_Max = 0.1045; % max distance from power cylinder pressure
sensor to piston [m]

aSound_b = sqrt(1.4.*8.314.*(273.15+mean(mean(DATA.T5)))/0.02897); %
mean speed of sound in crankcase [m/s]
aSound_PC = sqrt(1.4.*8.314.*(273.15+mean(mean(DATA.T4)))/0.02897); %
mean speed of sound in power cylinder [m/s]

tSound_b = L_b_Piston_Max/aSound_b; % max time for pressure wave to
transport from crankcase pressure sensor to piston [s]
tSound_PC = L_PC_Piston_Max/aSound_PC; % max time for pressure wave to
transport from power cylinder pressure sensor to piston [s]

PbDotMax = 0; % initial maximum rate of crankcase pressure change [Pa/s]
PEDotMax = 0; % initial maximum rate of power cylinder pressure change
[Pa/s]

for j = 1:NumCol % for each row (except first) in each column of voltage
data
    for i = 2:NumRow

        % calculate the absolute rate of pressure change from previous
data point [Pa/s]
        PbDot = (DATA.P4(i,j)-DATA.P4(i-1,j))/(TempVTime(i,j)-
TempVTime(i-1,j));

```

```

        PEDot = (DATA.P3(i,j)-DATA.P3(i-1,j))/(TempVTime(i,j)-
TempVTime(i-1,j));

        if PbDot>PbDotMax % if rate of pressure change is greater than
the previous maximum
            PbDotMax = PbDot; % replace the previous maximum [Pa/s]
        end

        if PEDot>PEDotMax % if rate of pressure change is greater than
the previous maximum
            PEDotMax = PEDot; % replace the previous maximum [Pa/s]
        end
    end
end

    UTrans_Pb = PbDotMax*tSound_b; % Systematic uncertainty caused by
pressure wave transport in crankcase [Pa]
    UTrans_PE = PEDotMax*tSound_PC; % Systematic uncertainty caused by
pressure wave transport in power cylinder [Pa]

    %% Combine Static and Dynamic Pressure

    % Mean engine pressure and uncertainty (Pa)
    DATA.PE_mean = ones(size(DATA.P2)).*(mean(DATA.P2)); % Mean engine
pressure
    DATA.U_P2 = sqrt(DATA.Ur_P2.^2+DATA.Us_P2.^2); % P2 combined uncertainty
    DATA.U_PE_mean = sqrt(sum(DATA.U_P2.^2)./500); % Mean engine pressure
uncerativity

    % Engine pressure and uncerativity (Pa)
    DATA.PE = DATA.PE_mean+DATA.P3; % Engine pressure
    DATA.U_PE_rel = sqrt(DATA.Ur_P3.^2+DATA.Us_P3.^2+UTrans_PE.^2); %
Relative engine pressure uncertainty

    % Mean buffer pressure and uncertainty (Pa)
    DATA.Pb_mean = ones(size(DATA.P1)).*(mean(DATA.P1)); % Mean buffer
pressure
    DATA.U_P1 = sqrt(DATA.Ur_P1.^2+DATA.Us_P1.^2); % P1 combined uncertainty
    DATA.U_Pb_mean = sqrt(sum(DATA.U_P1.^2)./500); % Mean buffer pressure
uncerativity

    % Buffer pressure and uncerativity (Pa)
    DATA.Pb = DATA.Pb_mean+DATA.P4; % Buffer pressure
    DATA.U_Pb_rel = sqrt(DATA.Ur_P4.^2+DATA.Us_P4.^2+UTrans_Pb.^2); %
Relative buffer pressure uncertainty

    %% Calibrate thermocouple temperature data

    % Thermocouple systematic uncerativity (+/- deg. C)
    DATA.Us_T = sqrt(3.135^2+1.488^2+0.1^2+0.35^2);
    % thermocouple tolerance, SCXI-1600 accuracy, calibration thermometer
resolution, cold junction repeatability error

    % T0 temperature correction
    DATA.T0 = TempT0+(TC_FIT.TC_0(1).*TempT0+TC_FIT.TC_0(2));

```

```

DATA.Ur_T0 = Ur_T0.*TC_FIT.TC_0(1); % T0 random uncertainty correction

% T1 temperature correction
DATA.T1 = TempT1+(TC_FIT.TC_1(1).*TempT1+TC_FIT.TC_1(2));
DATA.Ur_T1 = Ur_T1.*TC_FIT.TC_1(1); % T1 random uncertainty correction

% T2 temperature correction
DATA.T2 = TempT2+(TC_FIT.TC_2(1).*TempT2+TC_FIT.TC_2(2));
DATA.Ur_T2 = Ur_T2.*TC_FIT.TC_2(1); % T2 random uncertainty correction

% T3 temperature correction
DATA.T3 = TempT3+(TC_FIT.TC_3(1).*TempT3+TC_FIT.TC_3(2));
DATA.Ur_T3 = Ur_T3.*TC_FIT.TC_3(1); % T3 random uncertainty correction

% T4 temperature correction
DATA.T4 = TempT4+(TC_FIT.TC_4(1).*TempT4+TC_FIT.TC_4(2));
DATA.Ur_T4 = Ur_T4.*TC_FIT.TC_4(1); % T4 random uncertainty correction

% T5 temperature correction
DATA.T5 = TempT5+(TC_FIT.TC_5(1).*TempT5+TC_FIT.TC_5(2));
DATA.Ur_T5 = Ur_T5.*TC_FIT.TC_5(1); % T0 random uncertainty correction

%% Calibrate RTD temperature data

% RTD systematic uncertainty (+/- deg. C)
DATA.Us_RTD = sqrt(0.35^2+0.5^2+0.1^2);
% RTD deviation, RTD module accuracy, calibration thermometer resolution

% RTD0 temperature correction
DATA.RTD0 = TempRTD0+(RTD_FIT.RTD0(1).*TempRTD0.^3 +
RTD_FIT.RTD0(2).*TempRTD0.^2 + RTD_FIT.RTD0(3).*TempRTD0 + RTD_FIT.RTD0(4));
DATA.Ur_RTD0 = Ur_RTD0.*(DATA.RTD0./TempRTD0); % RTD0 uncertainty
correction

% RTD1 temperature correction
DATA.RTD1 = TempRTD1+(RTD_FIT.RTD1(1).*TempRTD1.^3 +
RTD_FIT.RTD1(2).*TempRTD1.^2 + RTD_FIT.RTD1(3).*TempRTD1 + RTD_FIT.RTD1(4));
DATA.Ur_RTD1 = Ur_RTD1.*(DATA.RTD1./TempRTD1); % RTD1 uncertainty
correction

% RTD2 temperature correction
DATA.RTD2 = TempRTD2+(RTD_FIT.RTD2(1).*TempRTD2.^3 +
RTD_FIT.RTD2(2).*TempRTD2.^2 + RTD_FIT.RTD2(3).*TempRTD2 + RTD_FIT.RTD2(4));
DATA.Ur_RTD2 = Ur_RTD2.*(DATA.RTD2./TempRTD2); % RTD2 uncertainty
correction

% RTD3 temperature correction
DATA.RTD3 = TempRTD3+(RTD_FIT.RTD3(1).*TempRTD3.^3 +
RTD_FIT.RTD3(2).*TempRTD3.^2 + RTD_FIT.RTD3(3).*TempRTD3 + RTD_FIT.RTD3(4));
DATA.Ur_RTD3 = Ur_RTD3.*(DATA.RTD3./TempRTD3); % RTD3 uncertainty
correction

%% Calculate Engine Volumes and Uncertainty

```

```

[Vc,Ve,Vb,Vtot,dVc,dVe,dVb,dVtot] = volume_DAM(TempTheta,
DATA.ENGINE_DATA); % calculate engine volumes (m^3)
[VcLead,VeLead,VbLead,VtotLead,dVcLead,dVeLead,dVbLead,dVtotLead] =
volume_DAM(TempTheta+U_Theta, DATA.ENGINE_DATA); % calculate leading engine
volumes
[VcLag,VeLag,VbLag,VtotLag,dVcLag,dVeLag,dVbLag,dVtotLag] =
volume_DAM(TempTheta-U_Theta, DATA.ENGINE_DATA); % calculate lagging engine
volumes

U_Vc = max(cat(3,abs(Vc-VcLead),abs(Vc-VcLag)),[],3); % compression space
volume uncertainty (m^3)
U_dVc = max(cat(3,abs(dVc-dVcLead),abs(dVc-dVcLag)),[],3); % compression
space volume change uncertainty (m^3)

U_Ve = max(cat(3,abs(Ve-VeLead),abs(Ve-VeLag)),[],3); % expansion space
volume uncertainty (m^3)
U_dVe = max(cat(3,abs(dVe-dVeLead),abs(dVe-dVeLag)),[],3); % expansion
space volume change uncertainty (m^3)

U_Vb = max(cat(3,abs(Vb-VbLead),abs(Vb-VbLag)),[],3); % buffer space
volume uncertainty (m^3)
U_dVb = max(cat(3,abs(dVb-dVbLead),abs(dVb-dVbLag)),[],3); % buffer space
volume change uncertainty (m^3)

U_Vtot = max(cat(3,abs(Vtot-VtotLead),abs(Vtot-VtotLag)),[],3); % total
engine volume uncertainty (m^3)
U_dVtot = max(cat(3,abs(dVtot-dVtotLead),abs(dVtot-dVtotLag)),[],3); %
total engine volume change uncertainty (m^3)

%% Organize Data Structure

DATA_PRO.FileName = RAW_FileName; % File Name

DATA_PRO.TH = DATA.TH; % Thermal Source Temperature (deg. C)
DATA_PRO.TC = DATA.TC; % Thermal Sink Temperature (deg. C)
DATA_PRO.PT = DATA.PT; % Target Mean Pressure (Pa)
% DATA_PRO.ENGINE_DATA = DATA.ENGINE_DATA; % Engine Data Structure
DATA_PRO.ENGINE_DATA = []; % Engine Data Structure

DATA_PRO.VTime = TempVTime; % Voltage DAQ Time (s) (Reference Time)
DATA_PRO.U_VTime = U_VTime; % Voltage Time Uncertainty (s)

DATA_PRO.Theta = TempTheta; % Absolute Crank Angle (rad)
DATA_PRO.U_Theta = U_Theta; % Crank Angle Uncertainty (rad)

DATA_PRO.ThetaVel = TempThetaVel; % Crankshaft Speed (rad/s)
DATA_PRO.U_ThetaVel = U_ThetaVel; % Crankshaft Speed Uncertainty (rad/s)

DATA_PRO.TOR = DATA.TOR; % Load Torque (Nm)
DATA_PRO.U_TOR = sqrt((max(max(DATA.Ur_TOR))^2+DATA.Us_TOR^2)); % Load
Torque Uncertainty (Nm)

DATA_PRO.PE = DATA.PE; % Engine Pressure (Pa)

```



```

DATA_PRO.U_PE_mean = DATA.U_PE_mean; % Mean Engine Pressure Uncertainty
(Pa)
DATA_PRO.U_PE_rel = DATA.U_PE_rel; % Relative Engine Pressure Uncertainty
(Pa)

DATA_PRO.Pb = DATA.Pb; % Buffer Pressure (Pa)
DATA_PRO.U_Pb_mean = DATA.U_Pb_mean; % Mean Buffer Pressure Uncertainty
(Pa)
DATA_PRO.U_Pb_rel = DATA.U_Pb_rel; % Relative Buffer Pressure Uncertainty
(Pa)

DATA_PRO.Vc = Vc; % Compression Space Volume (m^3)
DATA_PRO.U_Vc = U_Vc; % Compression Space Volume Uncertainty (m^3)
DATA_PRO.dVc = dVc; % Compression Space Volume change (m^3)
DATA_PRO.U_dVc = U_dVc; % Compression Space Volume change Uncertainty
(m^3)

DATA_PRO.Ve = Ve; % Expansion Space Volume (m^3)
DATA_PRO.U_Ve = U_Ve; % Expansion Space Volume Uncertainty (m^3)
DATA_PRO.dVe = dVe; % Expansion Space Volume change (m^3)
DATA_PRO.U_dVe = U_dVe; % Expansion Space Volume change Uncertainty (m^3)

DATA_PRO.Vb = Vb; % Buffer Space Volume (m^3)
DATA_PRO.U_Vb = U_Vb; % Buffer Space Volume Uncertainty (m^3)
DATA_PRO.dVb = dVb; % Buffer Space Volume change (m^3)
DATA_PRO.U_dVb = U_dVb; % Buffer Space Volume change Uncertainty (m^3)

DATA_PRO.Vtot = Vtot; % Total Engine Volume (m^3)
DATA_PRO.U_Vtot = U_Vtot; % Total Engine Volume Uncertainty (m^3)
DATA_PRO.dVtot = dVtot; % Total Engine Volume change (m^3)
DATA_PRO.U_dVtot = U_dVtot; % Total Engine Volume change Uncertainty
(m^3)
DATA_PRO.VtotLead = VtotLead; % Total Engine Volume (m^3)
DATA_PRO.VtotLag = VtotLag; % Total Engine Volume (m^3)

DATA_PRO.TTime = TempTTime; % Thermocouple DAQ Time (s)
DATA_PRO.U_TTime = U_TTime; % Thermocouple DAQ Time Uncertainty (s)

DATA_PRO.T0 = DATA.T0; % Expansion Space Temperature (deg. C)
DATA_PRO.U_T0 = sqrt((max(max(DATA.Ur_T0)))^2+DATA.Us_T^2); % Regen-
Cooler Bypass side Temperature Uncertainty (deg. C)

DATA_PRO.T1 = DATA.T1; % HH-Regen Temperature (deg. C)
DATA_PRO.U_T1 = sqrt((max(max(DATA.Ur_T1)))^2+DATA.Us_T^2); % Regen-
Cooler Bypass side Temperature Uncertainty (deg. C)

DATA_PRO.T2 = DATA.T2; % Regen-Cooler Bypass side Temperature (deg. C)
DATA_PRO.U_T2 = sqrt((max(max(DATA.Ur_T2)))^2+DATA.Us_T^2); % Regen-
Cooler Bypass side Temperature Uncertainty (deg. C)

DATA_PRO.T3 = DATA.T3; % Displacer Mount Temperature (deg. C)
DATA_PRO.U_T3 = sqrt((max(max(DATA.Ur_T3)))^2+DATA.Us_T^2); % Displacer
Mount Temperature Uncertainty (deg. C)

DATA_PRO.T4 = DATA.T4; % Power Cylinder Temperature (deg. C)

```

```

DATA_PRO.U_T4 = sqrt((max(max(DATA.Ur_T4)))^2+DATA.Us_T^2); % Power
Cylinder Temperature Uncertainty (deg. C)

DATA_PRO.T5 = DATA.T5; % Crankcase Temperature (deg. C)
DATA_PRO.U_T5 = sqrt((max(max(DATA.Ur_T5)))^2+DATA.Us_T^2); % Crankcase
Temperature Uncertainty (deg. C)

DATA_PRO.RTD0 = TempRTD0; % Cooler Water Inlet Temperature (deg. C)
DATA_PRO.U_RTD0 = sqrt((max(DATA.Ur_RTD0))^2+DATA.Us_RTD^2); % Cooler
Water Inlet Temperature Uncertainty (deg. C)

DATA_PRO.RTD1 = TempRTD1; % Cooler Water Outlet Temperature (deg. C)
DATA_PRO.U_RTD1 = sqrt((max(DATA.Ur_RTD1))^2+DATA.Us_RTD^2); % Cooler
Water Outlet Temperature Uncertainty (deg. C)

DATA_PRO.RTD2 = TempRTD2; % Power Cylinder Water Inlet Temperature (deg.
C)
DATA_PRO.U_RTD2 = sqrt((max(DATA.Ur_RTD2))^2+DATA.Us_RTD^2); % Power
Cylinder Water Inlet Temperature Uncertainty (deg. C)

DATA_PRO.RTD3 = TempRTD3; % Power Cylinder Water Outlet Temperature (deg.
C)
DATA_PRO.U_RTD3 = sqrt((max(DATA.Ur_RTD3))^2+DATA.Us_RTD^2); % Power
Cylinder Water Outlet Temperature Uncertainty (deg. C)

[DATA_PRO.WI, DATA_PRO.U_WI] = ExperimentIndicatedWork(DATA_PRO); %
Indicated Work and Uncertainty (J)
[DATA_PRO.PwrS, DATA_PRO.U_PwrS] = ExperimentShaftPower(DATA_PRO); %
Shaft Power and Uncertainty (W)

%% Calculate Engine Data for Model
DATA.ENGINE_DATA.pmean = mean(DATA_PRO.PE, 'all'); % mean engine pressure
(Pa)

DATA.ENGINE_DATA.Tsource = DATA_PRO.TH+273.15; % Thermal source
temperature (K)
DATA.ENGINE_DATA.Tsink = DATA_PRO.TC+273.15; % Thermal sink temperature
(K)

DATA.ENGINE_DATA.Tge = mean(DATA_PRO.T0, 'all')+273.15; % Expansion space
gas temperature (K)
DATA.ENGINE_DATA.Tgc = mean(DATA_PRO.T4, 'all')+273.15; % Compression
space gas temperature (K)

DATA.ENGINE_DATA.Tgk = mean([DATA_PRO.T2 DATA_PRO.T3], 'all')+273.15; %
Cooler gas temperature (K) mean of regen-cooler interface and
displacer mount
DATA.ENGINE_DATA.Twk = DATA.ENGINE_DATA.Tgk; % Cooler wall temperature
(K) same as gas temperature

DATA.ENGINE_DATA.Tgh = mean([DATA_PRO.T0 DATA_PRO.T1], 'all')+273.15; %
Heater gas temperature (K) mean of regen-cooler interface and
displacer mount
DATA.ENGINE_DATA.Twh = DATA.ENGINE_DATA.Tgh; % Heater wall temperature
(K) same as gas temperature

```

```

DATA.ENGINE_DATA.freq = mean(DATA_PRO.ThetaVel, 'all')/(2*pi); % Engine
Frequency (Hz)

%% Run Model For Condition And Save Results in Structure

crank_inc = 360/(size(DATA_PRO.VTime,1)); % crank increment to integrate
over in model (deg) 1 rotary encoder pulse
[SECOND_ORDER_DATA, REF_CYCLE_DATA, LOSSES_DATA, DATA.ENGINE_DATA] =
HTG_2nd_Order(DATA.ENGINE_DATA, crank_inc);

DATA_PRO.ENGINE_DATA = DATA.ENGINE_DATA; % Engine Data Structure
DATA_PRO.SECOND_ORDER_DATA = SECOND_ORDER_DATA; % Second Order Model
Results Structure
DATA_PRO.REF_CYCLE_DATA = REF_CYCLE_DATA; % Reference Cycle Results
Structure
DATA_PRO.LOSSES_DATA = LOSSES_DATA; % Decoupled Loss Calculation Results
Structure

% Save processed data structure as .mat file with same base name as log
files
PRO_FileName = strcat('PRO_', FileName);
evalc([matlab.lang.makeValidName(PRO_FileName), ' = DATA_PRO']);
save(strcat(PRO_FileLocation, '/', PRO_FileName, '.mat'), PRO_FileName);
clear(PRO_FileName);

clear DATA DATA_PRO

waitbar(FileNum/length(FilesInfo));
fprintf('\nLogfile %s Processed', FileName);

end
close(WaitBar)
clear vars
fprintf('\n*****\nAll Files Processed\n*****\n');
end

```

## Data Import Functions

---

Data processing imported data from three \*.log files. The voltage data import function imported voltage data. The thermocouple data import function imported thermocouple data. The RTD data import function imported RTD data.

### Voltage Data Import Function

```
function [Time,A1,Z1,TOR1,P1,P2,P3,P4] = PImport(filename)
%IMPORTFILE Import numeric data from a text file as column vectors.
% [Time,A1,Z1,TOR1,P1,P2,P3,P4] = PImport(filename) Reads data from
% text file FILENAME for the default selection.
%
% Example:
% [Time,A1,Z1,TOR1,P1,P2,P3,P4] = PImport('X:\01_Current_Students...
% ...\David Miller\06_DAQAndExperiments\02_DataProcessing...
% ...\02_DataSetProcessor\TestData_10s\TEST_LOG_Volt.log');

%% Import data from text file.
% Script for importing data from the following text file:
%
% X:\01_Current_Students\David
Miller\06_DAQAndExperiments\02_DataProcessing\02_DataSetProcessor\TestData_10
s\TEST_LOG_Volt.log
%
% To extend the code to different selected data or a different text file,
% generate a function instead of a script.

% Auto-generated by MATLAB on 2018/10/17 10:14:14

%% Initialize variables.
% filename = 'X:\01_Current_Students\David
Miller\06_DAQAndExperiments\02_DataProcessing\02_DataSetProcessor\TestData_10
s\TEST_LOG_Volt.log';
delimiter = '\t';
startRow = 6;

%% Format for each line of text:
% column1: double (%f)
% column2: double (%f)
% column3: double (%f)
% column4: double (%f)
% column5: double (%f)
% column6: double (%f)
% column7: double (%f)
% For more information, see the TEXTSCAN documentation.
formatSpec = '%f%f%f%f%f%f%f%[\n\r]';

%% Open the text file.
fileID = fopen(filename,'r');
```

```

%% Read columns of data according to the format.
% This call is based on the structure of the file used to generate this
% code. If an error occurs for a different file, try regenerating the code
% from the Import Tool.
dataArray = textscan(fileID, formatSpec, 'Delimiter', delimiter, 'TextType',
'string', 'EmptyValue', NaN, 'HeaderLines' ,startRow-1, 'ReturnOnError',
false, 'EndOfLine', '\r\n');

%% Close the text file.
fclose(fileID);

%% Post processing for unimportable data.
% No unimportable data rules were applied during the import, so no post
% processing code is included. To generate code which works for
% unimportable data, select unimportable cells in a file and regenerate the
% script.

%% Allocate imported array to column variable names
A1 = dataArray(:, 1);
Z1 = dataArray(:, 2);
TOR1 = dataArray(:, 3);
P1 = dataArray(:, 4);
P2 = dataArray(:, 5);
P3 = dataArray(:, 6);
P4 = dataArray(:, 7);

%% Clear temporary variables
% clearvars filename delimiter startRow formatSpec fileID dataArray ans;
% end of auto-generated script

%% Collect the Start and End Times of the voltage log file (by Connor Speer)
volt_log_file = fileread(filename);
start_index = regexp(volt_log_file, 'Start');
end_index = regexp(volt_log_file, 'End');
start_line = volt_log_file(start_index:end_index-1);
end_line = volt_log_file(end_index:end_index+14);
[token_start, remain_start] = strtok(start_line);
[token_end, remain_end] = strtok(end_line);
start_time = str2double(strip(remain_start));
end_time = str2double(strip(remain_end));

% Time for voltages
time_inc_Volt = (end_time-start_time)/length(A1);
N_Volt = length(A1);
Time = ((0:N_Volt-1)*time_inc_Volt)+start_time; % time starts when acquire
button clicked
Time = Time(:);

%% Clear temporary variables
clearvars filename delimiter startRow formatSpec fileID dataArray ans;
end

```

## Thermocouple Data Import Function

```
function [Time,T0,T1,T2,T3,T4,T5] = TImport(filename)
%IMPORTFILE Import numeric data from a text file as column vectors.
% [TTime,T0,T1,T2,T3,T4,T5] = TImport(Tfilename) Reads data from
% text file FILENAME for the default selection.
%
% Example:
% [TTime,T0,T1,T2,T3,T4,T5] = TImport('X:\01_Current_Students...
% ...\David Miller\06_DAQAndExperiments\02_DataProcessing...
% ...\02_DataSetProcessor\TestData_10s\TEST_LOG_Temp.log');

%% Import data from text file.
% Script for importing data from the following text file:
%
% X:\01_Current_Students\David
Miller\06_DAQAndExperiments\01_ExperimentData\2018-10-17-
Test10s\10172018_092300_200_20_060_ABA_L_Temp.log
%
% To extend the code to different selected data or a different text file,
% generate a function instead of a script.

% Auto-generated by MATLAB on 2018/10/25 16:19:30

%% Initialize variables.
% filename = 'X:\01_Current_Students\David
Miller\06_DAQAndExperiments\01_ExperimentData\2018-10-17-
Test10s\10172018_092300_200_20_060_ABA_L_Temp.log';
delimiter = '\t';
startRow = 6;

%% Format for each line of text:
% column1: double (%f)
% column2: double (%f)
% column3: double (%f)
% column4: double (%f)
% column5: double (%f)
% column6: double (%f)
% For more information, see the TEXTSCAN documentation.
formatSpec = '%f%f%f%f%f%f*s%[\n\r]';

%% Open the text file.
fileID = fopen(filename,'r');

%% Read columns of data according to the format.
% This call is based on the structure of the file used to generate this
% code. If an error occurs for a different file, try regenerating the code
% from the Import Tool.
dataArray = textscan(fileID, formatSpec, 'Delimiter', delimiter, 'TextType',
'string', 'EmptyValue', NaN, 'HeaderLines', startRow-1, 'ReturnOnError',
false, 'EndOfLine', '\r\n');

%% Close the text file.
fclose(fileID);
```

```

%% Post processing for unimportable data.
% No unimportable data rules were applied during the import, so no post
% processing code is included. To generate code which works for
% unimportable data, select unimportable cells in a file and regenerate the
% script.

%% Allocate imported array to column variable names
T0 = dataArray(:, 1);
T1 = dataArray(:, 2);
T2 = dataArray(:, 3);
T3 = dataArray(:, 4);
T4 = dataArray(:, 5);
T5 = dataArray(:, 6);

%% Clear temporary variables
% clearvars filename delimiter startRow formatSpec fileID dataArray ans;
% end of auto generated script

%% Prev version
% %% Import data from text file.
% % Script for importing data from the following text file:
% %
% % X:\01_Current_Students\David
Miller\06_DAQAndExperiments\02_DataProcessing\02_DataSetProcessor\TestData_10
s\TEST_LOG_Temp.log
% %
% % To extend the code to different selected data or a different text file,
% % generate a function instead of a script.
% %
% % Auto-generated by MATLAB on 2018/10/17 11:01:37
% %
% %% Initialize variables.
% % filename = 'X:\01_Current_Students\David
Miller\06_DAQAndExperiments\02_DataProcessing\02_DataSetProcessor\TestData_10
s\TEST_LOG_Temp.log';
% delimiter = '\t';
% startRow = 6;
% %
% %% Format for each line of text:
% % column1: double (%f)
% % column2: double (%f)
% % column3: double (%f)
% % column4: double (%f)
% % column5: double (%f)
% % column6: double (%f)
% % column7: double (%f)
% % For more information, see the TEXTSCAN documentation.
% formatSpec = '%f%f%f%f%f%f%f%[\n\r]';
% %
% %% Open the text file.
% fileID = fopen(filename,'r');
% %
% %% Read columns of data according to the format.
% % This call is based on the structure of the file used to generate this
% % code. If an error occurs for a different file, try regenerating the code

```

```

% % from the Import Tool.
% dataArray = textscan(fileID, formatSpec, 'Delimiter', delimiter,
'TextType', 'string', 'EmptyValue', NaN, 'HeaderLines' ,startRow-1,
'ReturnOnError', false, 'EndOfLine', '\r\n');
%
% %% Close the text file.
% fclose(fileID);
%
% %% Post processing for unimportable data.
% % No unimportable data rules were applied during the import, so no post
% % processing code is included. To generate code which works for
% % unimportable data, select unimportable cells in a file and regenerate the
% % script.
%
% %% Allocate imported array to column variable names
% T0 = dataArray(:, 1);
% T1 = dataArray(:, 2);
% T2 = dataArray(:, 3);
% T3 = dataArray(:, 4);
% T4 = dataArray(:, 5);
% T5 = dataArray(:, 6);
% T6 = dataArray(:, 7);
%
%
% %% Clear temporary variables
% % clearvars filename delimiter startRow formatSpec fileID dataArray ans;
% % end of auto-generated script

%% Collect the Start and End Times of the thermocouple log file
T_log_file = fileread(filename);
start_index = regexp(T_log_file, 'Start');
end_index = regexp(T_log_file, 'End');
start_line = T_log_file(start_index:end_index-1);
end_line = T_log_file(end_index:end_index+14);
[token_start, remain_start] = strtok(start_line);
[token_end, remain_end] = strtok(end_line);
start_time = str2double(strip(remain_start));
end_time = str2double(strip(remain_end));

% Time for thermocouples
time_inc_T = (end_time-start_time)/length(T0);
N_T = length(T0);
Time = ((0:N_T-1)*time_inc_T)+start_time; % time starts when aquire button
clicked
Time = Time(:);

%% Clear temporary variables
% clearvars filename delimiter startRow formatSpec fileID dataArray ans;
end

```



## RTD Data Import Function

```
function [Time,RTD0,RTD1,RTD2,RTD3] = RTDImport(filename)
%IMPORTFILE Import numeric data from a text file as column vectors.
% [Time,RTD0,RTD1,RTD2,RTD3] = RTDImport(filename) Reads data from
% text file FILENAME for the default selection.
%
% Example:
% [Time,RTD0,RTD1,RTD2,RTD3] = RTDImport('X:\01_Current_Students...
% ...\David Miller\06_DAQAndExperiments\02_DataProcessing...
% ...\02_DataSetProcessor\TestData_10s\TEST_LOG_RTD.log');

%% Import data from text file.
% Script for importing data from the following text file:
%
% X:\01_Current_Students\David
Miller\06_DAQAndExperiments\02_DataProcessing\02_DataSetProcessor\TestData_10
s\TEST_LOG_RTD.log
%
% To extend the code to different selected data or a different text file,
% generate a function instead of a script.

% Auto-generated by MATLAB on 2018/10/17 11:21:42

%% Initialize variables.
% filename = 'X:\01_Current_Students\David
Miller\06_DAQAndExperiments\02_DataProcessing\02_DataSetProcessor\TestData_10
s\TEST_LOG_RTD.log';
delimiter = '\t';
startRow = 6;

%% Format for each line of text:
% column1: double (%f)
% column2: double (%f)
% column3: double (%f)
% column4: double (%f)
% For more information, see the TEXTSCAN documentation.
formatSpec = '%f%f%f%f%[\n\r]';

%% Open the text file.
fileID = fopen(filename,'r');

%% Read columns of data according to the format.
% This call is based on the structure of the file used to generate this
% code. If an error occurs for a different file, try regenerating the code
% from the Import Tool.
dataArray = textscan(fileID, formatSpec, 'Delimiter', delimiter, 'TextType',
'string', 'HeaderLines', startRow-1, 'ReturnOnError', false, 'EndOfLine',
'\r\n');

%% Close the text file.
fclose(fileID);

%% Post processing for unimportable data.
% No unimportable data rules were applied during the import, so no post
```

```

% processing code is included. To generate code which works for
% unimportable data, select unimportable cells in a file and regenerate the
% script.

%% Allocate imported array to column variable names
RTD0 = dataArray(:, 1);
RTD1 = dataArray(:, 2);
RTD2 = dataArray(:, 3);
RTD3 = dataArray(:, 4);

%% Clear temporary variables
% clearvars filename delimiter startRow formatSpec fileID dataArray ans;
% end of auto-generated script

%% Collect the Start and End Times of the thermocouple log file
RTD_log_file = fileread(filename);
start_index = regexp(RTD_log_file, 'Start');
end_index = regexp(RTD_log_file, 'End');
start_line = RTD_log_file(start_index:end_index-1);
end_line = RTD_log_file(end_index:end_index+14);
[token_start, remain_start] = strtok(start_line);
[token_end, remain_end] = strtok(end_line);
start_time = str2double(strip(remain_start));
end_time = str2double(strip(remain_end));

% Time for thermocouples
time_inc_RTD = (end_time-start_time)/length(RTD0);
N_RTD = length(RTD0);
Time = ((0:N_RTD-1)*time_inc_RTD)+start_time; % time starts when aquire
button clicked
Time = Time(:);

%% Clear temporary variables
clearvars filename delimiter startRow formatSpec fileID dataArray ans;
end

```

# Calibration Functions

---

Data processing used five calibration functions. The general calibration function called on the thermocouple calibration function, Validyne calibration function, and RTD calibration function. The torque transducer calibration function calibrated torque data from manufacturer calibration data.

## General Calibration Function

```
% Write_Calibration_Functions.m
% Modified by David Miller - Oct. 2018
% Modified to reflect the current DAQ system and save the polynomial
% calibration corrections data structure as a .mat file
%
% Original File:
% Calibration_Function_Call.m
% Written by Connor Speer, November 2017

clear,clc,close all;

addpath('X:\01_Current_Students\David
Miller\06_DAQAndExperiments\02_DataProcessing\04_ImportFunctions');
addpath('X:\01_Current_Students\David
Miller\06_DAQAndExperiments\02_DataProcessing\05_SupportFunctions');

%% Plot Set-Up
% Set default plot properties
set(0,'defaultfigurecolor',[1 1 1])
set(0,'defaultAxesFontName','Times New Roman');
set(0,'defaultTextFontName','Times New Roman');
set(0,'defaultAxesFontSize',11);
set(0,'defaultTextFontSize',11);

% Set Figure Size
Width=8; %Centimeters
Height=7; %Centimeters
get(0,'ScreenSize');
set(0,'Units','centimeter');
a=get(0,'ScreenSize');
set(groot,'defaultFigureUnits','centimeters');
set(groot,'defaultFigurePosition',[5,5,Width,Height]);

%% Thermocouples
TC_Cal_Folder = 'X:\01_Current_Students\David
Miller\06_DAQAndExperiments\02_DataProcessing\01_Calibration\2018-10-
25_TCCalibration';
[TC_FIT] = TCCorrectionTerms(TC_Cal_Folder);
```

```

% Collect all the log file names from the test data folder
log_files_info = dir(fullfile(TC_Cal_Folder, '*.log'));

counter = 1;
for i = 1:length(log_files_info)
    filename_TC = strcat(TC_Cal_Folder, '\', log_files_info(i).name);
    [Time, T0, T1, T2, T3, T4, T5] = TImport(filename_TC);
    %     T_0 --> Expansion Space
    %     T_1 --> HH-Regen
    %     T_2 --> HH Flange - Bypass Side
    %     T_3 --> Displacer Mount
    %     T_4 --> Power Cylinder
    %     T_5 --> Crankcase

    % The true temperature from the reference thermometer and stored in the
    % file name
    TC_true(:, counter) = str2double(log_files_info(i).name(17:19))/10;

    TC_0_raw(:, counter) = T0; %(deg C)
    TC_1_raw(:, counter) = T1; %(deg C)
    TC_2_raw(:, counter) = T2; %(deg C)
    TC_3_raw(:, counter) = T3; %(deg C)
    TC_4_raw(:, counter) = T4; %(deg C)
    TC_5_raw(:, counter) = T5; %(deg C)

    % TC 0 temperature correction
    TC_0_calibrated(:, counter) =
TC_0_raw(:, counter) + (TC_0_raw(:, counter) .* TC_FIT.TC_0(1) + TC_FIT.TC_0(2));
    % TC 1 temperature correction
    TC_1_calibrated(:, counter) =
TC_1_raw(:, counter) + (TC_1_raw(:, counter) .* TC_FIT.TC_1(1) + TC_FIT.TC_1(2));
    % TC 2 temperature correction
    TC_2_calibrated(:, counter) =
TC_2_raw(:, counter) + (TC_2_raw(:, counter) .* TC_FIT.TC_2(1) + TC_FIT.TC_2(2));
    % TC 3 temperature correction
    TC_3_calibrated(:, counter) =
TC_3_raw(:, counter) + (TC_3_raw(:, counter) .* TC_FIT.TC_3(1) + TC_FIT.TC_3(2));
    % TC 4 temperature correction
    TC_4_calibrated(:, counter) =
TC_4_raw(:, counter) + (TC_4_raw(:, counter) .* TC_FIT.TC_4(1) + TC_FIT.TC_4(2));
    % TC 5 temperature correction
    TC_5_calibrated(:, counter) =
TC_5_raw(:, counter) + (TC_5_raw(:, counter) .* TC_FIT.TC_5(1) + TC_FIT.TC_5(2));

    counter = counter + 1;
end

% Save TC Fit Coefficients data structure
save('X:\01_Current_Students\David
Miller\06_DAQAndExperiments\02_DataProcessing\01_Calibration\TC_FIT.mat', 'TC_
FIT');

% Calculate thermocouple error
Us_T = ones(1, size(TC_0_calibrated, 2)) .* sqrt(2.2^2 + 1.488^2 + 0.1^2 + 0.35^2);

```

```

% Plot 5a - Measured Temperature vs. "True" Temperature before adjustment
% figure('Position', [x y 326 275])
% hold on
% % plot(mean(TC_0_raw),TC_true,'*k')
% % plot(mean(TC_1_raw),TC_true,'*g')
% plot(mean(TC_2_raw),TC_true,'*b')
% plot(mean(TC_3_raw),TC_true,'*m')
% plot(mean(TC_4_raw),TC_true,'*c')
% plot(mean(TC_5_raw),TC_true,'*r')
% plot(mean(TC_6_raw),TC_true,'*y')
% plot(TC_true,TC_true,'-r')
% hold off
% xlabel('"True" Temperature (\circC)')
% ylabel('Measured Temperature (\circC)')
% legend('TC_2','TC_3','TC_4','TC_5','TC_6','"True"
Temperature','Location','NorthWest')

% Plot 5b - Measured Temperature Error before adjustment
figure
hold on
plot(TC_true,mean(TC_0_raw)-TC_true,'ok','DisplayName','{\itT_e}')
plot(TC_true,mean(TC_1_raw)-TC_true,'sg','DisplayName','{\itT_{rh}}')
plot(TC_true,mean(TC_2_raw)-TC_true,'db','DisplayName','{\itT_{kr}}')
plot(TC_true,mean(TC_3_raw)-TC_true,'^m','DisplayName','{\itT_{ck}}')
plot(TC_true,mean(TC_4_raw)-TC_true,'>c','DisplayName','{\itT_c}')
plot(TC_true,mean(TC_5_raw)-TC_true,'<r','DisplayName','{\itT_b}')
hold off
ylim([-6 0]);
xlabel('True Temperature (\circC)')
ylabel('Measured Temperature Error (\circC)')
legend('location','best','NumColumns',3)
saveas(gcf,'X:\01_Current_Students\David
Miller\06_DAQAndExperiments\02_DataProcessing\01_Calibration\TCRawFig','meta'
)

% Plot 6a - Measured Temperature vs. "True" Temperature before adjustment
% figure('Position', [x y 326 275])
% hold on
% % plot(mean(TC_0_raw),TC_true,'*k')
% % plot(mean(TC_1_raw),TC_true,'*g')
% plot(mean(TC_2_raw),TC_true,'*b')
% plot(mean(TC_3_raw),TC_true,'*m')
% plot(mean(TC_4_raw),TC_true,'*c')
% plot(mean(TC_5_raw),TC_true,'*r')
% plot(mean(TC_6_raw),TC_true,'*y')
% plot(TC_true,TC_true,'-r')
% hold off
% xlabel('"True" Temperature (\circC)')
% ylabel('Measured Temperature (\circC)')
% legend('TC_2','TC_3','TC_4','TC_5','TC_6','"True"
Temperature','Location','NorthWest')

% Plot 6b - Measured Temperature Error after adjustment
figure

```

```

hold on
plot(TC_true,mean(TC_0_calibrated)-TC_true,'ok','DisplayName','{\itT_e}')
plot(TC_true,mean(TC_1_calibrated)-TC_true,'sg','DisplayName','{\itT_{rh}}')
plot(TC_true,mean(TC_2_calibrated)-TC_true,'db','DisplayName','{\itT_{kr}}')
plot(TC_true,mean(TC_3_calibrated)-TC_true,'^m','DisplayName','{\itT_{ck}}')
plot(TC_true,mean(TC_4_calibrated)-TC_true,'>c','DisplayName','{\itT_c}')
plot(TC_true,mean(TC_5_calibrated)-TC_true,'<r','DisplayName','{\itT_b}')
hold off
ylim([-1 1]);
xlabel('True Temperature (\circC)')
ylabel('Measured Temperature Error (\circC)')
legend('location','best','NumColumns',3)
saveas(gcf,'X:\01_Current_Students\David
Miller\06_DAQAndExperiments\02_DataProcessing\01_Calibration\TCCalFig','meta'
)

%% Validyne Absolute Pressure

P_Cal_Folder = 'X:\01_Current_Students\David
Miller\06_DAQAndExperiments\02_DataProcessing\01_Calibration\2018-11-
01_PresCalibration';

% Collect all the log file names from the test data folder
log_files_info = dir(fullfile(P_Cal_Folder, '*.log'));

Date = log_files_info(1).name(1:8); % Calibration date MMDDYYYY
[Pbaro] = BarometricPressure(Date); % barometric pressure on calibration day
(Pa)

[VAL_FIT] = ValidyneCorrectionTerms(P_Cal_Folder,Pbaro);

counter = 1;
for i = 1:length(log_files_info)

    filename_Volt = strcat(P_Cal_Folder,'\',log_files_info(i).name);
    [VTime,A,Z,TOR,P1,P2,P3,P4] = PImport(filename_Volt);
    %     P1 --> Validyne Crankcase
    %     P2 --> Validyne Power Cylinder

    P_cal_machine(:,counter) =
Pbaro+6894.76*str2double(log_files_info(i).name(24:26))/10; % (Pa)

    P1_raw(:,counter) = Pbaro+P1.*12.5.*6894.76; % (Pa)
    P2_raw(:,counter) = Pbaro+P2.*12.5.*6894.76; % (Pa)

    % Correct P1 (Pa)
    P1_calibrated(:,counter) = P1_raw(:,counter)+...

    (VAL_FIT.P1(1).*P1_raw(:,counter).^3+VAL_FIT.P1(2).*P1_raw(:,counter).^2+...
    VAL_FIT.P1(3).*P1_raw(:,counter)+VAL_FIT.P1(4));
    % Correct P2 (Pa)
    P2_calibrated(:,counter) = P2_raw(:,counter)+...

    (VAL_FIT.P2(1).*P2_raw(:,counter).^3+VAL_FIT.P2(2).*P2_raw(:,counter).^2+...
    VAL_FIT.P2(3).*P2_raw(:,counter)+VAL_FIT.P2(4)); % (Pa)

```

```

    counter = counter + 1;
end

% Calculate Validyne Uncertainty
ValFS = 6894.76*125; % Validyne transucer full scale (Pa)
Us_Val =
sqrt((0.005*ValFS)^2+(0.0005*ValFS)^2+(0.001*ValFS)^2+(0.00269*ValFS/10)^2+(0
.1*6894.75)^2+100^2); % (Pa)

t_0025 = tinverse(0.975,size(P1_calibrated,1)-1); % inverse 2 tail t-test with
95% confidence interval
Ur_P1 = t_0025*std(P1_calibrated)./sqrt(length(P1_calibrated)); % (Pa)
Ur_P2 = t_0025*std(P2_calibrated)./sqrt(length(P2_calibrated)); % (Pa)

U_P1 = sqrt(Us_Val.^2+Ur_P1.^2); % (Pa)
U_P2 = sqrt(Us_Val.^2+Ur_P2.^2); % (Pa)

% Save VAL_FIT data structure
save('X:\01_Current_Students\David
Miller\06_DAQAndExperiments\02_DataProcessing\01_Calibration\VAL_FIT.mat','VA
L_FIT');

% % Plot 5a - Measured Pressure vs. "True" Pressure before adjustment
% figure('Position', [x y 326 275])
% hold on
% plot(mean(P2_Pa_raw)./1000,P_cal_machine./1000,'*r')
% plot(mean(P3_Pa_raw)./1000,P_cal_machine./1000,'ok')
% plot(P_cal_machine./1000,P_cal_machine./1000,'-r')
% hold off
% xlabel('Calibration Machine Pressure (kPa)');
% ylabel('Measured Pressure (kPa)')
% legend('Power Cylinder','Crankcase','Cal Machine','Location','NorthWest')

% Plot 5b - Measured Pressure Error before adjustment
figure
hold on
plot(P_cal_machine./1000,mean(P1_raw,1)./1000-P_cal_machine./1000,'sr')
plot(P_cal_machine./1000,mean(P2_raw,1)./1000-P_cal_machine./1000,'ok')
hold off
ylim([-6 6]);
xlabel('Calibration Machine Pressure (kPa)');
ylabel('Measured Pressure Error (kPa)')
legend('Crankcase','Power Cylinder','Location','best')
saveas(gcf,'X:\01_Current_Students\David
Miller\06_DAQAndExperiments\02_DataProcessing\01_Calibration\ValRawFig','meta
')

% % Plot 6a - Measured Pressure vs. "True" Pressure before adjustment
% figure('Position', [x y 326 275])
% hold on
% plot(mean(P2_Pa_calibrated)./1000,P_cal_machine./1000,'*r')
% plot(mean(P3_Pa_calibrated)./1000,P_cal_machine./1000,'ok')
% plot(P_cal_machine./1000,P_cal_machine./1000,'-r')
% hold off

```

```

% xlabel('Calibration Machine Pressure (kPa)');
% ylabel('Measured Pressure (kPa)')
% legend('Power Cylinder','Crankcase','Cal Machine','Location','NorthWest')

% Plot 6b - Measured Pressure Error before adjustment
figure
hold on
plot(P_cal_machine./1000,mean(P1_calibrated,1)./1000-
P_cal_machine./1000,'sr')
plot(P_cal_machine./1000,mean(P2_calibrated,1)./1000-
P_cal_machine./1000,'ok')
hold off
ylim([-1 1]);
xlabel('Calibration Machine Pressure (kPa)');
ylabel('Measured Pressure Error (kPa)')
legend('Crankcase','Power Cylinder','Location','best')
saveas(gcf,'X:\01_Current_Students\David
Miller\06_DAQAndExperiments\02_DataProcessing\01_Calibration\ValCalFig','meta
')

%% RTDs
RTD_Cal_Folder = 'X:\01_Current_Students\David
Miller\06_DAQAndExperiments\02_DataProcessing\01_Calibration\2018-10-
25_RTDCalibration';
[RTD_FIT] = RTDCorrectionTerms(RTD_Cal_Folder);

% Collect all the log file names from the test data folder
log_files_info = dir(fullfile(RTD_Cal_Folder, '*.log'));

counter = 1;
for i = 1:length(log_files_info)
    filename_RTD = strcat(RTD_Cal_Folder,'\',log_files_info(i).name);
    [Time,RTD0,RTD1,RTD2,RTD3] = RTDImport(filename_RTD);
%     RTD_0 --> Cooler water inlet
%     RTD_1 --> Cooler water outlet
%     RTD_2 --> Con Pipe/Pow Cyl inlet
%     RTD_3 --> Con Pipe/Pow Cyl outlet

% True temperature is from reference thermometer and stored in file name
RTD_true(:,counter) = str2double(log_files_info(i).name(17:19))/10;

RTD_0_raw(:,counter) = RTD0; %(deg C)
RTD_1_raw(:,counter) = RTD1; %(deg C)
RTD_2_raw(:,counter) = RTD2; %(deg C)
RTD_3_raw(:,counter) = RTD3; %(deg C)

% RTD0 temperature correction
RTD_0_calibrated(:,counter) = RTD_0_raw(:,counter)+...

(RTD_FIT.RTD0(1).*RTD_0_raw(:,counter).^3+RTD_FIT.RTD0(2).*RTD_0_raw(:,counte
r).^2+...
    RTD_FIT.RTD0(3).*RTD_0_raw(:,counter)+RTD_FIT.RTD0(4));
% RTD1 temperature correction
RTD_1_calibrated(:,counter) = RTD_1_raw(:,counter)+...

```



```

(RTD_FIT.RTD1(1).*RTD_1_raw(:,counter).^3+RTD_FIT.RTD1(2).*RTD_1_raw(:,counte
r).^2+...
    RTD_FIT.RTD1(3).*RTD_1_raw(:,counter)+RTD_FIT.RTD1(4));
% RTD2 temperature correction
RTD_2_calibrated(:,counter) = RTD_2_raw(:,counter)+...

(RTD_FIT.RTD2(1).*RTD_2_raw(:,counter).^3+RTD_FIT.RTD2(2).*RTD_2_raw(:,counte
r).^2+...
    RTD_FIT.RTD2(3).*RTD_2_raw(:,counter)+RTD_FIT.RTD2(4));
% RTD3 temperature correction
RTD_3_calibrated(:,counter) = RTD_3_raw(:,counter)+...

(RTD_FIT.RTD3(1).*RTD_3_raw(:,counter).^3+RTD_FIT.RTD3(2).*RTD_3_raw(:,counte
r).^2+...
    RTD_FIT.RTD3(3).*RTD_3_raw(:,counter)+RTD_FIT.RTD3(4));

    counter = counter + 1;
end

% Save RTD Fit Coefficients data structure
save('X:\01_Current_Students\David
Miller\06_DAQAndExperiments\02_DataProcessing\01_Calibration\RTD_FIT.mat','RT
D_FIT');

% Calculate RTD uncertainty
Us_RTD = ones(1,size(RTD_0_calibrated,2)).*sqrt(0.35^2+0.5^2+0.1^2);

% Plot 5a - Measured Temperature vs. "True" Temperature before adjustment
% figure('Position', [x y 326 275])
% hold on
% plot(mean(RTD_0_raw),RTD_true,'*k')
% plot(mean(RTD_1_raw),RTD_true,'*g')
% plot(mean(RTD_2_raw),RTD_true,'*b')
% plot(mean(RTD_3_raw),RTD_true,'*m')
% plot(RTD_true,RTD_true,'-r')
% hold off
% xlabel('"True" Temperature (\circC)')
% ylabel('Measured Temperature (\circC)')
% legend('RTD_0','RTD_1','RTD_2','RTD_3','"True"
Temperature','Location','NorthWest')

% Plot 5b - Measured Temperature Error before adjustment
figure
hold on
plot(RTD_true,mean(RTD_0_raw)-
RTD_true,'ok','DisplayName',{'\itT_{cool,k,in}}')
plot(RTD_true,mean(RTD_1_raw)-
RTD_true,'sg','DisplayName',{'\itT_{cool,k,out}}')
plot(RTD_true,mean(RTD_2_raw)-
RTD_true,'db','DisplayName',{'\itT_{cool,c,in}}')
plot(RTD_true,mean(RTD_3_raw)-
RTD_true,'^m','DisplayName',{'\itT_{cool,c,out}}')
hold off
ylim([-1 4])
xlabel('True Temperature (\circC)')

```

```

ylabel('Measured Temperature Error (\circC)')
legend('location','best','NumColumns',2)
saveas(gcf,'X:\01_Current_Students\David
Miller\06_DAQAndExperiments\02_DataProcessing\01_Calibration\RTDRawFig','meta
')

% Plot 6a - Measured Temperature vs. "True" Temperature before adjustment
% figure('Position',[x y 326 275])
% hold on
% plot(mean(RTD_0_raw),RTD_true,'*k')
% plot(mean(RTD_1_raw),RTD_true,'*g')
% plot(mean(RTD_2_raw),RTD_true,'*b')
% plot(mean(RTD_3_raw),RTD_true,'*m')
% plot(RTD_true,RTD_true,'-r')
% hold off
% xlabel('"True" Temperature (\circC)')
% ylabel('Measured Temperature (\circC)')
% legend('RTD_0','RTD_1','RTD_2','RTD_3','"True"
Temperature','Location','NorthWest')

% Plot 6b - Measured Temperature Error after adjustment
figure
hold on
plot(RTD_true,mean(RTD_0_calibrated)-
RTD_true,'ok','DisplayName','{\itT_{cool,k,in}}')
plot(RTD_true,mean(RTD_1_calibrated)-
RTD_true,'sg','DisplayName','{\itT_{cool,k,out}}')
plot(RTD_true,mean(RTD_2_calibrated)-
RTD_true,'db','DisplayName','{\itT_{cool,c,in}}')
plot(RTD_true,mean(RTD_3_calibrated)-
RTD_true,'^m','DisplayName','{\itT_{cool,c,out}}')
hold off
ylim([-0.2 0.21])
xlabel('True Temperature (\circC)')
ylabel('Measured Temperature Error (\circC)')
legend('location','best','NumColumns',2)
saveas(gcf,'X:\01_Current_Students\David
Miller\06_DAQAndExperiments\02_DataProcessing\01_Calibration\RTDCalFig','meta
')

```

## Thermocouple Calibration Function

```
function [TC_FIT] = TCCorrectionTerms(TC_Cal_Folder)

% Written by Connor Speer - October '17
% Modified by Shahzeb Mirza Oct 2017
% Modified by Connor Speer - December '17
% The goal of this function is to collect calibration data from a specified
% folder and determine the correction terms and raw data statistics.
% Calibration correction factors are then used to adjust the raw data.
%
% Modified by David Miller - Oct. 2018
% Modifications update comments to foil the current DAQ system and
% calibrate thermocouples to the absolute temperature of a thermometer.

%%%%%%%%%%%%%%%%%%%%%%%%%%%%%%%%%%%%%%%%%%%%%%%%%%%%%%%%%%%%%%%%%%%%%%%%
% Collect all the log file names from the thermocouple test data folder
TC_log_files_info = dir(fullfile(TC_Cal_Folder, '*.log'));

% Preallocate space for the structure array
TC_DATA(length(TC_log_files_info)).TC_0_raw = [];
TC_DATA(length(TC_log_files_info)).TC_0_avg = [];
TC_DATA(length(TC_log_files_info)).TC_0_corr = [];

TC_DATA(length(TC_log_files_info)).TC_1_raw = [];
TC_DATA(length(TC_log_files_info)).TC_1_avg = [];
TC_DATA(length(TC_log_files_info)).TC_1_corr = [];

TC_DATA(length(TC_log_files_info)).TC_2_raw = [];
TC_DATA(length(TC_log_files_info)).TC_2_avg = [];
TC_DATA(length(TC_log_files_info)).TC_2_corr = [];

TC_DATA(length(TC_log_files_info)).TC_3_raw = [];
TC_DATA(length(TC_log_files_info)).TC_3_avg = [];
TC_DATA(length(TC_log_files_info)).TC_3_corr = [];

TC_DATA(length(TC_log_files_info)).TC_4_raw = [];
TC_DATA(length(TC_log_files_info)).TC_4_avg = [];
TC_DATA(length(TC_log_files_info)).TC_4_corr = [];

TC_DATA(length(TC_log_files_info)).TC_5_raw = [];
TC_DATA(length(TC_log_files_info)).TC_5_avg = [];
TC_DATA(length(TC_log_files_info)).TC_5_corr = [];

TC_DATA(length(TC_log_files_info)).TC_true = [];

% Initialize counter variable
counter = 1;
counter_max = 0.5*length(TC_log_files_info);

WaitBar = waitbar(0, 'Analyzing calibration data...');

% Open Calibration Log Files
for i = 1:1:length(TC_log_files_info)
```

```

filename_TC = strcat(TC_Cal_Folder, '\\', TC_log_files_info(i).name);
%   [TC_0,TC_1,TC_2,TC_3,TC_4,TC_5,TC_6] = ...
%   importfile_TC(filename_TC);
[Time,T0,T1,T2,T3,T4,T5] = TImport(filename_TC);
%   T_0 --> Expansion Space
%   T_1 --> HH-Regen
%   T_2 --> HH Flange - Bypass Side
%   T_3 --> Displacer Mount
%   T_4 --> Power Cylinder
%   T_5 --> Crankcase

%%%%%%%%%%%%%%%%%%%%%%%%%%%%%%%%%%%%%%%%%%%%%%%%%%%%%%%%%%%%%%%%%%%%%%%%
% Calculate Data from the file
%%%%%%%%%%%%%%%%%%%%%%%%%%%%%%%%%%%%%%%%%%%%%%%%%%%%%%%%%%%%%%%%%%%%%%%%
% Calculate the average reading for each RTD
TC_0_avg = mean(T0); %(deg C)
TC_1_avg = mean(T1); %(deg C)
TC_2_avg = mean(T2); %(deg C)
TC_3_avg = mean(T3); %(deg C)
TC_4_avg = mean(T4); %(deg C)
TC_5_avg = mean(T5); %(deg C)

% The true temperature from the reference thermometer and stored in the
% file name
TC_true = str2double(TC_log_files_info(i).name(17:19))/10;

% Calculate the correction term for each RTD
TC_0_corr = TC_true - TC_0_avg; %(deg C)
TC_1_corr = TC_true - TC_1_avg; %(deg C)
TC_2_corr = TC_true - TC_2_avg; %(deg C)
TC_3_corr = TC_true - TC_3_avg; %(deg C)
TC_4_corr = TC_true - TC_4_avg; %(deg C)
TC_5_corr = TC_true - TC_5_avg; %(deg C)

% Store the values from the log file in a structure
TC_DATA(counter).TC_0_raw = T0;
TC_DATA(counter).TC_0_avg = TC_0_avg;
TC_DATA(counter).TC_0_corr = TC_0_corr;

TC_DATA(counter).TC_1_raw = T1;
TC_DATA(counter).TC_1_avg = TC_1_avg;
TC_DATA(counter).TC_1_corr = TC_1_corr;

TC_DATA(counter).TC_2_raw = T2;
TC_DATA(counter).TC_2_avg = TC_2_avg;
TC_DATA(counter).TC_2_corr = TC_2_corr;

TC_DATA(counter).TC_3_raw = T3;
TC_DATA(counter).TC_3_avg = TC_3_avg;
TC_DATA(counter).TC_3_corr = TC_3_corr;

TC_DATA(counter).TC_4_raw = T4;
TC_DATA(counter).TC_4_avg = TC_4_avg;
TC_DATA(counter).TC_4_corr = TC_4_corr;

```

```

TC_DATA(counter).TC_5_raw = T5;
TC_DATA(counter).TC_5_avg = TC_5_avg;
TC_DATA(counter).TC_5_corr = TC_5_corr;

TC_DATA(counter).TC_true = TC_true;

% Increment the counter variable
counter = counter + 1;

% Update Wait Bar
waitbar(counter / counter_max)

end
close(WaitBar);

%% Fit Curves to Correction Terms
% Fit a curve to the correction terms. Each thermocouple gets its own
% curve. Could potentially use the R^2 value to quantify the systematic
% error.
TC_0_fit = fit([TC_DATA.TC_0_avg]', [TC_DATA.TC_0_corr]', 'poly1');
TC_1_fit = fit([TC_DATA.TC_1_avg]', [TC_DATA.TC_1_corr]', 'poly1');
TC_2_fit = fit([TC_DATA.TC_2_avg]', [TC_DATA.TC_2_corr]', 'poly1');
TC_3_fit = fit([TC_DATA.TC_3_avg]', [TC_DATA.TC_3_corr]', 'poly1');
TC_4_fit = fit([TC_DATA.TC_4_avg]', [TC_DATA.TC_4_corr]', 'poly1');
TC_5_fit = fit([TC_DATA.TC_5_avg]', [TC_DATA.TC_5_corr]', 'poly1');

% Store the coefficients of the fitted curve equations in a structure
TC_FIT.TC_0 = coeffvalues(TC_0_fit);
TC_FIT.TC_1 = coeffvalues(TC_1_fit);
TC_FIT.TC_2 = coeffvalues(TC_2_fit);
TC_FIT.TC_3 = coeffvalues(TC_3_fit);
TC_FIT.TC_4 = coeffvalues(TC_4_fit);
TC_FIT.TC_5 = coeffvalues(TC_5_fit);

```

## Validyne Pressure Transducer Calibration

```
function [VAL_FIT] = ValidyneCorrectionTerms(P_Cal_Folder,Pbaro)

% Written by Connor Speer - October '17
% Modified by Shahzeb Mirza Oct 2017
% Modified by Connor Speer - December '17
% The goal of this function is to collect calibration data from a specified
% folder and determine the correction terms and raw data statistics.
% Calibration correction factors are then used to adjust the raw data.
%
% Modified by David Miller - Oct. 2018
% Modified to foil the current DAQ system.

%%%%%%%%%%%%%%%%%%%%%%%%%%%%%%%%%%%%%%%%%%%%%%%%%%%%%%%%%%%%%%%%%%%%%%%%
% Collect all the log file names from the thermocouple test data folder
P_log_files_info = dir(fullfile(P_Cal_Folder, '*.log'));

% Preallocate space for the structure array
P_DATA(length(P_log_files_info)).P1_raw = [];
P_DATA(length(P_log_files_info)).P1_avg = [];
P_DATA(length(P_log_files_info)).P1_corr = [];

P_DATA(length(P_log_files_info)).P2_raw = [];
P_DATA(length(P_log_files_info)).P2_avg = [];
P_DATA(length(P_log_files_info)).P2_corr = [];

P_DATA(length(P_log_files_info)).Poverall_avg = [];

% Initialize counter variable
counter = 1;
counter_max = 0.5*length(P_log_files_info);

WaitBar = waitbar(0,'Analyzing calibration data...');

% Open Calibration Log Files
for i = 1:length(P_log_files_info)
    filename_Volt = strcat(P_Cal_Folder,'\',P_log_files_info(i).name);
    [Time,A1,Z1,TOR1,P1,P2,P3,P4] = PImport(filename_Volt);
%     A --> 500 PPR Rotary Encoder Output
%     Z --> 1 PPR Rotary Encoder Output
%     TOR --> Torque Transducer Output
%     P1 --> Validyne Crankcase
%     P2 --> Validyne Power Cylinder
%     P3 --> PCB Power Cylinder
%     P4 --> PCB Crankcase

%%%%%%%%%%%%%%%%%%%%%%%%%%%%%%%%%%%%%%%%%%%%%%%%%%%%%%%%%%%%%%%%%%%%%%%%
% Calculate Data from the file
%%%%%%%%%%%%%%%%%%%%%%%%%%%%%%%%%%%%%%%%%%%%%%%%%%%%%%%%%%%%%%%%%%%%%%%%
% Calculate the average reading for each pressure transducer
P1_avg = Pbaro+mean(P1).*12.5.*6894.76; %(Pa)
P2_avg = Pbaro+mean(P2).*12.5.*6894.76; %(Pa)
```

```

    % Collect the true pressure from the name of the log file
    Pcal_machine =
Pbaro+6894.76*str2double(P_log_files_info(i).name(24:26))/10; % (Pa)

    % Calculate the correction term for each pressure transducer
    P1_corr = Pcal_machine - P1_avg; % (Pa)
    P2_corr = Pcal_machine - P2_avg; % (Pa)

    % Store the values from the log file in a structure
    P_DATA(counter).P1_raw = P1;
    P_DATA(counter).P1_avg = P1_avg;
    P_DATA(counter).P1_corr = P1_corr;

    P_DATA(counter).P2_raw = P2;
    P_DATA(counter).P2_avg = P2_avg;
    P_DATA(counter).P2_corr = P2_corr;

    P_DATA(counter).P_cal_machine = Pcal_machine;

    % Increment the counter variable
    counter = counter + 1;

    % Update Wait Bar
    waitbar(counter / counter_max)

end
close(WaitBar);

%% Fit Curves to Correction Terms
% Fit a curve to the correction terms. Each pressure transducer gets its
% own curve.
P_1_fit = fit([P_DATA.P1_avg]', [P_DATA.P1_corr]', 'poly3');
P_2_fit = fit([P_DATA.P2_avg]', [P_DATA.P2_corr]', 'poly3');

% Store the coefficients of the fitted curve equations in a structure
VAL_FIT.P1 = coeffvalues(P_1_fit);
VAL_FIT.P2 = coeffvalues(P_2_fit);

```

## RTD Calibration Function

```
function [RTD_FIT] = RTDCorrectionTerms(RTD_Cal_Folder)

% Written by Connor Speer - October '17
% Modified by Shahzeb Mirza Oct 2017
% Modified by Connor Speer - December '17
% The goal of this function is to collect calibration data from a specified
% folder and determine the correction terms and raw data statistics.
% Calibration correction factors are then used to adjust the raw data.
%
% Modified by David Miller - Oct. 2018
% Modifications update comments to foil the current DAQ system and
% calibrate RTDs to the absolute temperature of a thermometer.

%%%%%%%%%%%%%%%%%%%%%%%%%%%%%%%%%%%%%%%%%%%%%%%%%%%%%%%%%%%%%%%%%%%%%%%%
% Collect all the log file names from the thermocouple test data folder
RTD_log_files_info = dir(fullfile(RTD_Cal_Folder, '*.log'));

% Preallocate space for the structure array
RTD_DATA(length(RTD_log_files_info)).RTD_0_raw = [];
RTD_DATA(length(RTD_log_files_info)).RTD_0_avg = [];
RTD_DATA(length(RTD_log_files_info)).RTD_0_corr = [];

RTD_DATA(length(RTD_log_files_info)).RTD_1_raw = [];
RTD_DATA(length(RTD_log_files_info)).RTD_1_avg = [];
RTD_DATA(length(RTD_log_files_info)).RTD_1_corr = [];

RTD_DATA(length(RTD_log_files_info)).RTD_2_raw = [];
RTD_DATA(length(RTD_log_files_info)).RTD_2_avg = [];
RTD_DATA(length(RTD_log_files_info)).RTD_2_corr = [];

RTD_DATA(length(RTD_log_files_info)).RTD_3_raw = [];
RTD_DATA(length(RTD_log_files_info)).RTD_3_avg = [];
RTD_DATA(length(RTD_log_files_info)).RTD_3_corr = [];

RTD_DATA(length(RTD_log_files_info)).RTD_true = [];

% Initialize counter variable
counter = 1;
counter_max = 0.5*length(RTD_log_files_info);

WaitBar = waitbar(0, 'Analyzing calibration data...');

% Open Calibration Log Files
for i = 1:1:length(RTD_log_files_info)

    FileName = strcat(RTD_Cal_Folder, '\', RTD_log_files_info(i).name);
    [Time, RTD0, RTD1, RTD2, RTD3] = RTDImport(FileName);
%     RTD_0 --> Cooler water inlet
%     RTD_1 --> Cooler water outlet
%     RTD_2 --> Con Pipe/Pow Cyl inlet
%     RTD_3 --> Con Pipe/Pow Cyl outlet
```



```

%%%%%%%%%%%%%%%%%%%%%%%%%%%%%%%%%%%%%%%%%%%%%%%%%%%%%%%%%%%%%%%%%%%%%%%%
% Calculate Data from the file
%%%%%%%%%%%%%%%%%%%%%%%%%%%%%%%%%%%%%%%%%%%%%%%%%%%%%%%%%%%%%%%%%%%%%%%%
% Calculate the average reading for each RTD
RTD_0_avg = mean(RTD0); %(deg C)
RTD_1_avg = mean(RTD1); %(deg C)
RTD_2_avg = mean(RTD2); %(deg C)
RTD_3_avg = mean(RTD3); %(deg C)

% True temperature is from reference thermometer and stored in file name
RTD_true = str2double(RTD_log_files_info(i).name(17:19))/10;

% Calculate the correction term for each RTD
RTD_0_corr = RTD_true - RTD_0_avg; %(deg C)
RTD_1_corr = RTD_true - RTD_1_avg; %(deg C)
RTD_2_corr = RTD_true - RTD_2_avg; %(deg C)
RTD_3_corr = RTD_true - RTD_3_avg; %(deg C)

% Store the values from the log file in a structure
RTD_DATA(counter).RTD_0_raw = RTD0;
RTD_DATA(counter).RTD_0_avg = RTD_0_avg;
RTD_DATA(counter).RTD_0_corr = RTD_0_corr;

RTD_DATA(counter).RTD_1_raw = RTD1;
RTD_DATA(counter).RTD_1_avg = RTD_1_avg;
RTD_DATA(counter).RTD_1_corr = RTD_1_corr;

RTD_DATA(counter).RTD_2_raw = RTD2;
RTD_DATA(counter).RTD_2_avg = RTD_2_avg;
RTD_DATA(counter).RTD_2_corr = RTD_2_corr;

RTD_DATA(counter).RTD_3_raw = RTD3;
RTD_DATA(counter).RTD_3_avg = RTD_3_avg;
RTD_DATA(counter).RTD_3_corr = RTD_3_corr;

RTD_DATA(counter).RTD_true = RTD_true;

% Increment the counter variable
counter = counter + 1;

% Update Wait Bar
waitbar(counter / counter_max)

end
close(WaitBar);

%% Fit Curves to Correction Terms
% Fit a curve to the correction terms. Each thermocouple gets its own
% curve. Could potentially use the R^2 value to quantify the systematic
% error.
RTD_0_fit = fit([RTD_DATA.RTD_0_avg]', [RTD_DATA.RTD_0_corr]', 'poly3');
RTD_1_fit = fit([RTD_DATA.RTD_1_avg]', [RTD_DATA.RTD_1_corr]', 'poly3');
RTD_2_fit = fit([RTD_DATA.RTD_2_avg]', [RTD_DATA.RTD_2_corr]', 'poly3');
RTD_3_fit = fit([RTD_DATA.RTD_3_avg]', [RTD_DATA.RTD_3_corr]', 'poly3');

```

```
% Store the coefficients of the fitted curve equations in a structure
RTD_FIT.RTD0 = coeffvalues(RTD_0_fit);
RTD_FIT.RTD1 = coeffvalues(RTD_1_fit);
RTD_FIT.RTD2 = coeffvalues(RTD_2_fit);
RTD_FIT.RTD3 = coeffvalues(RTD_3_fit);
```

## Torque Transducer Calibration Function

```
function [Torque_Nm,Ur_Nm,Us_Nm]...
    = Futek_Torque_1Nm_Calibration(Torque_Voltage,Ur_Volt)

% Written by Connor Speer - October '17
% The Futek torque transducer was shipped with calibration documents from
% the factory. This function corrects raw data using the calibration
% information provided by Futek.
%
% Modified by David Miller - Oct. 2018
% Modified to include uncertainty
% Modified for 1 Nm Torque Transducer

%% Inputs:
% Torque_Voltage --> Column vector of voltages collected from the torque
% transducer in (V)

%% Outputs:
% Torque_Nm --> Column vector of torques in (Nm) corresponding to the
% input voltages from the torque transducer.

%% Convert from voltage to torque
% Test data from the calibration certificate:
Cal_Input_Nm = [0.000; 0.1412; 0.2825; 0.4237; 0.5649; 1.0010; 0.0000;
0.0000; -0.1412; -0.2825; -0.2437; -0.5649; -1.0010; 0.0000];
Cal_Output_V = [0.000; 0.703; 1.410; 2.116; 2.821; 5.002; 0.001; 0.000; -
0.706; -1.411; -2.117; -2.824; -5.007; -0.008];

% Fit a linear polynomial to the calibration data.
Cal_Data_Fit = fit(Cal_Output_V,Cal_Input_Nm,'poly1');

% Extract the coefficients of the linear fit
Cal_Data_Fit_coeffs = coeffvalues(Cal_Data_Fit);

% Apply equation of fitted polynomial to calculate torque in (Nm)
Torque_Nm = Torque_Voltage.*Cal_Data_Fit_coeffs(1) + Cal_Data_Fit_coeffs(2);
%(Nm)

%% Uncertainty
RO = 1; % Rated Output [+/- Nm]

% Relative Uncertainty
Ur_Nm = Ur_Volt.*Cal_Data_Fit_coeffs(1);

% Systematic Uncertainty
U_nonlinear = 0.002*RO; % Nonlinearity error [Nm]
U_hysteresis = 0.001*RO; % Hysteresis error [Nm]
U_nonrepeat = 0.002*RO; % Nonrepeatability error [Nm]
U_DAQ = 0.00269*RO/10; % DAQ hardware error [Nm]

Us_Nm = sqrt(U_nonlinear^2+U_hysteresis^2+U_nonrepeat^2+U_DAQ^2); %
Systematic Uncertainty [Nm]
```

## Support Functions

---

There are four support functions. The first converts rotary encoder pulses to angular position. The second calculates instantaneous angular velocity from angular position and time. The third output a barometric pressure for a specific experiment day. The fourth calculates the volumes and volume changes from angular position.

### Encoder Pulse to Angular Position Function

```
function [AbTheta_deg] = Encoder_2_Angle(A,Z)

% Written by Connor Speer, October 2017. Subfunction to convert rotary
% encoder voltage data into crank angles in radians.

%% Inputs:
% A --> column vector of A-output voltages from the rotary encoder
% Z --> column vector of Z-output voltages from the rotary encoder
% *** A and Z must be the same length

%% Outputs
% theta_deg --> column vector of angles corresponding to rotary encoder
% outputs in (rad)

%% Find reference pulse in Z output
threshold = 3;
ref_pulse = find(Z > threshold, 1);

%% Work backwards from reference pulse to find pulse counts
if A(ref_pulse) > 2.5
    pulse_flag = 1;
else
    pulse_flag = 0;
end

A_count = zeros(size(A));

% bwd_counter = 500;
bwd_counter = 0;
row = ref_pulse - 1;

while row ~= 0
    if pulse_flag == 0 && A(row) < 2.5 && Z(row) < 2.5
        bwd_counter = bwd_counter - 1;
    end

    %     if bwd_counter == -1
    %     bwd_counter = 500;
    %     end
```

```

    A_count(row) = bwd_counter;

    if A(row) < 2.5
        pulse_flag = 1;
    else
        pulse_flag = 0;
    end
    row = row - 1;
end

%% Work forwards from reference pulse to find pulse counts
z_pulse_flag = 1;
if A(ref_pulse) > 2.5
    pulse_flag = 1;
else
    pulse_flag = 0;
end

fwd_counter = 0;

for row = ref_pulse:length(A)
    if z_pulse_flag == 0
        if pulse_flag == 0 && A(row) > 2.5
            fwd_counter = fwd_counter + 1;
        end
    else
        if Z(row) < 2.5
            z_pulse_flag = 0;
        end
    end
end

%     if fwd_counter == 501
%     fwd_counter = 0;
%     end

A_count(row) = fwd_counter;

if A(row) > 2.5
    pulse_flag = 1;
else
    pulse_flag = 0;
end
end

%% Use pulse count to calculate crank angles
AbTheta_deg = A_count*(2*pi/500); % [deg]
end

```

## Angular Velocity Function

```
function [ThetaVel,U_ThetaVel] = AngularVelocity(Theta,Time,U_Theta,U_Time)
% AngularVelocity
% By David Miller - Mar. 2019
%
% Calculates polynomial fit of angular position with time then uses the
% derivative to calculate angular velocity.
%
% Inputs:
%   Theta    -> Vector of crankshaft position [any unit]
%   Time     -> Vector of crankshaft position measurement times [s]
%   U_Theta  -> Scalar relative angular position uncertainty [any unit]
%   U_Time   -> Vector of time measurement uncertainty [s]
% Outputs:
%   ThetaVel -> Angular velocity vector [same unit as input/s]
%   U_ThetaVel -> Angular velocity vector uncertainty [same unit as input/s]
dTheta = Theta(2)-Theta(1);

% Set up polynomial fit
PolyOrder = 2; % order of the polynomial fit
NumPoints = 35; % number of samples to calculate fit with (must be odd
integer > PolyOrder)
P = (NumPoints-1)/2; % number of samples leading and lagging central value
used in fit

% Create vectors
endi = length(Theta); % number of data points
% ThetaCoef = zeros(endi,PolyOrder+1);
VelCoef = zeros(endi,PolyOrder); % velocity polynomial coefficients
ThetaVel = zeros(endi,1); % angular velocity
% RadPeriod = zeros(endi,1); % (s/rad)
% U_RadPeriod = zeros(endi,1); % (s/rad)
U_ThetaVel = zeros(endi,1); % angular velocity uncertainty

%% calculate fit coefficients for angular velocity
% Middle Points
for i = P+1:(endi-P-1) %:endi-2;
%   ThetaCoef(i,:) = polyfit(Time(i-P:i+P),Theta(i-P:i+P),PolyOrder);
%   VelCoef(i,:) = polyder(polyfit(Time(i-P:i+P),Theta(i-P:i+P),PolyOrder));
% angular velocity polynomial
%   U_ThetaVel(i) = (U_Theta/(Time(i+P)-Time(i-
P)))+(U_Time(i+P)*(2*P*dTheta/(Time(i+P)-Time(i-P))^2))...
%   + (U_Time(i-P)*(2*P*dTheta/(Time(i+P)-Time(i-P))^2));
end

% First and last points
VelCoef(1:P,:) = VelCoef(1:P,:)+VelCoef(P+1,:); % First points angular
velocity polynomial
VelCoef((endi-P):end,:) = VelCoef((endi-P):end,:)+VelCoef((endi-P-1),:); %
Last points angular velocity polynomial

U_ThetaVel(1:P) = U_ThetaVel(1:P)+U_ThetaVel(P+1); % first points angular
velocity uncertainty (temporary)
```

```

U_ThetaVel((endi-P):end) = U_ThetaVel((endi-P):end)+U_ThetaVel(endi-P-1); %
last points angular velocity uncertainty (temporary)

%% calculate angular velocity
for i = 1:endi
    ThetaVel(i) = polyval(VelCoef(i,:),Time(i)); % angular velocity
end

% figure; plot(Time(5000:6000),ThetaVel(5000:6000,1),'-r','DisplayName','Vel
From Fit'); hold on;
% xlabel('Time (s)'); ylabel('Angular Velocity (rad/s)');

% ThetaVel = movmean(ThetaVel,[5 5]); % moving mean to smooth velocity
% U_ThetaVel = sqrt((U_ThetaVel).^2 + (2.22.*movstd(ThetaVel,[5
5])./sqrt(11)).^2); % Angular velocity uncertainty (temporary)

% plot(Time(5000:6000),ThetaVel(5000:6000,1),'-k','DisplayName','Vel Move
Mean'); hold off;
% legend('NumColumns',2,'location','south');

end

```

## Barometric Pressure Function

```
function [Pbaro] = BarometricPressure(Date)
% BarometricPressure.m
% By David Miller - Nov. 2018
%
% This function outputs the barometric pressure in Pa for an experiment
% day.
%
% Input:
%   Date  -> The date of the experiment in the form MMDDYYYY
%
% Output:
%   Pbaro -> The barometric pressure of the experiment day in Pa

switch Date

    case '11012018'
        Pbaro = 93599; % barometric pressure (Pa)

    case '11022018'
        Pbaro = 92835; % barometric pressure (Pa)

    case '11082018'
        Pbaro = 94598; % barometric pressure (Pa)

    case '11092018'
        Pbaro = 92815; % barometric pressure (Pa)

    case '11142018'
        Pbaro = 92897; % barometric pressure (Pa)

    case '11152018'
        Pbaro = 93318; % barometric pressure (Pa)

    case '11162018'
        Pbaro = 95185; % barometric pressure (Pa)

    case '11202018'
        Pbaro = 92854; % barometric pressure (Pa)

    case '11212018'
        Pbaro = 92193; % barometric pressure (Pa)

    case '11232018'
        Pbaro = 92371; % barometric pressure (Pa)

    case '11272018'
        Pbaro = 91747; % barometric pressure (Pa)

    case '12042018'
        Pbaro = 93207; % barometric pressure (Pa)
```



```
case '12062018'  
Pbaro = 93652; % barometric pressure (Pa)  
  
case '12112018'  
Pbaro = 90896; % barometric pressure (Pa)  
  
case '02272019'  
Pbaro = 93638; % barometric pressure (Pa)  
  
otherwise  
error('No Barometric Pressure For Experiment Day');  
end  
end
```

## Volume and Volume Change Function

```
function [Vc,Ve,Vb,Vtot,dVc,dVe,dVb,dVtot] = volume_DAM(theta, ENGINE_DATA)
% determine working space volume variations and derivatives
% Israel Urieli, 7/6/2002
% Modified 2/14/2010 to include rockerV (rockdrive)
% Modified by Connor Speer October 2017
% Modified by David Miller October 2018

% Argument: theta - current cycle angle [radians]
% Returned values:
%   vc, ve, vb, vtot - compression, expansion, buffer, total engine space
volumes [m^3]
%   dvc, dve, dvb, dvtot - compression, expansion, buffer, total engine space
volume derivatives

% *** Note: For gamma engines, the total workspace volume is minimum at
% crank angle 0. For alpha engines, the compression space volume is maximum
% at crank angle zero.

engine_type = ENGINE_DATA.engine_type; % Letter indicating engine layout and
drive mechanism

if(strncmp(engine_type,'s',1)) % Sinusoidal alpha
%   [Vc,Ve,dVc,dVe] = sinevol(theta, ENGINE_DATA);
elseif(strncmp(engine_type,'y',1)) % Ross yoke mechanism alpha
%   [Vc,Ve,dVc,dVe] = yokevol(theta, ENGINE_DATA);
elseif(strncmp(engine_type,'r',1)) % Ross rocker V-drive alpha
%   [Vc,Ve,dVc,dVe] = rockvol(theta, ENGINE_DATA);
elseif(strncmp(engine_type,'g',1)) % Sinusoidal gamma
%   [Vc,Ve,dVc,dVe] = gammasinvol(theta, ENGINE_DATA);
elseif(strncmp(engine_type,'x',1)) % Slider-crank mechanism gamma
%   [Vc,Ve,Vb,Vtot,dVc,dVe,dVb,dVtot] = gammacrankvol(theta, ENGINE_DATA);
elseif(strncmp(engine_type,'a',1)) % Slider-crank mechanism alpha
%   [Vc,Ve,dVc,dVe] = alphacrankvol(theta, ENGINE_DATA);
end
%=====

% function [Vc,Ve,dVc,dVe] = sinevol(theta, ENGINE_DATA)
% % sinusoidal drive volume variations and derivatives
% % Israel Urieli, 7/6/2002
% % Argument: theta - current cycle angle [radians]
% % Returned values:
% %   vc, ve - compression, expansion space volumes [m^3]
% %   dvc, dve - compression, expansion space volume derivatives
%
% Vclc = ENGINE_DATA.Vclc;
% Vcle = ENGINE_DATA.Vcle;
% Vswc = ENGINE_DATA.Vswc;
% Vswe = ENGINE_DATA.Vswe;
% alpha = ENGINE_DATA.alpha;
%
% % Vclc Vcle % compression,expansion clearance vols [m^3]
% % Vswc Vswe % compression, expansion swept volumes [m^3]
% % alpha % phase angle advance of expansion space [radians]
```

```

%
%
% Vc = Vclc + 0.5*Vswc*(1 + cos(theta));
% Ve = Vcle + 0.5*Vswe*(1 + cos(theta + alpha));
% dVc = -0.5*Vswc*sin(theta);
% dVe = -0.5*Vswe*sin(theta + alpha);
%=====

% function [Vc, Ve, dVc, dVe] = yokevol(theta, ENGINE_DATA)
% % Ross yoke drive volume variations and derivatives
% % Israel Urieli, 7/6/2002
% % Modified by Connor Speer, October 2017.
% % Argument: theta - current cycle angle [radians]
% % Returned values:
% %   Vc, Ve - compression, expansion space volumes [m^3]
% %   dVc, dVe - compression, expansion space volume derivatives
%
% % compression, expansion clearance vols [m^3]
% Vclc = ENGINE_DATA.Vclc;
% Vcle = ENGINE_DATA.Vcle;
%
% b1 = ENGINE_DATA.b1; % Ross yoke length (1/2 yoke base) [m]
% b2 = ENGINE_DATA.b2; % Ross yoke height [m]
% crank = ENGINE_DATA.crank; % crank radius [m]
%
% % area of compression/expansion pistons [m^2]
% acomp = ENGINE_DATA.acomp;
% aexp = ENGINE_DATA.aexp;
%
% ymin = ENGINE_DATA.ymin; % minimum yoke vertical displacement [m]
%
% sinth = sin(theta);
% costh = cos(theta);
% bth = (b1^2 - (crank*costh)^2)^0.5;
% ye = crank*(sinth + (b2/b1)*costh) + bth;
% yc = crank*(sinth - (b2/b1)*costh) + bth;
%
% Ve = vcle + aexp*(ye - ymin);
% Vc = vclc + acomp*(yc - ymin);
% dVc = acomp*crank*(costh + (b2/b1)*sinth + crank*sinth*costh/bth);
% dVe = aexp*crank*(costh - (b2/b1)*sinth + crank*sinth*costh/bth);
%=====

% function [vc, ve, dvc, dve] = rockvol(theta, ENGINE_DATA)
% % Ross Rocker-V drive volume variations and derivatives
% % Israel Urieli, 7/6/2002 & Martine Long 2/25/2005
% % Argument: theta - current cycle angle [radians]
% % Returned values:
% %   vc, ve - compression, expansion space volumes [m^3]
% %   dvc, dve - compression, expansion space volume derivatives
%
% global vclc vcle % compression, expansion clearance vols [m^3]
% global crank % crank radius [m]
% global acomp aexp % area of compression/expansion pistons [m^2]
% global conrod conode % length of comp/exp piston connecting rods [m]
% global ycmx yemax % maximum comp/exp piston vertical displacement [m]

```

```

%
% sinh = sin(theta);
% cosh = cos(theta);
% beth = (conrode^2 - (crank*cosh)^2)^0.5;
% bcth = (conrodc^2 - (crank*sinh)^2)^0.5;
% ye = beth - crank*sinh;
% yc = bcth + crank*cosh;
%
% ve = vcle + aexp*(yemax - ye);
% vc = vclc + acomp*(ycmax - yc);
% dvc = acomp*crank*sinh*(crank*cosh/bcth + 1);
% dve = -aexp*crank*cosh*(crank*sinh/beth - 1);

% function [vc,ve,dvc,dve] = gammasinvol(theta, ENGINE_DATA);
% % gamma sinusoidal drive volume variations and derivatives
% % Added by Connor Speer - January 2017
% % Argument: theta - current cycle angle [radians]
% % Returned values:
% %   vc, ve - compression, expansion space volumes [m^3]
% %   dvc, dve - compression, expansion space volume derivatives
%
% global vclp vcl d % piston, displacer clearance vols [m^3]
% global vswp vswd % compression, expansion swept volumes [m^3]
% global beta % phase angle advance of displacer motion over piston [radians]
%
% *** Total volume is maximum at theta = 0 for gammas.
% vc = vcl d + vclp + (vswd*0.5)*(1 + ((vswp/vswd)*(1+cos(theta+pi)) -
cos(theta+pi+beta)));
% ve = vcl d + (vswd*0.5)*(1 + cos(theta+pi+beta));
% dvc = -(vswd*0.5)*(((vswp/vswd)*sin(theta+pi)) - sin(theta+pi+beta));
% dve = -(vswd*0.5)*sin(theta+pi+beta);
%=====

function [vc,ve,vb,vtot,dvc,dve,dvb,dvtot] = gammacrankvol(theta,
ENGINE_DATA)
% gamma crankshaft drive volume variations and derivatives
% Added by Connor Speer - February 2017
% Argument: theta - current cycle angle [radians]
% Returned values:
%   vc, ve, vb - compression, expansion, buffer space volumes [m^3]
%   dvc, dve - compression, expansion, buffer space volume derivatives

vclp = ENGINE_DATA.Vclp;
vcl d = ENGINE_DATA.Vcl d;
Dbore = ENGINE_DATA.Dbore;
Pbore = ENGINE_DATA.Pbore;
Dr1 = ENGINE_DATA.Dr1;
Dr2 = ENGINE_DATA.Dr2;
Dr3 = ENGINE_DATA.Dr3;
Pr1 = ENGINE_DATA.Pr1;
Pr2 = ENGINE_DATA.Pr2;
Pr3 = ENGINE_DATA.Pr3;
beta = ENGINE_DATA.beta_deg*(pi/180);
vb_max = ENGINE_DATA.V_buffer_max;

```

```

% vclp vcl d % piston, displacer clearance vols [m^3]
% Dbore Pbore % displacer, piston bores [m]
% Dr1 Pr1 % displacer, piston desaxe offset in [m]
% Dr2 Pr2 % displacer, piston crank length (half stroke) in [m]
% Dr3 Pr3 % displacer, piston connecting rod lengths [m]
% beta % phase angle advance of displacer motion over piston [radians]
% vb_max % maximum buffer space volume [m^3]

%*** Total volume is minimum at theta = 0 for gammas.
Ptheta2 = -theta;
Dtheta2 = Ptheta2 - beta;

Dtheta3 = pi - asin((-Dr1+(Dr2*sin(Dtheta2)))/Dr3);
Dr4 = Dr2*cos(Dtheta2) - Dr3*cos(Dtheta3);
Dr4max = sqrt(((Dr2+Dr3)^2)-(Dr1^2));
Dr4min = sqrt(((Dr3-Dr2)^2)-(Dr1^2));
ve = (vcl d*0.5) + ((pi/4)*(Dbore^2))*(Dr4max-Dr4);
DVc = (((pi/4)*(Dbore^2))*(Dr4max-Dr4min)) - ve;

Ptheta3 = pi - asin((-Pr1+(Pr2*sin(Ptheta2)))/Pr3);
Pr4 = Pr2*cos(Ptheta2) - Pr3*cos(Ptheta3);
Pr4max = sqrt(((Pr2+Pr3)^2)-(Pr1^2));
PVc = (((pi/4)*(Pbore^2))*(Pr4max-Pr4));
vc = (vcl d) + vcl p + DVc + PVc;

dDtheta3 = (Dr2.*cos(Dtheta2))./(Dr3.*sqrt(1-((( -
Dr1+(Dr2.*sin(Dtheta2)))/Dr3).^2)));
dDr4 = (Dr2.*sin(Dtheta2) + Dr3.*sin(Dtheta3)).*dDtheta3.*(theta(2,1)-
theta(1,1));
dve = -(pi/4)*(Dbore^2).*dDr4;

dPtheta3 = (Pr2.*cos(Ptheta2))./(Pr3.*sqrt(1-((( -
Pr1+(Pr2.*sin(Ptheta2)))/Pr3).^2)));
dPr4 = (Pr2.*sin(Ptheta2) + Pr3.*sin(Ptheta3)).*dPtheta3.*(theta(2,1)-
theta(1,1));
dPVc = -(pi/4)*(Pbore^2).*dPr4;
dDVc = -dve;
dvc = dDVc + dPVc;

vb = vb_max-PVc;
dvb = -dPVc;

vtot = vc+ve+ENGINE_DATA.Vdead; % total engine volume
dvtot = dvc+dve; % total volume change
%=====

% function [vc,ve,dvc,dve] = alphacrankvol(theta, ENGINE_DATA)
% % alpha crankshaft drive volume variations and derivatives
% % Added by Connor Speer - February 2017
% % Argument: theta - current cycle angle [radians]
% % Returned values:
% % vc, ve - compression, expansion space volumes [m^3]
% % dvc, dve - compression, expansion space volume derivatives
%
% vcl c = ENGINE_DATA.Vcl c;

```

```

% vcle = ENGINE_DATA.Vcle;
% Cbore = ENGINE_DATA.Cbore;
% Ebore = ENGINE_DATA.Ebore;
% Cr1 = ENGINE_DATA.Cr1;
% Cr2 = ENGINE_DATA.Cr2;
% Cr3 = ENGINE_DATA.Cr3;
% Er1 = ENGINE_DATA.Er1;
% Er2 = ENGINE_DATA.Er2;
% Er3 = ENGINE_DATA.Er3;
% alpha = ENGINE_DATA.alpha;
%
% % vclc vcle % compression, expansion clearance vols [m^3]
% % Cbore Ebore % compression, expansion piston bores [m]
% % Cr1 Er1 % compression, expansion desaxe offset in [m]
% % Cr2 Er2 % compression, expansion crank length (half stroke) in [m]
% % Cr3 Er3 % compression, expansion connecting rod lengths [m]
% % alpha % phase angle advance of expansion space [radians]
%
% *** Compression space volume is maximum at theta = 0 for alphas. Be
% careful defining crank angle 0 if using a desaxe offset.
% Ctheta2 = theta - pi;
% Etheta2 = Ctheta2 + alpha;
%
% Ctheta3 = pi - asin((-Cr1+(Cr2*sin(Ctheta2)))/Cr3);
% Cr4 = Cr2*cos(Ctheta2) - Cr3*cos(Ctheta3);
% Cr4max = sqrt(((Cr2+Cr3)^2)-(Cr1^2));
% vc = vclc + ((pi/4)*(Cbore^2))*(Cr4max-Cr4);
%
% Etheta3 = pi - asin((-Er1+(Er2*sin(Etheta2)))/Er3);
% Er4 = Er2*cos(Etheta2) - Er3*cos(Etheta3);
% Er4max = sqrt(((Er2+Er3)^2)-(Er1^2));
% ve = vcle + ((pi/4)*(Ebore^2))*(Er4max-Er4);
%
% dCtheta3 = (-Cr2*cos(Ctheta2))/(Cr3*sqrt(1-(((Cr1+(Cr2*sin(Ctheta2)))/Cr3).^2)));
% dCr4 = -Cr2*sin(Ctheta2) + Cr3*sin(Ctheta3)*dCtheta3;
% dvc = -(pi/4)*(Cbore^2)*(dCr4);
%
% dEtheta3 = (-Er2*cos(Etheta2))/(Er3*sqrt(1-(((Er1+(Er2*sin(Etheta2)))/Er3).^2)));
% dEr4 = -Er2*sin(Etheta2) + Er3*sin(Etheta3)*dEtheta3;
% dve = -(pi/4)*(Ebore^2)*(dEr4);
% %=====

```

---

## D. LOW-TEMPERATURE ST05G STIRLING ENGINE MECHANICAL DRAWINGS

---

The low-temperature ST05G is a derivative of the ST05G Stirling engine. It was modified from the ST05G-CNC to operate at reduced thermal source temperature by Speer [1]. Additional modifications were made to improve reliability.

The mechanical drawings in this appendix define the modifications to the ST05G-CNC to create the low-temperature ST05G that are not presented by Speer [1]. The assembly drawings below are: the complete engine assembly, connecting pipe assembly, glass cyclinder and mounting component assembly, graphite piston assembly, piston connecting rod assembly, and flywheel assembly.

### Appendix D References

---

- [1] Speer, C. P., 2018, "Modifications to Reduce the Minimum Thermal Source Temperature of the ST05G-CNC Stirling Engine," University of Alberta.

6

5

4

3

2

1

D

D

C

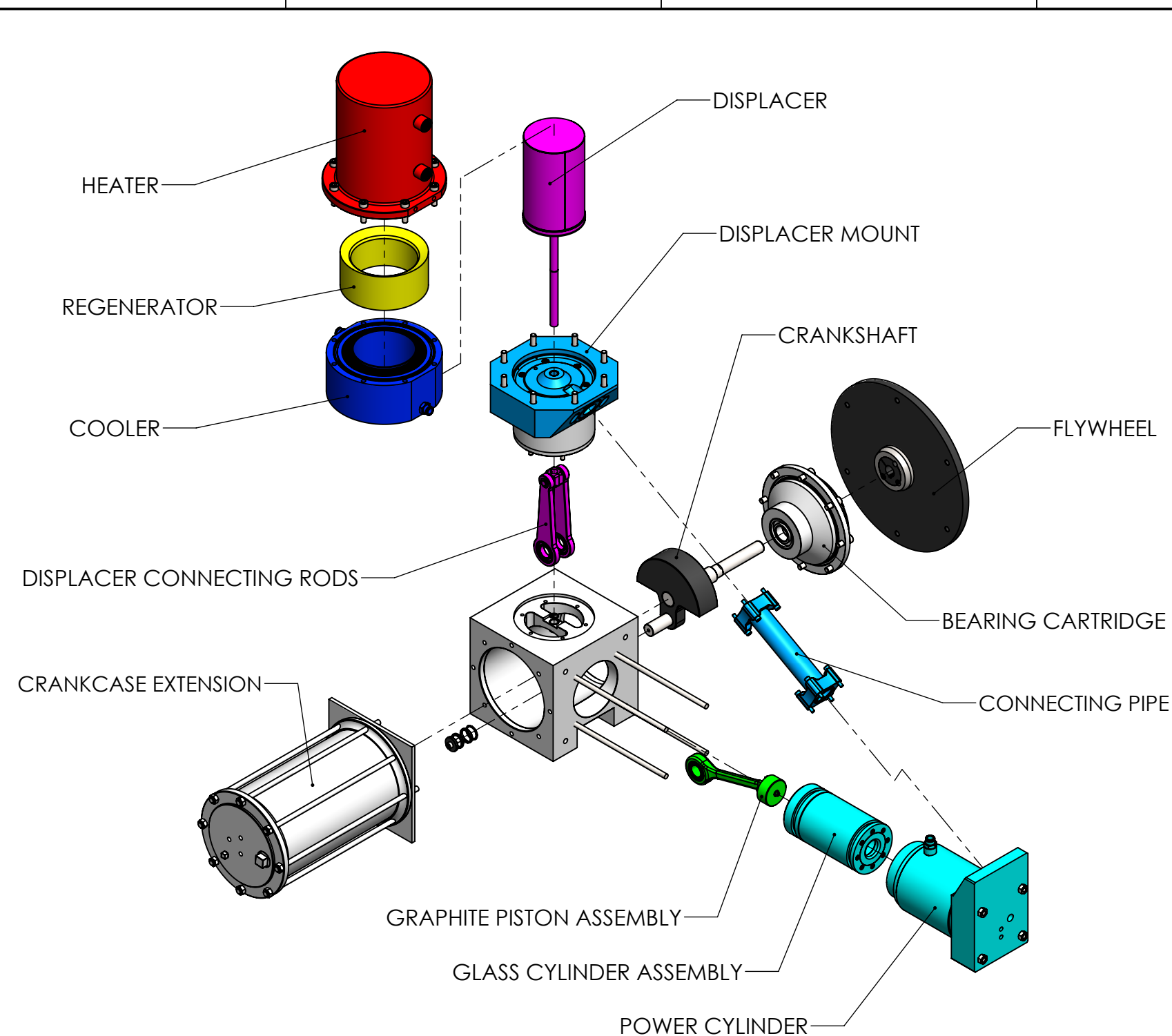
C

B

B

A

A



ITEM NO.	PART NUMBER	Material	Author	QTY.
1	C-CC-Z-00-CRANKCASE_ASM	N/A	David Miller	1
2	C-BC-Z-00-BEARING_CARTRIDGE_ASM	N/A	David Miller	1
3	C-CO-Z-01-COVER	N/A	DAVID MILLER	1
4	C-CS-Z-00-CRANKSHAFT_ASM	N/A	Anders Carlstad	1
5	C-ZZ-Z-03-SPACER_115	Alloy Steel	Sam Tseung	1
6	C-ZZ-Z-05-SPACER_117	Alloy Steel	Sam Tseung	2
7	C-ZZ-Z-04-SPACER_116	Alloy Steel	Sam Tseung	1
8	C-ZZ-Z-06-SPACER_118	1.0715 (11SMn30)	Sam Tseung	1
9	C-ZZ-F-00-FLYWHEEL_ASM	N/A	David Miller	1
10	C-ZZ-Z-07-THREADED_ROD	Plain Carbon Steel	DAVID MILLER	4
11	B18.2.4.1M - Hex nut, Style 1, M8 x 1.25 --D-N	Alloy Steel	SW LIBRARY	12
12	A-ZZ-Z-01-FOOT	Aluminum 6061-T6511	YANWEI ZHANG	1
13	A-DM-Z-00-DISP_MOUNT_ASM	N/A	DAVID MILLER	1
14	A-DC-Z-00-DISP_CYL_ASM	N/A	DAVID MILLER	1
15	A-ZZ-Z-02-R_CROSSHEAD	303 Stainless Steel	Connor Speer	1
16	A-ZZ-Z-03-L_CROSSHEAD	303 Stainless Steel	Connor Speer	1
17	A-ZZ-Z-04-DISP_PISTON_ROD_ASM1	N/A	DAVID MILLER	1
18	A-ZZ-Z-04-DISP_PISTON_ROD_ASM2	N/A	DAVID MILLER	1
19	A-DP-F-00-DISP_PISTON_ASM	N/A	DAVID MILLER	1
20	A-ZZ-Z-08-0.468in_Circlip_Shaft	Spring Steel	MCMMASTER-CARR	1
21	B18.3.1M - 5 x 0.8 x 35 Hex SHCS -- 22NHX	Alloy Steel	SW LIBRARY	8
22	B18.3.1M - 6 x 1.0 x 110 Hex SHCS -- 24NHX	Alloy Steel	SW LIBRARY	6
23	B18.3.1M - 6 x 1.0 x 20 Hex SHCS -- 20NHX	Alloy Steel	SW LIBRARY	1
24	B18.3.1M - 8 x 1.25 x 30 Hex SHCS -- 30NHX	Alloy Steel	SW LIBRARY	8
25	B18.3.1M - 8 x 1.25 x 20 Hex SHCS -- 20NHX	Alloy Steel	SW LIBRARY	8
26	B-PC-Z-00-POWER_CYL_ASM	N/A	David Miller	1
27	B-GC-Z-00-GLASS_CYLINDER_ASM	N/A	CONNOR SPEER	1
28	B-PR-Z-00-PISTON_ROD_ASM	N/A	DAVID MILLER	1
29	B-GP-Z-00-GRAPHITE_PISTON_ASM	N/A	DAVID MILLER	1
30	B-CP-Z-00-CON_PIPE_ASM.SLDPRT	N/A	DAVID MILLER	1
31	C-ZZ-Z-08-EXTENSION_THREADED_RODS	Brass	CONNOR SPEER	8
32	C-CE-Z-00-CRANKCASE_EXTENSION_ASM.SLDPRT	N/A	DAVID MILLER	1

Assemblies that have changed form Speer [1]:  
 the connecting pipe,  
 glass cylinder,  
 graphite piston,  
 graphite piston connectin rod, and  
 flywheel assembly.

UNLESS OTHERWISE SPECIFIED DIMENSIONS IN MILLIMETERS LINEAR TOL. $\pm 1$ mm ANGULAR TOL. $\pm 1^\circ$		COMMENTS		DYNAMIC THERMAL ENERGY CONVERSION LAB DEPARTMENT OF MECHANICAL ENGINEERING UNIVERSITY OF ALBERTA		
THIRD ANGLE PROJECTION		DRW DAVID MILLER		TITLE		
		SM DAVID MILLER		LOW-TEMPERATURE ST05G		
		CHK				
MAT. N/A		CREATED 4/20/2018		SIZE	DRW NO	REV
		EDITED 4/10/2019		B	00-MST05G-V3.1-GLASSCYLINDER	B
				SCALE 1:8	MASS: 51624.8131	SHEET 1 OF 3

6

5

4

3

2

1



6

5

4

3

2

1

D

D

C

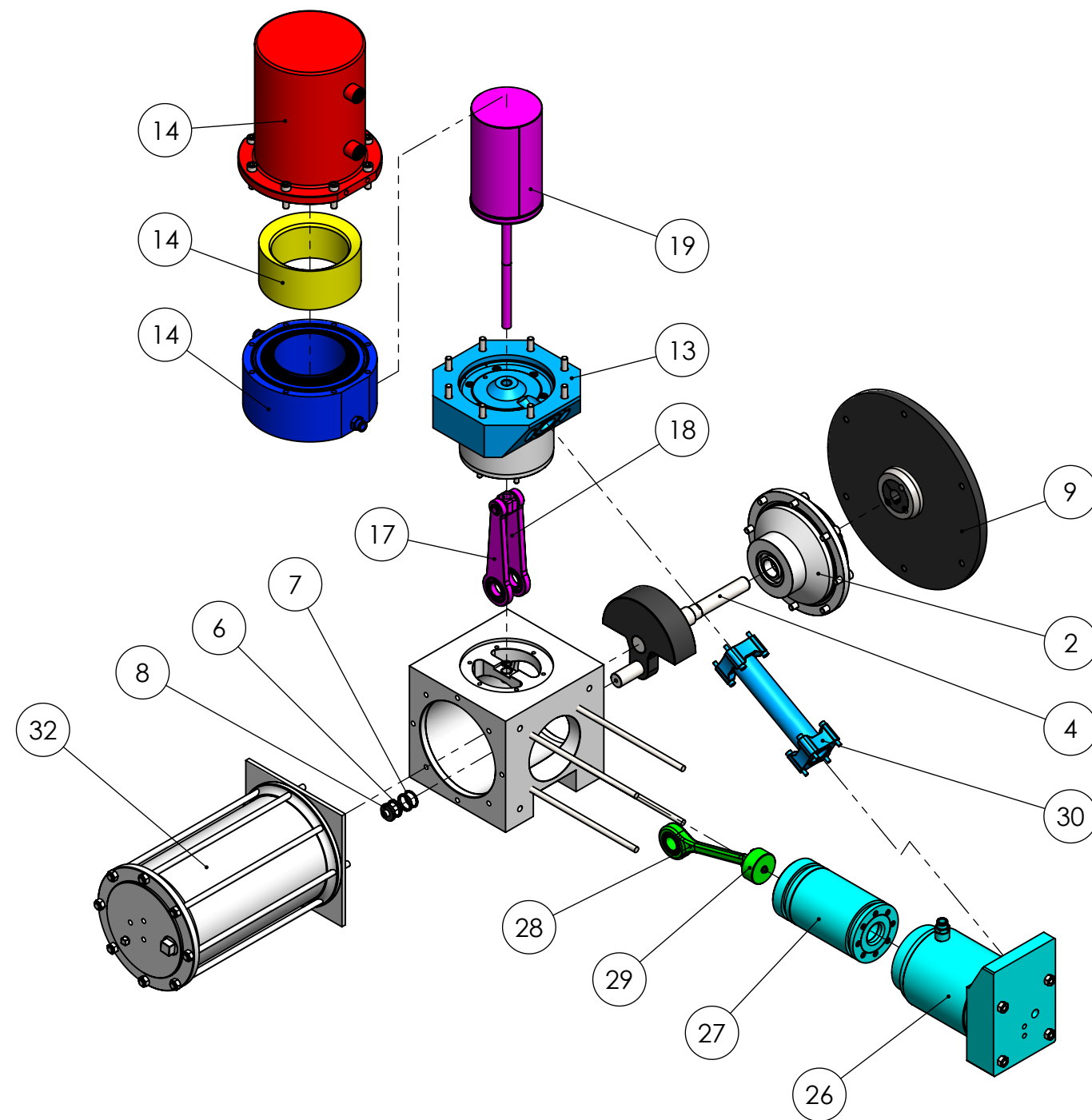
C

B

B

A

A

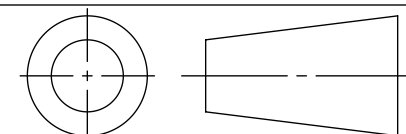


ITEM NO.	PART NUMBER	Material	Author	QTY.
1	C-CC-Z-00-CRANKCASE_ASM	N/A	David Miller	1
2	C-BC-Z-00-BEARING_CARTRIDGE_ASM	N/A	David Miller	1
3	C-CO-Z-01-COVER	N/A	DAVID MILLER	1
4	C-CS-Z-00-CRANKSHAFT_ASM	N/A	Anders Carlstad	1
5	C-ZZ-Z-03-SPACER_115	Alloy Steel	Sam Tseung	1
6	C-ZZ-Z-05-SPACER_117	Alloy Steel	Sam Tseung	2
7	C-ZZ-Z-04-SPACER_116	Alloy Steel	Sam Tseung	1
8	C-ZZ-Z-06-SPACER_118	1.0715 (11SMn30)	Sam Tseung	1
9	C-ZZ-F-00-FLYWHEEL_ASM	N/A	David Miller	1
10	C-ZZ-Z-07-THREADED_ROD	Plain Carbon Steel	DAVID MILLER	4
11	B18.2.4.1M - Hex nut, Style 1, M8 x 1.25 --D-N	Alloy Steel	SW LIBRARY	12
12	A-ZZ-Z-01-FOOT	Aluminum 6061-T6511	YANWEI ZHANG	1
13	A-DM-Z-00-DISP_MOUNT_ASM	N/A	DAVID MILLER	1
14	A-DC-Z-00-DISP_CYL_ASM	N/A	DAVID MILLER	1
15	A-ZZ-Z-02-R_CROSSHEAD	303 Stainless Steel	Connor Speer	1
16	A-ZZ-Z-03-L_CROSSHEAD	303 Stainless Steel	Connor Speer	1
17	A-ZZ-Z-04-DISP_PISTON_ROD_ASM1	N/A	DAVID MILLER	1
18	A-ZZ-Z-04-DISP_PISTON_ROD_ASM2	N/A	DAVID MILLER	1
19	A-DP-F-00-DISP_PISTON_ASM	N/A	DAVID MILLER	1
20	A-ZZ-Z-08-0.468in_Circlip_Shaft	Spring Steel	MCMMASTER-CARR	1
21	B18.3.1M - 5 x 0.8 x 35 Hex SHCS -- 22NHX	Alloy Steel	SW LIBRARY	8
22	B18.3.1M - 6 x 1.0 x 110 Hex SHCS -- 24NHX	Alloy Steel	SW LIBRARY	6
23	B18.3.1M - 6 x 1.0 x 20 Hex SHCS -- 20NHX	Alloy Steel	SW LIBRARY	1
24	B18.3.1M - 8 x 1.25 x 30 Hex SHCS -- 30NHX	Alloy Steel	SW LIBRARY	8
25	B18.3.1M - 8 x 1.25 x 20 Hex SHCS -- 20NHX	Alloy Steel	SW LIBRARY	8
26	B-PC-Z-00-POWER_CYL_ASM	N/A	David Miller	1
27	B-GC-Z-00-GLASS_CYLINDER_ASM	N/A	CONNOR SPEER	1
28	B-PR-Z-00-PISTON_ROD_ASM	N/A	DAVID MILLER	1
29	B-GP-Z-00-GRAPHITE_PISTON_ASM	N/A	DAVID MILLER	1
30	B-CP-Z-00-CON_PIPE_ASM.SLDPRT	N/A	DAVID MILLER	1
31	C-ZZ-Z-08-EXTENSION_THREADED_RODS	Brass	CONNOR SPEER	8
32	C-CE-Z-00-CRANKCASE_EXTENSION_ASM.SLDPRT	N/A	DAVID MILLER	1

Assemblies that have changed form Speer [1]:  
the connecting pipe,  
glass cylinder,  
graphite piston,  
graphite piston connectin rod, and  
flywheel assembly.

UNLESS OTHERWISE SPECIFIED  
DIMENSIONS IN MILLIMETERS  
LINEAR TOL.  $\pm 1$  mm  
ANGULAR TOL.  $\pm 1^\circ$

THIRD ANGLE PROJECTION



MAT. N/A

COMMENTS

DRW DAVID MILLER

SM DAVID MILLER

CHK

CREATED 4/20/2018

EDITED 4/10/2019

DYNAMIC THERMAL ENERGY CONVERSION LAB  
DEPARTMENT OF MECHANICAL ENGINEERING  
UNIVERSITY OF ALBERTA

TITLE

LOW-TEMPERATURE ST05G

SIZE

B

DRW NO

00-MST05G-V3.1-GLASSCYLINDER

REV

B

SCALE 1:8

MASS: 51624.8131

SHEET 2 OF 3

6

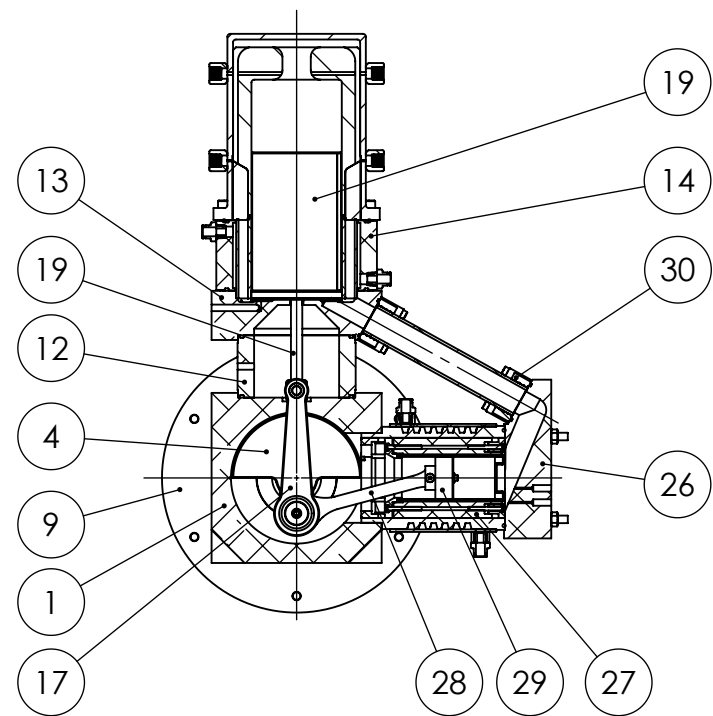
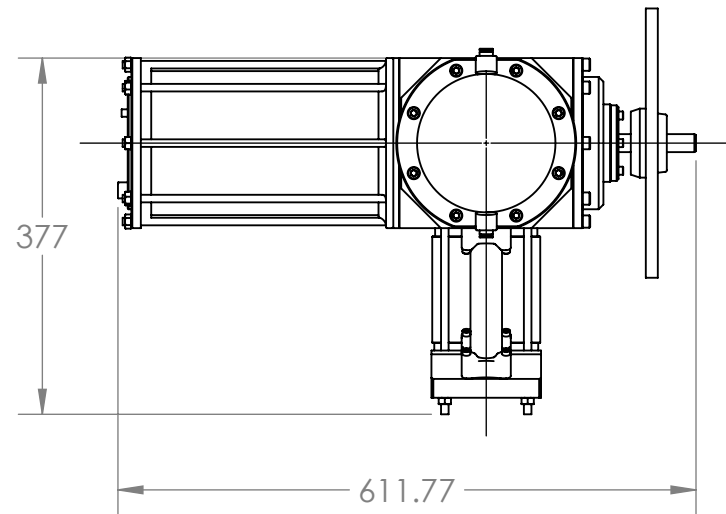
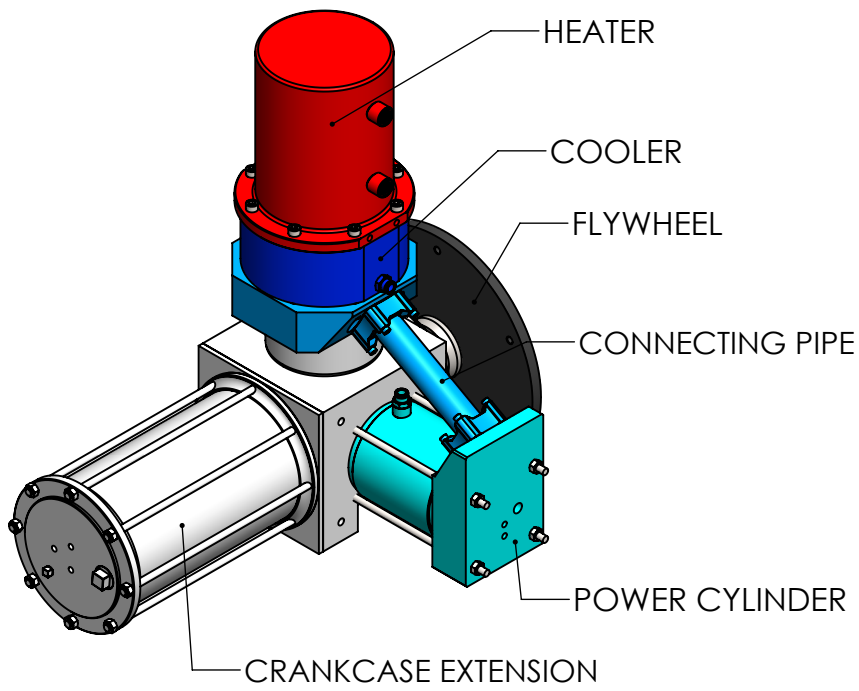
5

4

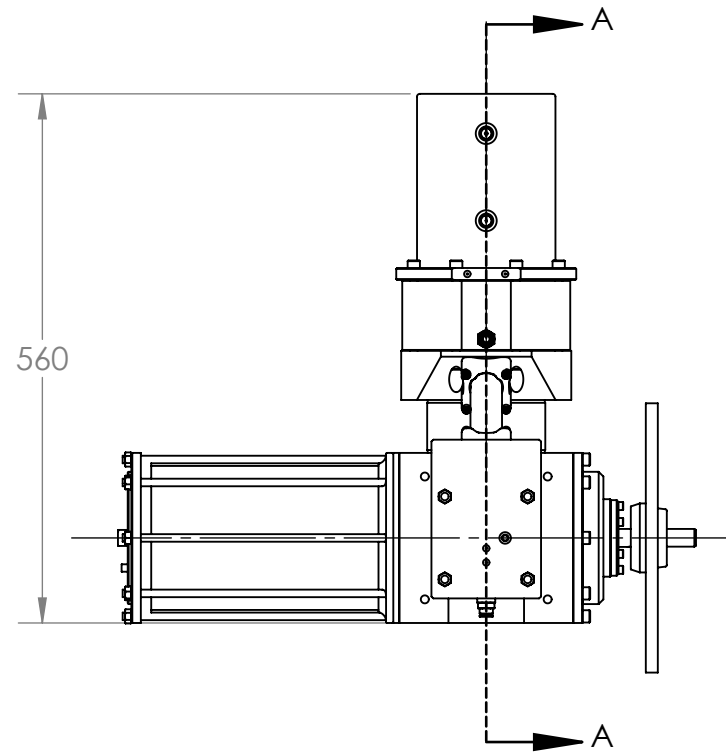
3

2

1



SECTION A-A



ITEM NO.	PART NUMBER	Material	Author	QTY.
1	C-CC-Z-00-CRANKCASE_ASM	N/A	David Miller	1
2	C-BC-Z-00-BEARING_CARTRIDGE_ASM	N/A	David Miller	1
3	C-CO-Z-01-COVER	N/A	DAVID MILLER	1
4	C-CS-Z-00-CRANKSHAFT_ASM	N/A	Anders Carlstad	1
5	C-ZZ-Z-03-SPACER_115	Alloy Steel	Sam Tseung	1
6	C-ZZ-Z-05-SPACER_117	Alloy Steel	Sam Tseung	2
7	C-ZZ-Z-04-SPACER_116	Alloy Steel	Sam Tseung	1
8	C-ZZ-Z-06-SPACER_118	1.0715 (11SMn30)	Sam Tseung	1
9	C-ZZ-F-00-FLYWHEEL_ASM	N/A	David Miller	1
10	C-ZZ-Z-07-THREADED_ROD	Plain Carbon Steel	DAVID MILLER	4
11	B18.2.4.1M - Hex nut, Style 1, M8 x 1.25 --D-N	Alloy Steel	SW LIBRARY	12
12	A-ZZ-Z-01-FOOT	Aluminum 6061-T6511	YANWEI ZHANG	1
13	A-DM-Z-00-DISP_MOUNT_ASM	N/A	DAVID MILLER	1
14	A-DC-Z-00-DISP_CYL_ASM	N/A	DAVID MILLER	1
15	A-ZZ-Z-02-R_CROSSHEAD	303 Stainless Steel	Connor Speer	1
16	A-ZZ-Z-03-L_CROSSHEAD	303 Stainless Steel	Connor Speer	1
17	A-ZZ-Z-04-DISP_PISTON_ROD_ASM1	N/A	DAVID MILLER	1
18	A-ZZ-Z-04-DISP_PISTON_ROD_ASM2	N/A	DAVID MILLER	1
19	A-DP-F-00-DISP_PISTON_ASM	N/A	DAVID MILLER	1
20	A-ZZ-Z-08-0.468in_Circlip_Shaft	Spring Steel	MCMMASTER-CARR	1
21	B18.3.1M - 5 x 0.8 x 35 Hex SHCS -- 22NHX	Alloy Steel	SW LIBRARY	8
22	B18.3.1M - 6 x 1.0 x 110 Hex SHCS -- 24NHX	Alloy Steel	SW LIBRARY	6
23	B18.3.1M - 6 x 1.0 x 20 Hex SHCS -- 20NHX	Alloy Steel	SW LIBRARY	1
24	B18.3.1M - 8 x 1.25 x 30 Hex SHCS -- 30NHX	Alloy Steel	SW LIBRARY	8
25	B18.3.1M - 8 x 1.25 x 20 Hex SHCS -- 20NHX	Alloy Steel	SW LIBRARY	8
26	B-PC-Z-00-POWER_CYL_ASM	N/A	David Miller	1
27	B-GC-Z-00-GLASS_CYLINDER_ASM	N/A	CONNOR SPEER	1
28	B-PR-Z-00-PISTON_ROD_ASM	N/A	DAVID MILLER	1
29	B-GP-Z-00-GRAPHITE_PISTON_ASM	N/A	DAVID MILLER	1
30	B-CP-Z-00-CON_PIPE_ASM.SLDPRT	N/A	DAVID MILLER	1
31	C-ZZ-Z-08-EXTENSION_THREADED_RODS	Brass	CONNOR SPEER	8
32	C-CE-Z-00-CRANKCASE_EXTENSION_ASM.SLDPRT	N/A	DAVID MILLER	1

Assemblies that have changed form Speer [1]:  
the connecting pipe,  
glass cylinder,  
graphite piston,  
graphite piston connectin rod, and  
flywheel assembly.

UNLESS OTHERWISE SPECIFIED DIMENSIONS IN MILLIMETERS LINEAR TOL. $\pm 1$ mm ANGULAR TOL. $\pm 1^\circ$	COMMENTS	DYNAMIC THERMAL ENERGY CONVERSION LAB DEPARTMENT OF MECHANICAL ENGINEERING UNIVERSITY OF ALBERTA		
	THIRD ANGLE PROJECTION	DRW DAVID MILLER	TITLE	
	SM DAVID MILLER	LOW-TEMPERATURE ST05G		
	CHK	CREATED 4/20/2018	SIZE B	REV B
MAT. N/A	EDITED 4/10/2019	DRW NO	00-MST05G-V3.1-GLASSCYLINDER	
		SCALE 1:8	MASS: 51624.8131	SHEET 3 OF 3

6

5

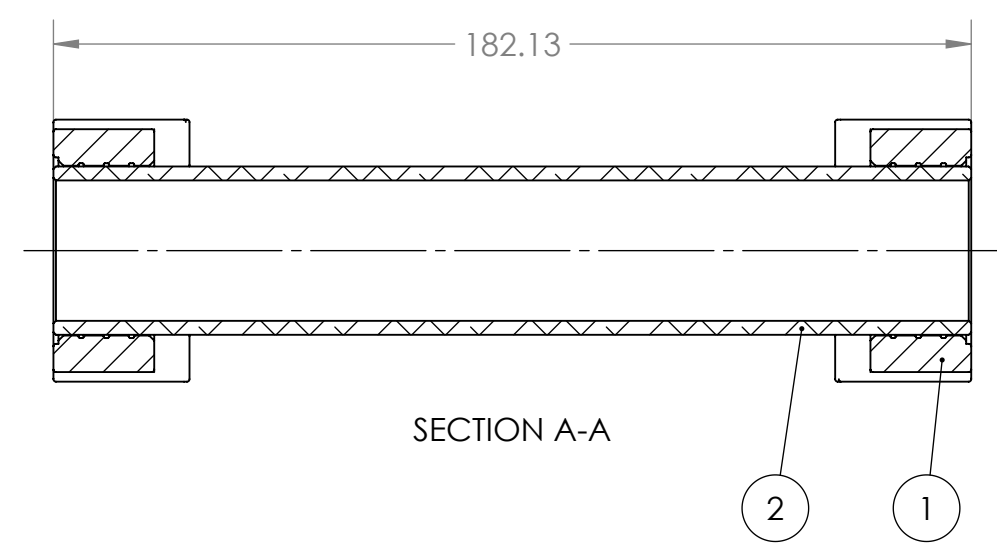
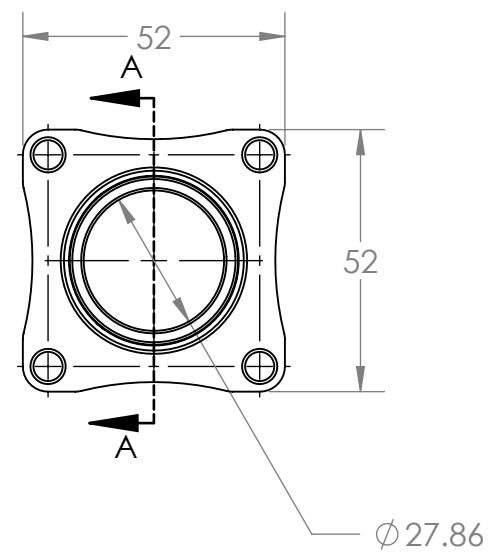
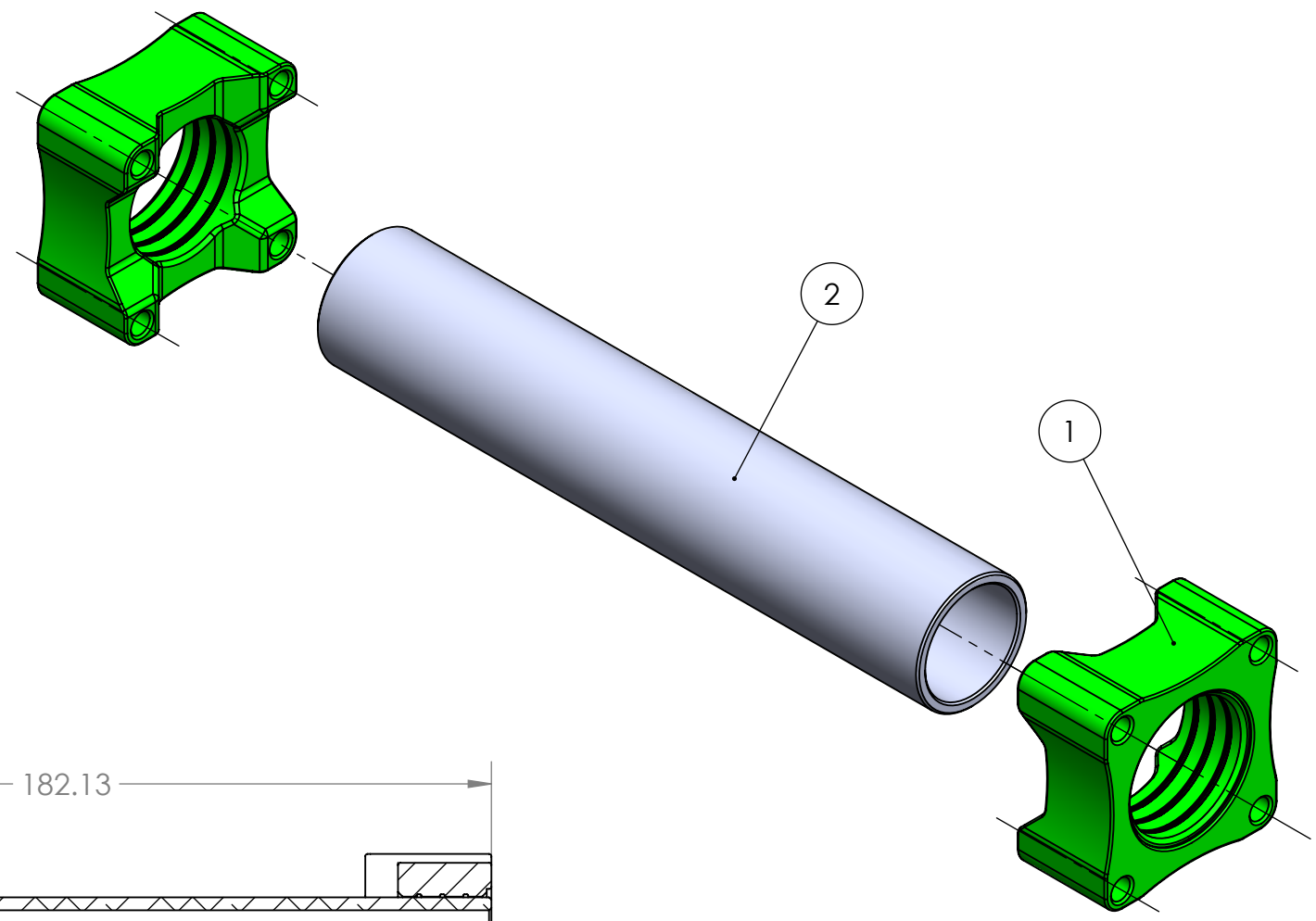
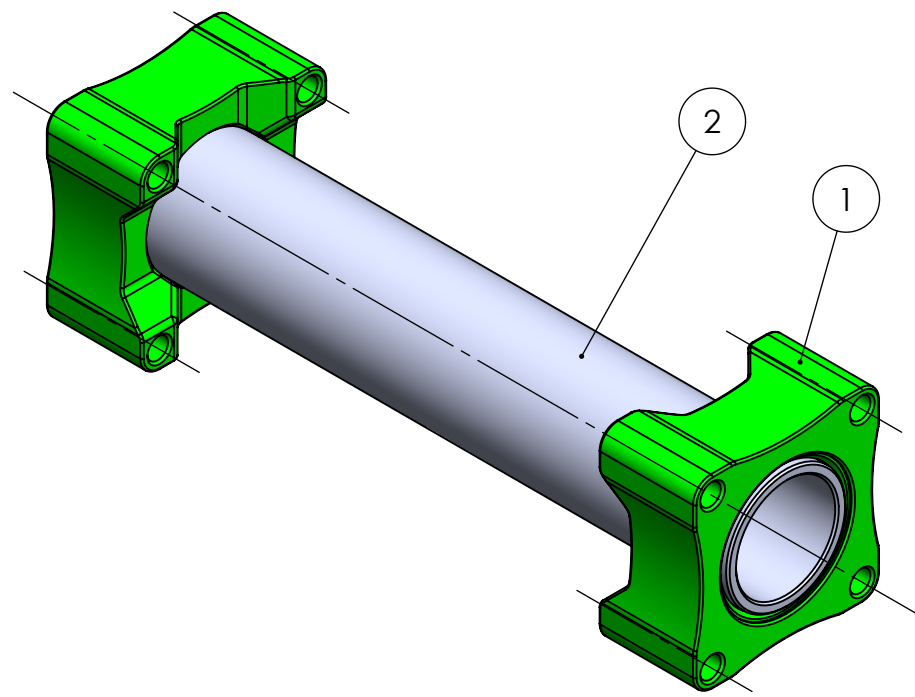
4

3

2

1

ITEM NO.	PART NUMBER	Material	SW-Author(Author)	QTY.
1	B-CP-Z-01-BLOCK	Form Clear Resin (Cured)	DAVID MILLER	2
2	B-CP-Z-02-PIPE	6061-T6 (SS)	CONNOR SPEER	1



UNLESS OTHERWISE SPECIFIED DIMENSIONS IN MILLIMETERS LINEAR TOL. $\pm 1$ mm ANGULAR TOL. $\pm 1^\circ$	COMMENTS		DYNAMIC THERMAL ENERGY CONVERSION LAB DEPARTMENT OF MECHANICAL ENGINEERING UNIVERSITY OF ALBERTA		
	THIRD ANGLE PROJECTION		TITLE		
			CONNECTING PIPE		
	MAT. N/A		DRW DAVID MILLER SM DAVID MILLER CHK CREATED 4/23/2018 EDITED 4/3/2019	SIZE <b>B</b>	DRW NO B-CP-Z-00-CON_PIPE_ASM.SLDPR
		SCALE 2:3	MASS: 200.9129	SHEET 1 OF 1	

6

5

4

3

2

1

D

D

C

C

B

B

A

A

6

5

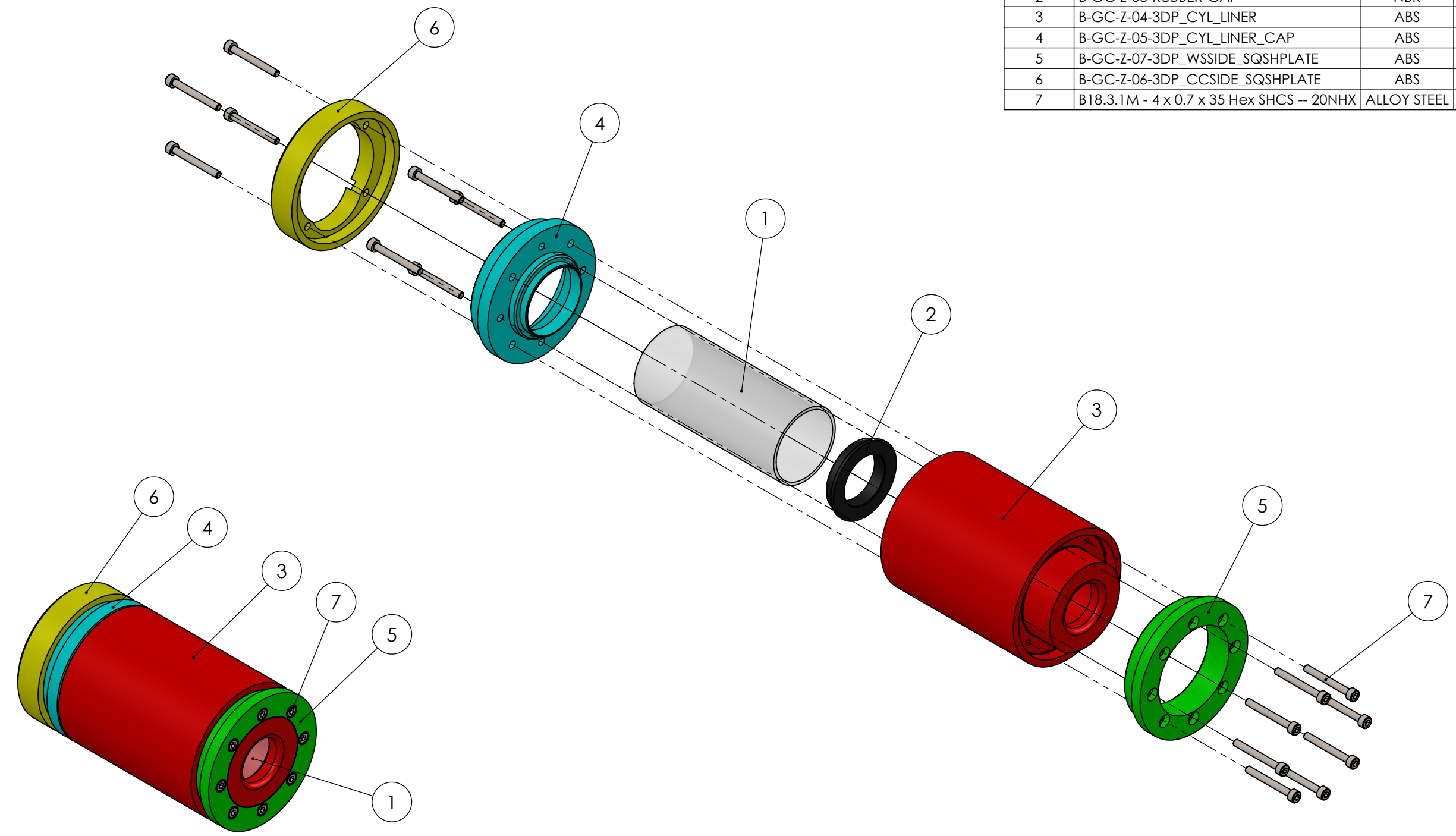
4

3

2

1

ITEM NO.	PART NUMBER	Material	SW-Author(Author)	QTY.
1	B-GC-Z-01-GLASS_CYLINDER	GLASS	CONNOR SPEER	1
2	B-GC-Z-03-RUBBER-CAP	NBR	CONNOR SPEER	1
3	B-GC-Z-04-3DP_CYL_LINER	ABS	CONNOR SPEER	1
4	B-GC-Z-05-3DP_CYL_LINER_CAP	ABS	CONNOR SPEER	1
5	B-GC-Z-07-3DP_WSSIDE_SQSHPLATE	ABS	CONNOR SPEER	1
6	B-GC-Z-06-3DP_CCSIDE_SQSHPLATE	ABS	CONNOR SPEER	1
7	B18.3.1M - 4 x 0.7 x 35 Hex SHCS -- 20NHX	ALLOY STEEL	SW LIBRARY	16



UNLESS OTHERWISE SPECIFIED DIMENSIONS IN MILLIMETERS LINEAR TOL. $\pm 1$ mm ANGULAR TOL. $\pm 1^\circ$		COMMENTS		DYNAMIC THERMAL ENERGY CONVERSION LAB DEPARTMENT OF MECHANICAL ENGINEERING UNIVERSITY OF ALBERTA	
THIRD ANGLE PROJECTION		DRW DAVID MILLER SM CONNOR SPEER		TITLE GRAPHITE CYLINDER MOUNTING ASSEMBLY	
		CHK		SIZE B	DRW NO B-GC-Z-00-GLASS_CYLINDER_ASM
		CREATED 1/16/2017		REV B	
MAT. N/A		EDITED 4/10/2019		SCALE 2:5	MASS: 584.83
				SHEET 1 OF 2	

6

5

4

3

2

1

D

D

C

C

B

B

A

A

6

5

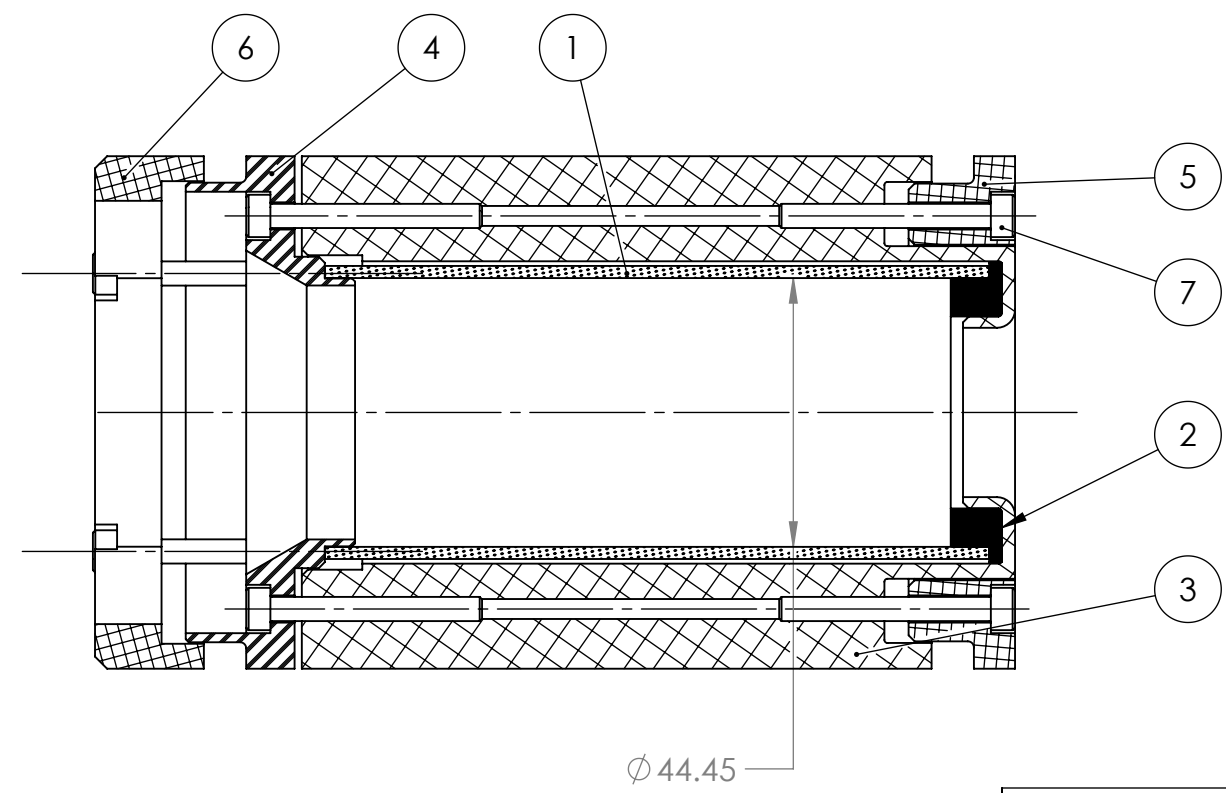
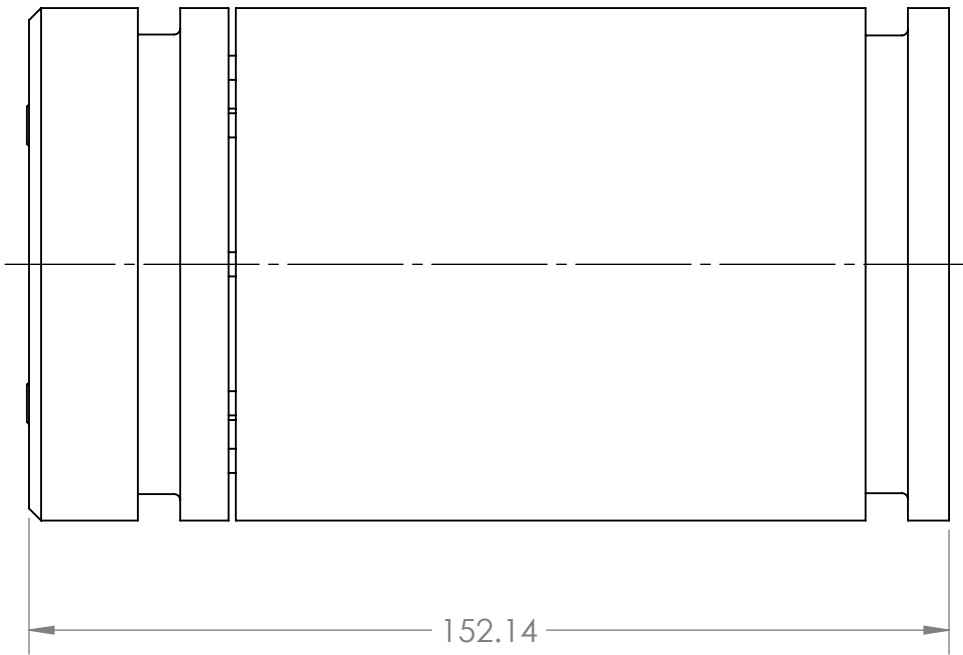
4

3

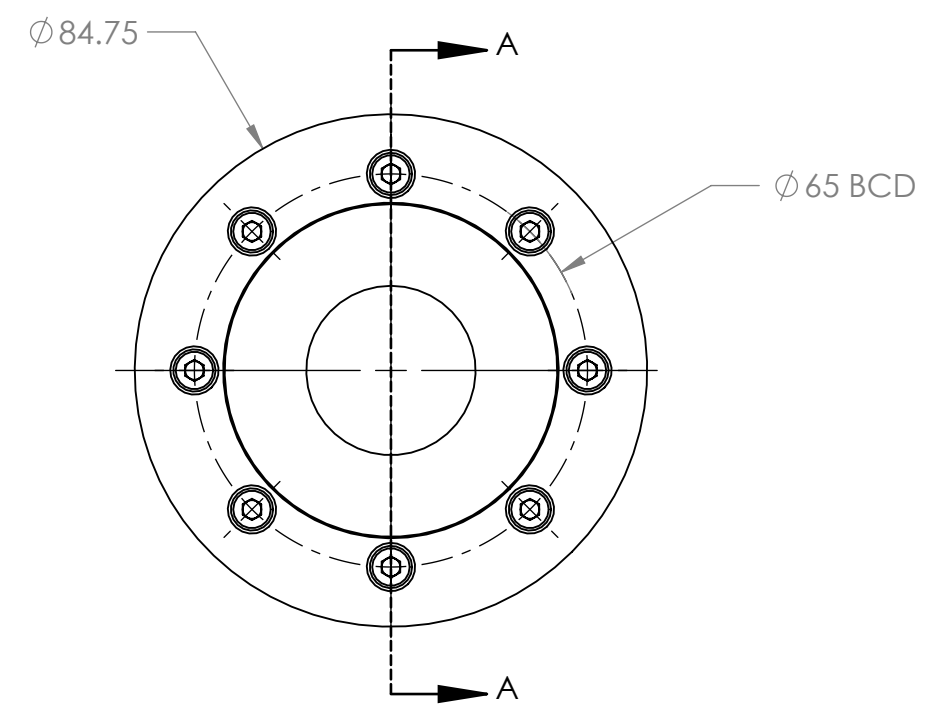
2

1

ITEM NO.	PART NUMBER	Material	SW-Author(Author)	QTY.
1	B-GC-Z-01-GLASS_CYLINDER	GLASS	CONNOR SPEER	1
2	B-GC-Z-03-RUBBER-CAP	NBR	CONNOR SPEER	1
3	B-GC-Z-04-3DP_CYL_LINER	ABS	CONNOR SPEER	1
4	B-GC-Z-05-3DP_CYL_LINER_CAP	ABS	CONNOR SPEER	1
5	B-GC-Z-07-3DP_WSSIDE_SQSHPLATE	ABS	CONNOR SPEER	1
6	B-GC-Z-06-3DP_CCSIDE_SQSHPLATE	ABS	CONNOR SPEER	1
7	B18.3.1M - 4 x 0.7 x 35 Hex SHCS -- 20NHX	ALLOY STEEL	SW LIBRARY	16



SECTION A-A



UNLESS OTHERWISE SPECIFIED DIMENSIONS IN MILLIMETERS LINEAR TOL. $\pm 1$ mm ANGULAR TOL. $\pm 1^\circ$		COMMENTS		DYNAMIC THERMAL ENERGY CONVERSION LAB DEPARTMENT OF MECHANICAL ENGINEERING UNIVERSITY OF ALBERTA	
THIRD ANGLE PROJECTION		DRW DAVID MILLER SM CONNOR SPEER		TITLE GRAPHITE CYLINDER MOUNTING ASSEMBLY	
		CHK		SIZE	REV
		CREATED 1/16/2017		B	B
MAT. N/A		EDITED 4/10/2019		SCALE 4:5	MASS: 584.83
				SHEET 2 OF 2	

6

5

4

3

2

1

D

D

C

C

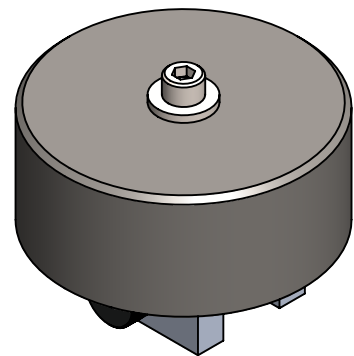
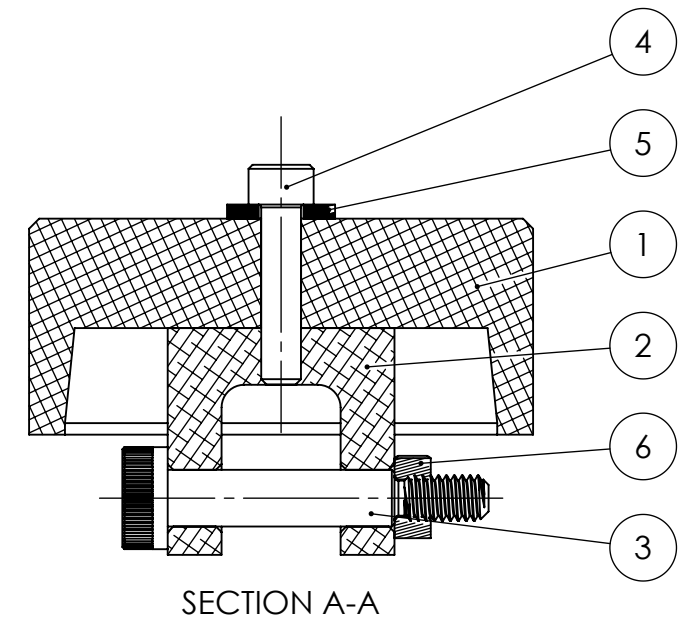
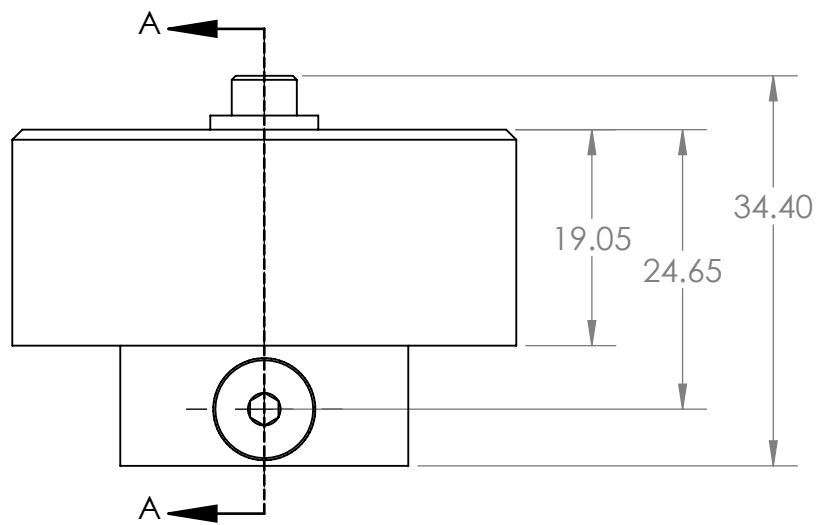
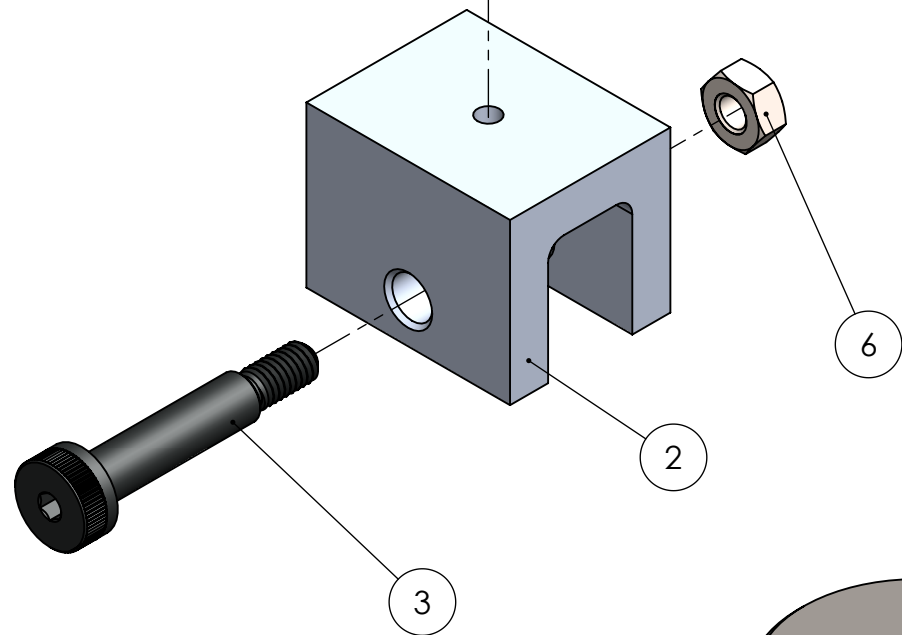
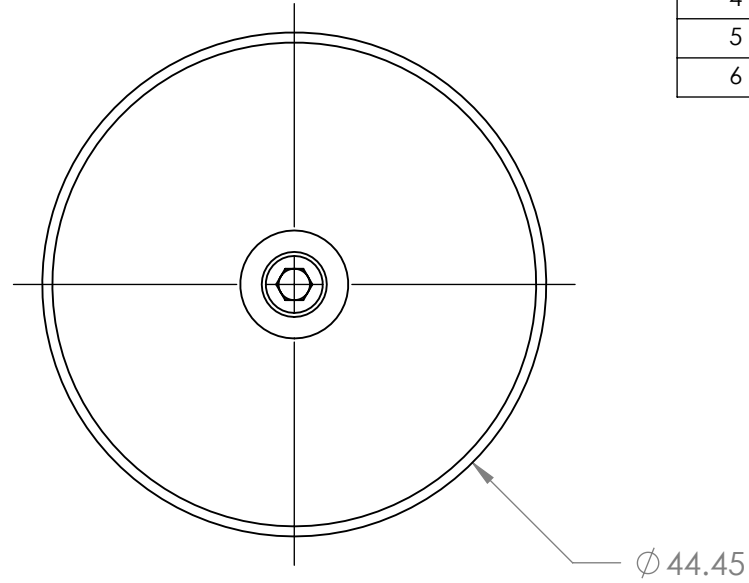
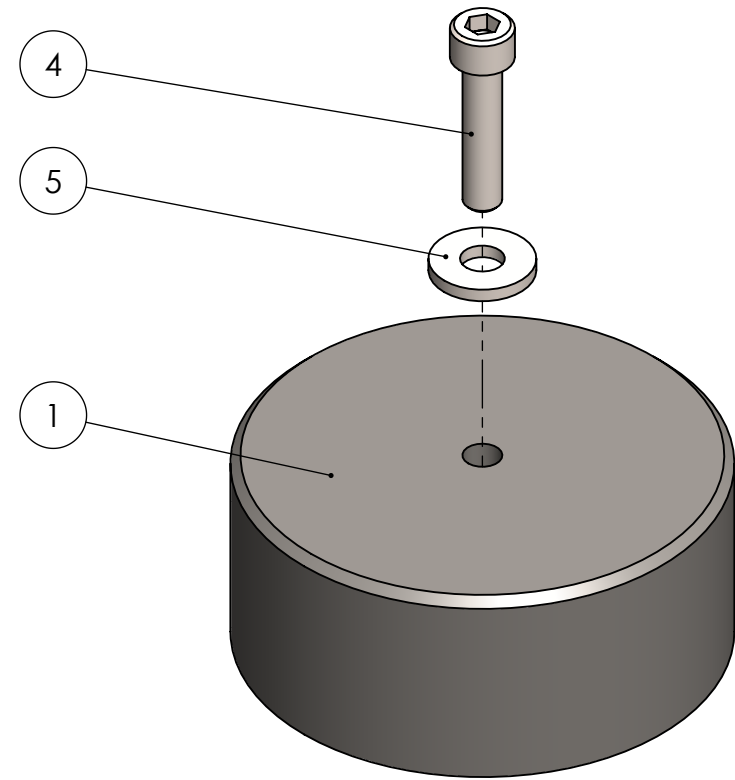
B

B

A

A

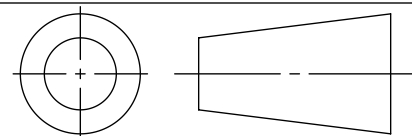
ITEM NO.	PART NUMBER	Material	SW-Author(Author)	QTY.
1	B-GP-Z-01-GRAPHITE_PISTON	C (Graphite)	DAVID MILLER	1
2	B-GP-Z-02-PISTON_MOUNT_MACHINED	6061-T6 (SS)	DAVID MILLER	1
3	92981A042	Alloy Steel	MCMaster-CARR	1
4	HX-SHCS 0.138-32x0.625x0.625-N	Alloy Steel	SW LIBRARY	1
5	Preferred Narrow FW 0.138	Alloy Steel	SW LIBRARY	1
6	B18.2.4.1M - Hex nut, Style 1, M4 x 0.7 --D-N	Alloy Steel	SW LIBRARY	1



SCALE 1:1

UNLESS OTHERWISE SPECIFIED  
DIMENSIONS IN MILLIMETERS  
LINEAR TOL.  $\pm 1$  mm  
ANGULAR TOL.  $\pm 1^\circ$

THIRD ANGLE PROJECTION



MAT. N/A

COMMENTS

DRW DAVID MILLER

SM DAVID MILLER

CHK

CREATED 4/20/2018

EDITED 4/10/2019

DYNAMIC THERMAL ENERGY CONVERSION LAB  
DEPARTMENT OF MECHANICAL ENGINEERING  
UNIVERSITY OF ALBERTA

TITLE

GRAPHITE PISTON ASSEMBLY

SIZE

B

DRW NO

B-GP-Z-00-GRAPHITE\_PISTON\_ASM

REV

B

SCALE 3:2

MASS: 64.7895

SHEET 1 OF 1

6

5

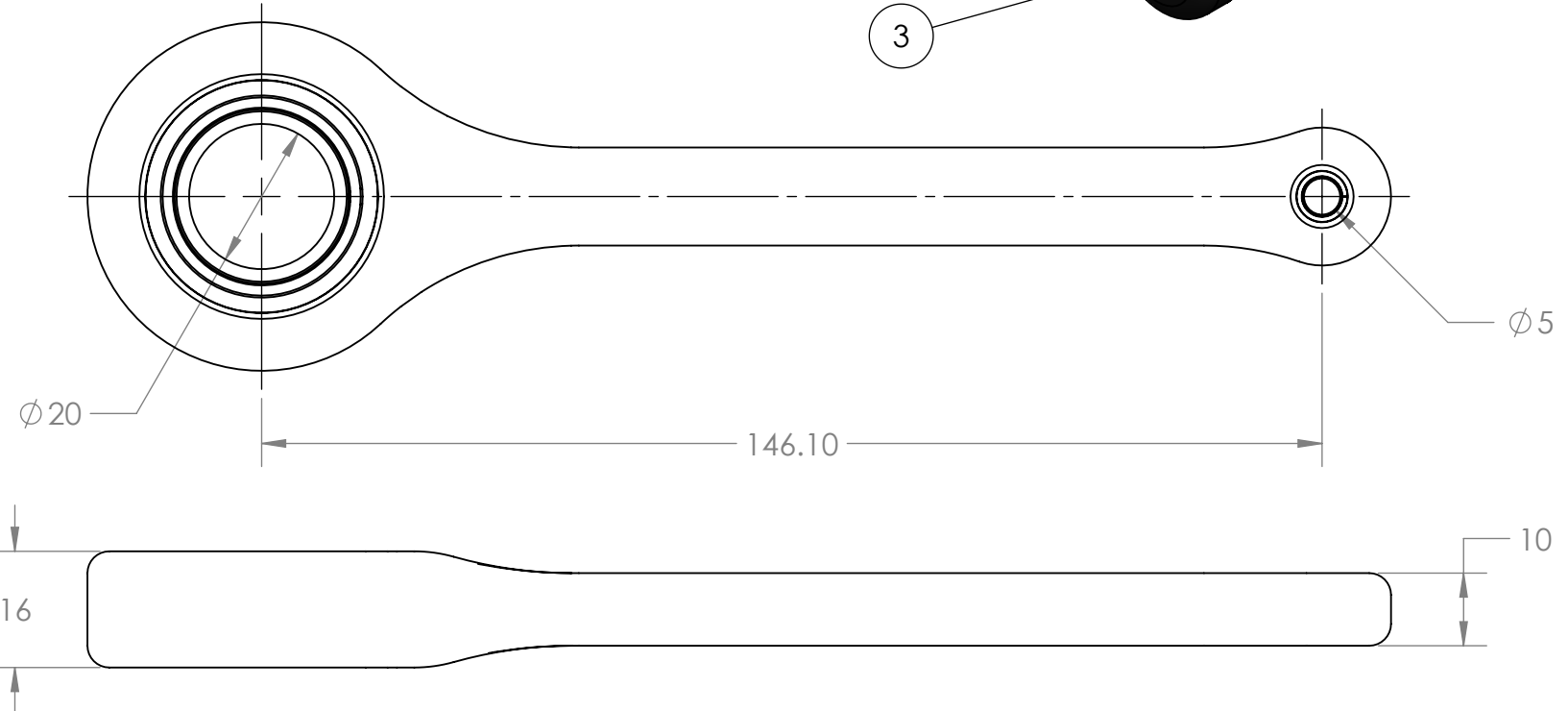
4

3

2

1

ITEM NO.	PART NUMBER	Material	SW-Author(Author)	QTY.
1	B-PR-Z-01-GRAPHITE-PISTON-ROD	Nylon 101	DAVID MILLER	1
2	B-PR-Z-04-CRANK_BEARING	AISI 316 Annealed Stainless Steel Bar (SS)	FAG Bearings	1
3	6679K32	VARIOUS	MCMaster-CARR	2



UNLESS OTHERWISE SPECIFIED DIMENSIONS IN MILLIMETERS LINEAR TOL. $\pm 1$ mm ANGULAR TOL. $\pm 1^\circ$		COMMENTS		DYNAMIC THERMAL ENERGY CONVERSION LAB DEPARTMENT OF MECHANICAL ENGINEERING UNIVERSITY OF ALBERTA	
THIRD ANGLE PROJECTION		DRW DAVID MILLER		TITLE	
		SM DAVID MILLER		44 mm PISTON CONNECTING ROD	
		CHK		SIZE	REV
MAT. N/A		CREATED 4/20/2018		B	B
		EDITED 4/10/2019		DRW NO	B-PR-Z-00-PISTON_ROD_ASM
				SCALE 1:1	SHEET 1 OF 1
				MASS: 83.5188	

6

5

4

3

2

1

D

D

C

C

B

B

A

A

6

5

4

3

2

1

ITEM NO.	PART NUMBER	Material	SW-Author(Author)	0.60 Moment of Inertia/QTY.
1	C-ZZ-F-01-DISC	Plain Carbon Steel	Connor Speer	1
2	Taper Lock Bushing	AISI 1045 Steel, cold drawn	MCMASTER-CARR	1
3	Weld-On Taper Lock Hub	AISI 1020	MCMASTER-CARR	1
4	C-ZZ-F-04-FLYWHEEL_EXTENSION	Plain Carbon Steel	DAVID MILLER	1
5	C-ZZ-F-04-FLYWHEEL_WEIGHT	Plain Carbon Steel	DAVID MILLER	12
6	8 x 20L Shoulder Screw	ALLOY STEEL	MCMASTER-CARR	6
7	B18.2.4.1M - Hex nut, Style 1, M6 x 1 --D-N	ALLOY STEEL	SW LIBRARY	6
8	B18.2.4.1M - Hex nut, Style 1, M5 x 0.8 --D-N	ALLOY STEEL	SW LIBRARY	12
9	6 x 26L Shoulder Screw	ALLOY STEEL	MCMASTER-CARR	12

D

D

C

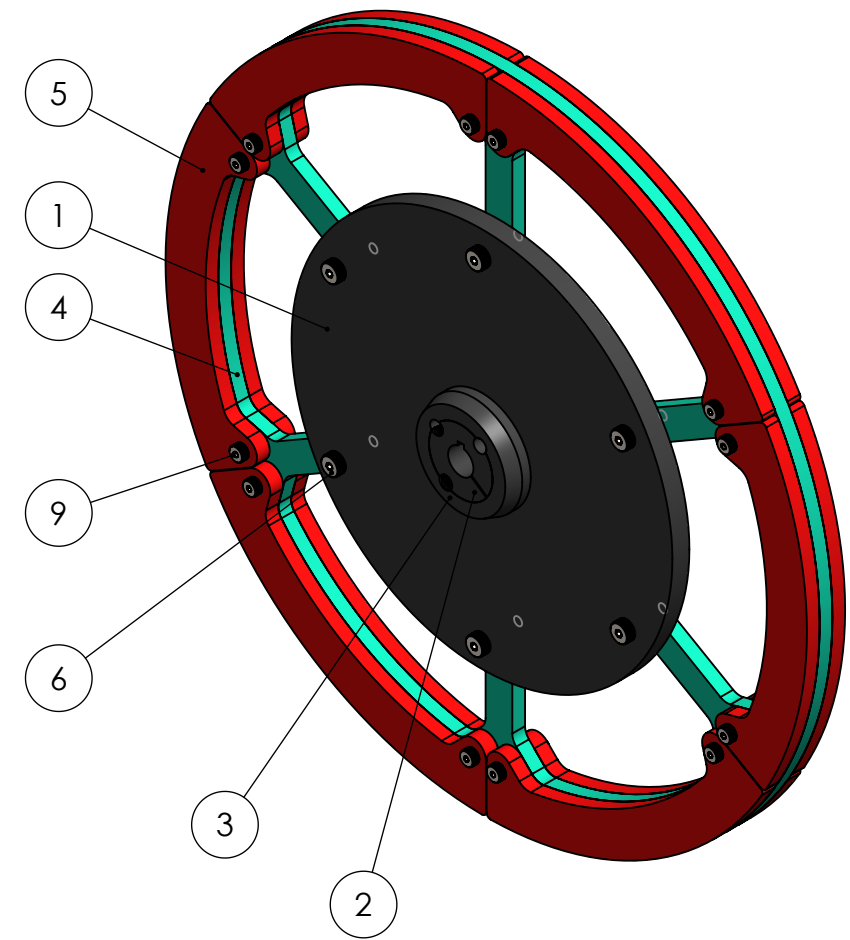
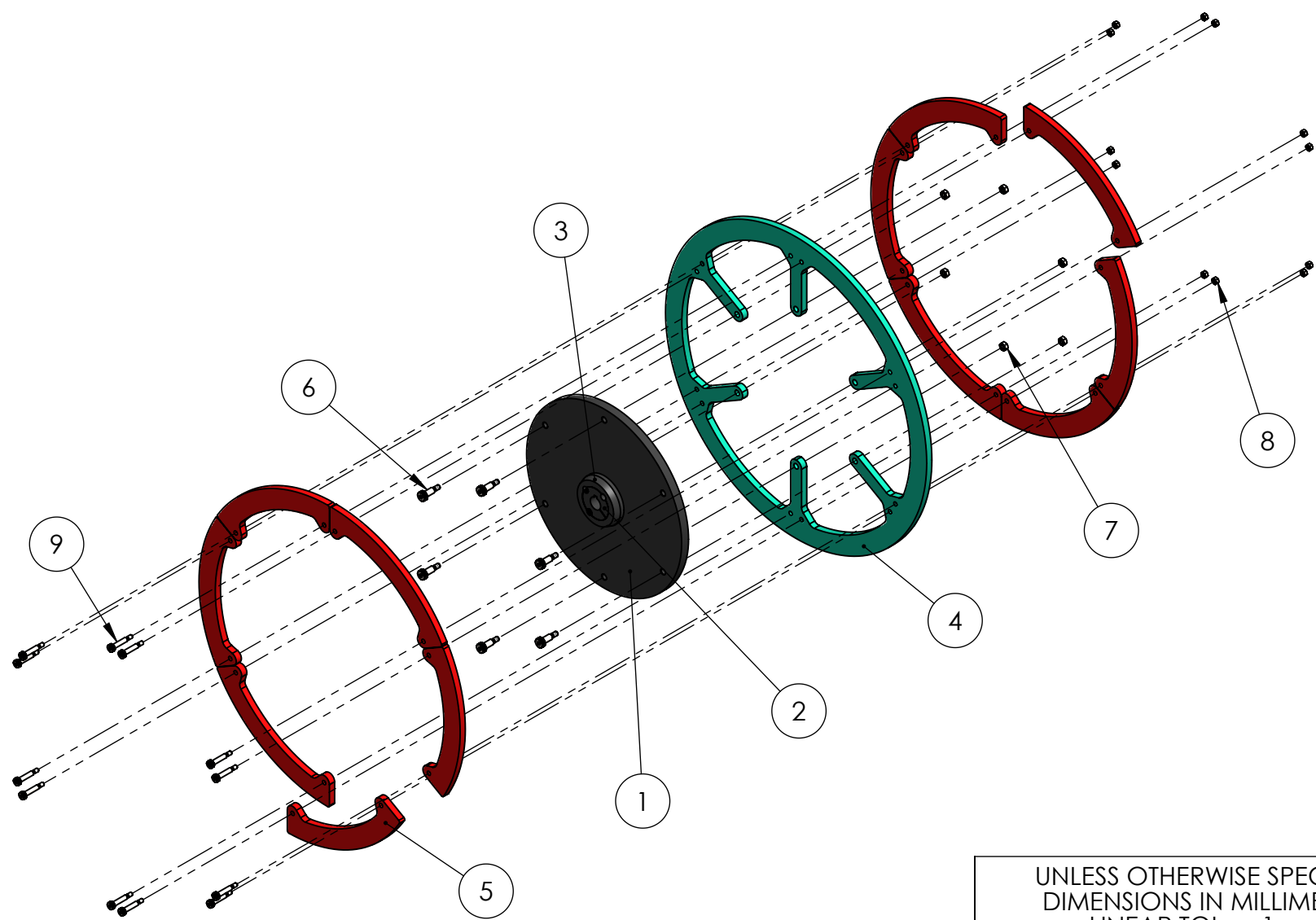
C

B

B

A

A



UNLESS OTHERWISE SPECIFIED DIMENSIONS IN MILLIMETERS LINEAR TOL. $\pm 1$ mm ANGULAR TOL. $\pm 1^\circ$		COMMENTS		DYNAMIC THERMAL ENERGY CONVERSION LAB DEPARTMENT OF MECHANICAL ENGINEERING UNIVERSITY OF ALBERTA	
THIRD ANGLE PROJECTION		DRW DAVID MILLER		TITLE	
		SM DAVID MILLER		FLYWHEEL ASSEMBLY	
		CHK		SIZE	REV
MAT. N/A		CREATED 12/18/2015		B	C-ZZ-F-00-FLYWHEEL_ASM
		EDITED 4/10/2019		SCALE 1:8	MASS : 6877.39
				SHEET 1 OF 3	

6

5

4

3

2

1



6

5

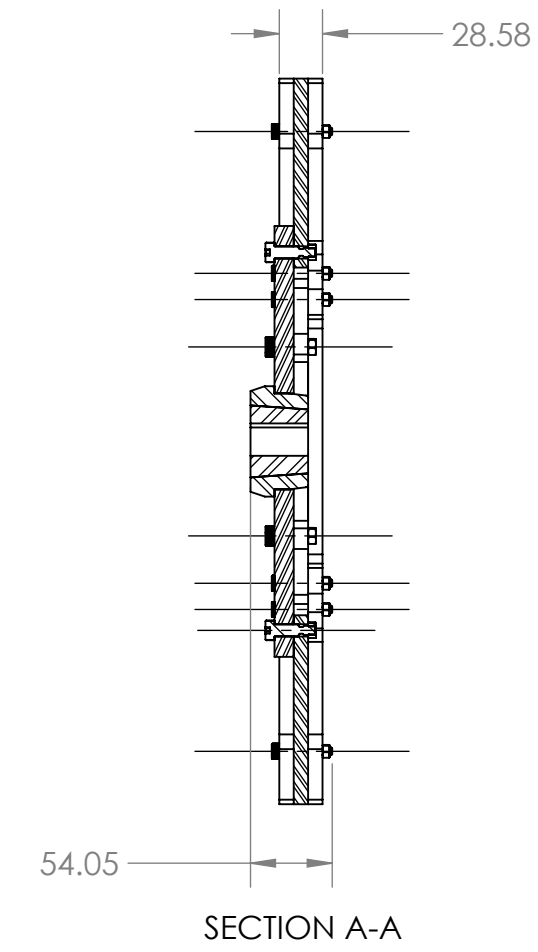
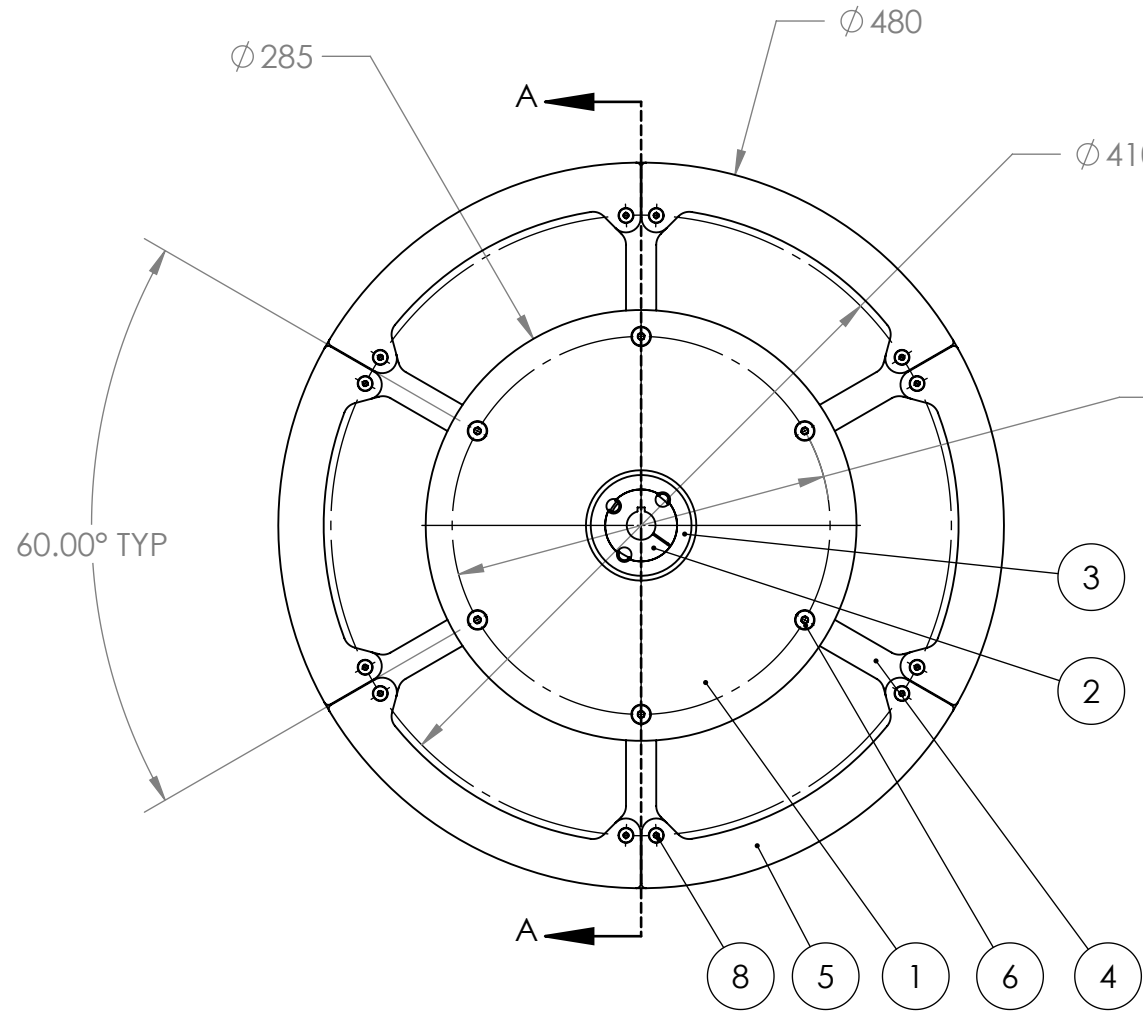
4

3

2

1

ITEM NO.	PART NUMBER	Material	SW-Author(Author)	0.60 Moment of Inertia/QTY.
1	C-ZZ-F-01-DISC	Plain Carbon Steel	Connor Speer	1
2	Taper Lock Bushing	AISI 1045 Steel, cold drawn	MCMaster-CARR	1
3	Weld-On Taper Lock Hub	AISI 1020	MCMaster-CARR	1
4	C-ZZ-F-04-FLYWHEEL_EXTENSION	Plain Carbon Steel	DAVID MILLER	1
5	C-ZZ-F-04-FLYWHEEL_WEIGHT	Plain Carbon Steel	DAVID MILLER	12
6	8 x 20L Shoulder Screw	ALLOY STEEL	MCMaster-CARR	6
7	B18.2.4.1M - Hex nut, Style 1, M6 x 1 --D-N	ALLOY STEEL	SW LIBRARY	6
8	B18.2.4.1M - Hex nut, Style 1, M5 x 0.8 --D-N	ALLOY STEEL	SW LIBRARY	12
9	6 x 26L Shoulder Screw	ALLOY STEEL	MCMaster-CARR	12



UNLESS OTHERWISE SPECIFIED DIMENSIONS IN MILLIMETERS LINEAR TOL. ± 1 mm ANGULAR TOL. ± 1°	COMMENTS	DYNAMIC THERMAL ENERGY CONVERSION LAB DEPARTMENT OF MECHANICAL ENGINEERING UNIVERSITY OF ALBERTA		
	THIRD ANGLE PROJECTION	DRW DAVID MILLER	TITLE FLYWHEEL ASSEMBLY	
	SM DAVID MILLER	SIZE B	DRW NO C-ZZ-F-00-FLYWHEEL_ASM	REV B
	CHK	SCALE 1:5	MASS : 6877.39	SHEET 2 OF 3
MAT. N/A	CREATED 12/18/2015			
	EDITED 4/10/2019			

6

5

4

3

2

1

D

D

C

C

B

B

A

A

6

5

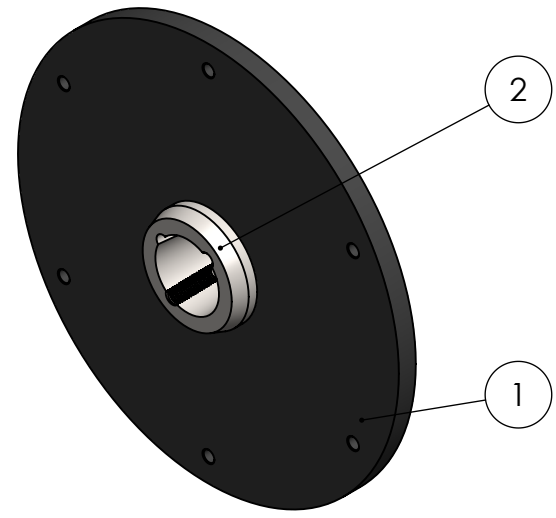
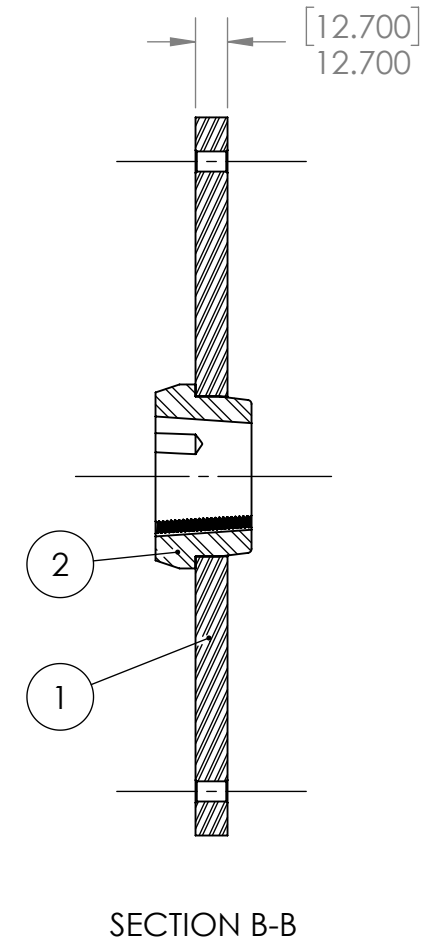
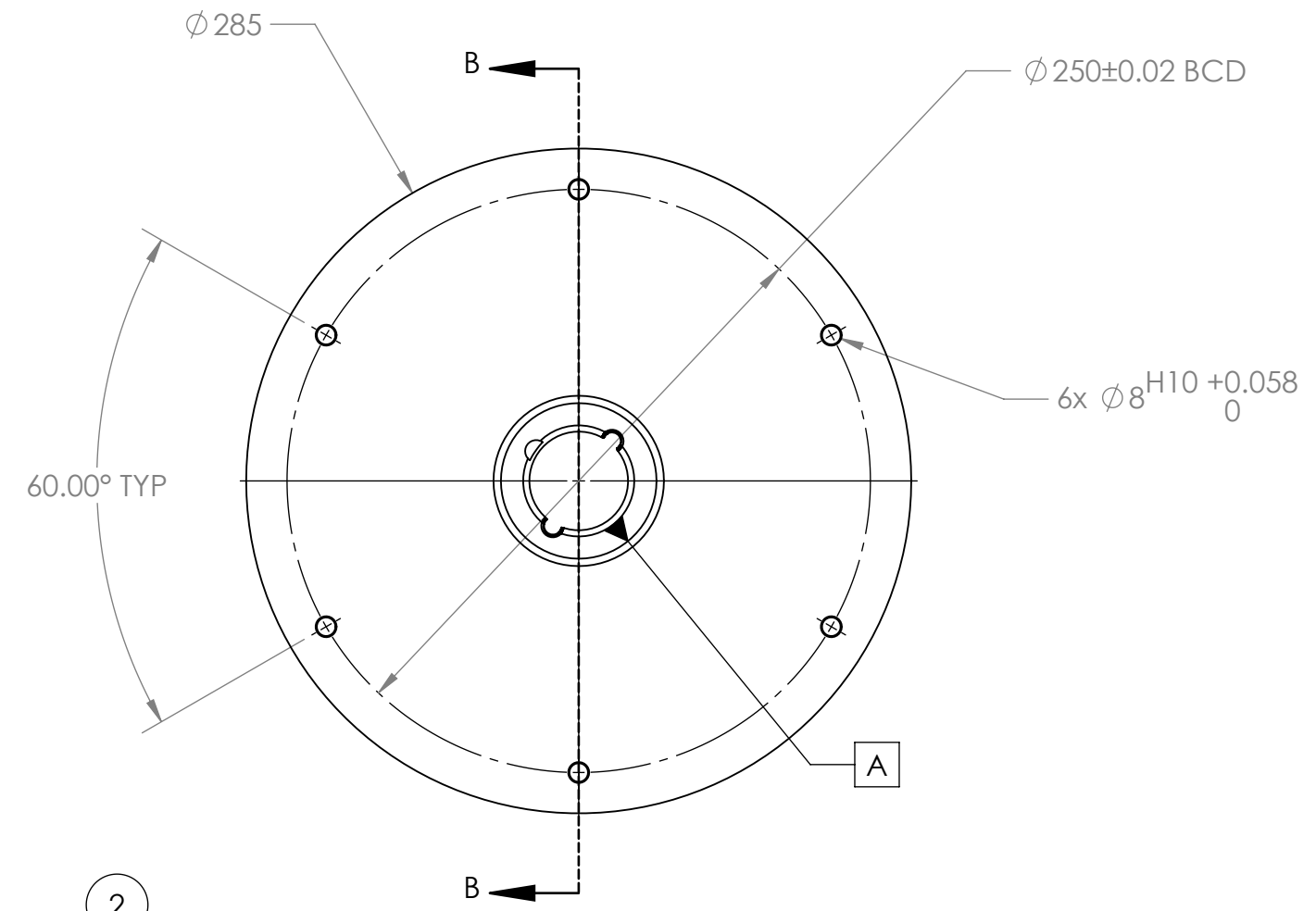
4

3

2

1

ITEM NO.	PART NUMBER	Material	SW-Author(Author)	No Taper Bushing/QTY.
1	C-ZZ-F-01-DISC	Plain Carbon Steel	Connor Speer	1
2	Weld-On Taper Lock Hub	AISI 1020	MCMaster-CARR	1



SCALE 1:4

UNLESS OTHERWISE SPECIFIED DIMENSIONS IN MILLIMETERS LINEAR TOL. $\pm 1$ mm ANGULAR TOL. $\pm 1^\circ$	COMMENTS	DYNAMIC THERMAL ENERGY CONVERSION LAB DEPARTMENT OF MECHANICAL ENGINEERING UNIVERSITY OF ALBERTA		
	THIRD ANGLE PROJECTION	TITLE FLYWHEEL ASSEMBLY		
		DRW DAVID MILLER	SIZE B	
		SM DAVID MILLER	DRW NO C-ZZ-F-00-FLYWHEEL_ASM	REV B
MAT. N/A	CHK	SCALE 1:3	MASS : 6877.39	SHEET 3 OF 3
	CREATED 12/18/2015 EDITED 4/10/2019			

6

5

4

3

2

1

D

C

B

A

D

C

B

A

6 5 4 3 2 1

D

D

C

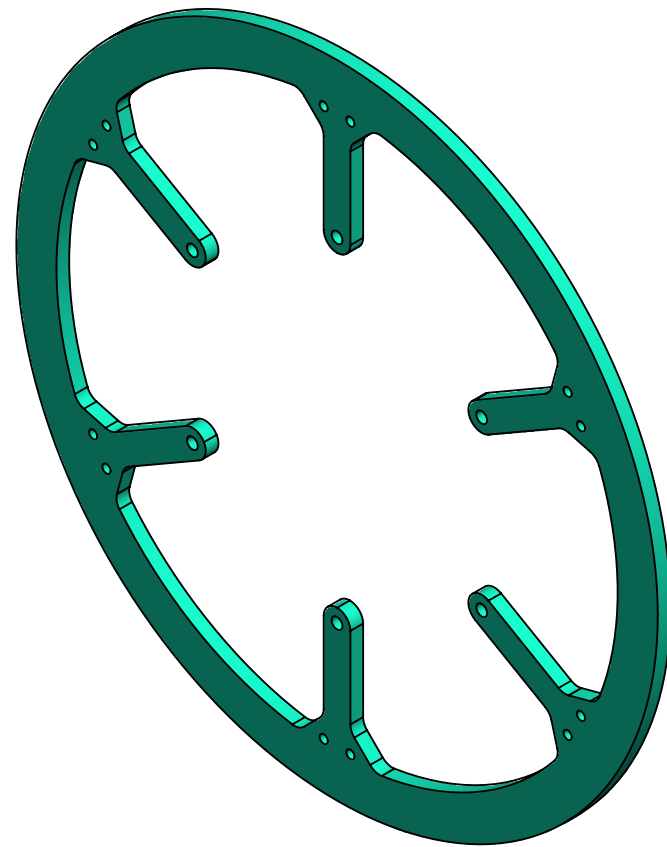
C

B

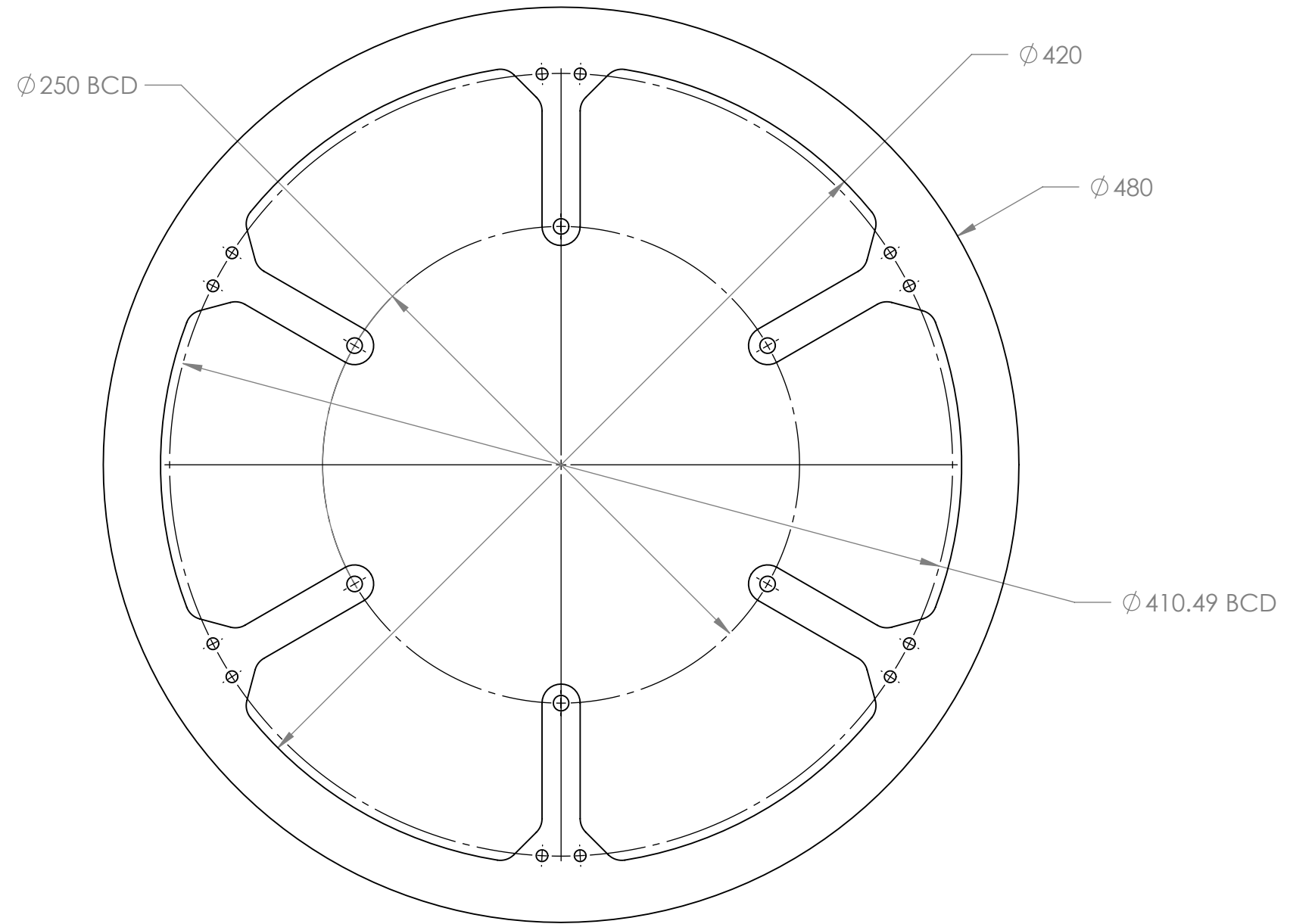
B

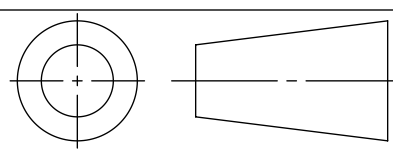
A

A



SCALE 1:4



UNLESS OTHERWISE SPECIFIED DIMENSIONS IN MILLIMETERS LINEAR TOL. $\pm 1$ mm ANGULAR TOL. $\pm 1^\circ$	COMMENTS	DYNAMIC THERMAL ENERGY CONVERSION LAB DEPARTMENT OF MECHANICAL ENGINEERING UNIVERSITY OF ALBERTA		
	THICKNESS: 9.525 (3/8") QTY: 1	TITLE		
THIRD ANGLE PROJECTION	DRW DAVID MILLER	ENLARGED FLYWHEEL DISC		
	SM DAVID MILLER	SIZE   DRW NO   REV		
	CHK	B	C-ZZ-F-04-FLYWHEEL_EXTENSION	B
MAT. PLAIN CARBON STEEL	CREATED 6/26/2018	SCALE 1:3	MASS: 4099.14717	SHEET 1 OF 1
	EDITED 10/25/2018			

6 5 4 3 2 1

6

5

4

3

2

1

D

D

C

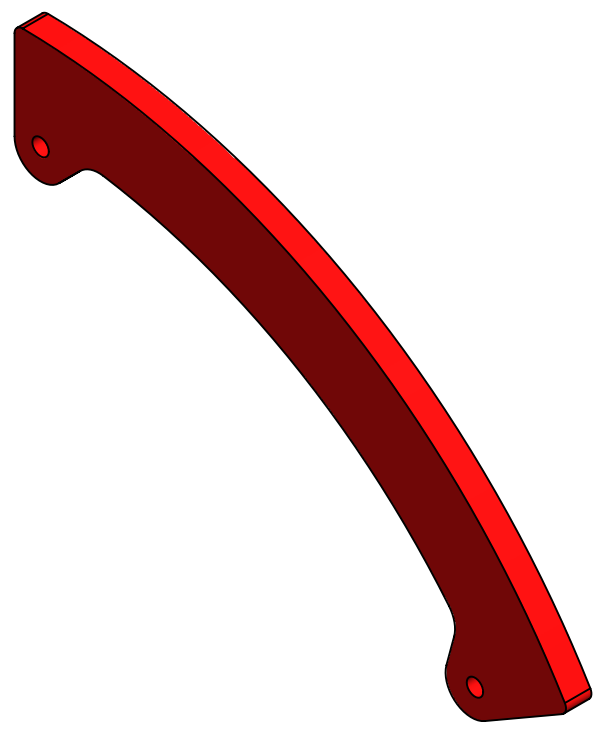
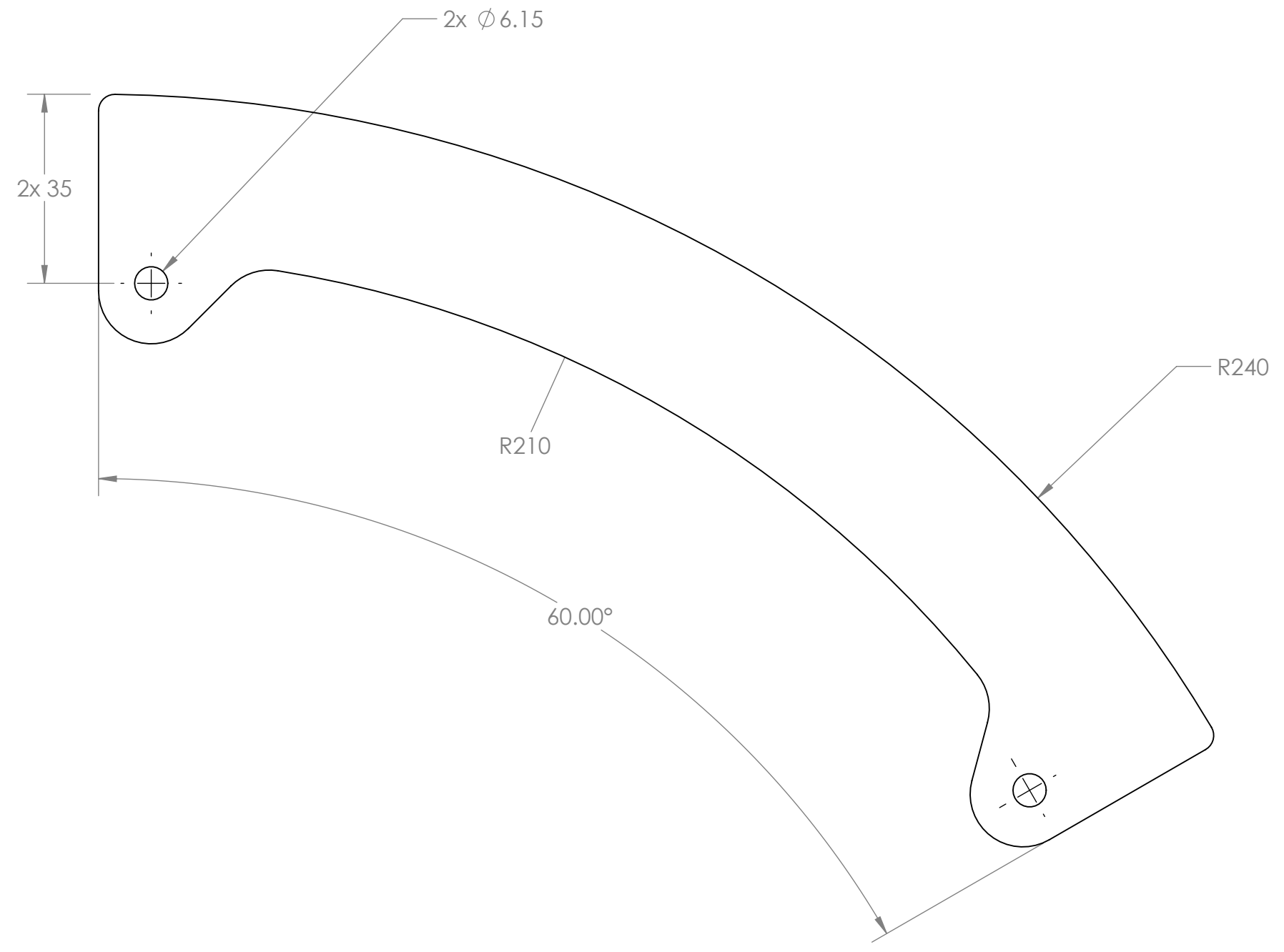
C

B

B

A

A



SCALE 1:2

UNLESS OTHERWISE SPECIFIED DIMENSIONS IN MILLIMETERS LINEAR TOL. $\pm 1$ mm ANGULAR TOL. $\pm 1^\circ$		COMMENTS THICKNESS: 9.525 (3/8") QTY: 12		DYNAMIC THERMAL ENERGY CONVERSION LAB DEPARTMENT OF MECHANICAL ENGINEERING UNIVERSITY OF ALBERTA	
THIRD ANGLE PROJECTION		DRW DAVID MILLER		TITLE ENLARGED FLYWHEEL WEIGHT	
		SM DAVID MILLER		SIZE   DRW NO	
		CHK		B   C-ZZ-F-04-FLYWHEEL_WEIGHT	
MAT. PLAIN CARBON STEEL		CREATED 6/26/2018		REV B	
		EDITED 10/11/2018		SCALE 1:1   MASS: 566.29010   SHEET 1 OF 1	

6

5

4

3

2

1